TECTONIC EVOLUTION OF THE SOUTHEAST PAMIR

A Dissertation Presented to

the Faculty of the Department of Earth and Atmospheric Sciences

University of Houston

In Partial Fulfillment

of the Requirements for the Degree

Doctor of Philosophy

By

Daniel Bryant Imrecke

December 2013

TECTONIC EVOLUTION OF THE SOUTHEAST PAMIR

_____
Daniel Bryant Imrecke

APPROVED:

_____
Dr. Alexander Robinson, Chairman

_____
Dr. Michael Murphy

_____
Dr. Thomas Lapen

_____
Dr. John Bershaw, Chevron

_____
Dan Wells, Dean, College of
Natural Sciences and Mathematics

ACKNOWLEDGEMENTS

I want to give special thanks to Dr. Alex Robinson for giving me this research opportunity, outlining the research objectives, and for continued guidance, feedback, and support throughout my graduate education. This research could not have been completed without funding by the National Science Foundation.

I would also like to thank my thesis committee members for their help and contributions to this dissertation. I would like to thank Dr. Tom Lapen for his help in the analytical analyses and metamorphic petrology. I would like to thank Dr. Mike Murphy for calling me late one night in 2009 to encourage me to take this opportunity. Dr. John Bershaw's questions gave me new perspectives to think about my interpretations.

Several fellow graduate students were tremendously helpful. I would like to thank Dr. Barry Shaulis as well for his help setting up the LA-ICPMS and reducing the zircon data. I would like to thank Dr. Veronica Sanchez for her help in the heavy liquids laboratory.

Finally, I would especially like to thank Carissa Imrecke, my wife, who made personal sacrifices for the sake of my completion of this degree.

TECTONIC EVOLUTION OF THE SOUTHEAST PAMIR

An Abstract of a Dissertation

Presented to

the Faculty of the Department of Earth and Atmospheric Sciences

University of Houston

In Partial Fulfillment

of the Requirements for the Degree

Doctor of Philosophy

By

Daniel Bryant Imrecke

December 2013

ABSTRACT

This study investigates the Mesozoic and Cenozoic tectonic evolution of the Southeast Pamir. Part one of this study focuses on the Neogene tectonic evolution of the Waqia Valley southeast of the Miocene Muztaghata Gneiss Dome. The valley was previously proposed to be bound to the northeast by the active left-slip Karakax Fault, which predicts active shortening structures and strike-slip separation in the valley. To test this model, geologic field mapping of sedimentary and basement units was conducted. The Waqia Valley is bound to the north and northeast by the Shen-Ti and Waqia Faults, which show extensional kinematics. Two distinct generations of sedimentary deposits occur in the valley: 1) Neogene deposits, which are up to ~1000 m thick, are cut by normal faults, onlap paleo-topography of basement units, and are in fault-contact with the Waqia Fault, and 2) undeformed Quaternary deposits which onlap previously eroded Neogene deposits. The absence of shortening or left-lateral strike slip structures or Quaternary deformation in the Waqia valley indicates the Karakax Fault does not project into the study area. Rather, the Waqia Valley basin formed by extension along the propagating tip of the Shen-Ti/Waqia Fault in the hanging wall of the Muztaghata Gneiss Dome. Part two of this study evaluates the Mesozoic deformation history and terrane architecture of the southeast Pamir. Structural field mapping of metasedimentary and igneous units in the study area, metamorphic petrology, garnet-biotite thermometry, and zircon U/Pb isotopic analysis were used to define and compare structural units north and south of the Muztaghata Gneiss Dome. North of Muztaghata, the Baoziya Thrust juxtaposes Triassic age amphibolite facies schists and gneisses with Triassic granites structurally above greenschist facies metasediments. South of the dome, the synformal

Torbashi Thrust juxtaposes Triassic age amphibolite facies schists and gneisses with Triassic granites structurally above footwall greenschist facies metasediments. Based on these similarities, I propose the Baoziya and Torbashi Thrust previously formed a continuous thrust nappe prior to being cut by exhumation of the Muztaghata dome. In the southern footwall of the Torbashi Thrust, greenschist facies Metasediments intruded by Ordovician granites lie structurally above low-grade Paleozoic metasediments of Gondwanan affinity. The juxtaposition of Gondwanan rocks to the south, against units of Asian affinity to the north, implies the presence of a suture through the study area and provide new constraints on the geometry and deflection of terranes across the western Tibetan Orogen.

Table of Contents

LIST OF FIGURES

CHAPTER 1: Neogene Tectonic Evolution of the Southeast Pamir

1. INTRODUCTION

The Tibetan orogen is the preeminent location to study deformation processes associated with continent-continent collision. One component interpreted to be important in accommodating convergence in continental collision zones is the development of conjugate strike-slip fault systems (Tapponnier et al., 1982; Yin and Taylor, 2011). Although strike-slip faults such as the Karakoram and Karakax/Altyn-Tagh fault are hundreds of kilometers long, their longevity and interaction as conjugate structures has been a matter of debate. One model argues these structures, particularly the Karakoram Fault, are long-lived with large magnitudes of slip along their entire fault trace, accommodating the lateral eastward extrusion of Tibet (Molnar and Tapponnier, 1975; Tapponnier et al., 1982; Peltzer and Tapponnier, 1988; Valli et al., 2007; Valli et al., 2008). Alternatively, the Karakoram Fault and Karakax Faults may be transient structures, relative to deformation in the Tibetan Orogen, that evolve and change over time (Dunlap et al., 1998; Murphy et al., 2000; Murphy and Copeland, 2005).

A critical test of the role and possible interactions of the Karakoram and Karakax Fault systems is to study the region at the proposed intersection of the two structures, the Waqia and Tashkurgan Valleys in the southeast Pamir (Tapponnier et al., 1982; Yin and Bain, 1992; Brunel et al., 1994; Strecker et al., 1995). Thus, the Waqia Valley (Figure 1,2,3) was chosen for this study for several reasons. 1) The Waqia Valley is situated at the previously proposed intersection of the Karakax and Karakoram Faults (Figure 1) (Tapponnier and Molnar, 1976; Tapponnier et al., 1982; Yin and Bain, 1992; Brunel et al., 1994). 2) The valley also is situated at the southeastern tip of the Muztaghata Gneiss Dome (Robinson et al., 2007). 3) The Waqia Valley contains a sequence of sedimentary

deposits that do not crop out in the adjacent Tashkurgan Valley, suggesting the two valleys have a different sedimentary/structural history (Figure 3).

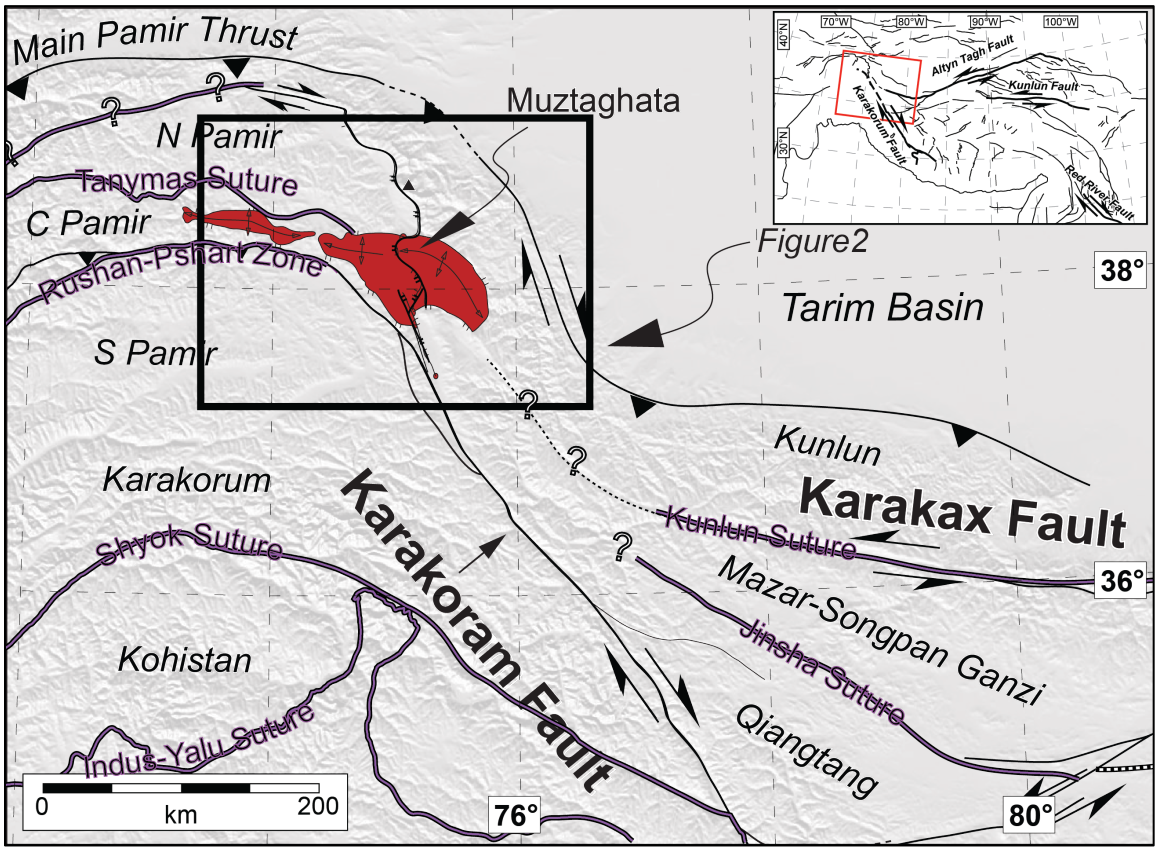

Figure 1: Simplified tectonic map of the Pamir and western Tibet showing the relationship of major regional structures modified from Robinson (2009b). The large red regions are the Miocene Central Pamir Gneiss Domes; the easternmost is the Muztaghata Gneiss Dome. Thick purple lines represent suture zones. Dark black lines represent major faults. The traces of suture zones in the vicinity of the Karakoram Fault are unclear, and thus not identified in this map.

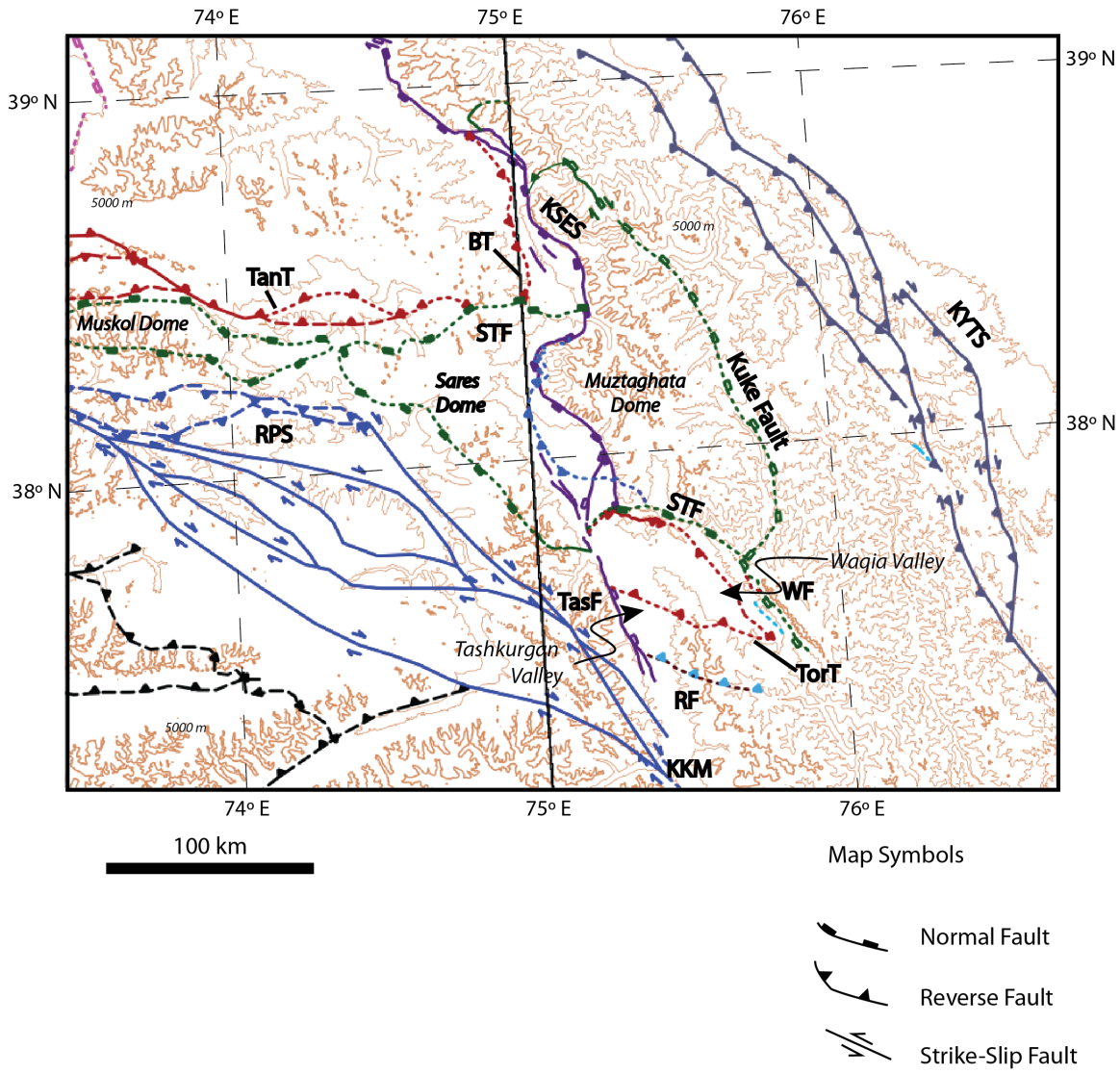

Figure 2: Simplified tectonic map showing the relationship of structures in the Eastern Pamir. Contour interval is 500m. KKM, Karakoram Fault; RPS, Rushan-Pshart Zone; STF, Shen-Ti Fault; TorT, Torbashi Thrust TanT, Tanymas Thrust;; TasF; Tashkurgan Fault; KYTS, Kashgar Yechang Transfer System.

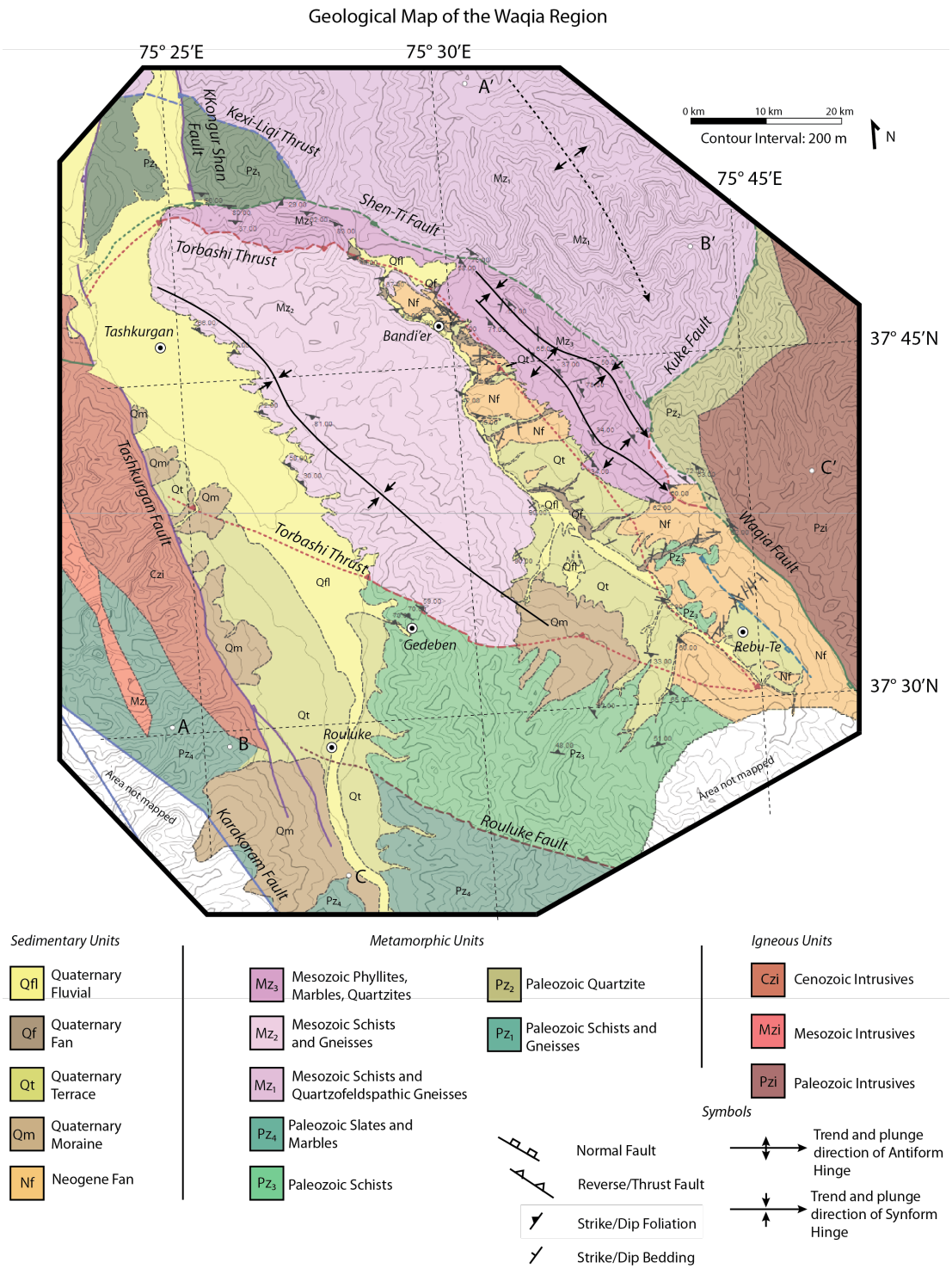

Figure 3: Geological map and cross sections (next page) of the Tashkurgan/Waqia Valley region.

Figure 3 (continued)

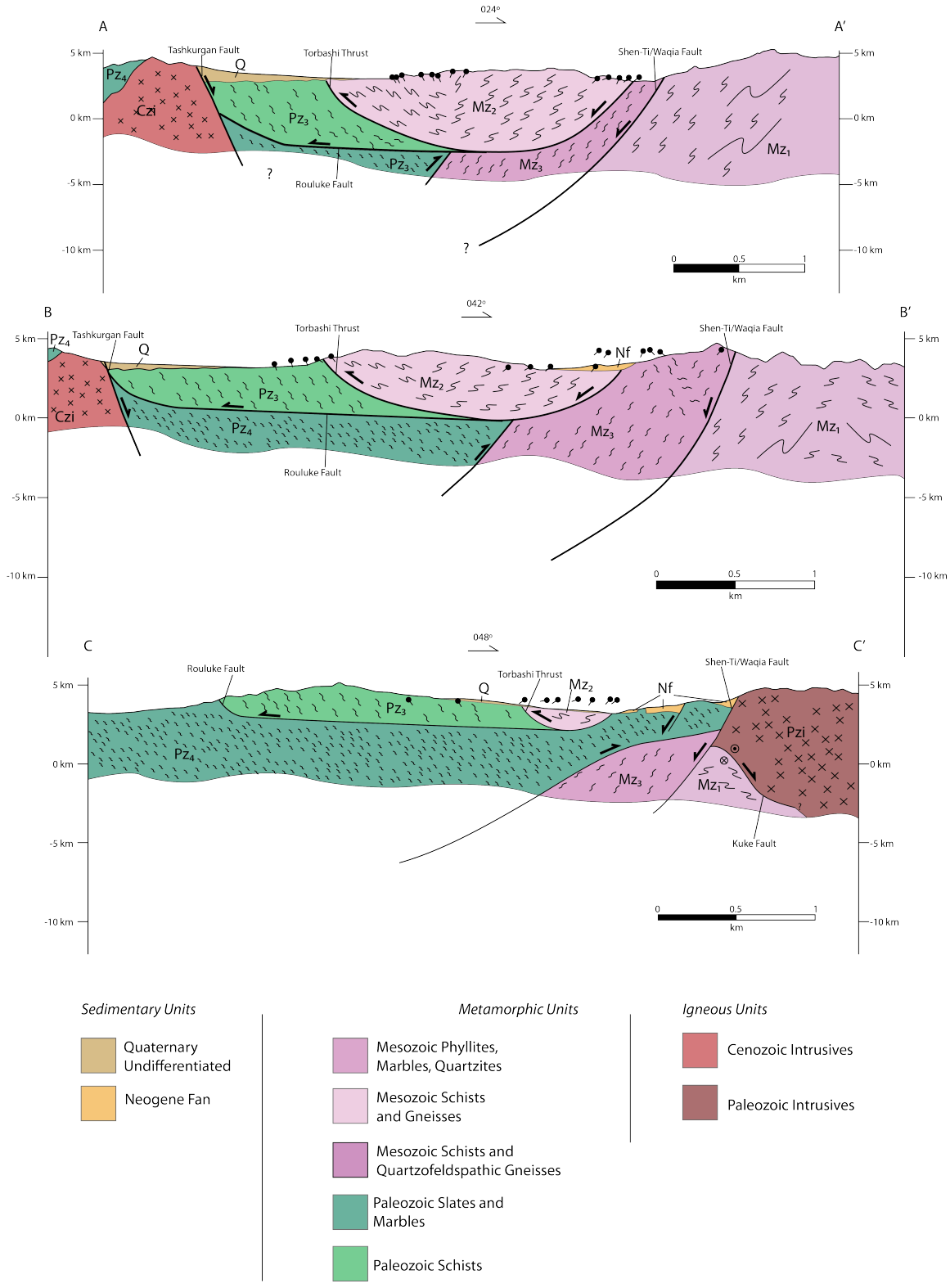

In this study, I evaluate the tectonic evolution of the Waqia Valley by mapping the distribution and deformation of basin sediments and the brittle deformation in the metamorphic basement. I use structural and stratigraphic observations in the Waqia Valley to document the Neogene deformation and interpret the relationship of local structures to regional tectonics. I test three models for the regional evolution of the study area based on its location relative to major tectonic systems. 1) The valley formed as a result of slip along the Karakax Fault, a major structure interpreted to project into the northwestern margin of the study area (Figure 4). This model predicts active northwest striking shortening structures and left-slip faults within the Waqia valley. 2) The Karakoram and Karakax faults acted as a conjugate pair. This model predicts northwest striking left-slip faults, northwest striking shortening structures, and/or northeast striking normal faults. 3) The valley formed as a result of hanging wall subsidence resulting from slip along the Shen-Ti normal fault accommodating tectonic exhumation of the Muztaghata Gneiss Dome. This model predicts deformation contemporaneous with the exhumation of the Miocene Pamir Gneiss Domes and dominantly northeast-directed extensional strain. I present data that does not support the interpretation that the Karakax Fault continues into the Southeast Pamir. Instead, Neogene deformation present in the study area is associated with the Miocene tectonic exhumation of the Central Pamir Gneiss Domes.

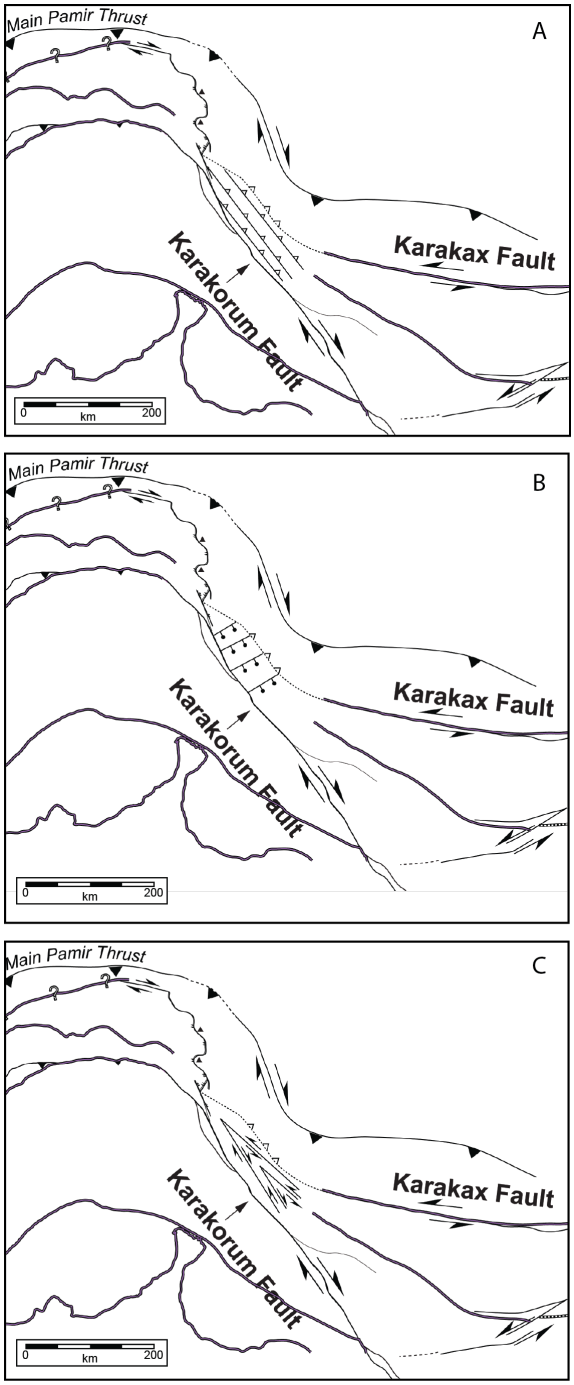

Figure 4: Model for predicted structure geometry and kinematics for the Waqia Valley region assuming Karakoram/Karakax Fault interactions. Map modified from Robinson (2009b). Model modified from (Yin and Taylor 2011). (A) Northwest striking shortening structures. Principle shortening direction would be northeast. (B) Northeast striking normal faults and extensional structures. Principle extension direction would be northwest. (C) Northwest striking strike slip faults. Left-slip strike slipping faults would be near the Karakax Fault, Right-Slip strike-slip faults would be near the Karakoram Fault.

2. TECTONIC SETTING

The Pamir Mountains are located in the northwest corner of the Himalayan-Tibetan orogen (Figure 1). Their topographic expression consists of an arcuate region of high topography bound to the north by the Main Pamir Thrust and the Alai Basin, to the south by the Karakoram Range, to the east by the Tarim Basin, and to the west by the Tadjik Basin. During the Cenozoic, the Pamir were translated north with respect to stable Asia by ~300-400 km via the Alai subduction system (Burtman and Molnar, 1993; Sobel et al., 2013). Additionally, Cenozoic shortening within the Pamir have been estimated to be ~300 km , resulting in a present day crustal thickness of 70 km (Burtman and Molnar, 1993; Sobel et al., 2011; Mechie et al., 2012; Sobel et al., 2013).

The Pamir are traditionally divided into three members (Figure 1,2). 1) The Northern Pamir is bound by the Main Pamir Thrust (MPT) to the north and the Tanymas suture zone in the south. 2) The Central Pamir is bound by the Tanymas suture in the north and the Rushan-Pshart zone in the south. 3) The Southern Pamir and Karakoram Terrane is bound to the north by the Rushan-Pshart zone and the Shyok suture in the south (Figure 3). While these boundaries have been traditionally used to delineate distinct tectonostratigraphic blocks (Burtman and Molnar, 1993), recent studies indicate a more complex geometry in the eastern Pamir (Schwab et al., 2004; Robinson et al., 2012). These studies show the northern Pamir is a composite of Kunlun and Songpan-Ganzi equivalent terranes, based on detrital zircon analyses (Robinson et al., 2012). Further, the South Pamir and Karakoram Terrane are interpreted to be separated by a suture, the Wakhan-Tirich Boundary Zone (Angiolini et al., 2013). Therefore, in this

chapter I refer to the North Pamir, Central Pamir, and South Pamir as geographical regions without reference to tectonostratigraphic relationships.

2.1. STRUCTURAL GEOLOGY OF THE EASTERN PAMIR

The Pamir have experienced a protracted tectonic history since the Permian involving accretion of Gondwanan continental fragments in the Triassic/Jurassic and Middle Cretaceous, followed by the India-Asia collision in the early Cenozoic (Robinson et al., 2012). Slab breakoff of the western Indian plate at ~25 Ma is interpreted to have reorganized the tectonic framework of the Pamir region (Figure 5) (Amidon and Hynek, 2010; Replumaz et al., 2010; Wilke et al., 2012; Sobel et al., 2013). Shortening was transferred along the Main Pamir Thrust accommodating northward translation, orocline formation, and internal deformation of the Pamir (Robinson et al., 2004, 2007; Sobel et al., 2013; Thiede et al., 2013). In this section, I summarize primary Cenozoic structures which contributed to the tectonic framework of the eastern Pamir.

2.1.1. Strike–Slip Faults

2.1.1.1. Karakoram Fault

The right-slip Karakoram Fault is a prominent structure of the Himalayan-Tibetan Orogen that bounds the western margin of the Tibetan Plateau (Figure 1). The fault runs from the Gurla Mandata massif in southwestern Tibet (Murphy et al., 2000) more than 1000 km northwest to the Pamir (Figure 1). The Karakoram Fault likely initiated in the Early-Middle Miocene (Phillips et al., 2004; Valli et al., 2008), accommodating right-lateral slip. The role of the Karakoram Fault in the Cenozoic evolution of the Himalayan-Tibetan orogen has been a matter of considerable debate. The Karakoram Fault has previously interpreted to have accommodated 500-1000 km total slip, be long-lived, and

to facilitate large-scale extrusion of Tibet (Tapponnier et al., 1982; Peltzer and Tapponnier, 1988; Lacassin et al., 2004; Schwab et al., 2004; Valli et al., 2008). However, recent studies have interpreted the Karakoram Fault to be a transient structure playing a limited role in the evolution of the Tibetan orogen, with ~168 km of right-lateral slip, (Burtman and Molnar, 1993; Ratschbacher et al., 1994; Searle, 1996; Searle et al., 1998; Seeber and Pêcher, 1998; Murphy et al., 2000; Robinson, 2009a; Sobel et al., 2013).

The geometry and kinematics of the Karakoram Fault as it traces into the Pamir is a matter of considerable debate. Some researchers argue the Kongur Shan Extensional System is the northward extension of the Karakoram Fault System (Phillips et al., 2004; Chevalier et al., 2011). However, several lines of evidence show that the Karakoram Fault links with the Rushan-Pshart Zone in the South Pamir, and is kinematically unrelated to the Kongur Shan fault system (Robinson, 2009b; Robinson, 2009a) 1) The Muztaghata gneiss dome is an along-strike equivalent of the Central Pamir Gneiss Domes with no observable offset by the Karakoram Fault (Robinson et al., 2007). 2) A south directed decrease in total displacement along the Kongur Shan Extensional System (KSES), ending at the southern tip of the Tashkurgan Fault conflicts with an interpretation linking the Karakoram Fault and the KSES (Robinson et al., 2007). 3) The Karakoram Fault is currently inactive, based on no evidence of offset Quaternary features in the Tashkurgan Valley (Robinson, 2009a; Owen et al., 2012), whereas the KSES is clearly active (Liu et al., 1993; Robinson et al., 2007).

2.1.1.2. Karakax Fault

The currently active Karakax Fault is a west-striking, left-slip fault that can be traced from the Altyn-Tagh Fault in the east, through the Karakax valley (Ding et al., 2004), to an unknown location in the west (Figure 1). Although the total slip of the fault system is difficult to quantify by offset bedrock markers, estimates of relatively high slip rates derived from offset Quaternary features along the western segment suggest the fault transfers slip a significant distance to the west beyond it's known western segment (Ryerson et al., 1997; Ryerson et al., 1999; Shen et al., 2001; Ding et al., 2004). Correlation of the Karakax Fault with structures in the Waqia or Tashkurgan valleys has not been established. However, several workers have interpreted the trace of the Karakax Fault to continue into the southeastern Pamir through the Waqia Valley (Yin and Bain, 1992; Brunel et al., 1994; Raterman et al., 2007) (Figure 1), where slip has been depicted as having extensional kinematics (Brunel et al., 1994).

2.1.1.3. Predictions

Several predictions, or models, can be made for the interaction of the Karakoram and/or the Karakax Fault in the Waqia and Tashkurgan valleys:

Model 1 suggests the Karakoram and Karakax Fault systems acted as conjugate strike-slip fault systems (Tapponnier et al., 1982). This model requires opposing slip sense and contemporaneous activity between the two structures. Although the Karakoram Fault is currently inactive, (Robinson, 2009a) and the Karakax Fault is currently active (Ryerson et al., 1997; Ryerson et al., 1999; Shen et al., 2001; Ding et al., 2004), I consider the scenario in which the faults acted as conjugate structures at some earlier time. The model predicts three possible geometries in the Waqia and Tashkurgan

Valleys: 1) northwest-striking thrust faults with northeast directed principal shortening and vertical extension directions; 2) northeast-striking normal faults with southeast principle extension and vertical shortening directions; and 3) northwest striking conjugate fault systems with northeast shortening and southeast extension directions. This model predicts right-slip faults in the Tashkurgan Valley and left-slip faults in the Waqia valley. Kinematic analysis of fault surfaces is predicted to record northwest-directed principal shortening and southeast-directed principal extension. Any combination of these three scenarios are predicted within the Waqia and Tashkurgan Valleys in this model

Model 2 suggests the Waqia Valley is bound on its northeastern section by the westward continuation of the Karakax Fault on its northeast margin (Brunel et al., 1994), but does not act as a conjugate to the Karakoram Fault. The Karakax Fault has left-slip kinematics along its fault trace in the Karakax Valley (Ding et al., 2004). However, the geometry of the interpreted fault trace in this region would require a zone of shortening and left-lateral offset in the Waqia Valley because the fault trace results in a right bend on a left-slip structure (Yin and Bain, 1992; Raterman et al., 2007). Therefore, if the Karakax fault continues into the study area, and the fault is not a conjugate with the Karakoram fault, then northwest striking thrust faults and fold axes are interpreted to be present.

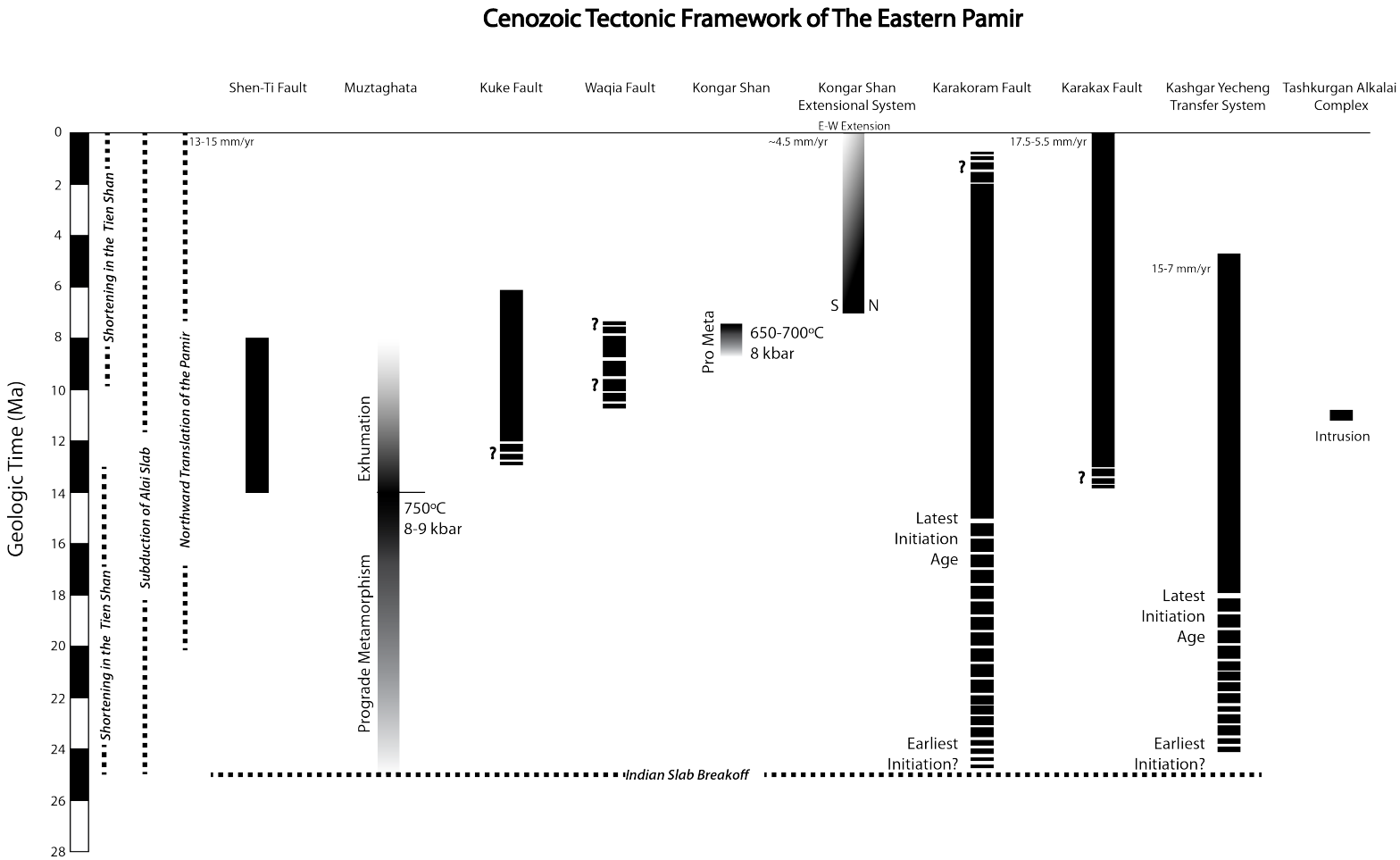

Figure 5: Cenozoic tectonic framework of the eastern Pamir. Vertical axis is geologic time. Black bars represent timing of activity. Shaded bars are schematic representations of events. Quaternary slip rates are indicated for structures at the top of the chart. Data is from (Ding et al. 2004; Robinson et al. 2004; Raterman et al 2007; Robinson et al. 2007; Robinson et al. 2009; Robinson et al. 2009b; Cowgill et al. 2010; Sobel et al. 2010).

2.1.2. Pamir Gneiss Domes

The Pamir gneiss domes are fault-bounded high-grade schists and gneisses in the Pamir (Figure 1,2) (Pashkov and Schvol'Man, 1979; Peykre et al., 1982; Schwab et al., 2004; Robinson et al., 2007) and are exposed as the Shakdara, Muskol, Sares, and Muztaghata, and Kongur Shan domes (Figure 2). These domes represent lower to mid-crustal rocks that which are suggested to be tectonically exhumed from ~40 km depth as a result of differential shortening in the lower crust (Figure 12 in Robinson et al. 2007). However, recent correlations of terranes in the eastern Pamir at Muztaghata suggest the predicted significant northward translation of lower crustal material is unlikely (Robinson et al., 2012). A newer model for Pamir dome exhumation suggests the driving mechanism is gravitational collapse of thickened Pamir crust (Stübner et al., 2013). In this section, I briefly describe and summarize the Pamir domes adjacent to the study area.

2.1.2.1. Muskol and Sares Domes

The Muskol and Sares Domes of the central Pamir are part of the Central Pamir Gneiss Domes (Figure 2). The cores consist of granitic gneisses, marbles, amphibolites, and high-grade schists (Pashkov and Schvol'Man, 1979; Peykre et al., 1982; Schwab et al., 2004; Schmidt et al., 2011). The Muskol dome reached peak metamorphic conditions (6-14 kbar and 500-800°C) at ~17 Ma (Schmidt et al., 2011). The Sares dome and the Muztaghata dome have been interpreted to be a continuous structure cut by the Kongur Shan Fault (Robinson et al., 2007). The domes are bound by low angle normal faults which accommodated extension from 14-8 Ma which originated as a regional décollement, the Pamir Shear Zone (Robinson et al., 2007; Sippl et al., 2013; Stübner et

al., 2013). Cessation of north-south extension occurred shortly after the onset of collision of the Pamir with the Tien Shan (Sobel et al., 2006), implying the Tien Shan may have provided compensation for gravitational collapse accommodating exhumation (Stübner et al., 2013).

2.1.2.2. Muztaghata Dome

The Muztaghata Gneiss dome (Figure 2) is the easternmost member of the Central Pamir Gneiss Domes and the southern member of the Eastern Pamir Gneiss Domes, which consist of the Muztaghata and Kongur Shan Domes. The Muztaghata dome consists of quartzofeldspathic gneisses structurally beneath high-grade schists and reached peak metamorphism (9-10 kbar 700-750°C) at 25-14 Ma (Robinson et al., 2007).

In the study area, the normal slip Shen-Ti and Kuke faults are the main bounding structures which accommodated tectonic exhumation of the Muztaghata gneiss dome (Robinson et al., 2007; Sobel et al., 2011). The Shen-Ti Fault strikes east-west along the Tashkurgan River (Figure 2,3) (Robinson et al., 2007). The fault juxtaposes amphibolite facies quartzofeldspathic gneisses and high-grade schists in the footwall against greenschist facies marbles and phyllites in the hanging wall (Robinson et al., 2007). Ductile shear kinematic indicators in the hanging wall and footwall of the fault record top to the south shear sense. The fault can be traced west, where it is cut by the Tashkurgan Fault. The Kuke Fault is the eastern structural boundary of the Muztaghata dome (Sobel et al., 2011; Xinjiang Bureau of Geology and Mineral Resources, 1993). The Kuke Fault strikes north-south and dips sub-vertically (Sobel et al., 2011). The steep dip, as well as cooling patterns in the Muztaghata antiform, suggests the Kuke Fault was rotated to its

present vertical orientation from a more shallow orientation as it evolved from 12-6 Ma (Sobel et al., 2011).

2.1.2.3. Doming and Exhumation

Mineral cooling ages are interpreted to document tectonic exhumation of the domes. East-directed diachronous cooling is evident in the Central Pamir Gneiss Domes from 25 to 6 Ma (Cao et al., 2013b). The Muskol and western Sares Dome were exhumed 25-17 Ma (Cao et al., 2013b). Post crystallization cooling of the Tashkurgan Pluton in the eastern Sares dome records rapid cooling and tectonic exhumation at 11-10 Ma (Cao et al., 2013b). In the easternmost member of the Central Pamir Gneiss Domes, the Muztaghata Gneiss Dome, cooling temperatures record syn-doming tectonic exhumation 12-6 Ma accommodated by slip along the Shen-Ti and Kuke Faults (Robinson et al., 2007; Sobel et al., 2011; Cao et al., 2013b).

2.1.2.4. Kongur Shan Dome

The Kongur Shan Dome (Figure 2), the northeastern-most member of the Pamir Gneiss Domes, is bound to east by the Kongur Shan Fault and the north and east by the Ghez Fault (Robinson et al., 2007; Robinson et al., 2012). The dome consists of quartzofeldspathic gneisses interlayered with occasional schists which reached peak metamorphic conditions (8 kbar and 600-750°C) at ~9 Ma (Robinson et al., 2004), possibly under the influence of a slab tear between the subducting Alai slab and Tarim Basin (Sobel et al., 2013; Thiede et al., 2013). Exhumation of the dome from since 7 Ma is accommodated by slip along the Kongur Shan Fault in the west (Brunel et al., 1994; Robinson et al., 2004; Sobel et al., 2011).

2.1.3. Kongur Shan Extensional System

Kongur-Shan Extensional System consists of the Muji Fault, Kongur Shan Fault, Tahaman Fault, and the Tashkurgan Fault of the eastern Pamir (Figure 2) (Robinson et al., 2004). The system has accommodated east-west extension in the eastern Pamir since the late Miocene and is currently active (Robinson et al., 2007; Robinson et al., 2010; Chevalier et al., 2011; Cao et al., 2013b). The magnitude of east-west extension decreases southward from Kongur Shan (~35 km extension) to the Tashkurgan Fault (<3 km extension) (Robinson et al., 2007). Timing of east extension is coincident with the onset of northwest-directed divergence of the Pamir toward the Tajik Basin after collision of the Pamir with the Tien Shan (Thiede et al., 2013).

2.1.3.1. Kongur Shan Fault

The Kongur Shan Fault is a sinuous north-south striking normal fault that accommodates east-west extension. The fault runs from the Kongur Shan Dome in the north to the Tahaman Fault in the south. The fault dips to the west ~30-60° (Robinson et al., 2007). Initiation of slip along the Kongur Shan Extensional System is as early as 8 Ma (Robinson et al., 2004, 2007; Robinson et al., 2010), however the fault may be as young as 6 Ma (Cao et al., 2013a; Cao et al., 2013b).

2.1.3.2. Tahman Fault

The steeply dipping Tahman Fault is a ~20 km long down-to-the-west normal fault accommodating extension between the Kongur Shan Fault in the north and the Tashkurgan Fault to the south. The fault is currently active, indicated by the presence of offset Quaternary deposits (1-2 m displacement) (Robinson et al., 2007).

2.1.3.3. Tashkurgan Fault

The southernmost feature of the Kongur Shan Extensional System is the Tashkurgan Fault. The Tashkurgan Fault is a ~75 km long down-to-the-east normal fault which bounds the western margin of the Tashkurgan Valley accommodating east-west extension. The fault juxtaposes quaternary glacial moraine and fluvial terrace deposits in the hanging wall against Cenozoic plutons of the Tashkurgan Alkaline complex (Zhang et al., 1996; Robinson et al., 2007). The fault is steeply dipping and accommodates low magnitudes of extension (~3 km) (Robinson et al., 2007). The presence of triangular facets along the fault trace indicates recent fault activity.

3. LITHOLOGIES

3.1. SHEN-TI/WAQIA FOOTWALL

3.1.1. Muztaghata Massif

The Muztaghata Gneiss Dome crops out in the footwall of the Shen-Ti/Waqia Fault (Figure 2,3) and consists of high-grade metasedimentary rocks underlain by quartzofeldspathic gneisses (Robinson et al., 2007). The metasedimentary rocks are composed of interlayered pelitic schists, marbles, and amphibolites with high-grade metamorphic mineral assemblages reaching 9-10 kbar ~750°C (Robinson et al., 2007). Compositionally banded Triassic quartzofeldspathic orthogneisses crop out to the east in the core of the dome (Robinson et al., 2007). Younger Mesozoic granites intrude the Muztaghata Gneiss Dome to the east (Yin and Bain, 1992).

3.1.2. Orodovician (?) Chert

Southwest of the quartzofeldspathic gneiss, massive Ordovician (?) quartzite (metamorphic chert) crops out in the footwall of the Shen-Ti/Waqia Fault, (Figure 3)

(Yin and Bain, 1992). The contact between the metachert and gneiss is interpreted to be a fault contact and correlative with the Kuke Fault (Sobel et al., 2011). The Quartzite is purple-grey in color and has relict original bedding oriented 124º/62º SW.

3.1.3. Paleozoic Plutons

Paleozoic granites crop out in the footwall of the Shen-Ti/Waqia Fault southeast of the Ordovician Chert (Yin and Bain, 1992). The intrusive rocks continue along the Waqia Fault footwall to the southeast of the study area.

3.2. SHEN-TI/WAQIA HANGING WALL

3.2.1. Metamorphic and Igneous Rocks

Metasedimentary and Igneous rocks crop out throughout the study area (Figure 3). The hanging wall of the Torbashi thrust consists of Triassic amphibolite facies schists and gneisses intruded by granites. The northern footwall consists of Triassic greenschist facies schists, phyllites, and marbles. In the Tashkurgan Valley, the southern footwall of the Torbashi consists of Paleozoic upper greenschist to lower amphibolite facies garnet-biotite schists, and quartzites intruded by Ordovician granites. Low grade Paleozoic marbles and slates crop out in the footwall of the Rouluke fault to the south. Alkali granites occur in the western margin of the Tashkurgan valley in the footwall of the Tashkurgan Fault.

3.2.2. Neogene Sedimentary Rocks – Waqia Valley

Several generations of sedimentary units crop out in the Waqia Valley (Figure 2,6). I distinguished and differentiated the basin sediments based on 1) correlative surfaces, 2) included clasts, and 3) relative age. Two primary age groups of sedimentary units were identified, which I categorize as Quaternary and Neogene in age.

A sequence of distinctively thick sedimentary deposits crop out throughout the Waqia Valley exclusively in the hanging-wall of the Shen-Ti/Waqia fault. Unpublished zircon (U-Th)/He ages of 7.8±0.6 and 8.0±0.6 Ma from samples in the footwall of the Waqia Fault (Sobel pers. comm.) record the timing of footwall exhumation. Assuming uplift of the footwall is coeval with faulting of the Shen-Ti/Waqia Fault and development of accommodation space within the hanging wall, I interpret the oldest sediments in the Waqia Valley to be Neogene age. The Neogene sedimentary units are described from northwest to southeast along the axis of the Waqia Valley.

3.2.2.1. Shen-Ti Segment

The northern section of the Waqia valley contains ~600 m thick Neogene sedimentary rocks which lie in a buttress unconformity above metamorphic basement (Figure 6a). Neogene sedimentary units are primarily confined to the river valley where the exposed thickness is ~200 m. However, conglomeratic units were observed capping the metamorphic basement at higher elevations (Figure 6, 10a). The oldest sediments exposed near the base of the valley are cobble conglomerates with lithic (metamorphic) clasts, primarily biotite schists and marbles. The Neogene units are thickly bedded and heavily weathered in this section. In most cases, bedding is identified by variations of color seen at a distance. Trenching and close inspection did not provide reliable surfaces to measure structural orientation of beds in most cases. Bedding is generally horizontal in the northern section of the Waqia Valley. However, tilting of the Neogene strata was observed near the town of Bandi'er, where there is monocline with a maximum limb dip of ~55° to the southeast (Figure 6b). Incised valleys of the Neogene units are onlapped by Quaternary fan, terrace, and fluvial deposits.

3.2.2.2. Waqia Segment

In the southern portion of the valley, Neogene sedimentary rocks are distributed over a wider area. The Neogene sediments crop out on the eastern side of the Waqia Valley where they are in fault-contact with metamorphosed chert and Paleozoic granites in the footwall of the Waqia Fault (Figure 6f). Exposed stratigraphic thickness along this segment of the Shen-Ti/Waqia Fault is a maximum of ~1000 m. Bedding orientation of Neogene strata is variable. Near the trace of the Waqia Fault, clast supported conglomerates dip ~15° southwest towards the valley axis. However, bedding changes to shallowly north-northeast dipping within 2 km southeast of the fault.

Grain size of Neogene sedimentary rocks decrease with distance from the Waqia Fault. Clast-supported boulder/cobble conglomerates occur proximal to the fault. Clasts are commonly angular to subangular and poorly sorted. Clast compositions are marble, quartzite, and rock fragments of granitic composition, in contrast to the dominantly pelitic schist clast compositions in Neogene sediments of the northern section of the valley. Fine-grained lithic sandstones and mudstones occur distal to the fault. Based on these observations, I interpret the Neogene sediments as alluvial fan deposits derived from the footwall of the Waqia Fault.

Neogene boulder-cobble conglomerates are interbedded with deposits of mono-lithologic (meta-chert) boulder beds ~10-20 m thick in the hanging wall near the Oligocene (?) meta-chert (Figure 6f). The meta-chert clast beds are interbedded with boulder/cobble conglomerate strata interpreted to have been deposited as alluvial fans. The occurrence of meta-chert beds interbedded with heterogeneous clast beds is

indicative of mass wasting, landslide deposits. These landslide deposits were only observed to crop out in the hanging wall adjacent to metachert bedrock in the footwall.

3.2.3. Quaternary Sedimentary Units

Quaternary deposits consist of fluvial, alluvial fan, and glacial moraine deposits. Quaternary deposits lie in buttress unconformity above metasedimentary basement or unconformably above older sedimentary units (Figure 6c,d). Quaternary fluvial deposits are actively being deposited along the axis of the Waqia Valley. Clast material is derived from surrounding bedrock and older sedimentary units within the basin. Grain size is highly variable, ranging from mud to cobble. Quaternary fan deposits onlap older bedrock and sedimentary units and are actively depositing sediment at the base of valleys, oriented orthogonal to major drainages. Sediment clasts in fans consist of cobble and pebble metasedimentary quartzites and schists, quartz + feldspar + rock fragment sands, and clay minerals. Quaternary glacial moraine deposits are exposed along the topographically higher regions of the southwestern portion of the Waqia and Tashkurgan Valleys. Moraine deposits were identified by the presence of boulders and diamict sediments at tributary valley mouths. Terrace deposits occur along the axis of the Tashkurgan and Waqia Valleys adjacent to the active fluvial system. Terrace deposits are onlapped by Quaternary fan deposits and fluvial deposits.

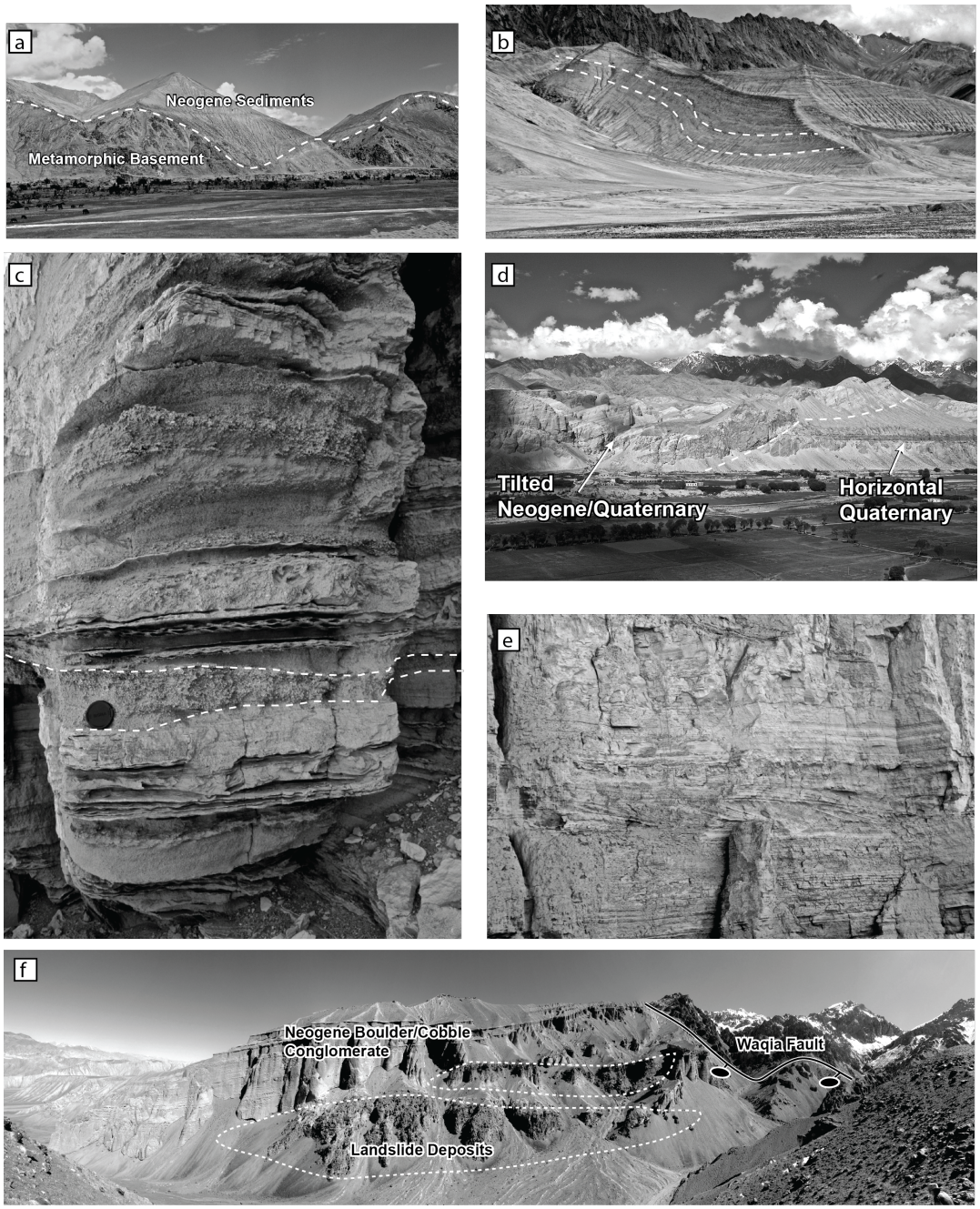

Figure 6: Field photographs of Neogene and Quaternary sedimentary units in the Waqia Valley. (A) Neogene sedimentary rocks at the northern section of the Waqia Valley. Horizontal Neogene sediments are in a buttress unconformity above metamorphic basement Units. (B) Monocline in Neogene sediments, dipping to the southwest. (C) Quaternary fluvial/lacustrine deposits. Highlighted are fluvial channel gravels. (D) Tilted Neogene or Quaternary units adjacent to horizontal quaternary units near Waqia town. The process for this deformation is interpreted to be glacially derived, not tectonic. (E) Horizontal bedding and cross bedding indicating fluvial/lacustrine depositional setting in Quaternary units. (F) Quartzite (meta-chert) landslide deposits interbedded with Neogene Boulder/Cobble conglomerates in the southern Waqia Valley. Neogene sediments are in fault contact with the Waqia Fault.

4. STRUCTURAL GEOLOGY

Detailed field mapping of geologic structures was carried out in the Waqia Valley to determine kinematics and cross-cutting relationships with Neogene and Quaternary sedimentary rocks. Stereographic projections of bedding, fault surfaces, and fault striations were made with OSX Stereonet 3 and strain axes were calculated using FaultKin 6 (Marrett and Allmendinger, 1990; Allmendinger et al., 2012; Cardozo and Allmendinger, 2013). Principle strain directions on faults are reported as trend/plunge based on Linked Bingham calculations of striated fault surfaces.

4.1. BEDDING ORIENTATION

In order to note significant differences in the Neogene bedding between the Shen-Ti and Waqia segments, I produced contoured stereographic projections of structural measurements of Neogene bedding (Figure 7). Poles to planes were contoured using the 1% area method and a 2% contour interval. Three clusters of bedding dip were observed for Neogene deposits along the Shen-Ti segment of the fault: 1) beds with a horizontal orientation, 2) beds with a strike and dip of 123°/31° SW, and 3) beds with a strike and dip of 135°/56° SW. Along the Waqia segment, two clusters of bedding dip were observed: 1) beds with a strike and dip of 345°/5° NE and 2) beds with a strike and dip of 000°/32°W.

Quaternary sediments do not show evidence of tectonic deformation. One notable feature in the Waqia Valley, near Waqia Town, consists of horizontal Quaternary terrace sediments in abrupt contact with adjacent to northeast dipping Quaternary or Neogene sediments (Figure 6d). No offset of bedrock units was observed along strike of this

contact. Field investigation of surrounding bedrock and sedimentary structures revealed this relationship to be related to glacial advance and retreat rather than tectonic in origin.

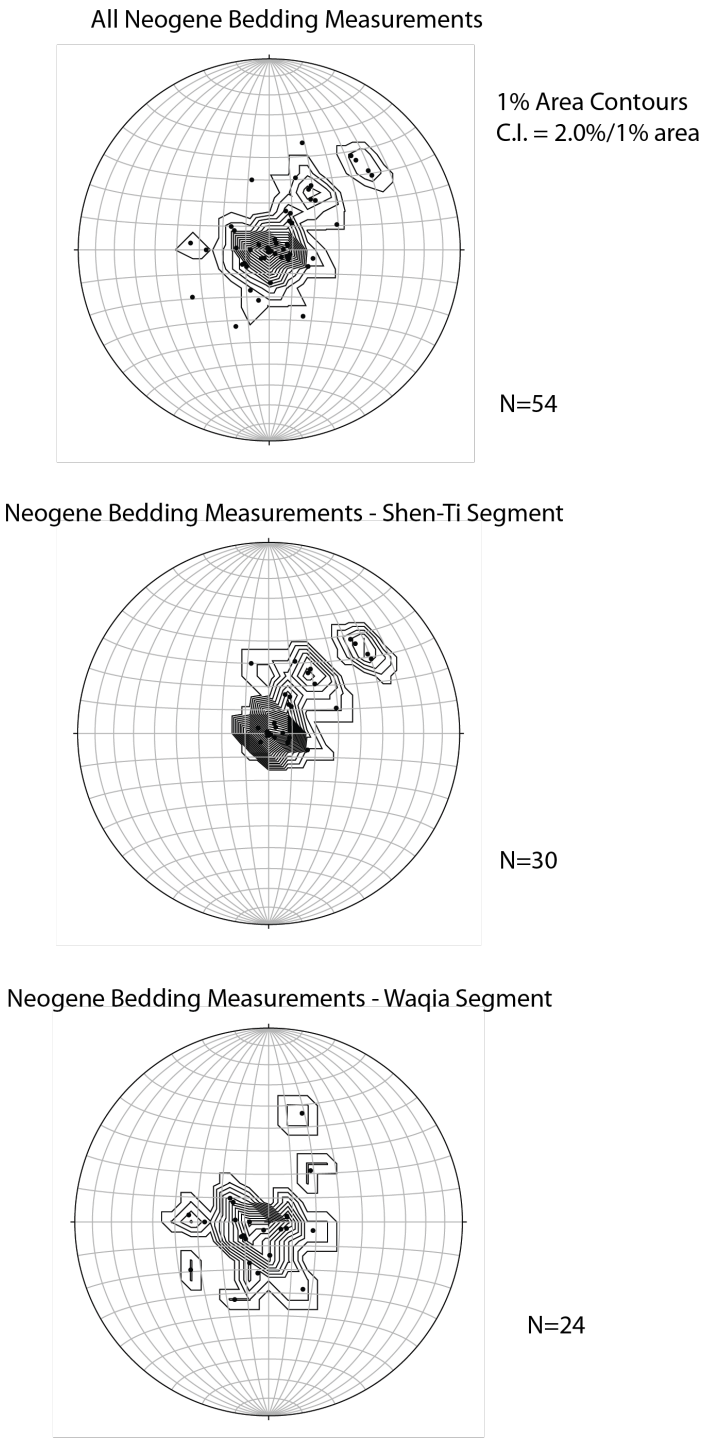

Figure 7: Stereonets of Neogene sedimentary unit bedding in the Waqia Valley. Poles to planes are plotted. (A) All bedding orientations plotted together. (B) Northwest Waqia Valley bedding orientations. (C) Southeast Waqia Valley bedding orientations

4.2. SHEN-TI/WAQIA FAULT

In order to analyze the Shen-Ti/Waqia Fault, structural measurements are divided into two main sections: 1) the structures less than ~500 m from the fault trace and 2) hanging wall structures in the hanging wall greater than ~500 m from the main fault trace.

4.2.1. Shen-Ti/Waqia Fault

The Shen-Ti Fault and the Waqia Fault form a continuous structure throughout the study area. The Shen-Ti Fault section bounds the northern margin of the Waqia Half-Graben (Figure 3). The fault is a down-to the-south normal fault that strikes east-west along its western trace with a moderate dip to the south. The fault juxtaposes quartzofeldspathic gneisses in the hanging wall against schists, phyllites and marbles in the footwall. At its western end, the Tashkurgan Fault cuts the Shen-Ti Fault (Figure 2). To the east, the fault strikes to the northwest with a southwest dip and continues behind the high topographic peaks of the northeastern boundary of the Waqia Valley until it intersects with the Kuke Fault. Southeast of the intersection with the Kuke fault, an abrupt deflection topographic peaks is a geomorphic expression of the fault trace entering the Waqia Valley, which I define as the Waqia segment. The Waqia Fault section is a ~24 km long down-to-the-west normal fault, striking ~N34W, which juxtaposes Oligocene metachert and Paleozoic granites in the footwall against Neogene cobble/boulder conglomerates in the hanging wall (Figure 3, 8). Kinematic indicators in the gouge zone of the Waqia Fault show normal slip displacement.

Forty-two measurements were taken along structures associated with the Shen-Ti/Waqia Fault. Fault orientations varied, but generally had a strike and dip ~155°/76°

SW. Slickenside lineations were measured on minor fault surfaces and show both dip-slip and strike-slip components (Figure 9b). Slickenside trends range from north-south to north-northwest south-southeast. Kinematic analysis of 7 fault surfaces yields a shortening direction of 18°/66° and an extension direction of 283°/2°.

4.2.2. Hanging wall structures

The hanging wall of the Shen-Ti Waqia fault consists of normal faulted Neogene sediments and metasedimentary basement rock throughout the Waqia Valley. Fault traces vary from ~10 kilometers (the Rebu-Te Fault) to <10 meters. Where present, fault surfaces showed normal slip kinematics. Fifty-eight measurements were made on normal fault structures in the Waqia Valley (Figure 9c). Fault surfaces orientations and fault striae trends are highly variable. The kinematic analysis of 12 fault surfaces with slip indicators yields a shortening direction of 166°/70° and an extension direction of 281°/8°.

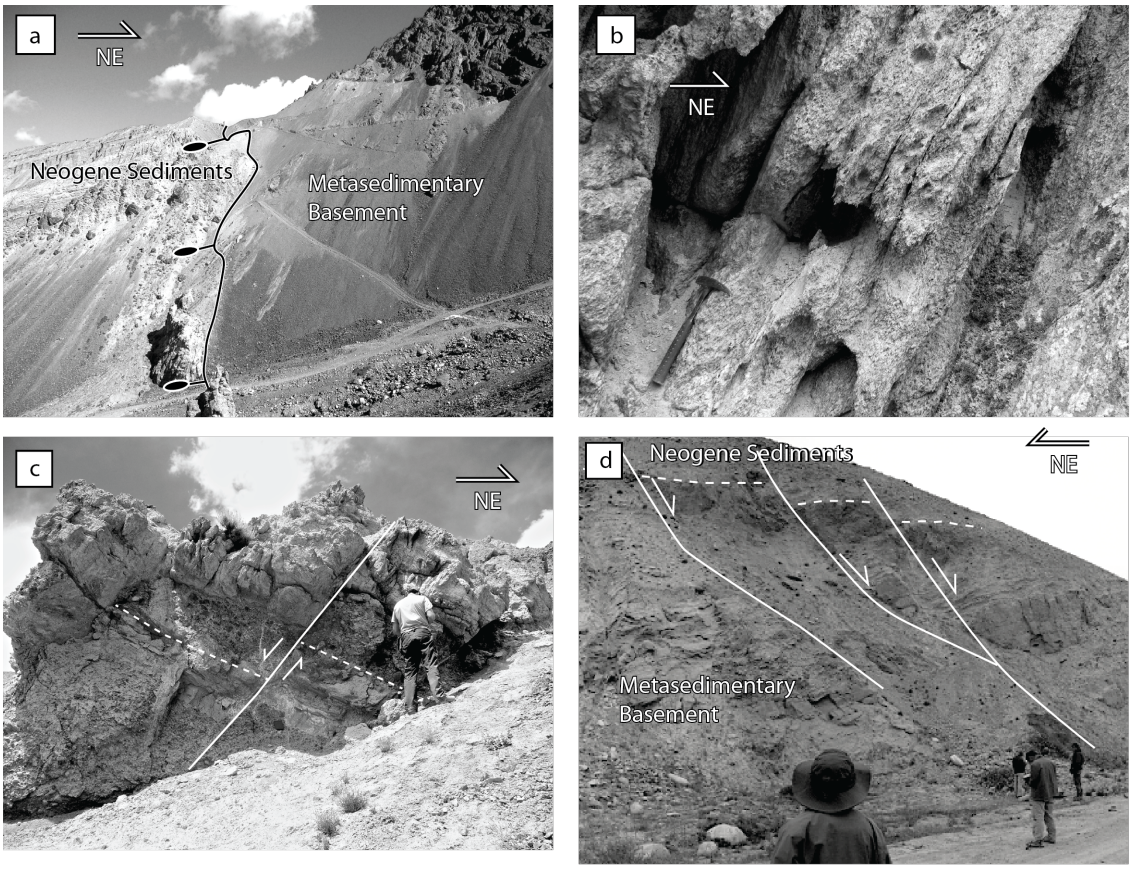

Figure 8: Field photographs of extensional structures in the Waqia Valley. (A) Neogene boulder-cobble conglomerates in the hanging wall of the Waqia Fault. Paleozoic Cherts are in the footwall. (B) Fault zone in the metasedimentary basement rocks near the Shen-Ti/Waqia-Kuke Fault Intersection. S-C fabrics indicating normal fault slip. (C) Normal slip along low-magnitude extensional structures in the Neogene sediments of the Waqia valley. (D) Normal slip faults offsetting Neogene sediments in the hanging wall of the Waqia Valley.

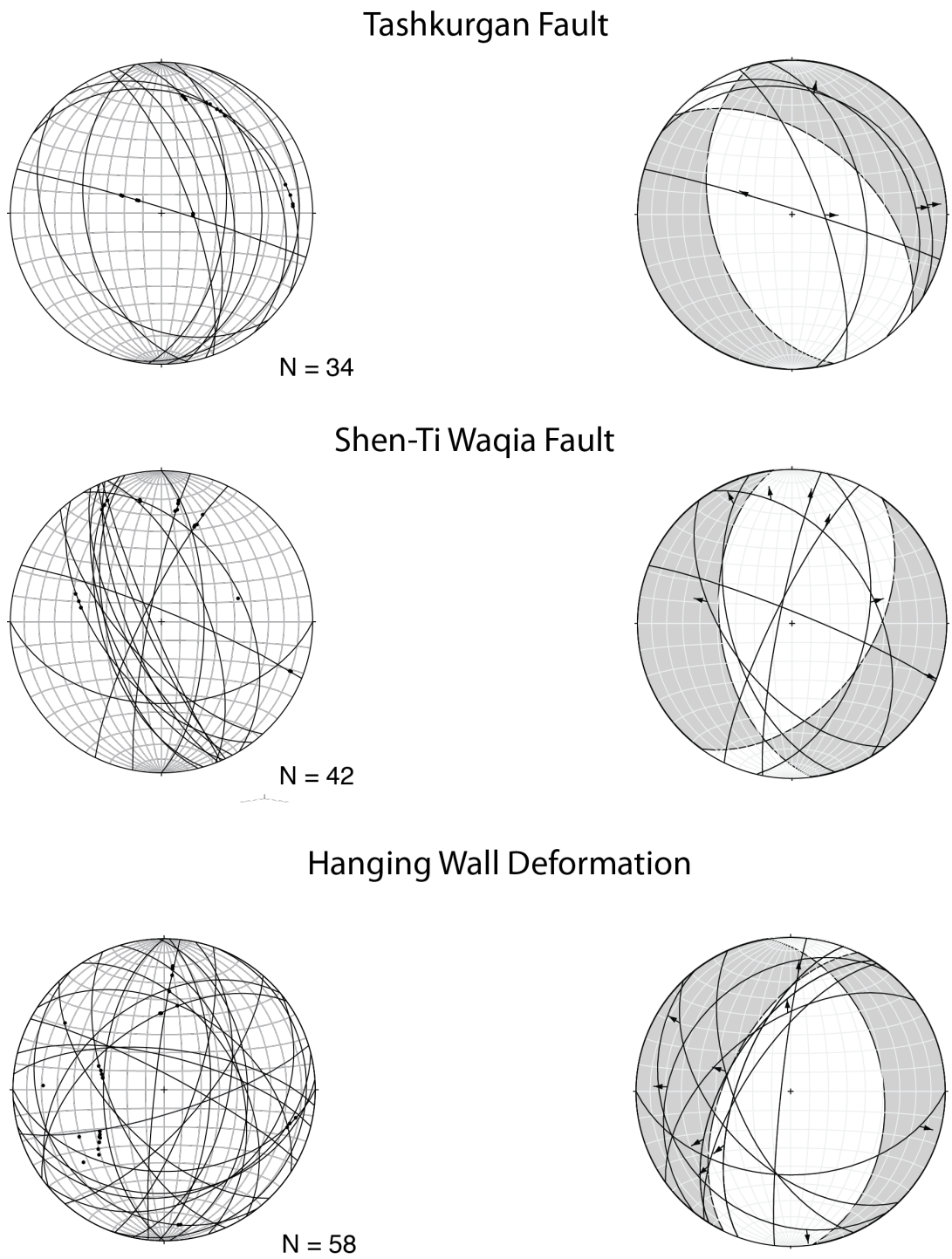

Figure 9: Stereographic projections of fault structure data. Left column: fault planes and slickenside lineations are plotted. Right column: Bingham fault plane solution results. Grey regions are extension.

4.3. BANDI'ER MONOCLINE

The Bandi'er Monocline is a southwest-dipping monocline in Neogene sedimentary rocks along the northern section of the Waqia Valley (Figure 6b, Figure 10). The monocline is ~4 km long and was observed to tip-out to the northwest and southeast. The monocline fold axis strikes N42°W and strata dip southwest a maximum ~55° at the center. The dip of the Neogene sedimentary rocks along strike of the monocline decreases towards the tips. As previously discussed, only the Neogene, deeply incised sediments are deformed, while younger Quaternary sediments filling incised valleys are undeformed.

Forward modeling was used to analyze the geometry and kinematics of the structure. In general, I considered two scenarios which could generate the observed monocline: 1) the monocline developed in response to dip-slip on a blind southwest-dipping normal fault, or 2) the monocline developed in response to dip-slip on a blind northeast-dipping thrust fault. For my test, I utilized the program Trishear 3D to reproduce measured bedding orientations taken from the field (Cardozo, 2008). The program assumes a trishear mode of deformation of the modeled sedimentary packages. The constraints for modeling include: 1) no visible fault surface in the field, 2) bedding geometry, including the maximum dip of the monocline (~55°), and 3) the wavelength of the fold (~500 m). The variables considered were: 1) dip of the fault plane (30-70°), 2) Trishear angle (30-60°), and 3) propagation to slip ratio (0.25-0.5). I modeled the monocline as having the greatest slip in the center, with incrementally smaller magnitudes of slip toward the tip.

I modeled a 4 km long monocline with a maximum dip of ~55° at its center. The monocline in the model is controlled by a dip-slip normal fault with 250 m of displacement across its surface. The propagation-to-slip ratio was modeled 0.25 to 0.5. Of the various parameters used for the model, only a large trishear angle (~60°) produced the observed bedding geometries and ~500 m wavelength. One unexpected output of the model, which was corroborated by observations in the field, was the geometry of surfaces in the hanging wall section of the model (Figure 8b). In hanging wall of the 3D model, the northern section contains sediments with a dip azimuth parallel to the trend of the fold axis (transition from red to blue colors in Figure 8b). In the field, on the northern section of the hanging wall side of the monocline, I observed sediments dipping to the southeast in a similar fashion to the dip of surfaces in the numerical model. I interpret this result as additional support to suggest my modeling is viable.

To test if a viable geometry for the Bandi'er monocline can be produced assuming it was produced by a blind thrust fault, I attempted to produce a 3D model for the Bandi'er monocline assuming a blind northeast-dipping thrust fault. I assumed similar parameters (dip angle, propagation-to-slip ratio, fold wavelength, etc) as the extensional model. The results show monocline generally dipping to the southwest. However, the model predicts an anticline with a fold axis perpendicular to the fold axis of the monocline at the northeast section of the monocline (the hanging wall of a blind northeast dipping thrust fault). This geometry was not observed in the field. Therefore, I prefer a scenario in which the Bandi'er Monocline is rooted by a blind normal fault.

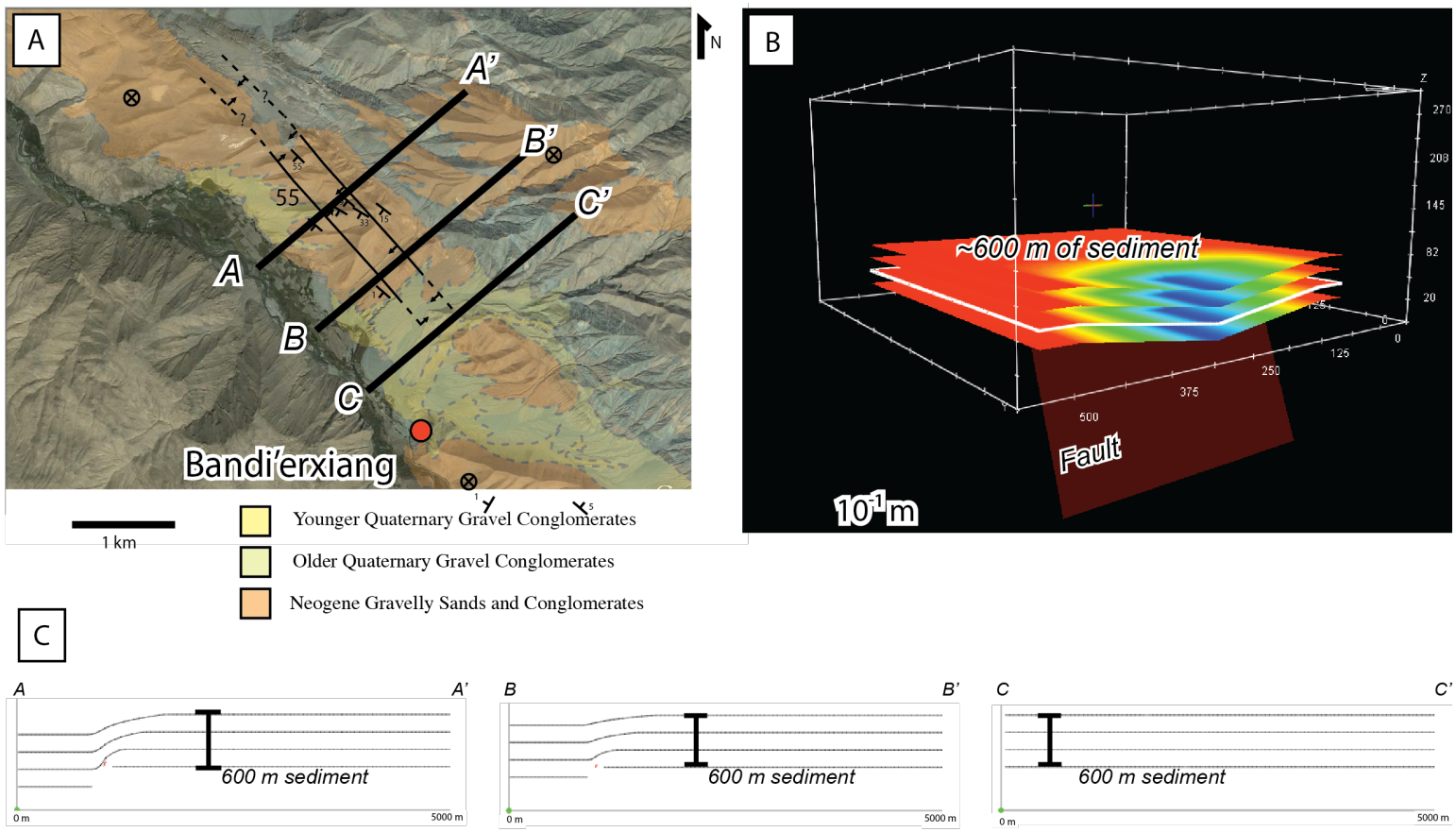

Figure 10: Model for the Bandi'er Monocline. (A) Close up map showing sedimentary units. (B) 3D model built in Trishear3D. Blue colors represent most deformed sediments, red colors are undeformed sediments. (C) Cross sections through the monocline.

4.4. REBU-TE FAULT

The Rebu-Te Fault of the southern section of the valley is a ~10 km long fault-line scarp which offsets Neogene sediments (Figure 3, 11). It strikes N40°W and dips to the southwest. In the footwall, incised sediments indicate a Neogene age for the fault based on: 1) the similarity in sediment character with Neogene sedimentary rocks in the northern section of the valley, and 2) the inferred thickness of the sedimentary units is consistent with Neogene sedimentary rocks in the rest of the valley. In the hanging wall, Quaternary sediments appear to onlap the fault contact. No significant lateral separation of topographic or stratigraphic features were observed, indicating deformation of the Rebu-Te Fault was primarily dip-slip.

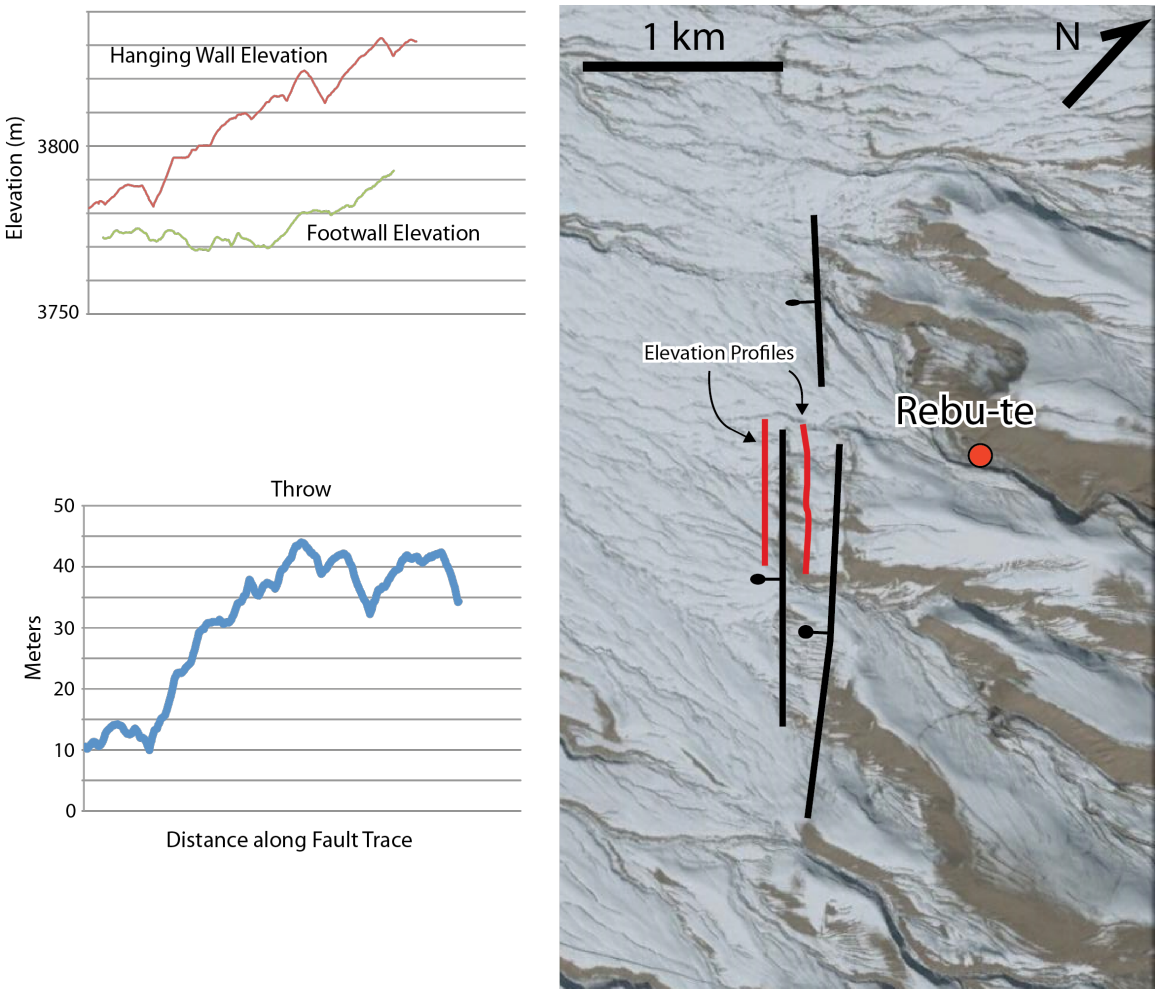

Figure 11: Data from the Rebu-Te Fault system. (a) Google earth image of Rebu-Te faults. (b) DGPS data from the hanging wall and footwall elevation profiles. (c) Calculated difference in elevation from hanging wall and footwall across the profiles.

4.5. TASHKURGAN FAULT

The Tashkurgan Fault is a ~40 km long north-south striking structure bounding the western edge of the Tashkurgan Valley (Figure 3). Triangular facets present along the fault trace indicate a relatively young age of faulting. 34 measurements were taken on structures associated with the Tashkurgan Fault (Figure 9a). Fault orientations are variable, but generally strike northwest and dip northeast. Fault surfaces show dip-slip and strike-slip components. Kinematic analysis of 5 fault surfaces yields an extension direction of 56°/1° and a shortening direction of 151°/71°.

5. DISCUSSION

5.1. SUMMARY OF KEY OBSERVATIONS

Several key observations are used to establish a geologic history for the Waqia Valley. These observations include geometry and kinematics of deformation in the study area, calculated extension direction of normal faults, composition in Neogene sedimentary rocks, and age of deformation.

Several observations in the study area show Neogene deformation is dominated by extension. 1) Neogene structures preserved throughout the Waqia Valley show normal slip sense. 2) Numerical modeling of the Bandi'er Monocline suggests the structure is rooted by a blind normal fault. 3) The Shen-Ti/Waqia Fault accommodated principally dip-slip motion. S/C shear fabrics along the trace of the Shen-Ti/Waqia fault record dip-slip kinematics for the primary fault trace. 4) Kinematic analysis of faults adjacent to the Shen-Ti/Waqia Fault, as well as structures in the hanging wall, records extension at a high angle to the main fault

trace. However, because kinematic analysis of fault surfaces is only reliable for faults with a simple slip history, the calculated results are treated with caution. Therefore, two possible scenarios for the slip history of the Waqia Fault include: a) consistent slip accommodated by the Waqia Fault oblique to the principle extension direction, or b) dip slip accommodating a bulk of the kinematic history followed by late stage strike-slip motion. Finally, Cenozoic deformation in the Tashkurgan Valley is limited to the Tashkurgan Fault, with no evidence of deformation in the eastern section of the valley. Normal slip kinematic indicators were recorded and principle extension direction is documented as perpendicular to the fault trace.

Clast composition within Neogene sedimentary rocks suggests total strike-slip deformation along the Shen-Ti/Waqia fault is negligible. In the footwall of the fault, several distinctly different lithologies crop out, including chert, granite, mica schist, and quartzofeldspathic gneisses. Neogene units in the hanging wall vary in clast composition along-strike in a consistent manor with changes in footwall lithologies. For example, purple chert clasts in Neogene sedimentary rocks are only found adjacent to purple chert in the footwall. If the Shen-Ti/Waqia Fault accommodated a large amount of strike-slip motion, chert clasts would be predicted to be in Neogene sediments further north.

The Waqia Fault and structures in the Waqia Valley are currently inactive, with no observed offset of Quaternary sediments. Deformed, thick, Neogene sedimentary rocks are heavily weathered and eroded with undeformed Quaternary sedimentary rocks which onlap paleo-valleys. While this relationship is present throughout the

valley, this is most clearly evident near the Bandi'er Monocline in the north Waqia Valley. Here, Neogene sediments dip southwest along the structure and are incised. Younger horizontal sedimentary fill, terraces, and fan deposits do not record a monocline geometry. Therefore, active deformation ceased prior to the deposition of the Quaternary units.

5.2. NO INTERACTION WITH KARAKORAM OR KARAKAX FAULT

According to some tectonic models, the Karakoram and Karakax Fault systems are a conjugate pair, which have accommodated lateral tectonic extrusion of Tibet (Tapponnier 1982). Five components are necessary for this model to be valid: 1) The Karakax Fault would be required to continue into the northeast section of the study area along the location of the Waqia Fault; 2) The Karakax Fault and Karakoram Fault systems accommodate contemporaneous slip; 3) opposing slip senses are required; 4) If the region is dominated by extension, normal faults accommodating south-southeast directed extension would be recorded in the Waqia/Tashkurgan valleys (Figure 4); and 5) The structures are required to connect at their tips. Some of these requirements are met as the Karakoram Fault and the Karakax Fault have accommodated contemporaneous slip with opposing slip senses in their history. However, the northern right-slip Karakoram Fault is currently inactive (Robinson, 2009a) whereas the left-slip Karakax Fault is currently active (Shen et al., 2001; Ding et al., 2004). Therefore, the Karakoram Fault and the Karakax Fault cannot be currently acting as a conjugate pair.

To evaluate if the Karakoram and Karakax Faults acted as a conjugate pair earlier in their history, Neogene deformation in the study area is considered. The geometries and kinematics of structures preserved in the Waqia and Tashkurgan Valleys are not

consistent with those predicted if the Karakoram and Karakax Faults acted as a conjugate pair. As stated earlier, northwest-striking thrust faults or strike-slip faults, or northeast-striking normal faults are predicted throughout the Waqia and Tashkurgan Valleys. The Waqia Valley is dominated by extension along northwest-striking normal faults, an orientation perpendicular to the predicted geometries for conjugate strike-slip faults. No evidence of Neogene shortening was observed. Additionally, if the Karakax and Karakoram Faults acted as a conjugate pair at some point in the past, deformation would be predicted to be distributed throughout the study area. The Waqia Valley records Neogene deformation throughout the hanging wall, however deformation in the Tashkurgan valley is limited to the Tashkurgan Fault. No evidence of Neogene deformation was observed along the eastern margin of the Tashkurgan valley.

For strike-slip faults to act as conjugate structures, they must connect at their tips. Thus, if the Shen-Ti/Waqia Fault connects with the Karakoram Fault, it would be geometrically possible for the structures to act as conjugates. However, the Karakoram Fault and the Karakax fault do not connect because the Tashkurgan Fault is not the northern continuation of the Karakoram Fault (Robinson et al., 2007; Robinson, 2009b) as some workers suggest (Chevalier et al., 2011). Northeast-directed extension derived from kinematic analysis of the Tashkurgan Fault in this study supports interpretations that the Karakoram Fault acts an independent structure. For example, if the Tashkurgan Fault, and therefore the Kongur Shan Extensional System, were the continuation of the Karakoram Fault, a southeast principle extension direction and primarily right-lateral strike-slip motion would be predicted. Instead, the Karakoram Fault strikes northwest and connects with the Rushan-Pshart Zone (Robinson, 2009b). There is no physical

connection between the Rushan-Pshart zone and the Shen-Ti/Waqia Fault. Therefore, the Shen-Ti/Waqia Fault does not connect with the Karakoram Fault and they cannot act as conjugate strike-slip structures.

The Karakax Fault, along its known trace, is a long-lived left-slip structure with active Quaternary deformation (Ryerson et al., 1997; Ryerson et al., 1999; Shen et al., 2001; Ding et al., 2004; Li et al., 2012). A right bend in the Karakax Fault where it is proposed to project into the study area predicts northwest-striking Neogene and Quaternary shortening structures with left-lateral components if it has not interacted with the Karakoram Fault. In this study, I did not find any evidence of Neogene or recent shortening structures or left-lateral separation in the Waqia valley. The Waqia and Shen-Ti faults were observed as southwest dipping with normal displacement in the Waqia Valley. This observation is inconsistent with predictions for a genetic link with the Karakax Fault. Therefore, the Shen-Ti/Waqia Fault is not geometrically or kinematically linked with the left-slip Karakax Fault.

5.3. STRUCTURAL CONTROL OF THE CENTRAL PAMIR GNEISS DOMES

Several aspects of the Shen-Ti and Waqia Faults suggest they are genetically linked. 1) Field mapping shows the Shen-Ti Fault and Waqia Fault are a continuous structure, and therefore preserve a similar slip history. 2) Kinematic indicators of both structures record normal dip-slip motion (Robinson 2007). 3) The footwalls of the Shen-Ti Fault and Waqia Fault record overlapping mineral cooling ages. The Shen-Ti Fault has been previously interpreted to have initiated in the Late Miocene based on cooling ages of footwall rocks (Robinson et al., 2007; Sobel et al., 2011). Unpublished Zircon (U-Th)/He ages from the footwall of the Waqia Fault overlap with cooling ages in the Shen-

Ti Fault footwall (Figure 5). Thus I propose the development of the Waqia Valley is related to normal faulting along the Shen-Ti/Waqia Fault in the Miocene, accommodating exhumation of the Muztaghata/Sares Gneiss Dome.

6. MODEL FOR THE NEOGENE TECTONIC EVOLUTION OF THE SOUTHEST PAMIR

I have established the Waqia Valley is not genetically related to slip along the Karakoram or Karakax Fault systems. Therefore, I propose Neogene deformation in the Waqia Valley is related the tectonic exhumation of the Muztaghata Gneiss Dome.

The Main Pamir Thrust has accommodated subduction of the Alai slab since ~25 Ma (Burtman and Molnar, 1993; Sippl et al., 2013; Sobel et al., 2013). The present-day steep angle of subduction (Sippl et al., 2013) is likely the product of slab rollback, which initiated ~15 Ma (Sobel et al., 2013). During slab rollback, gravitational collapse of overthickened crust of the Pamir underwent north-south extension (Rey et al., 2009; Rey et al., 2011; Schmidt et al., 2011; Mechie et al., 2012). Additionally, overthickened crust produced a weak middle crust in the Pamir that facilitated the development of a regional detachment surface, The Pamir Shear Zone, through which the Pamir domes were exhumed (Sippl et al., 2013; Stübner et al., 2013). At this time, exhumation of the Central Pamir domes via upper crustal extension/vertical extrusion, or a blind thrust fault in the lower crust, contributed to the development of the Waqia half-graben (Robinson et al., 2007; Stübner et al., 2013).

For my model, I consider the model for the evolution of extensional gneiss domes of Kapp et al. (2008). In their model (Figure 4 of Kapp et al. 2008), a sedimentary basin develops in the hanging wall of a single master fault early in the extensional phase.

During continued extension, lateral migration of the sedimentary basin towards the fault tips is facilitated by 1) isostatically driven uplift of both the hanging wall and footwall in areas with high extension and 2) hanging wall subsidence in regions of low extension.

There are important differences between the Kapp et al. (2008) model for an extensional dome and the Central Pamir Gneiss Domes. 1) The Muztaghata/Sares Dome is bound on all sides by normal faults. Maps and models of the Muskol and Sares domes indicate the domes are tectonically exhumed by one or two master faults which are continuous around the structures (Robinson et al., 2007). 2) A sedimentary basin is only observed in one location relative to the Gneiss Domes. Therefore, a viable evolutionary model for the Muztaghata/Sares dome is required to 1) explain the occurrence of normal faults bounding all sides of the structure, and 2) explain the occurrence of one sedimentary basin (the Waqia Valley). Herein, I propose a four-stage model for the development of the Waqia Valley in response to exhumation of Pamir domes (Figure 12).

A

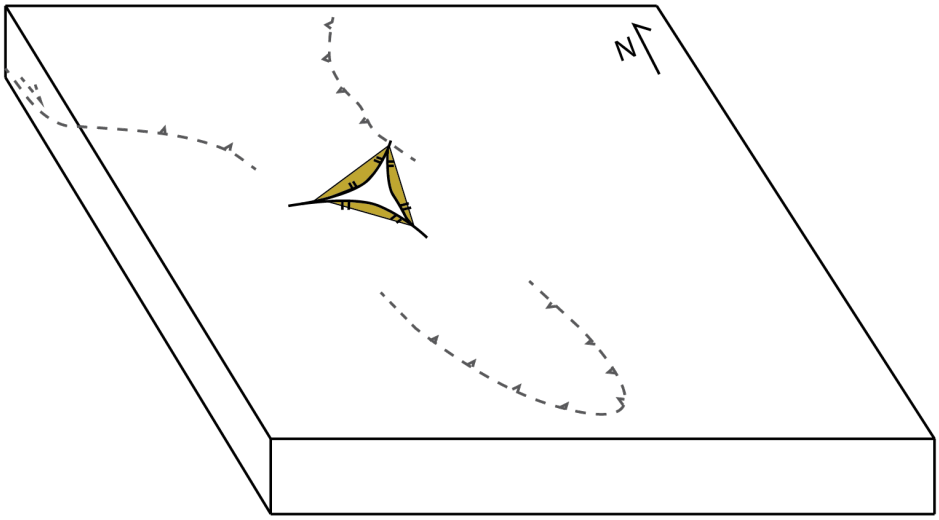

B

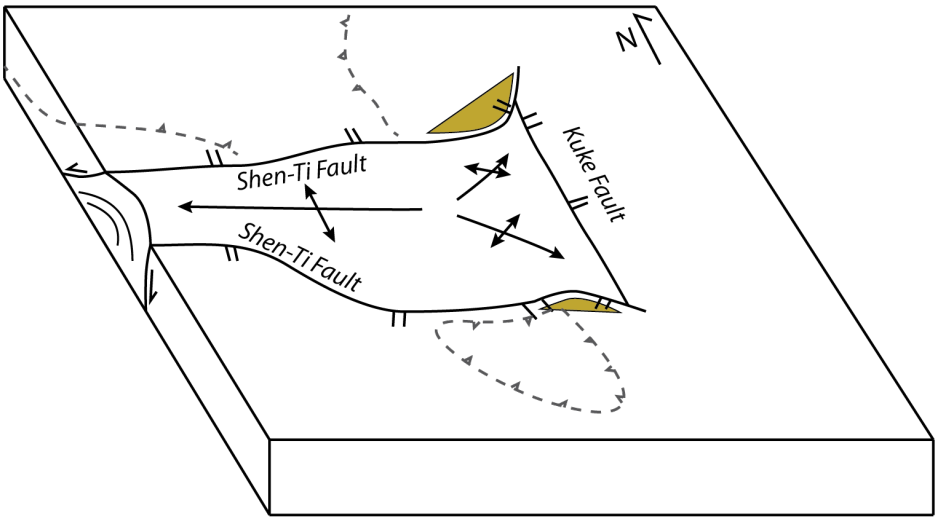

Figure 12: Model for the Neogene evolution of the eastern Pamir, with emphasis on the Waqia Valley. Grey dashed thrust fault in the four figures represents the present-day trace of the Torbashi Thrust. Yellow regions are sedimentary basins. (A) Initiation of the Muztaghata/Sares Dome. (B) West propagation of the Shen-Ti/Waqia Fault facilitates north-south extension and exhumation of the Sares/Muztaghtata dome. Doming in the western Waqia Valley facilitates local uplift.

C

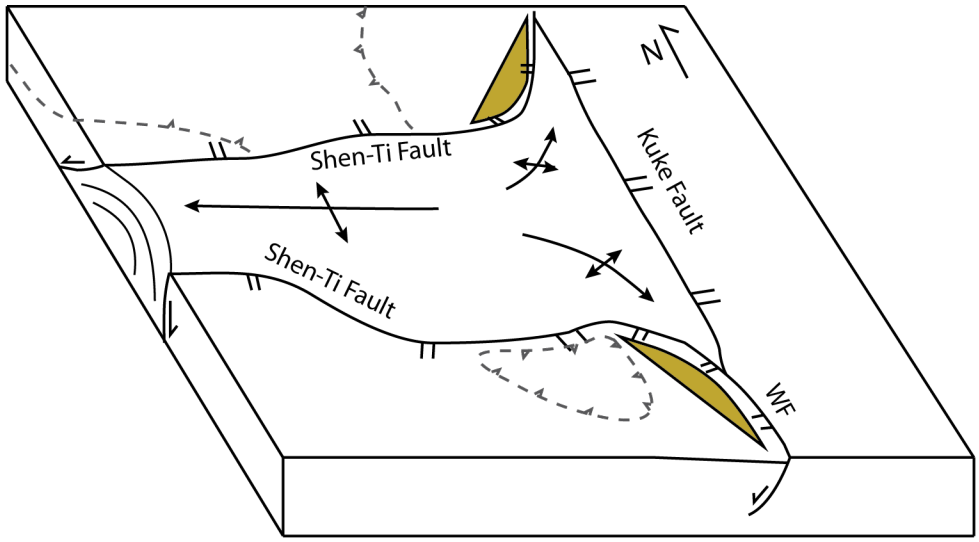

D

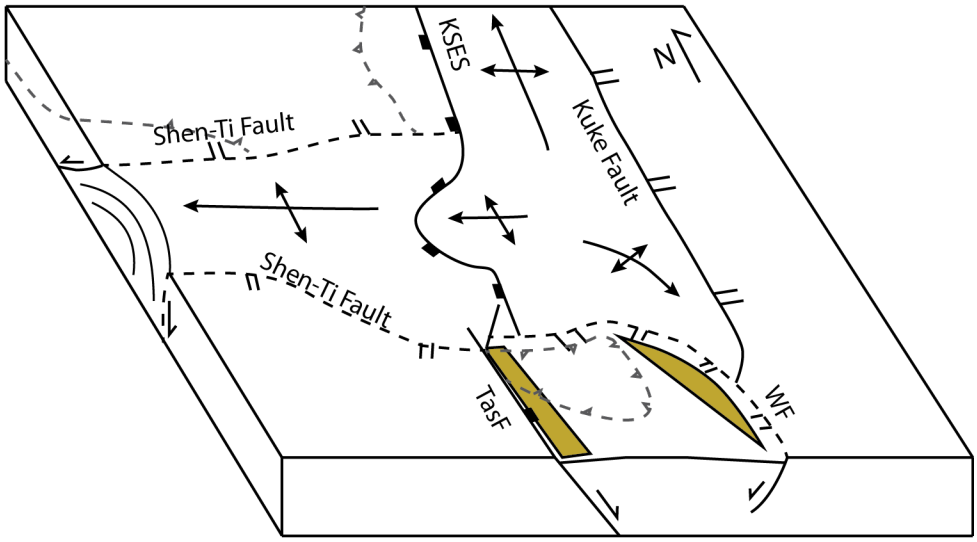

Figure 12 (continued): (C) Continued slip along the Shen-Ti faults. Rotation of the Kuke Fault from near horizontal to vertical extends the dome to the east. (D) North-South extension along the Kongur-Shan Extensional System.

6.1. STAGE 1 - EXHUMATION OF MUZTAGHATA/SARES DOME

The initial stage of exhumation of the Muztaghata/Sares dome begins with upper crustal extension accommodated by gravitational collapse of the upper crust (Tirel et al., 2008; Rey et al., 2009; Rey et al., 2011; Stübner et al., 2013). The specific initial geometry of extension in the upper crust is unknown, and several geometries are possible (Tirel et al., 2008; Rey et al., 2009; Rey et al., 2011). Extension was accommodated by brittle normal faults in the upper crust that evolved into the present-day Shen-Ti/Waqia Fault, and Kuke Faults (Figure 12a). The initial state of extension accommodated little to moderate magnitudes of extension along high-angle normal faults. Within the hanging walls of these normal faults, thin sedimentary basins likely developed.

6.2. STAGE 2: CONTINUED EXTENSION ALONG THE SHEN-TI FAULT SYSTEM

During stage two (Figure 12b,c), continued north-south extension occurs along east-west-striking normal faults (the north and south Shen-Ti Faults) and east-west extension along the Kuke Fault (Sobel et al., 2011). During this stage, the Sares/Muztaghata dome developed as an east-west-trending antiformal structure via westward propagation of the Shen-Ti/Waqia Fault. In this stage, the center of the Shen-Ti fault system has accommodated large magnitudes of extension, whereas the tips have accommodated low magnitudes of extension. Either 1) the sedimentary basin migrated from the northwest to the southeast with the southeast directed propagation of the Shen-Ti Fault, or 2) the sedimentary basin was stationary if the Shen-Ti Fault did not laterally propagate southeast.

I prefer a model in which the Shen-Ti Fault laterally propagated southeast with a sedimentary basin laterally propagating near the fault tip. The observation in the Waqia Valley to support this interpretation include metasedimentary basement capped with patches of Neogene sedimentary rocks at high elevations in the northern section of the Waqia Valley, in contrast to thicker preserved Neogene sedimentary rocks at the southeast section of the valley. The northern section is interpreted to have accommodated extension and deposition of Neogene sedimentary rocks, however continued extension resulted in isostatically driven uplift of both the hanging wall and the footwall in the north. This resulted in incision and erosion of the Neogene sedimentary rocks in the north Waqia Valley exposing the metasedimentary basement. This process is similar to the development of the sedimentary basin in the hanging wall of an extensional gneiss dome modeled by Kapp et al. (2008).

6.3. STAGE 3: EXTENSION ALONG THE KONGUR SHAN EXTENSIONAL SYSTEM

By 7-6 Ma, slip along the Shen-Ti and Waqia faults cease, in response to compensation of gravitational collapse by collision of the Pamir with the Tien Shan (Sobel et al., 2006; Thiede et al., 2013). A slab tear between the down going Alai Slab and the Tarim Block allowed for upwelling hot asthenosphere in the vicinity of the East Pamir Gneiss Domes which weakened the Pamir Crust (Sobel et al., 2013). The upwelling hot asthenosphere in the east Pamir facilitated and localized east-west extension along the Kongur Shan Extensional System and Kuke Faults (Robinson et al., 2004, 2007; Cao et al., 2013a; Cao et al., 2013b; Thiede et al., 2013). While I cannot rule out the possibility of an early phase of east-west extension is recorded by late stage slip in

the Waqia Valley, deformation in the Waqia Valley clearly ceased by the Quaternary, whereas it is still active along the KSES.

7. CONCLUSIONS

Structural field mapping in the southeast Pamir, integrated with previously published research, documents important relationships regarding the Cenozoic tectonics of the western Himalayan-Tibetan Orogen. 1) The Waqia Valley consists of a series of sedimentary units deposited in the half-graben since the Miocene. 2) Accommodation within the Waqia Valley was facilitated by normal dip-slip motion along the south and southwest dipping Shen-Ti/Waqia Fault during the Neogene. 3) Structures in the Waqia Valley are currently inactive.

Predicted deformation associated with the Karakoram and Karakax Faults is inconsistent with observations in the study area. The Karakoram and Karakax Faults do not project into the study area and do not connect, as previously suggested (Tapponnier et al., 1982). The geometry of normal faults and calculated extension direction in the study area are orthogonal to the predicted orientation if the Karakoram and Karakax faults acted as a conjugate pair. Thus, The Karakoram and Karakax faults have not acted as conjugate strike-slip faults in their histories. Additionally, the absence of shortening or left-lateral strike slip structures, or Quaternary deformation, in the Waqia Valley indicates the Karakax Fault does not project into the study area as previously suggested.

I propose the development of the Waqia Valley is controlled by the lateral propagation of the Shen-Ti/Waqia Fault tip during exhumation of the Muztaghata Gneiss Dome. The Waqia Valley is situated in a half-graben that developed in a region of low magnitude extension along the eastern segment of the present day Shen-Ti/Waqia Fault.

Following subsequent extension, doming, and isostatic adjustment of the hanging wall and footwall in the northwest, the northwestern segment of the Waqia Valley sediments was eroded, thus preserving the thickest Neogene sedimentary rocks in the southeastern section of the Waqia Valley.

CHAPTER 2: Mesozoic Evolution of the Eastern Pamir

1. INTRODUCTION

The Himalayan-Tibetan orogen is considered a paradigm in understanding deformation processes associated with continent-continent collision. In order to fully understand the geometry and kinematics of major structures in the orogen, such as the Karakoram Fault, accurate correlation of lithologic units is required. For example, westward continuity of tectonostratigraphic units into the vicinity, and west of, the Karakoram Fault has been a matter of considerable debate (Burtman and Molnar, 1993; Yin and Harrison, 2000; Lacassin et al., 2004; Schwab et al., 2004; Robinson et al., 2012). Total slip along the Cenozoic Karakoram Fault has been estimated to range from ~160 km to >500 km based on different correlations across the structure (Valli et al., 2007; Valli et al., 2008; Robinson, 2009b). Furthermore, the trace of the Karakoram Fault where it enters into the Pamir region at its northern end is a topic of considerable debate (Robinson et al., 2007; Robinson, 2009b; Robinson, 2009a; Chevalier et al., 2011). Adequate understanding of offset tectonostratigraphic units, and their boundaries, across the Karakoram Fault provides constraints on the geometry of the northward continuation of the Karakoram Fault.

Many aspects of the geologic evolution of the Pamir region (Figure 1) in the northwestern corner of the Himalayan-Tibetan orogen are relatively poorly understood. One of these is the continuity of geologic units in the Pamir which do not appear to be laterally continuous in older geologic maps (Yin and Bain, 1992). These maps depict a wide variety of age assignments that cannot be tectonically or stratigraphically correlated across the region (Yin and Bain, 1992; Strecker et al., 1995; Sobel and Dumitru, 1997; Schwab et al., 2004; Robinson et al., 2007). Further, the age of many of these units

(especially those of medium to high metamorphic grade) is not well constrained. Recent results have begun to address this issue through detrital zircon analyses of metamorphic terranes, which show lithologies in the Northern Pamir and the Eastern Pamir Gneiss Domes are Triassic or younger, in contrast to previous interpretations suggesting Paleozoic to Proterozoic ages (Robinson et al., 2012).

While progress has been made in understanding the correlative relationships between units in the Pamir, several questions remain. 1) What is the metamorphic history of units in the southeast Pamir? 2) Is there a genetic relationship between metamorphic rocks with Triassic maximum depositional ages in the southeast Pamir with Triassic metasedimentary rocks in the northern Pamir? 3) Where are the boundaries between major tectonostratigraphic terranes in the southeast Pamir, most notably the boundary between Gondwanan crustal fragments and the Paleozoic-Early Mesozoic southern boundary of Asia? Answers to these questions will allow for a better understanding of the tectonic history of the Pamir region and the greater Himalayan-Tibetan Orogen.

In this study, I conducted detailed field mapping to document the geometry of major structures and evaluated the significant metamorphic grade boundaries of metasedimentary rocks using petrographic analysis and garnet-biotite Fe/Mg exchange thermometry. I then evaluate U/Pb zircon geochronologic analyses of igneous and metasedimentary samples from the hanging wall and footwall of major structures across the eastern Pamir to evaluate: 1) correlations in detrital zircon age frequency, 2) maximum depositional ages for sedimentary units, and 3) the age of igneous activity in the region. Finally, I compare my results with recent results in the Pamir and relationships to tectonostratigraphic blocks in the greater Tibetan Orogen.

2. REGIONAL GEOLOGY

2.1. TECTONIC SETTING

The Pamir are an arcuate region situated in the northwest corner of the Himalayan-Tibetan Plateau (Figure 1,2). The Pamir are bound to the north by the Tien Shan and Alai Basin, to the west by the Tajik Basin, to the east by the Tarim Basin, and to the south the Karakoram Mountains. A total of at least 600 to 900 km of shortening has been accommodated the Pamir leading to a present-day crustal thickness of ~70 ±10 km (Burtman and Molnar, 1993; DiPietro and Pogue, 2004; Negredo et al., 2007; Schmidt et al., 2011; Mechie et al., 2012). A minimum of 300 km of shortening has been absorbed by crustal thickening within the Pamir since the Cretaceous (Burtman and Molnar, 1993). The estimates of shortening within the Pamir, as well as quantified exhumation depths for high-grade rocks in the Pamir, suggest the initial thickness crustal thickness of the Pamir prior to India-Asia collision was 30-40 km (Burtman and Molnar, 1993; Schmidt et al., 2011).

2.2. REGIONAL GEOGRAPHIC AND TECTONIC DIVISIONS

The Himalayan-Tibetan Orogen has long been recognized to consist of a series of distinct tectonostratigraphic units (terranes), accreted to the southern margin of Asia prior to the Cenozoic India-Asia collision (Yin and Harrison, 2000). While the Tibetan terranes are generally assumed to continue to the west across the entire orogen, the location of terrane boundaries near to, and west of, the Karakoram Fault is still unresolved (Tapponnier et al., 1981; Burtman and Molnar, 1993; Lacassin et al., 2004; Schwab et al., 2004; Valli et al., 2007; Valli et al., 2008; Robinson et al., 2012). In the Cenozoic, the Pamir have been translated northward ~300 km since ~25 Ma, possibly due

to slab rollback of the Alai slab in the north and west (Sobel et al., 2013). This northward translation has been accommodated in the east by the right-slip Kashgar Yecheng Transfer System (KYTS) (Cowgill, 2010). The result of Pamir indention is the northward deflection of tectonostratigraphic units and their boundaries (sutures) relative to their proposed western continuation in Tibet.

A well-documented relationship of terranes in the Pamir with those in Tibet is necessary for further understanding of regional tectonic processes in greater Tibetan Orogen. The Pamir have traditionally been divided, geographically and geologically, into the North, Central, and South Pamir (Figure 1) (Burtman and Molnar, 1993). These regions have historically been thought to represent distinct terranes correlative to the Himalyan-Tibetan Orogen (Burtman and Molnar, 1993). However, recent observations of trends of intrusive structures (Schwab et al., 2004) and detrital zircon populations (Robinson et al., 2012) have documented a more complex relationship of terrane correlations between the Pamir and Tibet.

2.2.1. North Pamir

The North Pamir are bounded by the Main Pamir Thrust in the north and the Tanymas Suture in the south. Early workers interpreted the Northern Pamir as a single distinct terrane equivalent with the Kunlun Terrane. However, Schwab et al. (2004) and Robinson et al. (2012) documented distinct differences between lithologies in the northern and southern portions of this region and interpreted the North Pamir to consist of two distinct tectonostratigraphic blocks (Schwab et al., 2004; Robinson et al., 2012). The northern terrane, the Kunlun terrane, is bound to the north by the Main Pamir Thrust and to the south by the Cretaceous Shala-Tala Fault (Robinson et al. 2012). It consists of

schists interbedded with marble, quartzite, and metavolcanics (Robinson et al., 2004). It is interpreted as a conglomerate of arcs and micro-continents with a similar tectonic history to the Kunlun Terrane of Tibet (Yin and Harrison, 2000). The southern terrane in the North Pamir is the Karakul-Mazar terrane, correlative with the Hoh-Xil/Songpan Ganzi Terrane of Tibet (Schwab et al., 2004; Robinson et al., 2012). The Karakul-Mazar/Hoh-Xil/Songpan Ganzi Terrane is interpreted to be a Late Permian to Early Jurassic arc accretionary complex developed at the southern margin of Asia (Yin and Harrison, 2000; Robinson et al., 2012).

2.2.2. Central Pamir

The Central Pamir are bounded by the Tanymas Suture in the north and the Rushan-Pshart zone in the south. The rocks have been interpreted to consist of Paleozoic to Triassic metasedimentary units overlying basement that collided with the southern margin of Asia in the Late Triassic Early Jurassic (Burtman and Molnar, 1993; Robinson et al., 2012). East-west trending Miocene Gneiss Domes, (Figure 1,2) which include the Muskol, Sares and Muztaghata Gneiss Domes, crop out in the Central Pamir. The Muskol and Sares domes are high-grade Barrovian sequence metasedimentary units intruded by gabbro and diorite (Schwab et al., 2004). Much of the published work concerning the Central Pamir has been focused on these structures (Pashkov and Schvol'Man, 1979; Peykre et al., 1982; Schmidt et al., 2011). As a result, the hanging wall units of these structures are not as well documented.

2.2.3. South Pamir

The South Pamir is bordered by the Rushan-Pshart zone in the north (Burtman and Molnar, 1993) and its southern continuation may be continuous with the Karakoram

region (Robinson et al., 2012). Alternatively, the Karakoram may be separated by the South Pamir by the Wakhan-Tirich Boundary Zone (Angiolini et al., 2013). While the South Pamir and Lhasa Terrane contain coeval magmatic belts (Schwab et al., 2004), Robinson et al. (2009b) documented limited offset of the northern Karakoram Fault (~160 km), invalidating a South Pamir-Lhasa terrane correlation. Instead, the South Pamir is likely correlated with the Qiangtang Terrane.

2.3. STRUCTURAL DESCRIPTIONS

2.3.1. Tanymas Thrust

The Tanymas Thrust represents the fault boundary between the North Pamir and the Central Pamir (Figure 2,13). The thrust strikes approximately east-west and dips to the north. The Tanymas Fault forms a low-angle structure resulting in a series of synformal nappes in the Central Pamir. Total shortening of the Tanymas Thrust is ~80 km (Burtman and Molnar, 1993). In the hanging wall are amphibolite facies metasedimentary units which increase in metamorphic grade to the east (Robinson et al., 2004). The metasedimentary rocks in the hanging wall yield Triassic maximum depositional ages and are crosscut by Triassic intrusions. The footwall of the Tanymas Thrust consists of Carboniferous to Triassic metasedimentary rocks in normal fault contact with the Sares dome.

2.3.2. Baoziya Thrust

The Baoziya Thrust in the northeast Pamir is located in the hanging wall of the Kongur Shan Extensional System and the Shen-Ti Fault, northwest of the Muztaghata Gneiss Dome (Figure 2,13). The fault strikes approximately north-south with a moderate westerly dip. The hanging wall (Block IIb) consists of an east-directed Buchan-style

increase in metamorphic grade from greenschist facies biotite-chlorite schists to amphibolite facies garnet +biotite + sillimanite schists and gneisses intruded by Triassic granites (Robinson et al., 2004). The footwall (Block Ib) is composed of greenschist facies marbles, phyllites, and quartzites (Robinson et al., 2004).

2.3.3. Torbashi Thrust

The Torbashi Thrust is located south of the Muztaghata Gneiss Dome in the hanging wall of the Shen-Ti Fault (Figure 2,13). The Torbashi thrust has previously been identified based on high-grade metamorphic rocks structurally overlying greenschist facies marbles, phyllites, and quartzites. The thrust is mapped as a synformal klippe, with a northwest-trending fold axis. Biotite cooling ages of the hanging wall rocks suggests the age of the thrust to be Late Cretaceous (Robinson et al., 2007; Robinson et al., 2012).

2.3.4. Muztaghata and Sares Gneiss Domes

The Muztaghata Gneiss dome is part of a series of Miocene compressional domes that crop out along the Central Pamir and continue across the Kongur Shan Extensional System (Figure 2,13) (Robinson et al., 2007; Cao et al., 2013b). The Central Pamir Gneiss Domes are composed of the Muskol, Sares, and Muztaghata Domes. The Central Pamir Domes experienced prograde metamorphism from 25-14 Ma followed by exhumation from 14-8 Ma (Robinson et al., 2007; Cao et al., 2013b). Muztaghata reached peak metamorphic conditions (9-10 kbar, 700°C -750°C) at ~14 Ma, with rapid cooling at ~10-8 Ma accommodated by normal slip along the Shen-Ti Fault (Robinson et al., 2007; Cao et al., 2013b). The core of the Muztaghata dome is composed of Triassic orthogneisses with Triassic schists interpreted to be equivalent with the Karakul-Mazar

terrane (Robinson et al., 2012). On the western flank, Paleozoic metasedimentary units record detrital zircon signatures indicating a Gondwanan affinity (Yang et al., 2010; Robinson et al., 2012). The Sares dome of the Central Pamir is interpreted consist of Paleozoic units equivalent with the Qiangtang Terrane of Central Tibet structurally above the Muztaghata Dome (Robinson et al., 2012).

2.3.5. Shen-Ti Fault

The Shen-Ti Fault accommodated tectonic exhumation of the Muztaghata/Sares Gneiss dome in the Miocene (Robinson et al., 2007). The Shen-Ti Fault crops out north and south of the Sares/Muztaghata dome and generally strikes east-west, parallel with the axis of the Sares/Muztaghata fold axis. It juxtaposes migmatitic schists and quartzofeldspathic gneisses in the footwall against greenschist facies metasediments in the hanging wall. Ductile shear sense indicators in the hanging wall and footwall of the southern portion of the fault show top-to-the-south shear sense. The Shen-Ti Fault cuts the Tanymas thrust on the north side of the Muztaghata dome. Cooling ages in the footwall document Late Miocene activity (Robinson et al., 2007).

2.3.6. Kuke Fault

The Kuke Fault is the eastern structural boundary of the Muztaghata dome (Sobel et al., 2011; Xinjiang Bureau of Geology and Mineral Resources, 1993). The Kuke Fault strikes north-south and dips sub-vertically (Sobel et al., 2011). The steep dip, as well as cooling patterns in the Muztaghata antiform, suggests rotation to the present vertical orientation from a more shallow orientation as it evolved from 12-6 Ma (Sobel et al., 2011). It projects into the Shen-Ti Fault in the south (Robinson et al., 2007; Sobel et al.,

2011). In the north, the fault links with the Ghez fault, which juxtaposes Kunlun terrane above Karakul-Mazar Terrane (Robinson et al., 2012).

2.3.7. Kongur Shan Extensional System

The Kongur Shan Extensional System (KSES) is a north-south striking system of normal faults, which accommodate east-west extension (Figure 2,13). Onset of normal faulting along the KSES began ~7-8 Ma in the north and 6-5 Ma in the south across the Muztaghata massif, implying south directed propagation of the system (Robinson et al., 2007; Robinson, 2009b; Cao et al., 2013b). The KSES is currently active (Robinson et al., 2004, 2007; Chevalier et al., 2011).

2.4. PREVIOUS AGE ASSIGNMENTS

The eastern Pamir is generally composed of medium-to high-grade metamorphic rocks; therefore the lack of fossil assemblages has historically made age assignments difficult. However, Robinson et al. (2012) documented that the hanging wall of the Baoziya Thrust, north of Muztaghata, to be Triassic in age. Zhang et al. (2007) and Yang et al. (2010) documented Triassic maximum depositional ages in metasedimentary units south of the Muztagata gneiss dome, suggesting possible correlations with units in the North Pamir (Zhang et al., 2007; Yang et al., 2010; Robinson et al., 2012).

3. GEOLOGIC MAPPING

3.1. METHODS

Structural field mapping was conducted in the Tashkurgan and Waqia Valleys using ASTER images as map bases to characterize and define metasedimentary and igneous units in the eastern Pamir (Figure 3). Objectives for geologic mapping included 1) document the distribution of metamorphic grades, 2) documentation of the geometries

of major structures, and 3) identification of shear sense in metamorphic rocks to interpret transport direction. While mapping, sample collection was conducted for U-Pb geochronology and petrographic analysis.

Map units are defined by lithology and metamorphic grade as well as zircon U/Pb characteristics. Foliation measurements were plotted on southern hemisphere equal area stereonets using the program Stereonet 3 (Cardozo and Allmendinger, 2013). Peak metamorphic conditions of pelitic metasedimentary rocks are based on coexisting metamorphic mineral assemblages seen in thin section. Several deformation fabrics characterized for this study: 1) Quartz deformation fabrics were evaluated for bulging, subgrain rotation, grain boundary migration, and grain boundary area reduction. 2) Shear sense indicators were observed such as mineral fish, S/C fabrics, and rotated porphyroblasts (Lister and Snoke, 1984; Hirth and Tullis, 1992). Descriptions for the boundaries of structural blocks, followed by lithological characteristics of structural blocks, are given along a general transect northeast to southwest through the study area.

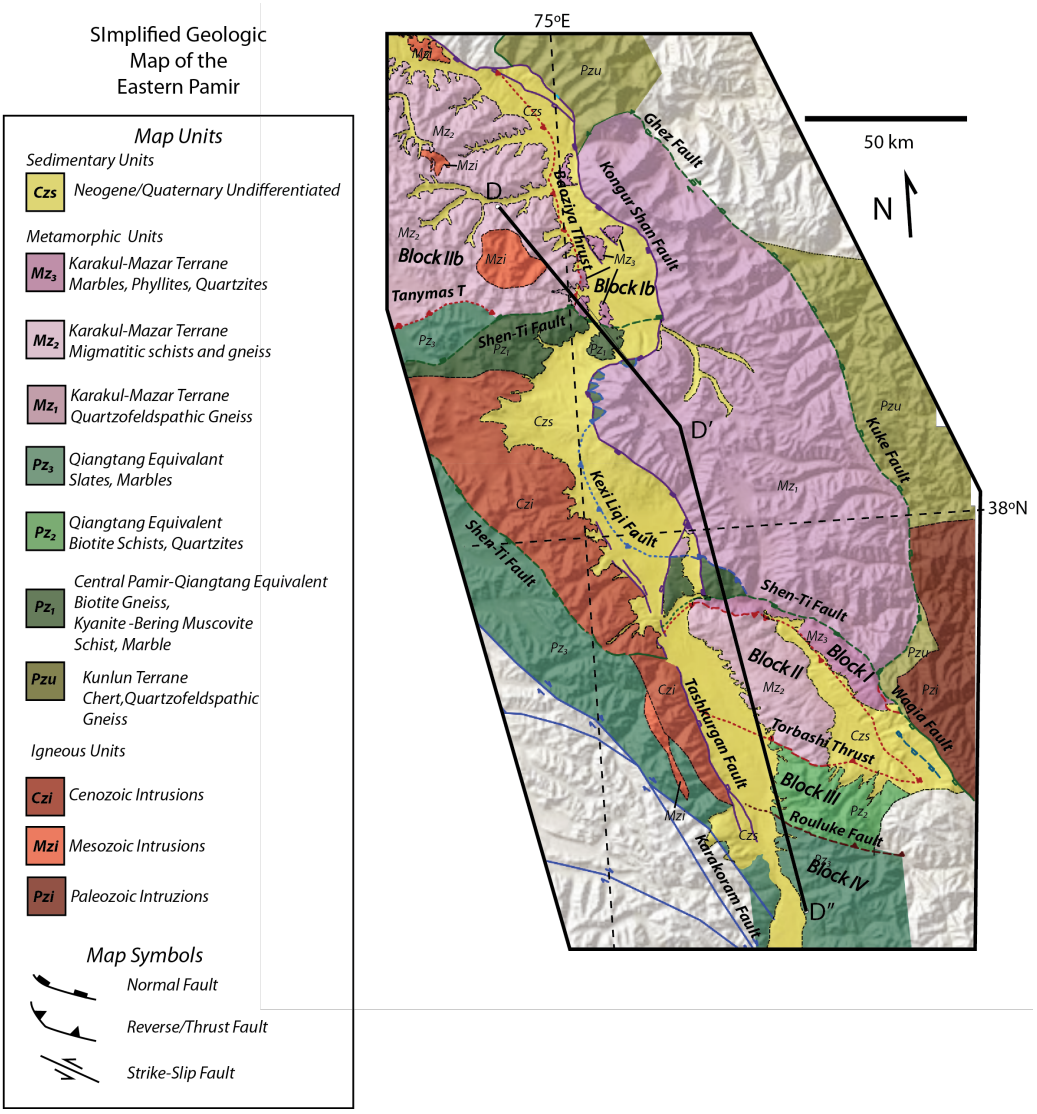

Figure 13: Simplified geological map of the eastern Pamir, with emphasis on structural blocks mentioned in the text.

3.2. STRUCTURAL BOUNDARIES

The study area south of Muztaghata is divided into four structural blocks bound by normal faults and thrust faults. The northernmost structural boundary is the Shen-Ti/Waqia Fault, a down-to-the-south/southwest normal fault (Figure 3). At its southeast end, the Shen-Ti/Waqia Fault juxtaposes Ordovician (?) meta-chert and Paleozoic granites in the footwall against Neogene sediments in the hanging wall. Based on thickness of Neogene sediments, the Shen-Ti/Waqia Fault has accommodated > 1 km of vertical separation in the Neogene. To the northwest, the fault juxtaposes quartzofeldspathic gneisses and schists from the Muztaghata massif in the footwall (Robinson et al., 2007) against phyllites and marbles from Block I in the hanging wall.

The Torbashi thrust is mapped as a synformal klippe, consistent with Robison et al. (2007). Identification of the Torbashi Thrust in the eastern Pamir is based the juxtaposition of high-grade schists and gneisses intruded by granites structurally above lower grade schists, phyllites, marbles and quartzites. The Torbashi thrust crops out along the Tashkurgan River where it strikes ~E-W. The strike changes to NW-SE at the northern end of the Waqia valley where it continues along the eastern side of the valley. Shear-sense indicators of metamorphic fabrics near the Tashkurgan river valley show top to the south shear-sense. In the Tashkurgan Valley, upper amphibolite facies schists and gneisses are structurally above lower amphibolite/upper greenschist facies schists, near the town of Gedeben, which indicates a thrust contact. In the Waqia Valley, the trace of the Torbashi Thrust is generally buried beneath Neogene to Quaternary sedimentary rocks. The fault is observed in a few localities and identified by 1) structural

juxtaposition of units with contrasting metamorphic grade and 2) a high strain zone. The fault trace strikes parallel to the Waqia Valley axis through most of the valley.

Near the town of Rouluke, biotite-garnet schists and quartzites with northeast dipping foliations structurally overlie low-grade slates and marbles with north-dipping foliations indicating the presence of a northeast-dipping thrust fault, previously identified as the southern boundary of the Torbashi Thrust (Yin and Bain, 1992; Robinson et al., 2007). Based on more detailed field mapping, the southern trace of the Torbashi Thrust is redefined as an independent structure called the Rouluke Fault. The fault dips to the northeast and strikes northwest with fault striations showing top to the south sense of shear. The lateral extent of the Rouluke Fault is not clear. While the western continuation of the fault is truncated by younger Tashkurgan normal fault, the eastern continuation of the Rouluke Fault is unclear.

3.3. NORTHERN FW TORBASHI (BLOCK I)

Block I is defined as the metasedimentary units in the hanging wall of the Shen-Ti Fault and the northern footwall Torbashi Thrust in the south. Block I is characterized by phyllites, marbles, quartzites, and garnet-biotite schists. Peak metamorphic assemblages include biotite + garnet ± white mica and white mica + chlorite + quartz (Figure 14c,d). Quartz shows bulging deformation and subgrain rotation along quartz-quartz grain boundaries of quartz rich microlithons of biotite schists. Rotated garnet porphyroblasts suggest syntectonic growth. Foliation is commonly exhibited as a continuous or spaced cleavage. Where present, shear sense indicators indicate top-to-the-south shear.

One notable sample for Block I is AR-7-3-00-4 (Figure 14d). The sample consists of garnet + quartz + chlorite. The garnet in the sample is subidioblastic and

shows ~90 degree rotation based on internal inclusions relative to the surrounding foliation, and strain shadows occur around the garnet indicating it's growth during prograde metamorphism.

Foliations in Block I generally dip to the southwest (Figure 14c,d). However, second order folds occur (Figure 3) adjacent to the Shen-Ti Fault. With the assumption that folding throughout Block I is resultant from similar deformation events, a beta axis was calculated for the fold with a trend and plunge of 120°/18° (Figure 15). Mineral stretching lineations are oriented northwest-southeast with top-to-the-south sense of shear recorded by asymmetric kink folds in phyllite (Figure 14c).

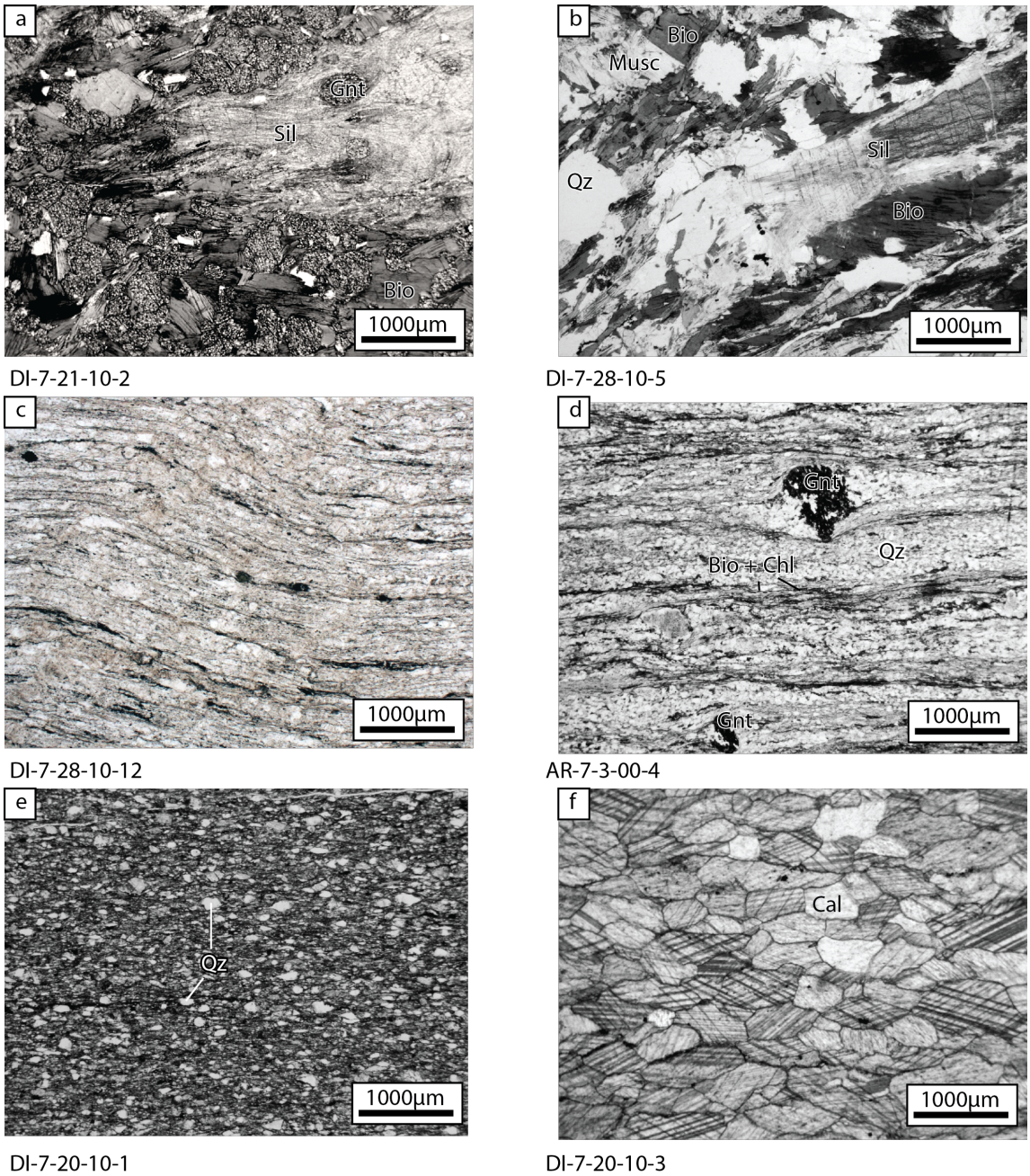

Figure 14: Photomicrographs of metamorphic units in the Tashkurgan and Waqia Valley areas. (A) Sillimanite+Garnet+Biotite+Plagioclase migmatitic schist and (B) Sillimanite+Muscovite+Biotite+Quartz schist from the hanging wall of the Torbashi Thrust. (C) Kink folds in phyllite and (D) Muscovite+Garnet phyllitic schist showing a rotated garnet, 90 degrees, from the footwall of the Torbashi Thrust. (E) Slate from the footwall of the Rouluke Fault. (F) Marble from the footwall of the Rouluke fault.

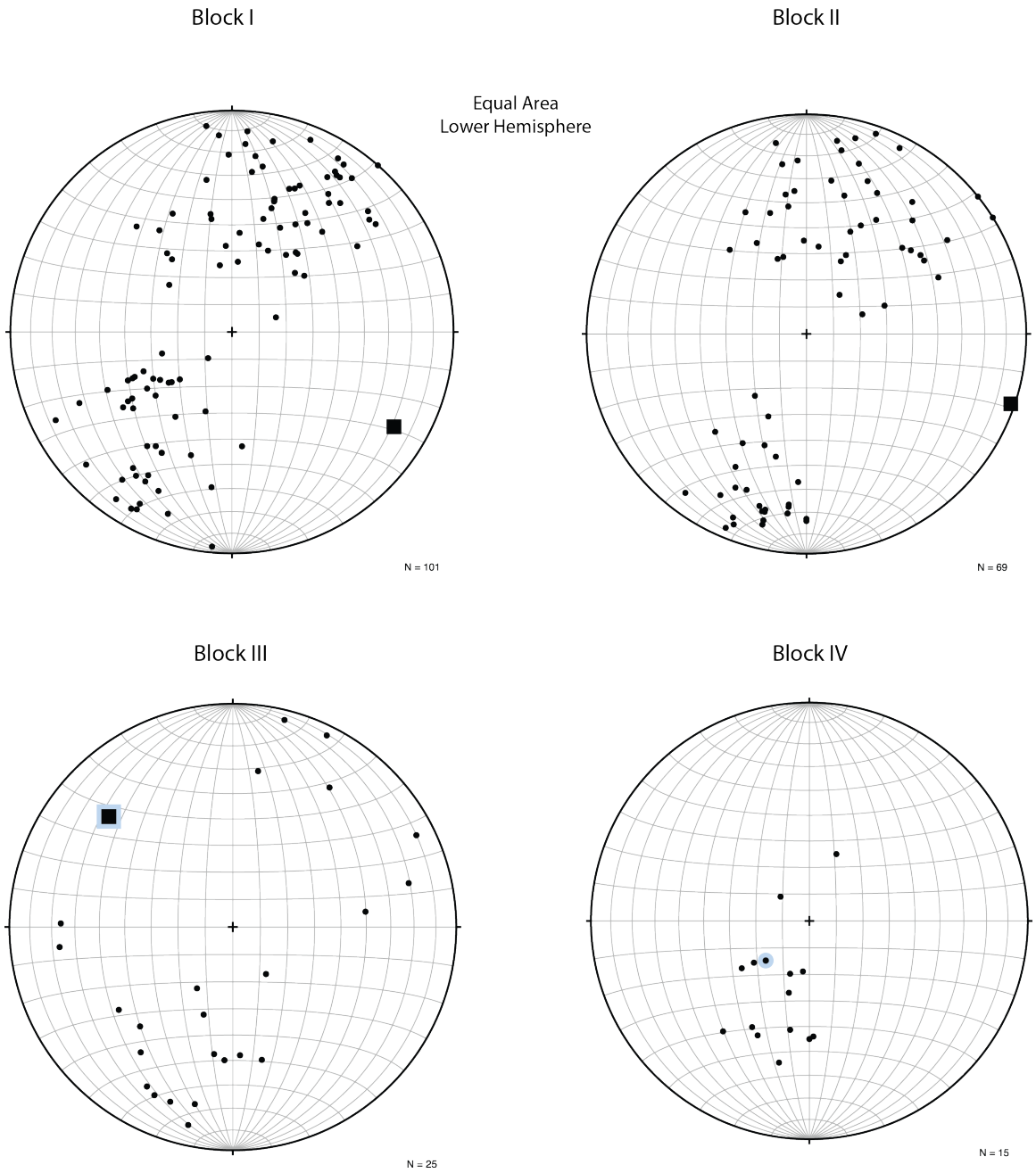

Figure 15: Foliation measurements divided by structural block in which they were collected. Poles to planes are plotted as dots on equal area projection lower hemispheres. Fold beta axes are plotted as large black boxes.

Block I

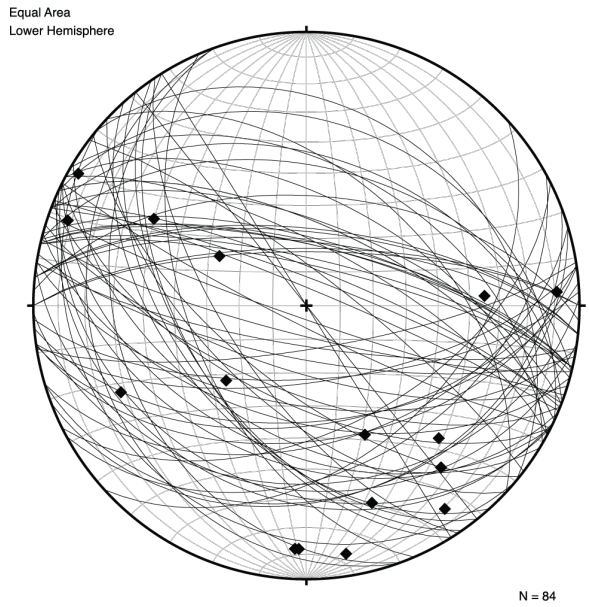

Block II

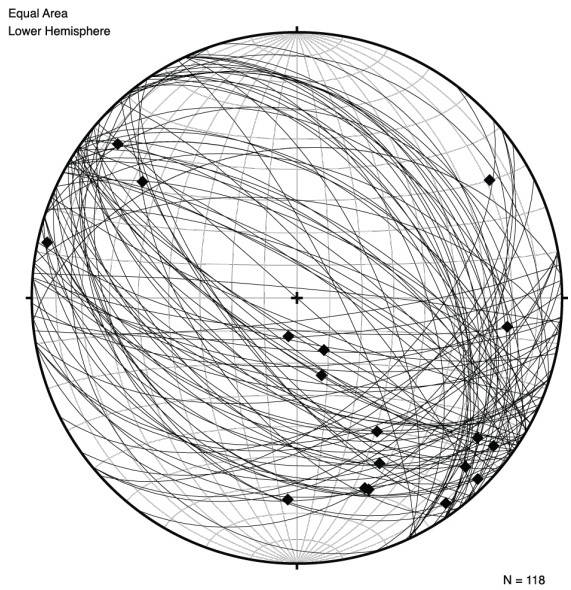

Figure 16: Foliation/lineation measurements divided by structural block. Foliation planes are plotted with mineral stretching lineation measurements (Black Diamonds).

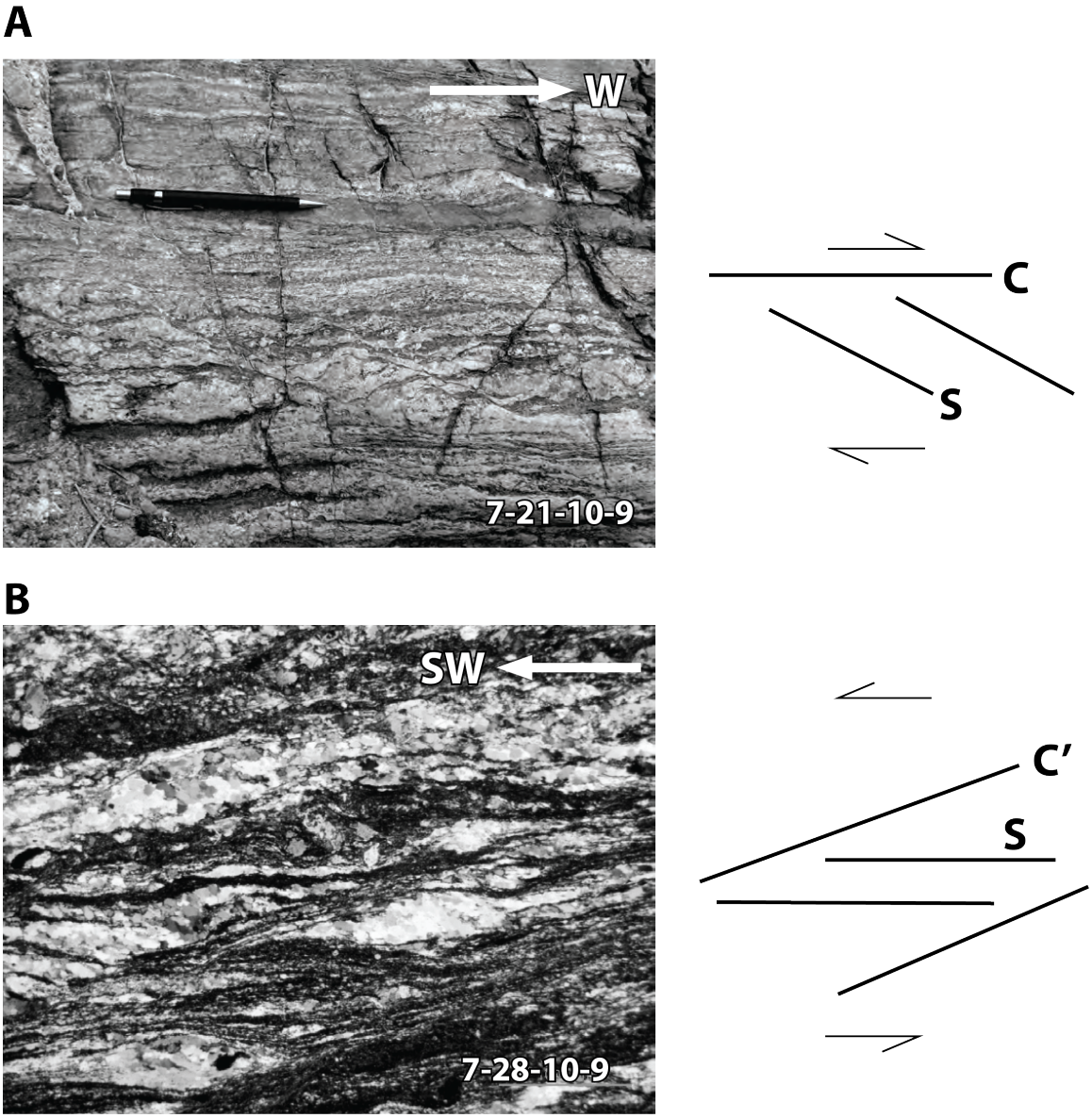

Figure 17: Shear sense indicators. (A) Top to the west shear sense defined by S/C fabric in migmatitic biotite schist of the Torbashi Fault hanging wall. (B) Quartz rich chloritic schist showing top to the southwest shear sense in the Waqia Valley footwall of the Torabshi Thrust.

3.4. HW TORBASHI (BLOCK II)

Block II, The hanging wall of the Torbashi Thrust, is characterized by high-grade metasedimentary schists, migmatites, and gneisses intruded by granites. Typical peak metamorphic assemblages include sillimanite + garnet + biotite ± feldspar (Figure 14a,b). Quartz-rich lithologies near the axis of the fold show grain-boundary migration deformation fabrics. In the Waqia Valley, near the Torbashi Thrust, grain-boundary migration is overprinted by bulging deformation. Garnet porphyroblasts are commonly syntectonic to post-tectonic.

A typical sample for the hanging wall of the Torbashi Thrust is AR-7-21-10-2 (Figure 14a). The metamorphic mineral assemblage in this sample consists of sillimanite + garnet + biotite suggesting upper amphibolite facies metamorphic conditions. Garnets and biotites in this sample exhibit no strain shadows and foliation is defined by compositional layering, not the orientation of grains (i.e. biotite is not preferentially aligned crystallographically), suggesting post-tectonic growth. Additionally, Garnets are subidioblastic, ranging 1-5 mm in size. Sillimanite regularly occurs as fibrolite.

Foliation in Block II is defined by schistose and gneissic banding of pelitic and migmatitic units (Figure 14a,b). Map patterns of Block II indicate a first-order synformal fold geometry. Based on foliation dip, the axis of the fold has a southeast trend through the center of the block (Figure 3). Trend and plunge of the fold axis is 110º/2º (Figure 15b). Mineral stretching lineations were measured on foliation planes (Figure 16b). Top to the southwest shear sense was recorded in S-C fabrics throughout Block II (Figure 17a).

3.5. SOUTHERN FW TORBASHI (BLOCK III)

Block III consists of the southern footwall of the Torbashi Thrust and the hanging wall of the Rouluke Fault. The region described in this paper as the southern footwall of the Torbashi Thrust has previously been described as part of the hanging wall of a larger Torbashi Thrust (Robinson et al., 2007) (Figure 3). However, petrographic data show significantly higher metamorphic grade in the hanging wall of the Torbashi Thrust compared with lithologies in Block III. Petrographic data are supported by zircon U/Pb analysis (described later in this paper) of a granite in Block III which records an Ordovician crystallization age, whereas results from detrital zircon analysis record a Triassic/Jurassic maximum depositional age for metasediments in samples of Block II. Therefore, a new location of the southern contact of the Torbashi Thrust is defined ~20 km north from its previous location (Figure 3). Consistent northeast dipping foliations and top-to-the-south shear sense indicators near the interpreted fault contact suggest this is a thrust. Hereafter I refer to the northern footwall (Block II) and southern footwall (Block III) of the Torbashi Thrust independently.

Lithologies in this region are commonly micaceous quartzites, phyllites, marbles, and schists. Peak metamorphic assemblages are biotite + garnet + quartz (Figure 18). Quartz deformation occurs in the microlithons between foliation surfaces in the quartzites and show bulging and subgrain rotation deformation. Quartz shows minor evidence of buldging deformation in quartz rich microlithons.

Foliation in the schists and phyllites is commonly continuous schistosity or continuous cleavage (Figure 18). Quartzites exhibit spaced, smooth, anastomosing, discrete shistosity. Regional foliation strikes northwest and dips northeast. Asymmetric

3rd order (outcrop scale) folds show top to the southwest shear sense and fold axes have a trend and plunge of ~295º/30º. The beta axis calculated from foliation measurements across the structural block is 305º/25º (Figure 15).

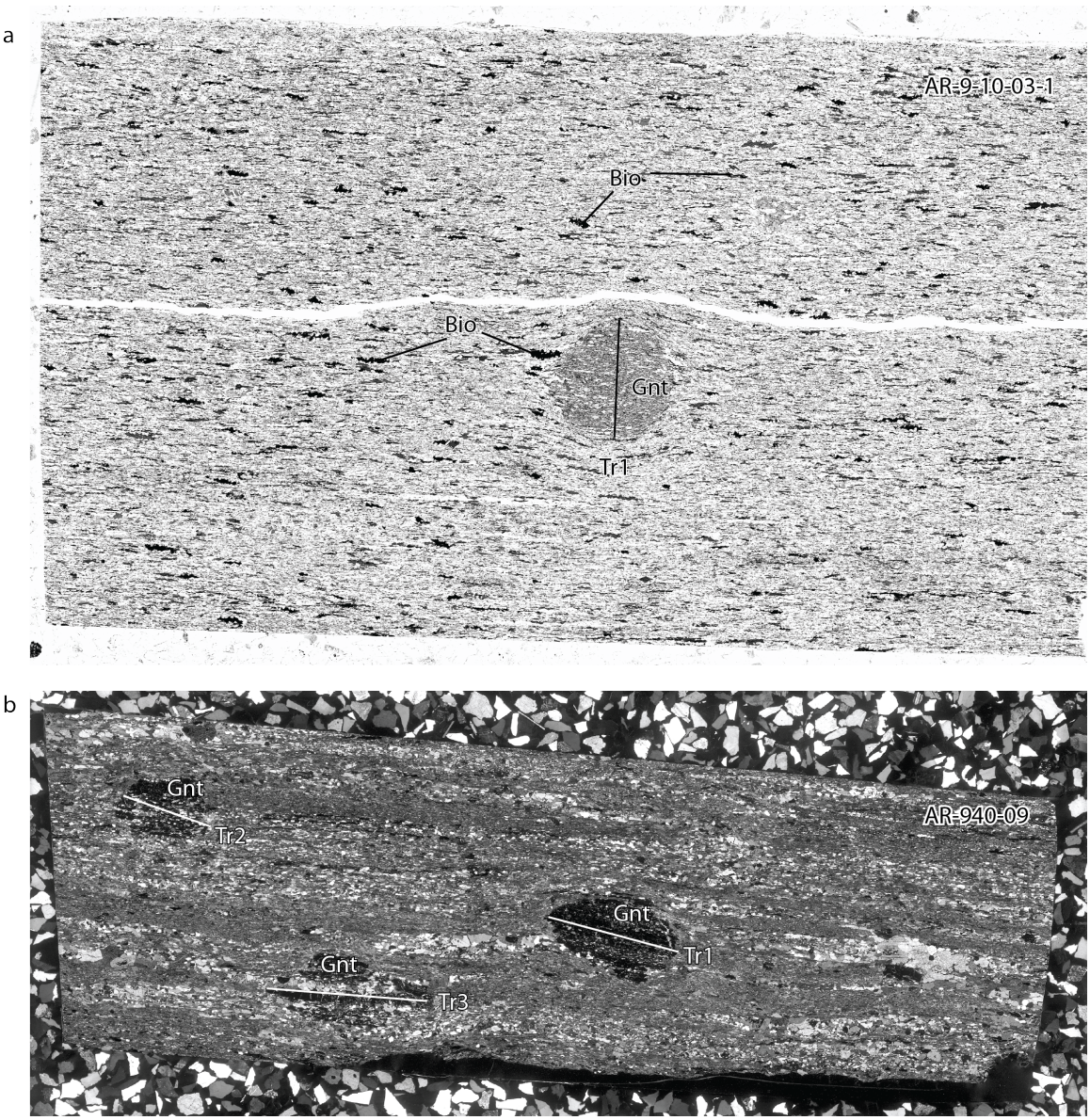

Figure 18: Photomicrographs of thin sections used for garnet-biotite thermometry. Garnet profile transects are indicated. Bio – Biotite. Gnt- Garnet.

3.6. FOOTWALL ROULUKE FAULT (BLOCK IV)

The footwall of the Rouluke Fault (Block IV) consists of slates, phyllites, quartzites, and marbles. Marbles are granoblastic (Figure 14f). Strain of quartz grains is identified to be limited to linearly oriented inclusions. Peak metamorphic mineral assemblages are limited to post-tectonic biotite. Foliation in Block IV is defined by slaty cleavage of low-grade metamorphic rocks and generally strikes northwest and dips northeast (Figure 15d). Weak continuous foliation and cataclastic microtextures are present in the silicate-rich samples. Tension gashes indicate the presence of top to the southwest shear zones in Block IV. One sample, a biotite-and marble-bearing quartzite (DI-7-15-10-4) shows biotite growth across weakly defined foliation boundaries.

4. QUANTITATIVE GARNET-BIOTITE THERMOMETRY

4.1. METHODS

To quantitatively determine temperature conditions of peak metamorphism for the footwall of the southern boundary of the Torbashi Thrust (Block III), I prepared and analyzed two samples from the southern footwall of the Torbashi Thrust using the garnet-biotite Fe-Mg exchange thermometer. Electron Microprobe analyses were conducted at Texas A&M University using a 1 μm spot size with a 15 kV accelerating voltage, a 20 nA beam current, and a 30 second counting time for each element. Activities of garnet phases and equilibrium Clapeyron slopes were calculated using the programs AX and Thermocalc 2.7 (Powell et al., 1998). I conducted electron microprobe traverses to identify zoning patterns in garnets to interpret the temperature results.

Garnet profiles were created using Fe# and activities of garnet end members derived from Thermocalc . I report Fe#, calculated as Fe/(Fe+Mg) to evaluate zoning

within garnets. Pyrope activities (a_{py}) are included in Table 1, but not reported here or interpreted for compositional variation due to the low values in the analysis. For comparison, I note the presence of garnet + biotite typically suggests temperatures >450°C (Spear, 1995). I report temperatures based on an assumption of 4 kbar pressure conditions, based on iterative results and reasonable geothermal gradient conditions.

4.2. RESULTS

4.2.1. AR-940-09

Sample 940-09 is a quartz-rich garnet biotite schist (Figure 18b). The primary metamorphic mineral assemblage is garnet + biotite + quartz. Foliation is smooth, zonal, parallel to anastomosing, with discrete boundaries between biotite-rich schistose domains and quartz-rich microlithons. Garnets are subidioblastic to xenoblastic and appear to be late syn-tectonic to post-tectonic, evidenced by consistent foliation internal and external to garnet grains and the apparent lack of strain shadows. Electron microprobe transects were completed across three garnet grains in the sample. While biotite was analyzed near the garnet grains and away from the garnet grains to asses lateral variability, no significant variability was detected. I used average activities of biotite end-members (phlogopite and annite) based on a series of tests for compositional variation.

Three garnet transects were analyzed in sample AR 940-09. Garnet transect 1 shows moderate zoning in Mn, a_{sp} and Fe, a_{al} and and Ca, a_{gr}. a_{gr} is inversly related to a_{sp} and a_{al} (Figure 19a). The Fe# is invariable across the garnet grain. The Garnet Biotite thermometer in transect 1 shows minimum temperatures ~500°C and maximum temperatures ~560. An interesting note for transect 1 is the occurrence of a compositional break at ~3000 μm. A plausible interpretation for this compositional break

is the grain, originally sampled as one garnet grain, is may be two amalgamated garnet grains that grew together during metamorphism. The garnet rims are interpreted to record of peak metamorphic temperatures. Garnet transect 2 shows less pronounced zoning than Garnet transect 1 (Figure 19b). Zoning occurs within <500 μm from the rims in Mn, or a_{sp}. Fe (a_{al}) and Ca (a_{gr}) and the Fe# do not show evidence of clear compositional zoning across the transect. Estimates of temperature are variable, from ~500°C to ~530°C. Garnet transect 3 shows little evidence of compositional zoning, except with a_{al} (Figure 19c). a_{al} shows a sharp peak near the rim and flattens within <500 μm of the core. Fe# is invariable across the transect. Temperature estimates are not symmetric across the grain, with minimum temperature estimates ~510°C to maximum estimates ~565°C.

4.2.2. AR-9-10-03-1

Sample AR-9-10-03-1 is a garnet-biotite schist (Figure 18a). The metamorphic mineral assemblage is garnet + biotite + quartz. Foliation is defined as continuous schistosity. Inclusions within the garnet indicate ~25 degrees of rotation. Some biotites are syn-tectonic, while some show post-tectonic growth patterns.

An electron microprobe transect was completed across the single garnet grain in the sample. The garnet shows strong compositional zoning in Mn and Fe (Figure 20a). The Mn profile, a_{sp}, shows a bell shaped curve from the core to the rims, characteristic of garnet growth during prograde metamorphism (Hollister 1966). The a_{al} profile shows an inverse relationship to X_{sp} across the grain and Fe# is invariable. The temperature profile, calculated from Fe-Mg exchange reaction in biotite and garnet, also shows a general trend to higher temperatures from core to rim. Minimum temperatures at the core of the

garnet are ~380°C and near the rims are 470-490°C. Garnet petrofabric analysis showing rotated inclusions and quantitative major element zonation are consistent, suggesting the garnet grew during tectonic deformation.

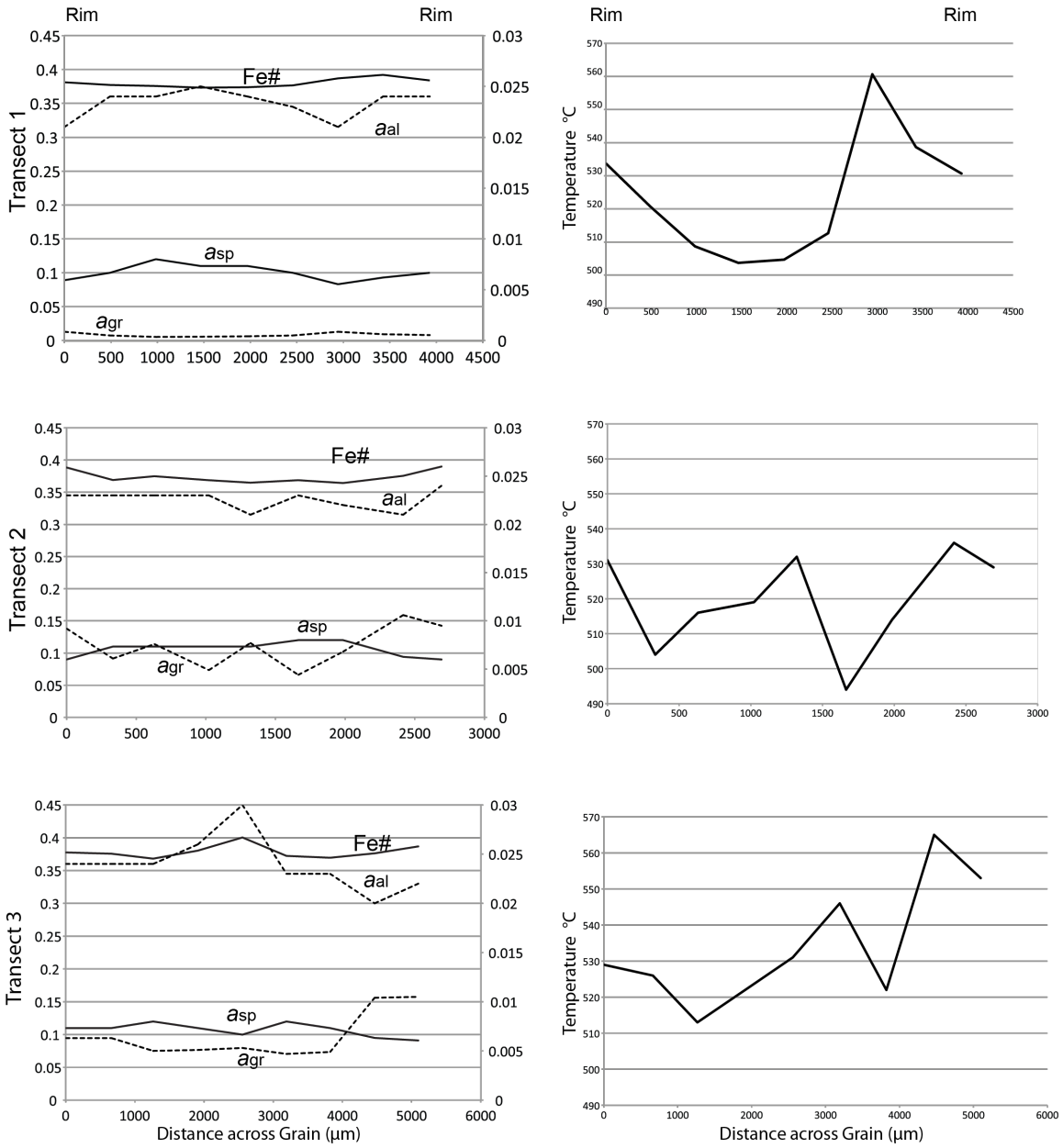

Figure 19: Profiles across garnet transects for sample AR-940-09. Left column: Garnet zoning, rim to rim, of three garnet transects in sample AR-940-09. Activity values for spessartine, almandine, and grossular are derived from thermocalc. asp - Spessartine activities, aal - Almandine activation energy, agr - grossular activation energy, Fe# - Fe/(Fe+Mg). Solid curves are referenced to the left-side Y axis. Dashed curves are referenced to the right-side Y axis. Right column: Temperature profiles for the garnet transects.

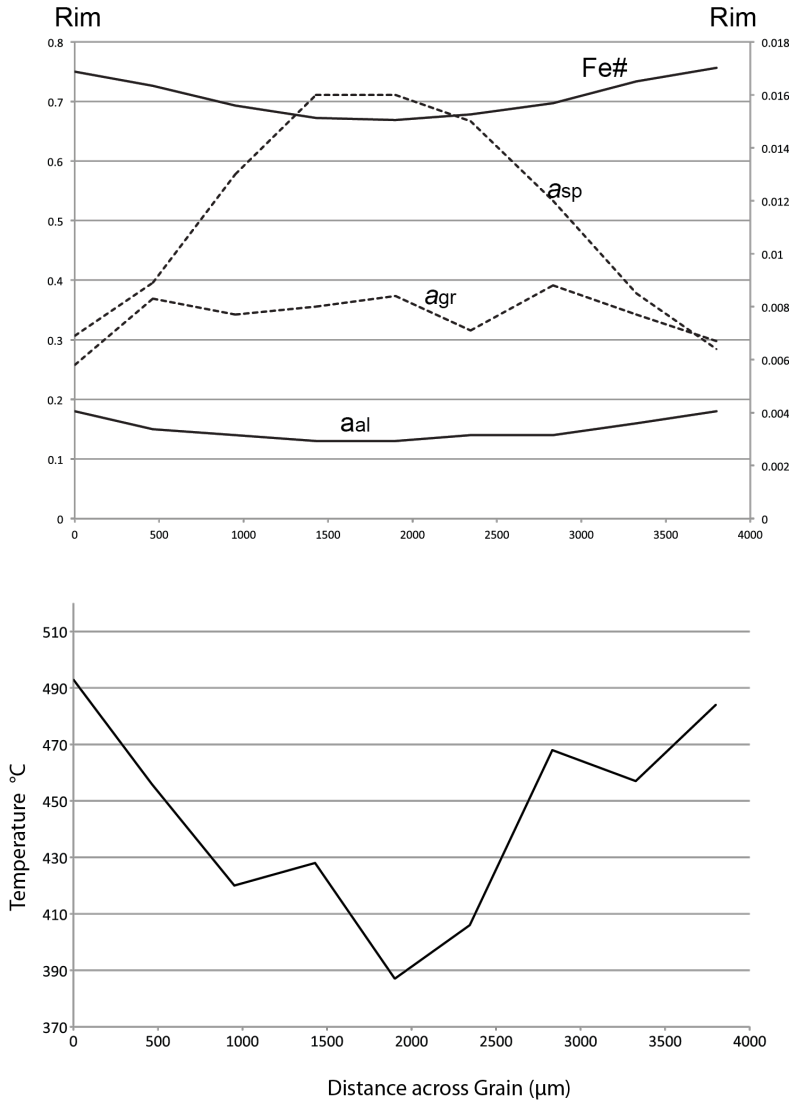

Figure 20: Garnet profiles for sample AR-9-10-03-1. Top: Garnet zoning profile, rim to rim, of sample AR-9-10-03-1. Activity values for spessartine, almandine, and grossular are derived from thermocalc. . *a*sp - Spessartine activation energy, *a*al - Almandine activation energy, *a*gr - grossular activation energy, Fe# - Fe/(Fe+Mg). Solid curves are referenced to the left-side Y axis. Dashed curves are referenced to the right-side Y axis. Bottom: Temperature profile for the garnet transects.

5. U-PB GEOCHRONOLOGY

5.1. METHODS

Igneous and metasedimentary samples were selected across defined structural blocks in the study area (Figure 21). Zircon grains were separated from the samples using conventional techniques. 1) The samples were crushed and sieved through a 32 mesh sieve. 2) The samples were passed through a neodymium magnet to remove iron filings from the crushing process. 3) A water table was used to remove low density material from the sample. 4) The remaining material was then processed through Methylene Iodide liquid to separate the dense fraction. 5) Heavy minerals separated from the MI were then processed through a Franz magnetic separator. The remaining fraction was mounted in epoxy and polished to expose grain interiors. The metasedimentary samples and the igneous sample AR-9-10-03-4 were not manually picked for zircon to eliminate manual bias, while igneous sample AR-9-10-03-7 was manually picked for zircon.

U-Th-Pb analyses were performed at the University of Houston on a Varian quadrupole ICP-MS. Laser ablation analyses were performed at the University of Houston with a Cetac LSX-213 laser with a 50-20 nm beam diameter at 15 Hz and a Photon Machines Analyte 193 excimer laser with a 20 μm beam diameter at 10 Hz. Instrument fractionation of U/Pb and 206Pb/207Pb during analysis by analyzing fragments of zircon standard Plesovice (age at 2 sigma) in between 5 consecutive unknown analyses. Analyses of zircon standard FC5z (1096.2 ± 1 ma (2σ) or Peixe (564 ± 4 (2σ) (Shaulis et al., 2010) were conducted after every 10 unknown to analyses to monitor the calibration. Analyses were not corrected for common Pb. All uncertainties

are reported at the 2σ level. Age probability plots were created using Isoplot 3.0 (Ludwig, 2003). Detrital zircon probability plots exclude isotopic ratios with a discordance of >30% and less than -5%. Ages >1.0 Ga are reported as 206Pb/207Pb ages and zircon ages <1.0 Ga are reported as 206Pb/238U ages. Maximum depositional ages are reported as the calculation of the weighted mean age of the youngest three overlapping zircon ages in the sample. Igneous ages are reported from the calculation of 206Pb/238U ages using the Isoplot TuffZirc age extractor.

5.2. RESULTS

5.2.1. Igneous Rock Zircons

5.2.1.1. Sample AR-9-10-03-4

Sample AR-9-10-03-4 is a quartzofeldspathic orthogneiss with a weak foliation. 30 zircons were analyzed with 21 concordant analyses. A TuffZirc age of 479.02 $^{+14.23}/_{-2.85}$ Ma was calculated for the concordant grains (Figure 22a).

5.2.1.2. Sample AR-9-10-03-7

Sample AR-9-10-03-7 is a garnet-bearing biotite granite sill showing weak to no foliation. 45 analyses were performed on the sample, with 14 concordant analyses. A TuffZirc age of 197.56 $^{+3.27}/_{-4.78}$ Ma was calculated for the concordant grains (Figure 22b).

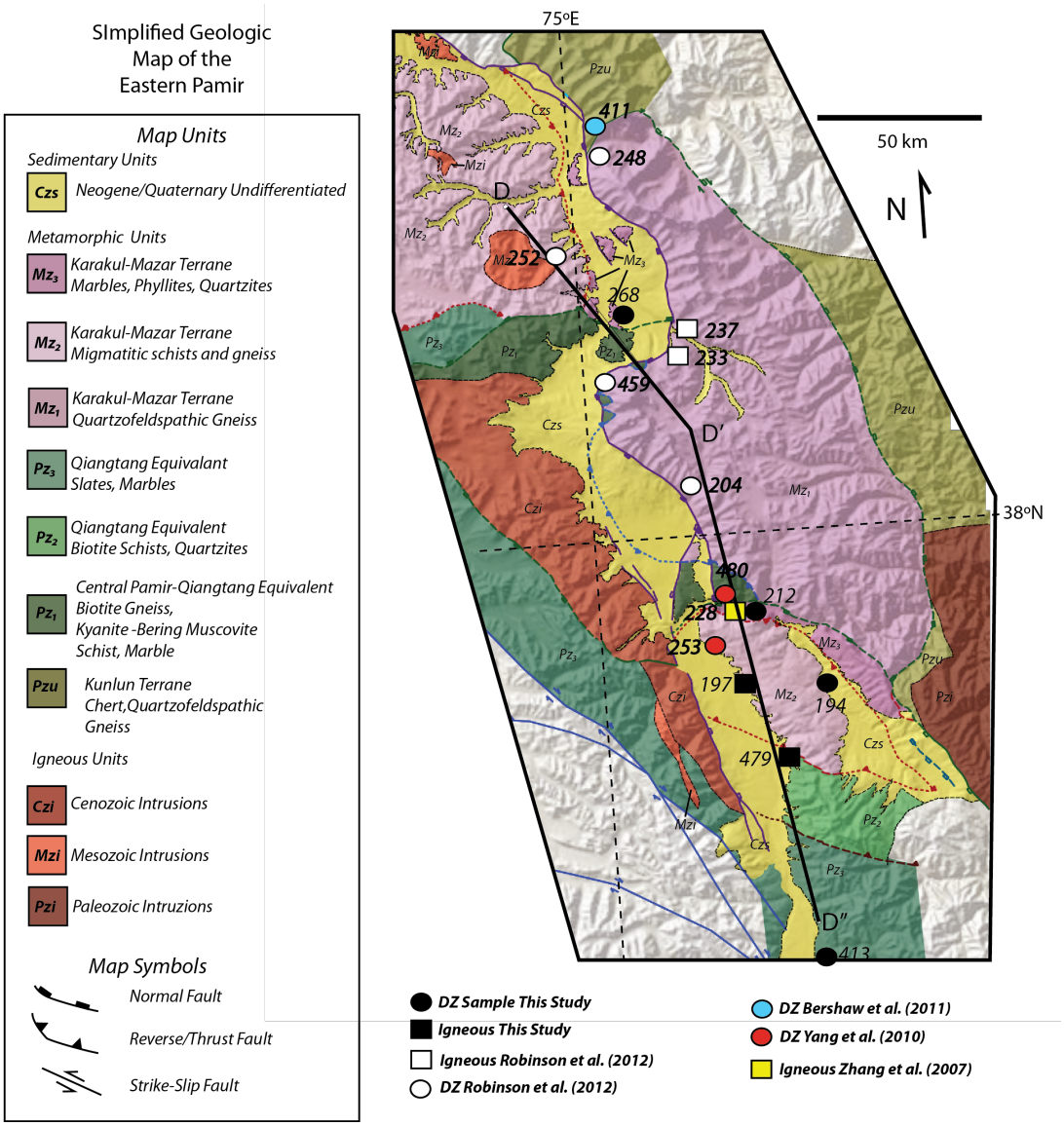

Figure 21: Sample locations for zircon U/Pb analysis. Samples from this study are indicated in black. Samples in white are from Robinson et al. (2012). Samples in yellow are from Zhang et al. (2007). Samples in blue are from Bershaw et al. (2012). Samples in red are from Yang et al. (2010). Circles indicate detrital zircon analysis. Boxes indicate igneous samples.

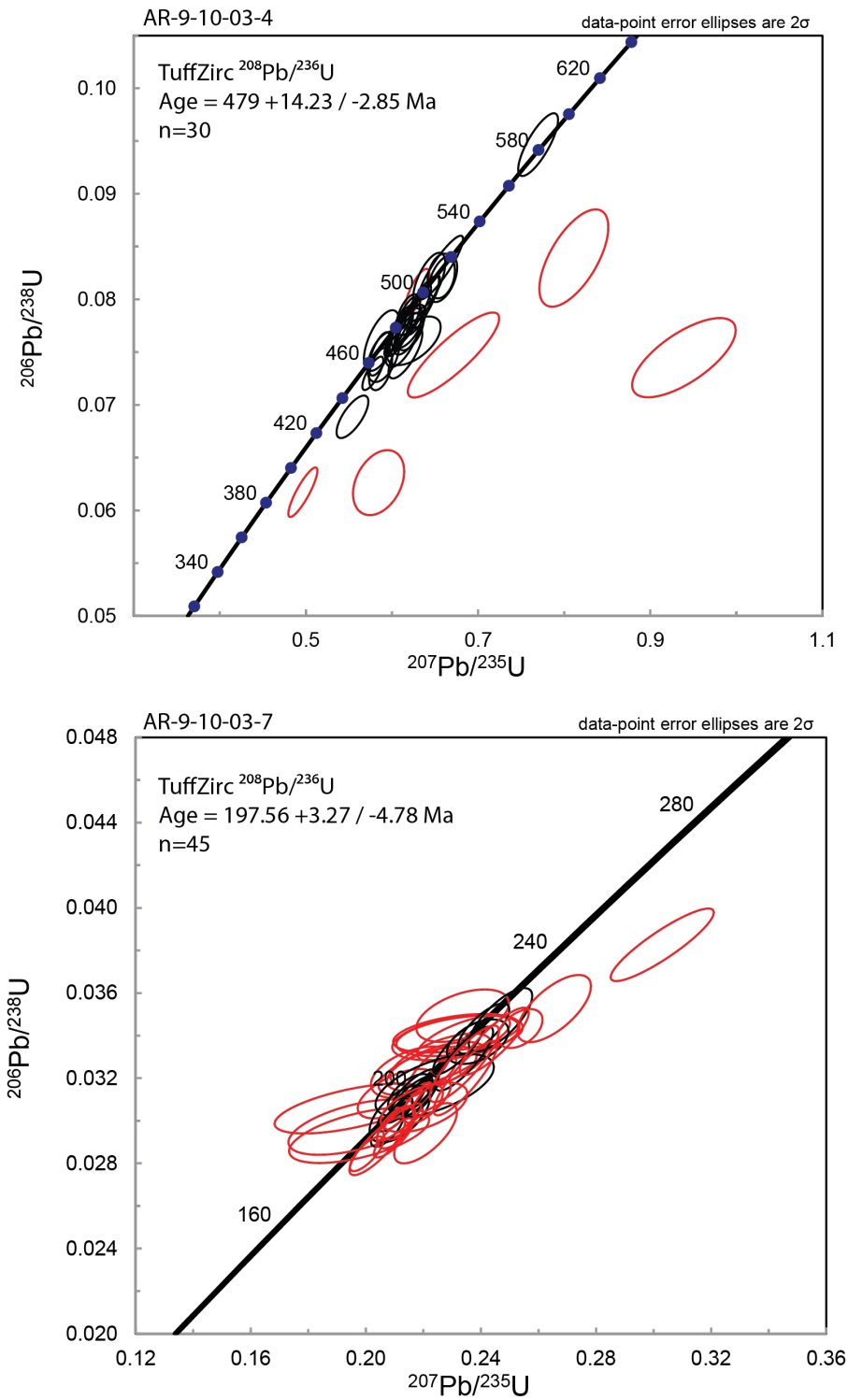

Figure 22: U/Pb concordia plots for the two igneous zircon samples from the Tashkurgan Valley. Concordia plots show error ellipses for (black) concordant and (red) discordant zircons. Calculated ages are generated from the Isoplot TuffZirc age extractor.

5.2.2. Detrital Rock Zircons

5.2.2.1. Sample AR-6-26-00-7

Sample AR-6-26-00-7 is a dark grey phyllite from the footwall of the Rouluke Thrust in the Tashkurgan Valley. 164 zircons were analyzed yielding 92 concordant ages (Figure 23d). The three youngest zircons overlapping in age yield a maximum depositional age of 413 ± 17 Ma (Figure 24a). Prominent Pre-Cambrian age peaks are 590-716 Ma, 730-1040 Ma, and 1690-1880 Ma with smaller peaks 2050-2140 Ma and 2340-2470 Ma. Phanerozoic ages range from ~405-480 Ma with maximums at 424 and 452 Ma.

5.2.2.2. Sample AR-4-28-00-11a

Sample AR-4-28-00-11a is a garnet-biotite gneiss from the hanging wall of the Torbashi Thrust in the Waqia Valley. 120 zircons were analyzed and 53 were concordant (Figure 23c). Zircons in this sample have an age range of 187-239 Ma, with a maximum peak at 206 Ma (Figure 24b). The maximum depositional age is calculated to be 194 ± 2.7 Ma.

5.2.2.3. Sample AR-4-28-00-7

Sample AR-4-28-00-7 is a quartz-rich phyllite from the northern footwall of the Torbashi Thrust. 120 zircons were analyzed and 82 were concordant (Figure 23b). Overlap of the three youngest zircons yields a maximum depositional age of 212 ± 3 Ma (Figure 24c). Pre-Cambrian age peaks include 610-650 Ma, 690-780 Ma, 890-980 Ma, 1230-1390 Ma, and 1590-1650 Ma. Phanerozoic age peaks ~211 Ma, ~295 Ma, ~325 Ma, and 390-520 Ma.

5.2.2.4. Sample AR-4-27-00-9

Sample AR-4-27-00-9 is a chlorite-bearing quartz-rich schist from the footwall of the Baoziya Thrust north of Muztaghata (Block Ib). 136 zircons were analyzed with 73 concordant analyses (Figure 23). Conservative analysis of the three youngest zircons overlapping in age yields a maximum depositional age of 268 ± 11 Ma (Figure 24a). However, concordant grains in this sample with 218 ± 5.4 Ma and 234 ± 6.2 Ma ages suggest the sample may be Late Triassic in age. Precambrian age peaks occur ~791, ~863, ~960, 1600 Ma to 2100 Ma, and ~2500 Ma. Phanerozoic age peaks include ~270 Ma, ~335 Ma, and ~410 Ma. K-S Test analysis yields statistical similarity to 1) two samples from the footwall of the Kongur Shan extensional system (AR-8-29-99-6, AR-5-20-00-3), 2) a Cretaceous sediment sample from the Oytag region of the west Tarim Basin (PMR-26 Bershaw et al. (2012)), 3) and 2 Triassic age samples from the Hoh-Xil terrane (samples “2007K410” and “2005K119” from Ding et al. (2013)).

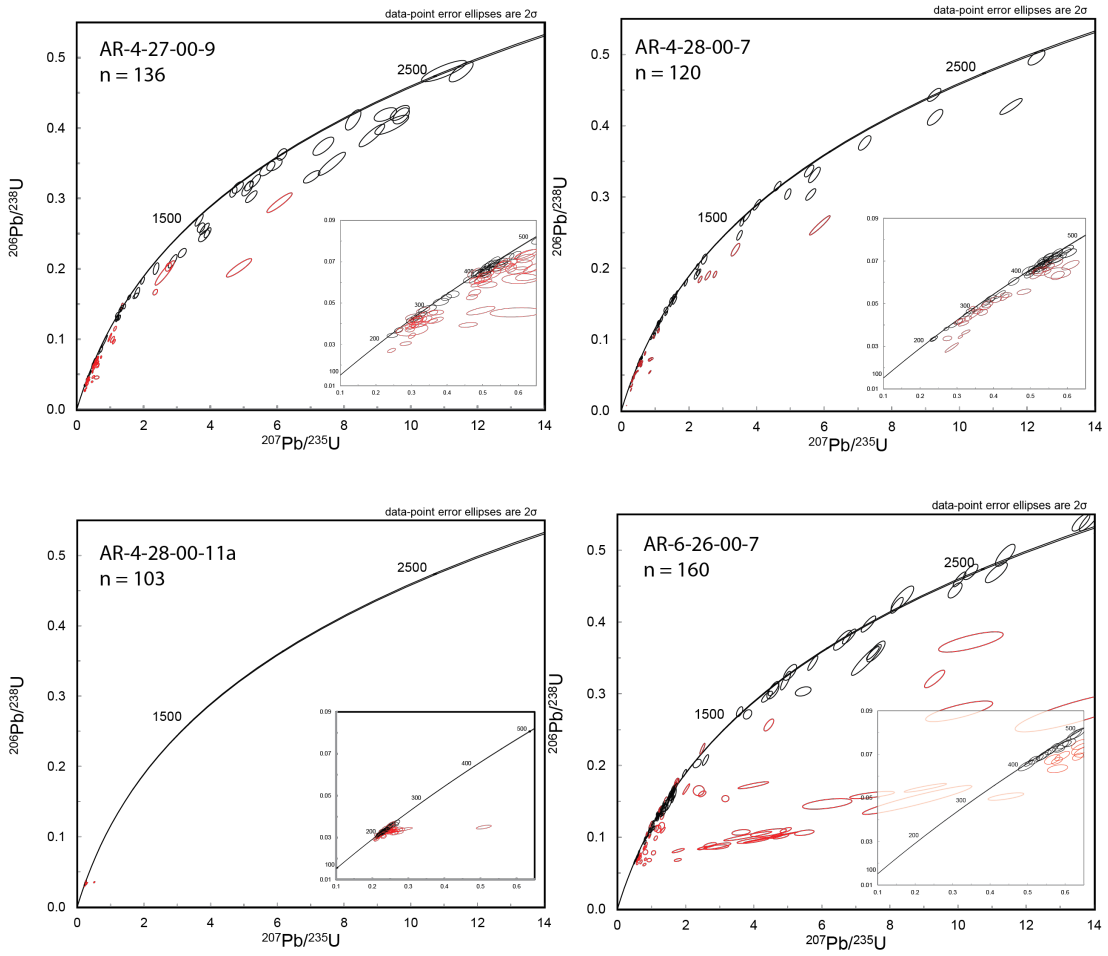

Figure 23: U/Pb concordia for the 4 detrital zircon samples from the Eastern Pamir. Concordia plots show error ellipses for (black) concordant and (red) discordant zircons.

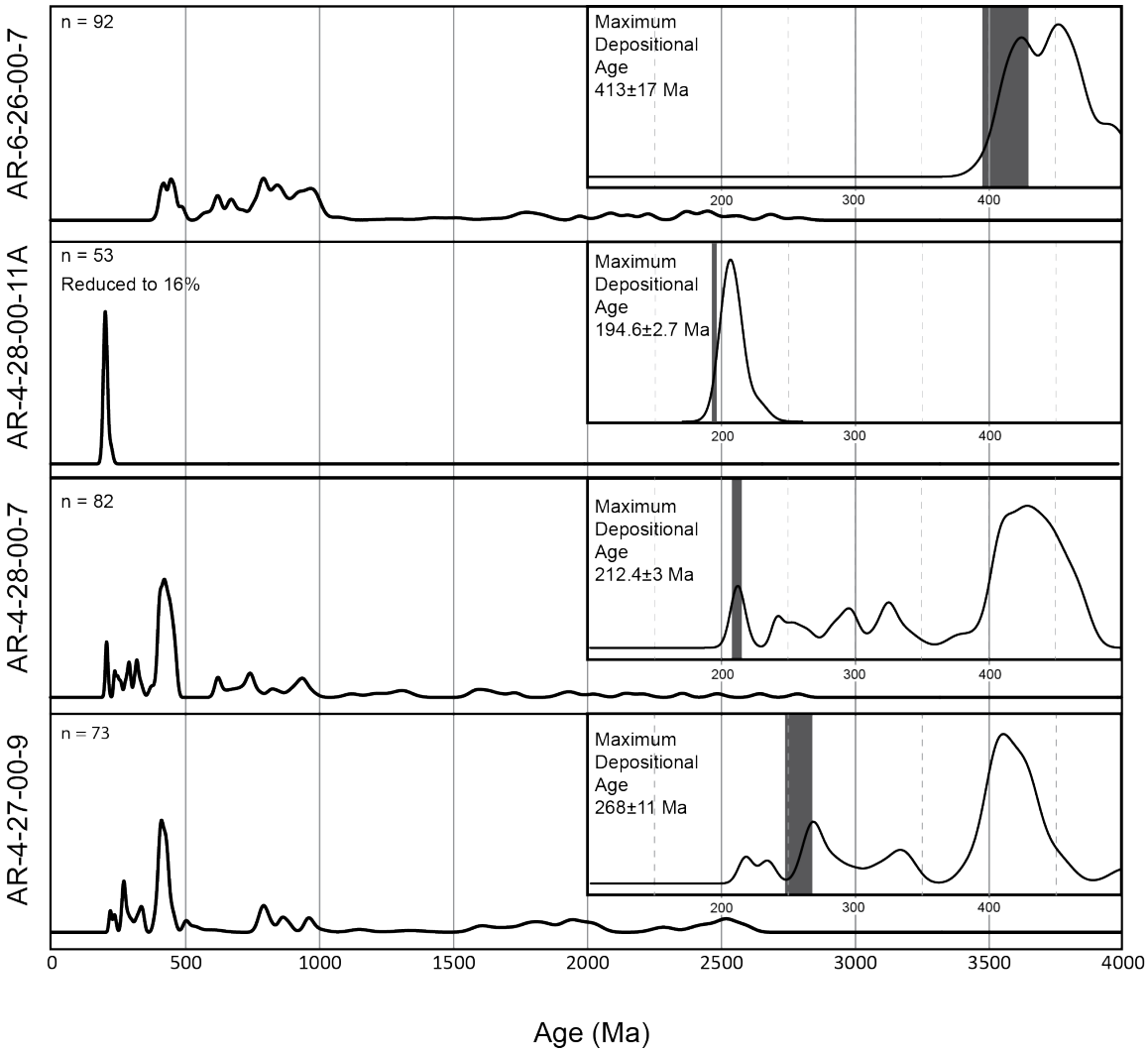

Figure 24: U/Pb cumulative age probability plots for the four metasedimentary samples from the eastern Pamir.

6. DISCUSSION

In this section, a revised structural and tectonic model for the eastern Pamir is presented. First, key first-order observations are synthesized. Next, a revised structural architecture in which correlations are made between the southeast and north Pamir is discussed. Finally, correlations are presented between terranes of the Pamir and Tibet based on results from this study.

6.1. STRUCTURAL AND METAMORPHIC RELATIONSHIPS

Previous work identified the northern boundary of the Torbashi Thrust along the southern end of the east-west Tashkurgan River, with a southeast bend along the eastern side of the Waqia Valley (Robinson et al., 2007). My results are consistent with this interpretation. To the south, the southern boundary of the Torbashi Thrust has previously been mapped to crop out near the town of Rouluke in the Tashkurgan Valley, with a general northwest strike (Robinson et al., 2007). The Torbashi Thrust is mapped as a synformal klippe, identified in the field in part by high-grade (biotite + sillimanite + garnet metamorphic mineral assemblages) metasedimentary rocks structurally above lower-grade metasedimentary rocks (Figure 3). The southern contact strikes northwest and crops out near the town of Gedeben where upper amphibolite facies metasedimentary rocks are structurally above lower amphibolite/upper greenschist facies units of Block III.

Two main divisions can be made for the four structural blocks south of Muztaghata. 1) Metasedimentary units with Triassic/Jurassic maximum depositional ages crop out in Blocks I and II. The overlap in uncertainty between the maximum depositional age of metasediments and the crystallization age of intrusions in Block II suggests coeval deposition and magmatic intrusion. 2) The second set of structural blocks

consists of units with Paleozoic maximum depositional ages and early Paleozoic to Neoproterozoic detrital zircon ages (Figure 24). The Early Ordovician crystallization age for the intrusion sampled in Block III (Figure 23) indicates the metasediments surrounding the intrusion are no younger than Early Ordovician.

6.1.1. Synthesis of Triassic/Jurassic Metasediments

Maximum depositional age results and crosscutting relationships of intrusive bodies from detrital zircon analysis of Blocks I and II suggest a Triassic/Jurassic age. In addition to metamorphic grade, discussed in the next section, Blocks I and II differ by the lack of intrusive bodies in Block I. Block I yields a similar, yet slightly older, maximum depositional age compared to Block II. Late Triassic sedimentation of Block I received sediments from the Paleozoic Kunlun terrane, based on the occurrence of bimodal detrital zircon age peaks in the Phanerozoic with a few zircons of Precambrian age. In contrast, the single Triassic peak suggests Block II sediment deposited in the basin probably was derived only from the Late Triassic/Early Jurassic magmatic arc, which possibly resulted from a topographic barrier restricting continental sediment. These zircons are igneous in origin, evidenced by low U/Th ratios. It is speculated that this topographic barrier was the magmatic arc, which may have migrated toward the trench in the Late Triassic. The topographic barrier may not have been long lived, as evidenced from the presence of older zircons in a sample elsewhere in Block II from Yang et al. (2010). Possible support for migration of the arc is in the apparent coeval intrusions crosscutting the metasediments of Block II, suggesting that arc migration continued into the forearc basin. The relatively short time-gap between crystallization of detrital zircons in the parent igneous bodies, erosion of those zircons from their provenance, deposition in a

sedimentary basin, burial, and subsequent intrusion is indicative of contemporaneous volcanic activity along a magmatic arc with sedimentation.

Block I experienced greenschist facies metamorphic conditions. Phyllites, schists, marbles, and quartzites, of Block I have with peak metamorphic assemblages of chlorite + biotite + garnet in the Tashkurgan river valley (Figure 14c,d). The presence of garnet suggests temperatures of at least ~400°C, but likely not higher than ~550°C based on the presence of chlorite (Spear, 1995). Garnets were not observed in pelitic units in the Waqia Valley, and I suggest this is indicative of peak metamorphic conditions <500°C. The presence of quartz deformation provides a further constraint. Quartz bulging deformation typically suggests a temperature estimate of 300°C -400°C whereas subgrain rotation is indicative of higher temperatures (~400°C -500°C). Subgrain rotation deformation of quartz microlithons present in some samples of Block I is interpreted to provide a maximum estimate of deformation temperature. Bulging deformation observed in Block I quartz-rich microlithons of pelites may be related to increased strain rate of quartz during deformation at high temperatures (Hirth and Tullis 1992). Therefore, I estimate peak metamorphic conditions ~400-450°C (upper greenschist) for the northern footwall of the Torbashi Thrust.

In the Torbashi Thrust hanging wall, the presence of garnet + biotite + sillimanite suggests the hanging wall of the Torbashi Thrust experienced upper amphibolite to granulite peak metamorphic conditions (>700°C) in the Cretaceous (Figure 14a,b) (Robinson et al. 2007; Yang et al. 2010; this study). Grain boundary migration deformation fabrics present in quartz-rich microlithons are consistent with high temperature deformation. Evidence from petrographic analysis provides clues to the

barometric conditions for peak metamorphism. The presence of sillimanite as fibrolite suggests a lower pressure growth of sillimanite from muscovite; less than or equal to 6.5 kbar which is consistent with a reasonable 35°C/km geothermal gradient. Therefore, rough qualitative estimates suggest Block II was tectonically exhumed from ~20 km depth.

6.1.2. Synthesis of Paleozoic Metasediments

Zircon U/Pb ages from Blocks III and IV show evidence of a genetic origin independent of Blocks I and II. First, an Ordovician crystallization age for the granite sample in the previously interpreted hanging wall of the Torbashi Thrust is inconsistent with a Triassic maximum depositional age for the metasedimentary country rock (Figure 21) (Yang et al. 2007; this study). This relationship implies Block III metasediments are Ordovician or older. Across the Rouluke Fault to the south, Block IV consists of low-grade metasediments with a Devonian maximum depositional age. The orientation of foliation and juxtaposition of medium grade Ordovician rocks above low-grade Silurian (or younger) rocks of block IV provides a robust argument for a thrust relationship for the Rouluke Fault.

South of the southern boundary of the Torbashi Thrust, petrographic data and analytical data from garnet-biotite Fe/Mg-exchange calculations are consistent in the interpretation of lower amphibolite facies/greenschist facies peak metamorphism. Sample AR-9-10-03-1 records a bell shaped Mn curve from core to rim, indicative of growth zoning (Figure 20a). The occurrence of a rotated inclusion trail, and the presence of strain shadows around the garnet grain, and growth zoning from microprobe analysis suggests the garnet grew during prograde metamorphism. Based on growth zoning profiles in the

garnet, rim analysis of the garnet records peak metamorphic conditions. Alternatively, Sample AR-940-09 indicates post-tectonic garnet growth as indicated by the lack of strain-shadows and straight inclusion trails between internal and external foliation (Figure 18b). I interpret Fe/Mg-exchange calculations to record lower amphibolite/upper greenschist peak metamorphic conditions for the Block III.

The footwall of the Rouluke Fault (Block IV), consisting of slates, marbles, and quartzites, reached only low-grade metamorphic conditions. Weakly deformed post-tectonic biotite and muscovite suggest Block IV might have reached the biotite isograd, lower greenschist facies conditions. However, pelitic samples elsewhere in Block IV do not show evidence of reaching the biotite isograd.

6.2. 3-D STRUCTURAL ARCHITECTURE OF THE EAST PAMIR

My results show two distinct tectonostratigraphic blocks in the southeastern Pamir defined as Triassic/Jurassic and Paleozoic metasedimentary units. In this section, data from this study is synthesized with previously published correlations based on 1) detrital zircon maximum depositional ages, and 2) zircon relative age probability plots from the hanging wall of the Baoziya Thrust and the footwall of the Kongur Shan Extensional System north of Muztaghata (Robinson et al., 2012), and 3) εNd values from the footwalls of the Torbashi and Baoziya Thrusts.

6.2.1. Baoziya Thrust - Torbashi Thrust

The hanging wall of the Baoziya Thrust and Torbashi Thrust (Blocks II and IIb) consist of amphibolite facies Permo-Triassic metasedimentary rocks intruded by Late Triassic-Early Jurassic granites. The footwalls of these faults (Blocks I and Ib) consist of greenschist facies phyllites, schists, marbles, and quartzites (Robinson et al., 2004, 2007,

2012; this study) with Triassic Maximum depositional ages and similar detrital zircon populations. The similarities between the hanging wall and footwall of the Baoziya and Torbashi Thrusts are correlative and the thrusts are the same structure Figure 25).

The correlation of the Torbashi Thrust, south of Muztaghata, with the Baoziya Thrust, north of Muztaghata, allows us to place constraints on the pressure-temperature conditions for the Torbashi Thrust. Robinson et al. (2004) reported an increase in metamorphic grade from west to east in the hanging wall of the Baoziya Thrust, with a transition from andalusite to sillimanite. This was interpreted to represent peak metamorphic pressures of ~4 kbar for the hanging wall of the Baoziya Thrust. Therefore, peak pressure conditions during metamorphism of Block II likely was ~4 kbar.

6.2.2. Central/Southern Pamir

The southern contacts of Block II and Block IIb are equivalent structures. Block IIb is the hanging wall for the Baoziya and Tanymas Thrust. The Tanymas Thrust places Permo-Triassic metasediments above early Paleozoic metasediments of the Central Pamir region (Schwab et al., 2004; Yang et al., 2010; Robinson et al., 2012). Similarly the southern boundary of Block II places Permo-Triassic metasediments intruded by granites upper greenschist to lower amphibolite facies early Paleozoic units. Therefore, the Tanymas Thrust and the southern contact of the Torbashi Thrust are interpreted to be correlative structures.

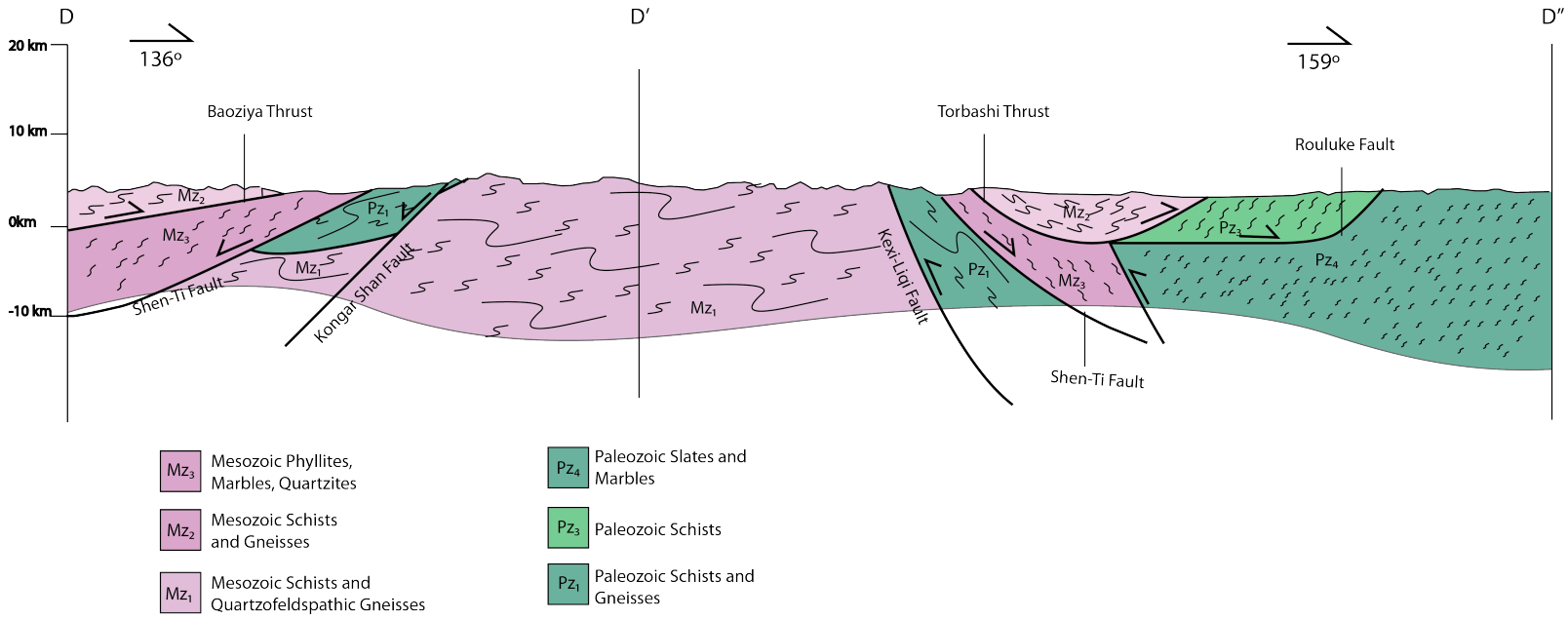

Figure 25: Cross section and structural architecture for the eastern Pamir. Location of D-D″ can be found in Figure 4.

6.3. REGIONAL COMPARISONS ACROSS THE HIMALYAN TIBETAN PLATEAU

Detrital zircon U/Pb analysis suggests a correlation can be made between terranes in the Pamir with those in Tibet (Figure 26,27). Detrital zircon signatures for the Karakul-Mazar terrane in the Pamir and Hoh-Xil/Songpan Ganzi terrane of Tibet show similarities and are distinctly different from detrital zircon signatures from the Central Pamir and Qiangtang terrane of Tibet. Detrital zircon ages from Mesozoic sediments from the Hoh-Xil/Songpan Ganzi terrane of Tibet yield Triassic maximum depositional ages with a concentration of Phanerozoic Peaks (Gehrels et al., 2011; Robinson et al., 2012; Ding et al., 2013). Detrital zircon age populations derived from Paleozoic age sedimentary rocks from the Qiangtang Terrane of Tibet yield Ordovician maximum depositional ages with a concentration of Neoproterozoic peak ages. In this section, I correlate structural blocks in this study to terranes in the greater Himalayan-Tibetan orogen.

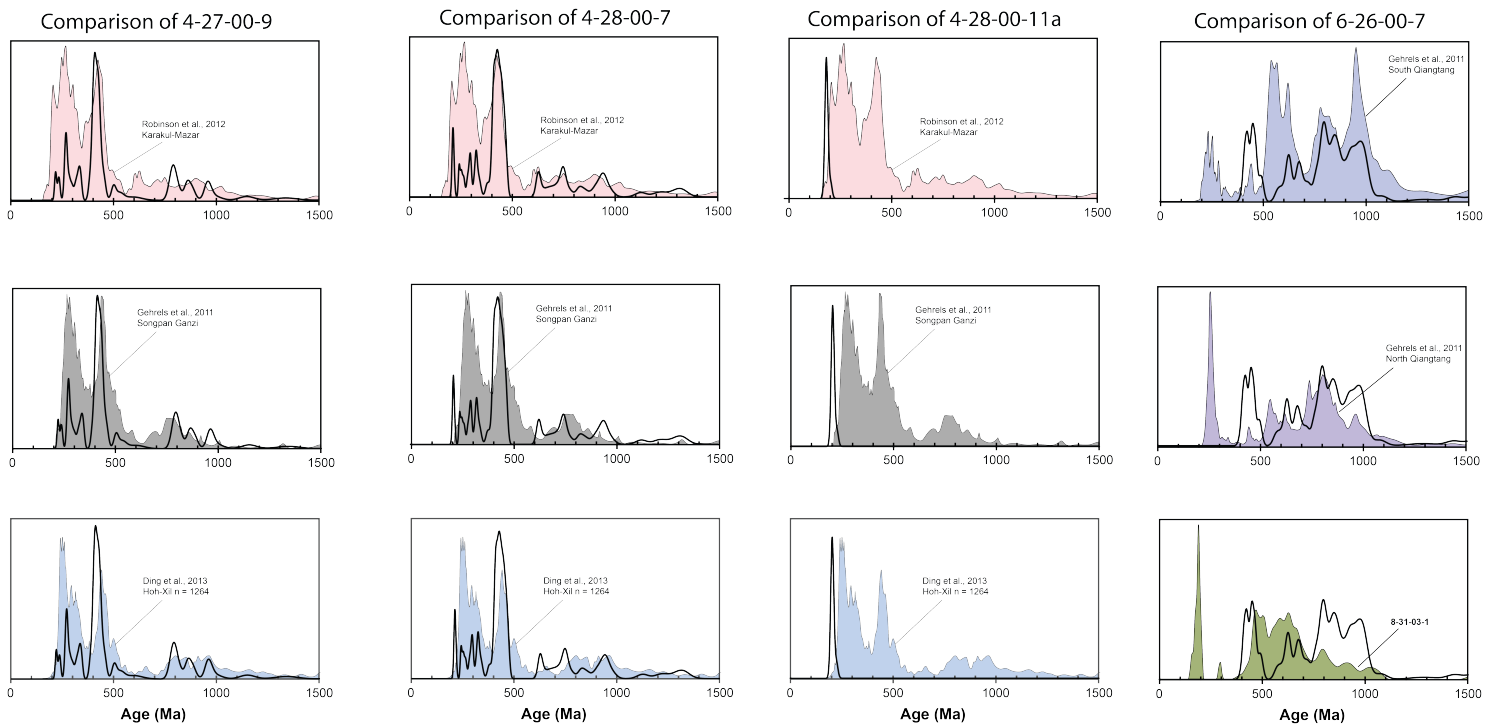

Figure 26: Comparison of detrital zircon results from this study with composite relative age probability plots from the Karakul Mazar Terrane, the Songpan-Ganzi Terrane, and the Hoh-Xil Terrane.

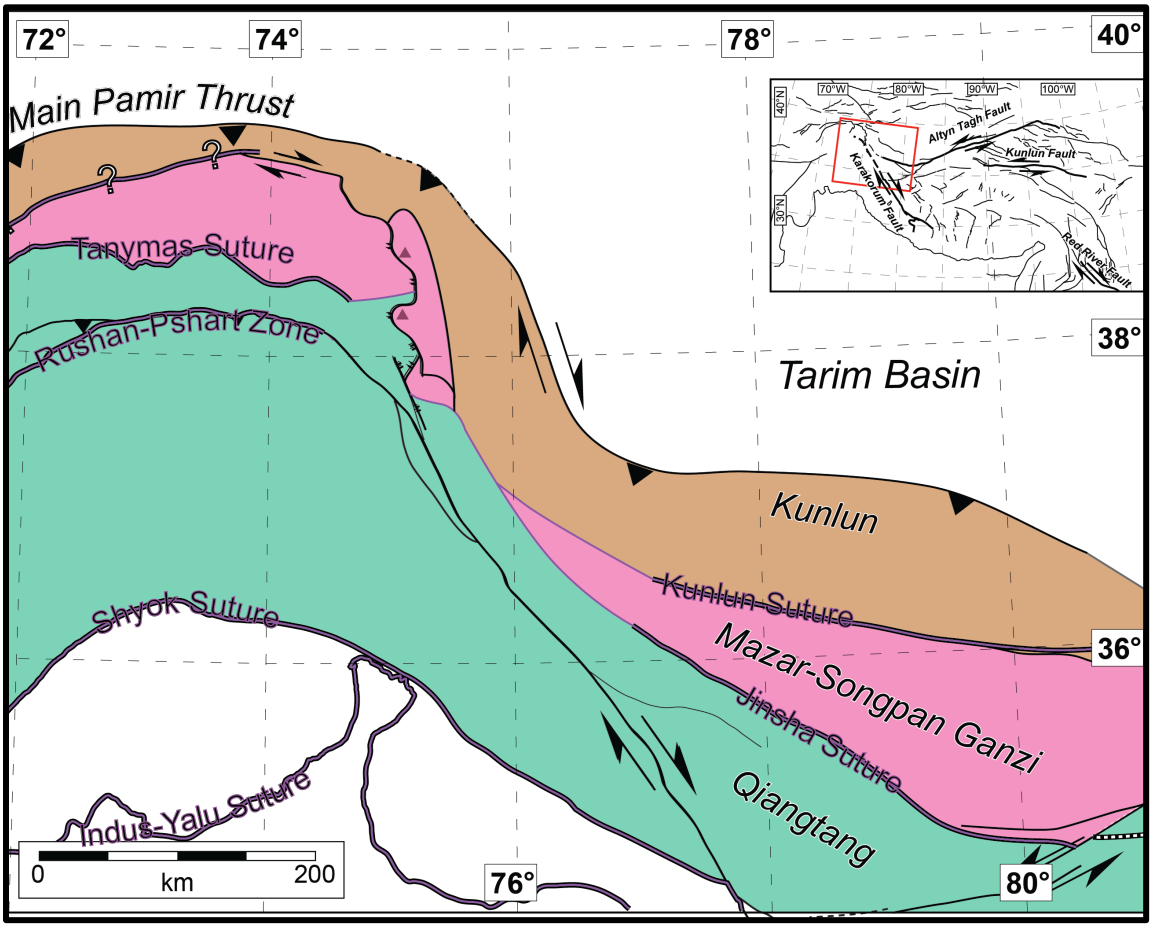

Figure 27: Proposed terrane correlation between the Pamir and Tibet based on results form this study and previous research. Figure modified from Robinson (2009b)

6.3.1. Karakul-Mazar/Hoh-Xil / Songpan Ganzi of Tibet

Results from this study have been compared with those of other workers in the Pamir and Tibet (Figure 26). Based on similar lithology, maximum depositional age, and detrital zircon probability plots from this study and previous workers, the Permo-Triassic metasedimentary units of Blocks I, Ib II, and IIb correlate with the Karakul-Mazar Terrane (Schwab et al., 2004; Yang et al., 2010; Robinson et al., 2012). Samples from Block I and II and Ib also yield similar overlapping detrital zircon age populations with the Hoh-Xil Terrane and the Songpan Ganzi Terrane of Tibet and are likely along-strike equivalent terranes.

6.3.2. Central Pamir – South Pamir – Qiangtang Terrane

Block IV yields a detrital zircon signature significantly different from the others in this study, which indicates the presence of a terrane boundary. Sample 6-26-00-7 (Block IV) has a zircon age population signature similar to the Central Pamir (Robinson et al., 2012). Additionally, overlap and similarity of zircon ages is consistent with those found in the South Qiangtang Terrane, suggesting it is an along-strike equivalent (Figure 26) (Gehrels et al., 2011). The presence of slightly younger maximum depositional age compared to those of the Qiangtang Terrane is coincident with magmatism associated with the Lhasa plutons. The presence of slightly younger zircons in Block IV suggests 1) the sample received sediments from intrusive rocks of correlative age with the Lhasa plutons or 2) the southeast Pamir received a large flux of sediment from the Lhasa plutons.

6.3.3. Implications for Orogenesis

Closure of the Paleo-Tethys Ocean between rocks of Songpan-Ganzi/Hoh-Xil affinity in the north, and Qiangtang equivalent rocks (of Gondwanan affinity) to the south occurred in the early Jurassic along the Jinsha Suture in Tibet (Kapp et al., 2000; Yin and Harrison, 2000; Kapp et al., 2003; Pullen et al., 2008; Pullen et al., 2011; Robinson et al., 2012). The correlations, in this study, of Songpan-Ganzi and Qiangtang terranes of Tibet with terranes in the Pamir implies the Jinsha suture runs through the study area. One key observation allows us to narrow the location of the Jinsha suture study area is the presence or absence of granitic intrusions in footwall rocks of the Torbashi Thrust. In the eastern margin of the Tashkurgan Valley, the units of Block III are of Qiangtang affinity and are intruded by Early Ordovician granites. No intrusive bodies were observed for Block I, of Songpan-Ganzi affinity. In the southeastern section of the Waqia Valley, amphibolite facies units in the footwall of the Torbashi Thrust are intruded by granites of unknown age. I propose the Jinsha suture is located in the Waqia Valley, in the footwall of the Torbashi Thrust at the contact between metasedimentary units intruded by granites and metasedimentary units not intruded by granites (Figure 3). From the Waqia Valley to the west, the Jinsha suture is structurally buried beneath the Cretaceous Torbashi Thrust. The Suture is offset the Tashkurgan Fault and the Shen-Ti Fault where it continues west structurally beneath the Tanymas/Baoziya Thrust. Thus, my results imply a tectonic wedging similar to one suggested by Robinson et al. (2012). An obvious test for this proposed model for the location of the Jinsha suture would be to determine the crystallization age for granites intruding the southeast Waqia Valley. A Paleozoic age for

the southeast Waqia Valley intrusions would support the model, whereas a Triassic or younger crystallization age would invalidate it.

The Torbashi Thrust is a regionally extensive thrust nappe structurally above the suture between the Karakul Mazar and the Central/South Pamir. The southern boundary of the Torbashi-Tanymas Thrust, as mapped in this study, is a major tectonostratigraphic boundary between a southern and northern terrane based on significant differences in detrital zircon signatures north and south of the structure. However, these relationships imply the Tanymas-Torbashi Thrust should not be considered the suture because its development is not related to closure of an ocean basin (Robinson et al., 2007; Robinson et al., 2012). The Paleo-Tethys suture is structurally buried beneath the Torbashi-Tanymas Thrust (Figure 13).

By understanding the relationship of terrane boundaries across the Himalayan-Tibetan Orogen, constraints can be made on the total offset of major bounding structures. For example, my results place constraints on the role of the Karakoram Fault for the tectonic evolution of the Himalayan-Tibetan Orogen. My detrital zircon results show that the Jinsha suture is located in my study area, defined by the southern trace of the Torbashi fault, which invalidates large offsets on the Karakoram Fault. These results are consistent with interpretations which suggest the Karakoram Fault has accommodated limited total offset (i.e. ~160 km).

6.4. SHORTENING ESTIMATES

My new documentation of regional fault geometries, structural architecture, variations in metamorphic grade between structural blocks, and kinematics of deformation, allow us to estimate shortening along the Baoziya-Torbashi Thrust (Figure

1). Our assumptions in the calculation include 1) a 30 degree north-northeast-directed dip of the basal thrust and 2) a geothermal gradient of 35°C /km. Based on juxtaposition of metamorphic grade, I take minimum and maximum temperature estimates based on metamorphic mineral assemblages and microprobe data.

I based my model on the following variables. 1) For the footwall of the Torbashi thrust, I use values of 300°C to 450°C and in the hanging wall values of 750°C. I then converted these values to depth based on geothermal gradients ranging from 30-40°C/km. 2) I considered variable dip angles from 30° to 60° dip. I calculated a range of values based on inputs of these variables to produce a plot of probable shortening accommodated by the Torbashi thrust.

My results suggest the Torbashi Thrust has accommodated between approximately 9 and 31 km of horizontal shortening. The model assumes peak metamorphic conditions are stratified sub-horizontally. While the second assumption may be weak, I feel this model provides a good first-order estimate for the shortening accommodated by the Torbashi Thrust. The shortening estimates for the Torbashi klippe are consistent with shortening estimates for equivalent structures further west. Burtman and Molnar (1993) reported several thrust nappes, correlated with the Tanymas hanging wall, within the Central Pamir which accommodate 10 to 20 km of shortening.

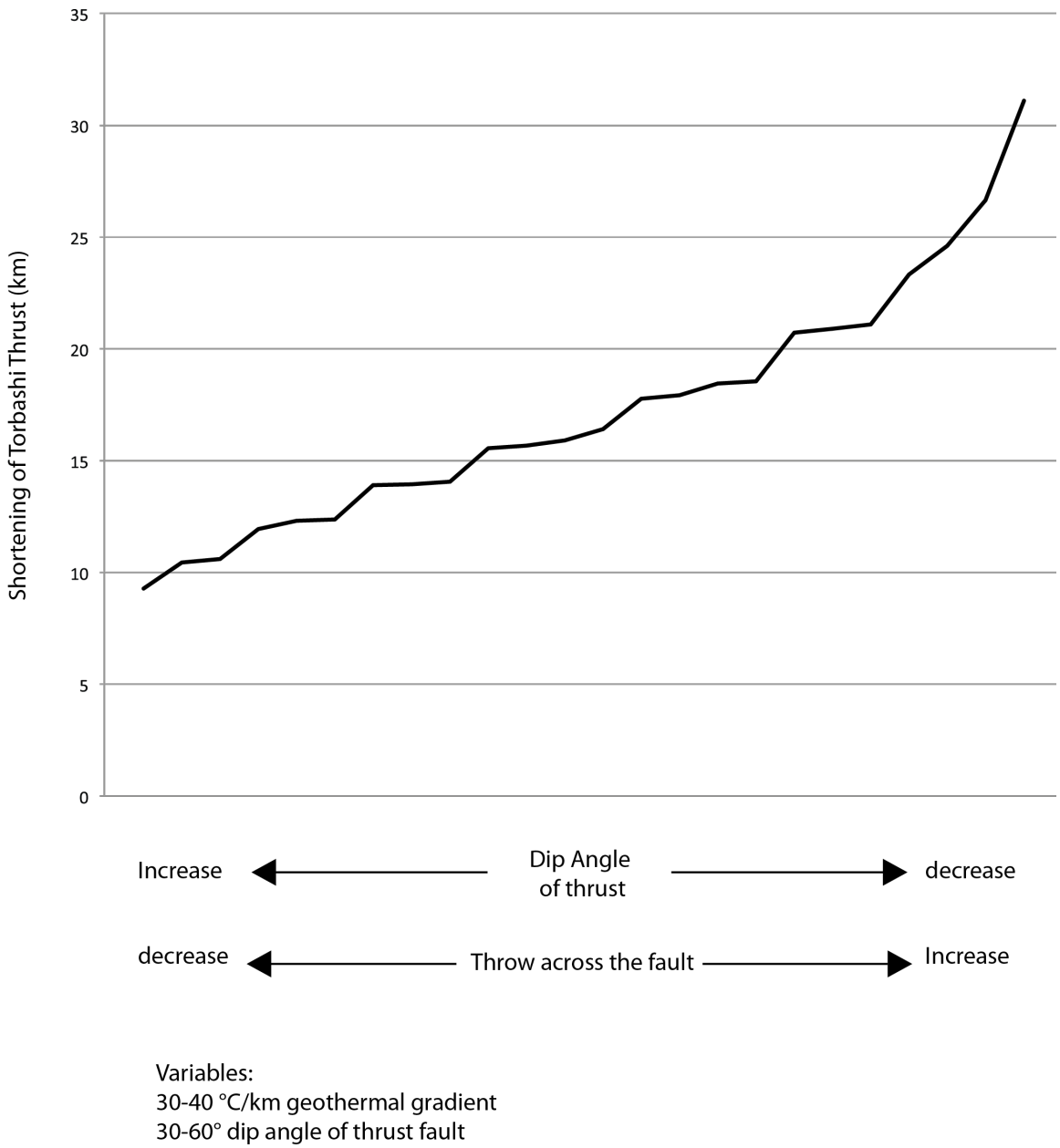

Figure 28: Calculated shortening for the Torbashi/Baoziya Thrust based on parameters described in the text.

6.5. MODEL FOR THE SOUTHEAST PAMIR

Here I provide a tectonic model for the evolution of the southeast Pamir. North-directed subduction of the Paleo-Tethys ocean beneath the Karakul-Mazar Terrane in the late Triassic produced subduction-related magmatism (Robinson et al., 2012). The development of a magmatic arc along the southern boundary of the Karakul-Mazar Terrane provided volcanically derived sediment to a forearc basin. During the early Jurassic, before the closure of the Paleo-Tethys, establishment of drainages with sources north of the magmatic arc provided sediment from the southern margin of Asia (i.e. Kunlun terrane), evidenced by the occurrence of Paleozoic and Precambrian zircon age populations. The strong late Triassic peak in zircon ages for the sample from Block II suggests the catchment area was limited to the magmatic arc during deposition of sediments for Block II. One possibility for the lack of older zircons is the origin may be related to slab rollback. Slab rollback along a north-dipping subduction zone would result in migration of the established magmatic arc closer to the trench. The new location of the magmatic arc could have temporarily blocked drainage from the Kunlun terrane. Closure of the Paleo-Tethys resulted in prograde metamorphism of Blocks I-IV (Robinson et al., 2012). Block I and II of the Karakul-Mazar terrane were thrust beneath Blocks III and IV of the South Pamir. A second deformation event occurred in the Cretaceous with retroarc shortening associated with the down-going Meso-Tethys slab (Robinson et al., 2007; Robinson et al., 2012). Cretaceous south-directed thrusting and metamorphism of the Baoziya/Tanymas/Torbashi and and Rouluke Thrusts structurally buried the Jinsha suture in the study area. Finally, in the Cenozoic, Miocene extension

and exhumation of the Central Pamir Gneiss Domes cut the Baoziya/Tanymas/Torbashi Thrust into their preset geometries.

7. CONCLUSIONS

My results provide a comprehensive history for the geometry and metamorphic history for the southeast Pamir. The hanging wall of the Baoziya and Torbashi Thrusts are composed of upper amphibolite facies schists and gneisses and yield Triassic/Jurassic maximum depositional ages and are intruded by Triassic/Jurassic granites. The northern footwall of the Torbashi Thrust and the footwall of the Baoziya Thrust are composed of greenschist facies phyllites marbles and quartzites with Triassic maximum depositional ages.

I interpret similarity in lithology, metamorphic facies, maximum depositional age, and zircon populations in metasedimentary units to document previously unrecognized structural relationships in the eastern Pamir. I correlate the Baoziya and Torbashi Thrusts across the Miocene Muztaghata gneiss dome and suggest the structures represent a continuous thrust nappe across the eastern Pamir. Additionally, the southern trace of the Torbashi thrust has been revised due to the intrusive relationship of Ordovician granites in the previously interpreted hanging wall. South of the Torbashi Thrust, a second thrust relationship is interpreted based on juxtaposition of metamorphic facies, metamorphic foliation orientation, and interpreted depositional age of sediments.

This study correlates terranes from the Pamir with terranes in the Tibetan orogen. Triassic metasedimentary units within the study area are correlated with the Hon-Xil/Songpan Ganzi terrane of Tibet, whereas Paleozoic units in the southern portion of the study area correlate with the Qiangtang terrane. These results place key constraints

on understanding the geometry of major terrane boundaries and help define structural relationships for key features, such as the Karakoram Fault, previously interpreted to play a major role in the evolution of the Himalayan-Tibetan Orogen.

REFERENCES

Allmendinger, R. W., Cardozo, N., and Fisher, D., 2012, Structural Geology Algorithms: Vectors and Tensors, Cambridge University Press.

Angiolini, L., Zanchi, A., Zanchetta, S., Nicora, A., and Vezzoli, G., 2013, The Cimmerian geopuzzle: new data from South Pamir: Terra Nova, v. 25, p. 352-360

Bershaw, J., Garzione, C. N., Schoenbohm, L., Gehrels, G., and Tao, L., 2012, Cenozoic evolution of the Pamir plateau based on stratigraphy, zircon provenance, and stable isotopes of foreland basin sediments at Oytag (Wuyitake) in the Tarim Basin (west China): Journal of Asian Earth Sciences, v. 44, p. 136-148.

Brunel, M., Arnaud, N., Tapponnier, P., Pan, Y., and Wang, Y., 1994, Kongur Shan normal fault: Type example of mountain building assisted by extension (Karakoram fault, eastern Pamir): Geology, v. 22, no. 8, p. 707-710.

Burtman, V. V. S., and Molnar, P. H., 1993, Geological and geophysical evidence for deep subduction of continental crust beneath the Pamir: Geological Society of America Special Paper 281, 76p.

Cao, K., Bernet, M., Wang, G.-C., van der Beek, P., Wang, A., Zhang, K.-X., and Enkelmann, E., 2013a, Focused Pliocene–Quaternary exhumation of the Eastern Pamir domes, western China: Earth and Planetary Science Letters, v. 363, p. 16-26.

Cao, K., Wang, G.-C., van der Beek, P., Bernet, M., and Zhang, K.-X., 2013b, Cenozoic thermo-tectonic evolution of the northeastern Pamir revealed by zircon and apatite fission-track thermochronology: Tectonophysics, v. 589, p. 17-32

Cardozo, N., 2008, Trishear in 3D. Algorithms, implementation, and limitations: Journal of Structural Geology, v. 30, no. 3, p. 327-340.

Cardozo, N., and Allmendinger, R. W., 2013, Spherical projections with OSXStereonet: Computers and Geosciences, v. 51, p. 193-205.

Chevalier, M. L., Li, H., Pan, J., Pei, J., Wu, F., Xu, W., Sun, Z., and Liu, D., 2011, Fast slip-rate along the northern end of the Karakorum fault system, western Tibet: Geophysical Research Letters, v. 38, no. 22.

Cowgill, E., 2010, Cenozoic right-slip faulting along the eastern margin of the Pamir salient, northwestern China: Geological Society of America Bulletin, v. 122, no. 1-2, p. 145-161.

Ding, G., Chen, J., Tian, Q., Shen, X., Xing, C., and Wei, K., 2004, Active faults and magnitudes of left-lateral displacement along the northern margin of the Tibetan Plateau: Tectonophysics, v. 380, no. 3, p. 243-260.

Ding, L., Yang, D., Cai, F. L., Pullen, A., Kapp, P., Gehrels, G. E., Zhang, L. Y., Zhang, Q. H., Lai, Q. Z., and Yue, Y. H., 2013, Provenance analysis of the Mesozoic Hoh-Xil-Songpan-Ganzi turbidites in northern Tibet: Implications for the tectonic evolution of the eastern Paleo-Tethys Ocean: Tectonics, v. 32, p. 34-48

DiPietro, J. A., and Pogue, K. R., 2004, Tectonostratigraphic subdivisions of the Himalaya: A view from the west: Tectonics, v. 23, TC5001, doi:10.1029/2003TC001554.

Dunlap, W. J., Weinberg, R. F., and Searle, M. P., 1998, Karakoram fault zone rocks cool in two phases: Journal of the Geological Society, v. 155, no. 6, p. 903-912.

Gehrels, G., Kapp, P., DeCelles, P., Pullen, A., Blakey, R., Weislogel, A., Ding, L., Guynn, J., Martin, A., and McQuarrie, N., 2011, Detrital zircon geochronology of pre-Tertiary strata in the Tibetan-Himalayan orogen: Tectonics, v. 30, no. 5, p. TC5016.

Hirth, G., and Tullis, J., 1992, Dislocation creep regimes in quartz aggregates: Journal of Structural Geology, v. 14, no. 2, p. 145-159.

Kapp, P., Taylor, M., Stockli, D., and Ding, L., 2008, Development of active low-angle normal fault systems during orogenic collapse: Insight from Tibet: Geology, v. 36, no. 1, p. 7-10.

Kapp, P., Yin, A., Manning, C. E., Harrison, T. M., Taylor, M. H., and Ding, L., 2003, Tectonic evolution of the early Mesozoic blueschist-bearing Qiangtang metamorphic belt, central Tibet: Tectonics, v. 22, 1043, doi:10.1029/2002TC001383.

Kapp, P., Yin, A., Manning, C. E., Murphy, M., Harrison, T. M., Spurlin, M., Lin, D., Xi-Guang, D., and Cun-Ming, W., 2000, Blueschist-bearing metamorphic core complexes in the Qiangtang block reveal deep crustal structure of northern Tibet: Geology, v. 28, no. 1, p. 19-22.

Lacassin, R., Valli, F., Arnaud, N., Leloup, P. H., Paquette, J. L., Haibing, L., Tapponnier, P., Chevalier, M.-L., Guillot, S., and Maheo, G., 2004, Large-scale geometry, offset and kinematic evolution of the Karakorum fault, Tibet: Earth and Planetary Science Letters, v. 219, no. 3, p. 255-269.

Li, H., Van der Woerd, J., Sun, Z., Si, J., Tapponnier, P., Pan, J., Liu, D., and Chevalier, M.-L., 2012, Co-seismic and cumulative offsets of the recent earthquakes along the Karakax left-lateral strike-slip fault in western Tibet: Gondwana Research, v. 21, no. 1, p. 64-87.

Lister, G., and Snoke, A., 1984, SC mylonites: Journal of Structural Geology, v. 6, no. 6, p. 617-638.

Liu, Q., Tapponnier, P., Bourjot, L., and Zhang, Q., 1993, Kinematics of recent faulting along the Muji-Tashkorgan graben, northern extension of the Karakoram fault: European Union of Geosciences VIIStrasbourg, FranceApril, p. 4-8.

Ludwig, K. R., 2003, User's manual for Isoplot 3.00: A geochronological toolkit for Microsoft Excel, Berkeley Geochronol. Cent. Spec. Publ. 4: Berkeley, Calif, Berkeley Geochronol. Cent.

Marrett, R. A., and Allmendinger, R. W., 1990, Kinematic Analysis of fault-slip data: Journal of Structural Geology, v. 12, p. 973-986.

Mechie, J., Yuan, X., Schurr, B., Schneider, F., Sippl, C., Ratschbacher, L., Minaev, V., Gadoev, M., Oimahmadov, I., and Abdybachaev, U., 2012, Crustal and uppermost mantle velocity structure along a profile across the Pamir and southern Tien Shan as derived from project TIPAGE wide-angle seismic data: Geophysical Journal International, v. 188, no. 2, p. 385-407.

Molnar, P., and Tapponnier, P., 1975, Cenozoic tectonics of Asia: Effects of a continental collision: Science, v. 189, no. 4201, p. 419-426.

Murphy, M. A., and Copeland, P., 2005, Transtensional deformation in the central Himalaya and its role in accommodating growth of the Himalayan orogen: Tectonics, v. 24, no. 4, TC4012, doi:10.1029/2004TC001659.

Murphy, M. A., Yin, A., Kapp, P., Harrison, T. M., Lin, D., and Jinghui, G., 2000, Southward propagation of the Karakoram fault system, southwest Tibet: Timing and magnitude of slip: Geology, v. 28, no. 5, p. 451-454.

Negredo, A. M., Replumaz, A., Villaseñor, A., and Guillot, S., 2007, Modeling the evolution of continental subduction processes in the Pamir–Hindu Kush region: Earth and Planetary Science Letters, v. 259, no. 1, p. 212-225.

Owen, L. A., Chen, J., Hedrick, K. A., Caffee, M. W., Robinson, A. C., Schoenbohm, L. M., Yuan, Z., Li, W., Imrecke, D. B., and Liu, J., 2012, Quaternary glaciation of the Tashkurgan Valley, Southeast Pamir: Quaternary Science Reviews, v. 47, p. 56-72.

Pashkov, B. R., and Schvol'Man, 1979, Rift Margins of Tethys in the Pamirs: Geotectonics, v. 13, no. 6, p. 447-456.

Peltzer, G., and Tapponnier, P., 1988, Formation and evolution of strike-slip faults, rifts, and basins during the India-Asia collision: An experimental approach: Journal of Geophysical Research: Solid Earth (1978–2012), v. 93, no. B12, p. 15085-15117.

Peykre, Y. B., Pokhvisneva, Y. A., and Zotov, I. A., 1982, The Muzkol'metamorphic complex of the Central Pamir: International Geology Review, v. 24, no. 3, p. 297-303.

Phillips, R. J., Parrish, R. R., and Searle, M. P., 2004, Age constraints on ductile deformation and long-term slip rates along the Karakoram fault zone, Ladakh: Earth and Planetary Science Letters, v. 226, no. 3, p. 305-319.

Powell, R., Holland, T., and Worley, B., 1998, Calculating phase diagrams involving solid solutions via non-linear equations, with examples using THERMOCALC: Journal of Metamorphic Geology, v. 16, no. 4, p. 577-588.

Pullen, A., Kapp, P., Gehrels, G. E., Ding, L., and Zhang, Q., 2011, Metamorphic rocks in central Tibet: Lateral variations and implications for crustal structure: Geological Society of America Bulletin, v. 123, no. 3-4, p. 585-600.

Pullen, A., Kapp, P., Gehrels, G. E., Vervoort, J. D., and Ding, L., 2008, Triassic continental subduction in central Tibet and Mediterranean-style closure of the Paleo-Tethys Ocean: Geology, v. 36, no. 5, p. 351-354.

Raterman, N. S., Cowgill, E., and Lin, D., 2007, Variable structural style along the Karakoram fault explained using triple-junction analysis of intersecting faults: Geosphere, v. 3, no. 2, p. 71-85.

Ratschbacher, L., Frisch, W., Liu, G., and Chen, C., 1994, Distributed deformation in southern and western Tibet during and after the India‐Asia collision: Journal of Geophysical Research: Solid Earth (1978–2012), v. 99, no. B10, p. 19917-19945.

Rey, P., Teyssier, C., and Whitney, D., 2009, The role of partial melting and extensional strain rates in the development of metamorphic core complexes: Tectonophysics, v. 477, no. 3, p. 135-144.

Rey, P. F., Teyssier, C., Kruckenberg, S. C., and Whitney, D. L., 2011, Viscous collision in channel explains double domes in metamorphic core complexes: Geology, v. 39, no. 4, p. 387-390.

Robinson, A. C., 2009a, Evidence against Quaternary slip on the northern Karakorum Fault suggests kinematic reorganization at the western end of the Himalayan–Tibetan orogen: Earth and Planetary Science Letters, v. 286, no. 1, p. 158-170.

Robinson, A. C., 2009b, Geologic offsets across the northern Karakorum fault: Implications for its role and terrane correlations in the western Himalayan-Tibetan orogen: Earth and Planetary Science Letters, v. 279, no. 1, p. 123-130.

Robinson, A. C., Ducea, M., and Lapen, T. J., 2012, Detrital zircon and isotopic constraints on the crustal architecture and tectonic evolution of the northeastern Pamir: Tectonics, v. 31, no. 2, doi:10.1029/2011TC003013.

Robinson, A. C., Yin, A., and Lovera, O. M., 2010, The role of footwall deformation and denudation in controlling cooling age patterns of detachment systems: An

application to the Kongur Shan extensional system in the Eastern Pamir, China: Tectonophysics, v. 496, no. 1, p. 28-43.

Robinson, A. C., Yin, A., Manning, C. E., Harrison, T. M., Zhang, S.-H., and Wang, X.-F., 2004, Tectonic evolution of the northeastern Pamir: Constraints from the northern portion of the Cenozoic Kongur Shan extensional system, western China: Geological Society of America Bulletin, v. 116, no. 7-8, p. 953-973.

-, 2007, Cenozoic evolution of the eastern Pamir: Implications for strain-accommodation mechanisms at the western end of the Himalayan-Tibetan orogen: Geological Society of America Bulletin, v. 119, no. 7-8, p. 882-896.

Ryerson, F. J., Finkel, R. C., Meriaux, A., Caffee, M. W., Peltzer, G., Farr, T., Chadwick, G., and Clarke, D. H., Rapid slip on the Altyn Tagh fault: Karakax Valley segment, *in* Proceedings GSA Abstr1997, Volume 29, p. 143.

Ryerson, F. J., Peltzer, G., Tapponnier, P., Finkel, R. C., Meriaux, A. S., Van der Woerd, J., and Caffee, M. W., 1999, Active slip-rates on the Altyn Tagh Fault–Karakax Valley segment: Constraints from surface exposure dating: Eos Trans. AGU, v. 80, no. 46, p. F1008.

Schmidt, J., Hacker, B. R., Ratschbacher, L., Stübner, K., Stearns, M., Kylander-Clark, A., Cottle, J. M., Alexander, A., Webb, G., and Gehrels, G., 2011, Cenozoic deep crust in the Pamir: Earth and Planetary Science Letters, v. 312, no. 3, p. 411-421.

Schwab, M., Ratschbacher, L., Siebel, W., McWilliams, M., Minaev, V., Lutkov, V., Chen, F., Stanek, K., Nelson, B., and Frisch, W., 2004, Assembly of the Pamirs: Age and origin of magmatic belts from the southern Tien Shan to the southern Pamirs and their relation to Tibet: Tectonics, v. 23, TC4002, doi:10.1029/2003TC001583.

Searle, M. P., 1996, Geological evidence against large-scale pre-Holocene offsets along the Karakoram Fault: Implications for the limited extrusion of the Tibetan plateau: Tectonics, v. 15, no. 1, p. 171-186.

Searle, M. P., Weinberg, R. F., and Dunlap, W. J., 1998, Transpressional tectonics along the Karakoram fault zone, northern Ladakh: constraints on Tibetan extrusion: Geological Society, London, Special Publications, v. 135, no. 1, p. 307-326.

Seeber, L., and Pêcher, A., 1998, Strain partitioning along the Himalayan arc and the Nanga Parbat antiform: Geology, v. 26, no. 9, p. 791-794.

Shaulis, B., Lapen, T. J., and Toms, A., 2010, Signal linearity of an extended range pulse counting detector: Applications to accurate and precise U-Pb dating of zircon by laser ablation quadrupole ICP-MS: Geochemistry, Geophysics, Geosystems, v. 11, no. 11, Q0AA11, doi:10.1029/2010GC003198.

Shen, Z. K., Wang, M., Li, Y., Jackson, D. D., Yin, A., Dong, D., and Fang, P., 2001, Crustal deformation along the Altyn Tagh fault system, western China, from GPS: Journal of Geophysical Research: Solid Earth (1978–2012), v. 106, no. B12, p. 30607-30621.

Sippl, C., Schurr, B., Tympel, J., Angiboust, S., Mechie, J., Yuan, X., Schneider, F. M., Sobolev, S. V., Ratschbacher, L., and Haberland, C., 2013, Deep burial of Asian continental crust beneath the Pamir imaged with local earthquake tomography: Earth and Planetary Science Letters, v. 384, p. 165-177.

Sobel, E. R., Chen, J., and Heermance, R. V., 2006, Late Oligocene–Early Miocene initiation of shortening in the Southwestern Chinese Tian Shan: implications for Neogene shortening rate variations: Earth and Planetary Science Letters, v. 247, no. 1, p. 70-81.

Sobel, E. R., Chen, J., Schoenbohm, L. M., Thiede, R., Stockli, D. F., Sudo, M., and Strecker, M. R., 2013, Oceanic-style subduction controls late Cenozoic deformation of the Northern Pamir orogen: Earth and Planetary Science Letters, v. 363, p. 204-218.

Sobel, E. R., and Dumitru, T. A., 1997, Thrusting and exhumation around the margins of the western Tarim basin during the India-Asia collision: Journal of Geophysical Research, v. 102, no. B3, p. 5043-5063.

Sobel, E. R., Schoenbohm, L. M., Chen, J., Thiede, R., Stockli, D. F., Sudo, M., and Strecker, M. R., 2011, Late Miocene–Pliocene deceleration of dextral slip between Pamir and Tarim: Implications for Pamir orogenesis: Earth and Planetary Science Letters, v. 304, no. 3, p. 369-378.

Spear, F. S., 1995, Metamorphic phase equilibria and pressure-temperature-time paths. Mineralogical Society of America Publication, Washington D.C..

Strecker, M. R., Frisch, W., Hamburger, M. W., Ratschbacher, L., Semiletkin, S., Zamoruyev, A., and Sturchio, N., 1995, Quaternary deformation in the eastern Pamirs, Tadzhikistan and Kyrgyzstan: Tectonics, v. 14, no. 5, p. 1061-1079.

Stübner, K., Ratschbacher, L., Rutte, D., Stanek, K., Minaev, V., Wiesinger, M., and Gloaguen, R., 2013, The giant Shakhdara migmatitic gneiss dome, Pamir, India-Asia collision zone: 1. Geometry and kinematics: Tectonics, v. 32, no. 4, p. 948-979.

Tapponnier, P., Mattauer, M., Proust, F., and Cassaigneau, C., 1981, Mesozoic ophiolites, sutures, and large-scale tectonic movements in Afghanistan: Earth and Planetary Science Letters, v. 52, no. 2, p. 355-371.

Tapponnier, P., and Molnar, P., 1976, Slip-line field theory and large-scale continental tectonics: Nature, v. 264, no. 25, p. 319-324.

Tapponnier, P., Peltzer, G., Le Dain, A. Y., Armijo, R., and Cobbold, P., 1982, Propagating extrusion tectonics in Asia: New insights from simple experiments with plasticine: Geology, v. 10, no. 12, p. 611-616.

Thiede, R. C., Sobel, E. R., Chen, J., Schoenbohm, L. M., Stockli, D. F., Sudo, M., and Strecker, M. R., 2013, Late Cenozoic extension and crustal doming in the India-Eurasia collision zone: New thermochronologic constraints from the NE Chinese Pamir: Tectonics, v.32, p.763–779, doi:10.1002/tect.20050.

Tirel, C., Brun, J. P., and Burov, E., 2008, Dynamics and structural development of metamorphic core complexes: Journal of Geophysical Research: Solid Earth (1978–2012), v. 113, B04403, doi:10.1029/2005JB003694.

Valli, F., Arnaud, N., Leloup, P. H., Sobel, E. R., Mahéo, G., Lacassin, R., Guillot, S., Li, H., Tapponnier, P., and Xu, Z., 2007, Twenty million years of continuous deformation along the Karakorum fault, western Tibet: A thermochronological analysis: Tectonics, v. 26, no. 4.

Valli, F., Leloup, P. H., Paquette, J. L., Arnaud, N., Li, H., Tapponnier, P., Lacassin, R., Guillot, S., Liu, D., and Deloule, E., 2008, New U-Th/Pb constraints on timing of shearing and long-term slip-rate on the Karakorum fault: Tectonics, v. 27, TC5007, doi:10.1029/2007TC002184.

Xinjiang Bureau of Geology and Mineral Resources, 1993, Regional geology of Xinjiang Uygur autonomous region: Geological Publishing House, scale 1 : 1,500,000 841pp.

Yang, W., Liu, L., Cao, Y., Wang, C., He, S., Li, R., and Zhu, X., 2010, Geochronological evidence of Indosinian (high-pressure) metamorphic event and its tectonic significance in Taxkorgan area of the Western Kunlun Mountains, NW China: Science China Earth Sciences, v. 53, no. 10, p. 1445-1459.

Yin, A., and Harrison, T. M., 2000, Geologic evolution of the Himalayan-Tibetan orogen: Annual Review of Earth and Planetary Sciences, v. 28, no. 1, p. 211-280.

Yin, A., and Taylor, M. H., 2011, Mechanics of V-shaped conjugate strike-slip faults and the corresponding continuum mode of continental deformation: Geological Society of America Bulletin, v. 123, no. 9-10, p. 1798-1821.

Yin, J., and Bain, Q., 1992, Geologic map of the Karakoram-Western Kunlun and adjacent region: Science Press, scale 1:2,000,000.

Zhang, C., Lu, S., Yu, H., and Ye, H., 2007, Tectonic evolution of the Western Kunlun orogenic belt in northern Qinghai-Tibet Plateau: Evidence from zircon SHRIMP and LA-ICP-MS U-Pb geochronology: Science in China Series D: Earth Sciences, v. 50, no. 6, p. 825-835.

Zhang, Y., Xie, Y., Xu, R., Vidal, P., and Arnaud, N., 1996, Geochemistry of granitoid rocks, *in* Pan, Y., ed., Geological Evolution of the Karakoram and Kunlun Mountains: Beijing, Seismological Press, p. 94-136.

APPENDIX

Table 1: Biotite Data

	Oxide Wt%															Cations Per Unit Formula										
Sample	F	Na2O	MgO	Al2O3	SiO2	K2O	CaO	Cl	TiO2	FeO	MnO	Cr2O3	H2O	F=O	Total (wt%)	Na	Mg	Al	Si	K	Ca	Cl=O	Ti	Fe	Mn	Cr
940_9_bio01	0.21	0.09	11.47	17.35	35.93	9.92	0.00	0.31	3.33	16.981	0.76	0	3.8	-0.09	100.06	0.03	2.58	3.08	5.42	1.91	0.00	-0.07	0.38	2.14	0.10	0.00
940_9_bio02	0.24	0.06	11.58	17.22	36.08	9.95	0.02	0.30	3.08	16.989	0.74	0	3.783	-0.10	99.93	0.02	2.61	3.06	5.45	1.92	0.00	-0.07	0.35	2.14	0.09	0.00
940_9_bio03	0.34	0.05	12.52	16.58	36.63	9.83	0.05	0.35	2.98	16.297	0.67	0.026	3.74	-0.14	99.92	0.02	2.81	2.94	5.51	1.89	0.01	-0.08	0.34	2.05	0.09	0.00
940_9_bio04	0.32	0.07	11.65	16.73	36.78	9.85	0.00	0.34	3.31	17.398	0.69	0.013	3.768	-0.14	100.78	0.02	2.60	2.95	5.51	1.88	0.00	-0.08	0.37	2.18	0.09	0.00
940_9_bio05	0.27	0.08	11.69	16.87	36.27	9.84	0.00	0.33	3.11	16.904	0.62	0	3.754	-0.11	99.62	0.03	2.64	3.01	5.49	1.90	0.00	-0.08	0.35	2.14	0.08	0.00
940_9_bio06	0.29	0.07	11.32	17.33	35.98	9.84	0.00	0.32	3.50	17.339	0.77	0	3.766	-0.12	100.41	0.02	2.54	3.07	5.41	1.89	0.00	-0.07	0.40	2.18	0.10	0.00
940_9_bio07	0.28	0.08	11.86	17.88	36.23	9.78	0.01	0.30	2.80	16.231	0.64	0.022	3.781	-0.12	99.78	0.02	2.66	3.17	5.44	1.87	0.00	-0.07	0.32	2.04	0.08	0.00
940_9_bio08	0.30	0.05	11.79	16.88	35.89	9.87	0.01	0.34	3.21	16.958	0.72	0.004	3.73	-0.13	99.62	0.01	2.66	3.01	5.44	1.91	0.00	-0.08	0.37	2.15	0.09	0.00
940_9_bio09	0.30	0.07	12.23	17.12	36.25	9.87	0.00	0.33	3.14	16.913	0.75	0	3.775	-0.13	100.62	0.02	2.73	3.02	5.43	1.89	0.00	-0.08	0.35	2.12	0.10	0.00
940_9_bio10	0.33	0.07	11.94	17.18	36.15	9.97	0.00	0.31	3.15	16.806	0.78	0	3.755	-0.14	100.31	0.02	2.68	3.04	5.43	1.91	0.00	-0.07	0.36	2.11	0.10	0.00
940_9_bio11	0.30	0.08	12.02	17.40	36.32	10.05	0.01	0.32	3.09	16.638	0.68	0.003	3.78	-0.13	100.56	0.02	2.68	3.07	5.44	1.92	0.00	-0.07	0.35	2.08	0.09	0.00
940_9_bio12	0.37	0.08	12.36	16.45	36.85	9.98	0.00	0.33	3.11	16.544	0.70	0	3.74	-0.16	100.36	0.02	2.76	2.91	5.52	1.91	0.00	-0.08	0.35	2.07	0.09	0.00
940_9_bio13	0.29	0.10	11.38	17.10	35.05	9.80	0.01	0.34	3.12	17.488	0.75	0.024	3.69	-0.12	99.01	0.03	2.60	3.09	5.37	1.91	0.00	-0.08	0.36	2.24	0.10	0.00
940_9_bio14	0.30	0.08	11.43	17.50	36.11	9.76	0.06	0.33	2.89	16.73	0.61	0.016	3.74	-0.13	99.45	0.02	2.58	3.12	5.46	1.88	0.01	-0.07	0.33	2.12	0.08	0.00
9_10_03_1_bio01	0.40	0.13	9.55	16.76	35.76	9.74	0.00	0.11	3.64	19.554	0.62	0.017	3.71	-0.17	99.81	0.04	2.17	3.02	5.46	1.90	0.00	-0.03	0.42	2.50	0.08	0.00
9_10_03_1_bio02	0.47	0.14	9.91	16.49	36.04	9.74	0.02	0.13	3.45	19.763	0.67	0.019	3.687	-0.20	100.32	0.04	2.25	2.96	5.48	1.89	0.00	-0.03	0.40	2.51	0.09	0.00
9_10_03_1_bio03	0.48	0.08	9.56	16.24	35.72	9.86	0.00	0.10	4.01	20.644	0.63	0	3.688	-0.20	100.81	0.03	2.17	2.91	5.44	1.91	0.00	-0.02	0.46	2.63	0.08	0.00
9_10_03_1_bio04	0.43	0.10	9.88	16.29	35.70	9.86	0.00	0.11	3.98	19.591	0.60	0.006	3.701	-0.18	100.07	0.03	2.25	2.93	5.45	1.92	0.00	-0.03	0.46	2.50	0.08	0.00
9_10_03_1_bio05	0.40	0.08	9.71	16.23	35.87	9.75	0.01	0.10	3.96	19.626	0.64	0.005	3.713	-0.17	99.92	0.02	2.21	2.92	5.48	1.90	0.00	-0.02	0.45	2.51	0.08	0.00
9_10_03_1_bio06	0.48	0.04	9.93	16.74	35.78	9.90	0.00	0.09	3.54	19.77	0.61	0.006	3.693	-0.20	100.38	0.01	2.25	3.00	5.44	1.92	0.00	-0.02	0.41	2.51	0.08	0.00
9_10_03_1_bio07	0.41	0.11	9.60	16.30	35.77	9.79	0.01	0.09	4.10	20.386	0.60	0.014	3.729	-0.17	100.72	0.03	2.17	2.92	5.44	1.90	0.00	-0.02	0.47	2.59	0.08	0.00
9_10_03_1_bio08	0.45	0.10	10.05	16.35	35.77	9.89	0.00	0.09	3.72	19.511	0.53	0	3.694	-0.19	99.97	0.03	2.29	2.94	5.46	1.93	0.00	-0.02	0.43	2.49	0.07	0.00
9_10_03_1_bio09	0.42	0.09	9.83	16.68	35.49	9.71	0.02	0.09	3.72	19.745	0.56	0.016	3.703	-0.18	99.90	0.03	2.24	3.00	5.42	1.89	0.00	-0.02	0.43	2.52	0.07	0.00
9_10_03_1_bio10	0.39	0.11	9.77	16.97	35.77	9.85	0.00	0.10	4.05	19.433	0.46	0	3.747	-0.17	100.49	0.03	2.21	3.03	5.42	1.90	0.00	-0.02	0.46	2.46	0.06	0.00

Table 2: Garnet Data

	Oxide Wt%										Cations Per Unit Formula										activities					Temperatures (Celcius)				
Sample	SiO2	TiO2	Al2O3	Cr2O3	Fe2O3	FeO	MnO	MgO	CaO	Total	Si	Ti	Al	Cr	Fe 3+	Fe2+	Mn	Mg	Ca	Fe#	asps	agrs	aal	apy	Distance across grain	Temps at 3 kbar	Temps at 4kbar	Temps at 5 kbar	Temps at 6 kbar	temps at 7 kbar
Garnet																														
940_9_gt01	37.04	0.46	21.02	0.02	0.00	12.68	19.61	1.07	8.09	99.987	5.948	0.055	3.979	0.003	0.000	1.703	2.668	0.257	1.392	0.3896										
940_9_gt02	37.36	0.23	21.38	0.01	0.00	12.67	21.41	0.98	6.56	100.602	5.974	0.028	4.030	0.001	0.000	1.694	2.900	0.233	1.124	0.3688										
940_9_gt03	36.90	0.40	21.13	0.00	0.00	12.89	21.54	1.10	5.65	99.6	5.965	0.049	4.026	0.000	0.000	1.742	2.950	0.265	0.979	0.3713										
940_9_gt_tr1	36.86	0.45	20.92	0.00	0.00	12.44	19.93	1.06	7.77	99.441	5.954	0.055	3.982	0.000	0.000	1.680	2.727	0.256	1.345	0.3813	0.089	0.013	0.021	0.0002	0	532	537	542	547	552
940_9_gt_tr1	36.94	0.60	21.18	0.00	0.00	12.95	21.12	1.11	6.49	100.369	5.928	0.072	4.007	0.000	0.000	1.738	2.871	0.264	1.116	0.3771	0.1	0.0075	0.024	0.0002	489.197302	514	519	524	528	533
940_9_gt_tr1	36.93	0.36	21.13	0.00	0.00	13.33	21.87	1.10	5.73	100.445	5.941	0.044	4.005	0.000	0.000	1.793	2.980	0.263	0.988	0.3756	0.12	0.0052	0.024	0.0002	984.797947	502	507	512	517	522
940_9_gt_tr1	36.94	0.52	21.15	0.00	0.00	13.06	21.66	1.09	5.85	100.267	5.941	0.063	4.009	0.000	0.000	1.757	2.951	0.262	1.007	0.3732	0.11	0.0056	0.025	0.0002	1462.63579	497	502	506	511	516
940_9_gt_tr1	36.82	0.55	21.15	0.00	0.00	12.87	21.29	1.06	6.09	99.829	5.941	0.067	4.021	0.000	0.000	1.736	2.909	0.254	1.053	0.3737	0.11	0.0063	0.024	0.0002	1968.91733	498	503	508	513	518
940_9_gt_tr1	36.87	0.58	20.99	0.00	0.00	12.73	20.81	1.05	6.39	99.404	5.963	0.070	4.001	0.000	0.000	1.722	2.851	0.252	1.107	0.3765	0.1	0.0073	0.023	0.0002	2456.22216	506	511	516	521	526
940_9_gt_tr1	36.91	0.58	21.06	0.00	0.00	12.46	19.50	1.11	7.81	99.421	5.951	0.070	4.001	0.000	0.000	1.680	2.662	0.266	1.350	0.3869	0.083	0.013	0.021	0.0003	2943.34535	554	559	559	564	569
940_9_gt_tr1	36.96	0.47	21.04	0.00	0.00	13.31	20.38	1.15	6.97	100.265	5.938	0.057	3.984	0.000	0.000	1.788	2.773	0.275	1.199	0.3921	0.093	0.0093	0.024	0.0003	3426.03055	532	537	542	547	552
940_9_gt_tr1	37.17	0.31	21.38	0.00	0.00	13.04	20.66	1.13	6.66	100.354	5.954	0.037	4.036	0.000	0.000	1.747	2.803	0.269	1.144	0.384	0.1	0.0081	0.024	0.0002	3929.85988		529			
940_9_gt_tr1	36.86	0.45	20.92	0.00	0.00	12.44	19.93	1.06	7.77	99.441	5.954	0.055	3.982	0.000	0.000	1.680	2.727	0.256	1.345	0.3813	0.089	0.013	0.021	0.0002						
940_9_gt_tr1	36.94	0.60	21.18	0.00	0.00	12.95	21.12	1.11	6.49	100.369	5.928	0.072	4.007	0.000	0.000	1.738	2.871	0.264	1.116	0.3771	0.1	0.0075	0.024	0.0002						
940_9_gt_tr1	36.93	0.36	21.13	0.00	0.00	13.33	21.87	1.10	5.73	100.445	5.941	0.044	4.005	0.000	0.000	1.793	2.980	0.263	0.988	0.3756	0.12	0.0052	0.024	0.0002						
940_9_gt_tr1	36.94	0.52	21.15	0.00	0.00	13.06	21.66	1.09	5.85	100.267	5.941	0.063	4.009	0.000	0.000	1.757	2.951	0.262	1.007	0.3732	0.11	0.0056	0.025	0.0002						
940_9_gt_tr1	36.82	0.55	21.15	0.00	0.00	12.87	21.29	1.06	6.09	99.829	5.941	0.067	4.021	0.000	0.000	1.736	2.909	0.254	1.053	0.3737	0.11	0.0063	0.024	0.0002						
940_9_gt_tr1	36.87	0.58	20.99	0.00	0.00	12.73	20.81	1.05	6.39	99.404	5.963	0.070	4.001	0.000	0.000	1.722	2.851	0.252	1.107	0.3765	0.1	0.0073	0.023	0.0002						
940_9_gt_tr1	36.91	0.58	21.06	0.00	0.00	12.46	19.50	1.11	7.81	99.421	5.951	0.070	4.001	0.000	0.000	1.680	2.662	0.266	1.350	0.3869	0.008	0.013	0.021	0.0003						
940_9_gt_tr1	36.96	0.47	21.04	0.00	0.00	13.31	20.38	1.15	6.97	100.265	5.938	0.057	3.984	0.000	0.000	1.788	2.773	0.275	1.199	0.3921	0.093	0.0093	0.024	0.0003						
940_9_gt_tr1	37.17	0.31	21.38	0.00	0.00	13.04	20.66	1.13	6.66	100.354	5.954	0.037	4.036	0.000	0.000	1.747	2.803	0.269	1.144	0.384	0.1	0.0081	0.024	0.0002						
940_9_gt_tr2	36.99	0.49	21.15	0.00	0.00	12.88	20.03	1.09	6.92	99.539	5.963	0.059	4.019	0.000	0.000	1.736	2.735	0.261	1.195	0.3883	0.09	0.0092	0.023	0.0002	0	526	531	536	541	546
940_9_gt_tr2	36.79	0.62	20.92	0.00	0.00	12.82	21.65	1.06	6.05	99.906	5.942	0.075	3.982	0.000	0.000	1.731	2.962	0.255	1.046	0.3689	0.11	0.0061	0.023	0.0002	332.951948	499	504	508	513	518
940_9_gt_tr2	36.84	0.43	21.15	0.00	0.00	12.86	21.17	1.08	6.50	100.018	5.935	0.052	4.017	0.000	0.000	1.732	2.888	0.260	1.121	0.3749	0.11	0.0076	0.023	0.0002	631.280626	511	516	521	526	531
940_9_gt_tr2	36.70	0.41	21.16	0.00	0.00	12.58	21.27	1.09	5.54	98.731	5.971	0.050	4.058	0.000	0.000	1.712	2.931	0.263	0.965	0.3687	0.11	0.0049	0.023	0.0002	1022.16168	514	519	524	529	534
940_9_gt_tr2	36.78	0.60	21.04	0.00	0.00	12.40	21.31	1.09	6.51	99.733	5.937	0.073	4.003	0.000	0.000	1.674	2.913	0.263	1.125	0.3649	0.11	0.0077	0.021	0.0002	1319.836	527	532	537	542	547
940_9_gt_tr2	36.50	0.51	21.03	0.00	0.00	12.65	21.38	1.01	5.33	98.414	5.965	0.063	4.051	0.000	0.000	1.728	2.960	0.247	0.933	0.3687	0.12	0.0044	0.023	0.0002	1664.43142	489	494	498	503	508
940_9_gt_tr2	36.48	0.55	20.88	0.00	0.00	12.47	21.49	1.06	6.20	99.139	5.933	0.068	4.003	0.000	0.000	1.696	2.960	0.256	1.081	0.3642	0.12	0.0068	0.022	0.0002	1984.63135	510	514	519	524	529
940_9_gt_tr2	36.80	0.41	21.08	0.00	0.00	12.29	20.21	1.06	7.24	99.087	5.959	0.050	4.023	0.000	0.000	1.665	2.771	0.257	1.255	0.3753	0.094	0.0106	0.021	0.0002	2416.66145	531	536	541	546	551
940_9_gt_tr2	36.85	0.45	20.98	0.00	0.00	12.90	19.93	1.10	6.97	99.185	5.966	0.055	4.003	0.000	0.000	1.747	2.732	0.266	1.209	0.39	0.09	0.0095	0.024	0.0002	2692.72665	524	529	534	539	544
940_9_gt_tr2T	36.91	0.42	21.22	0.00	0.00	12.40	20.65	1.04	6.78	99.412	5.960	0.050	4.038	0.000	0.000	1.675	2.824	0.251	1.173	0.3722	0.1	0.0086	0.021	0.0002						
940_9_gt_tr2B	36.61	0.42	21.04	0.00	0.00	12.98	20.88	1.10	6.18	99.217	5.943	0.051	4.024	0.000	0.000	1.762	2.871	0.267	1.075	0.3803	0.11	0.0067	0.025	0.0002						
940_9_gt_tr3	36.86	0.24	21.36	0.00	0.00	13.01	21.17	1.15	6.08	99.88	5.942	0.029	4.058	0.000	0.000	1.754	2.890	0.277	1.050	0.3776	11.22	0.0063	0.024	0.0002	0	524	529	534	539	544
940_9_gt_tr3	36.66	0.68	20.97	0.00	0.00	12.91	21.18	1.14	6.04	99.575	5.932	0.083	3.999	0.000	0.000	1.747	2.902	0.275	1.047	0.3757	11.22	0.0063	0.024	0.0002	663.771798	521	526	531	536	541
940_9_gt_tr3	36.61	0.41	21.25	0.00	0.00	12.83	21.74	1.11	5.58	99.526	5.930	0.050	4.055	0.000	0.000	1.737	2.982	0.269	0.969	0.3681	12.24	0.005	0.024	0.0002	1265.62311	508	513	518	523	527
940_9_gt_tr3	36.48	0.33	21.06	0.00	0.00	13.12	21.10	1.17	5.58	98.827	5.946	0.040	4.045	0.000	0.000	1.788	2.913	0.285	0.975	0.3804	11.22	0.0051	0.026	0.0002	1911.36764	517	522	527	532	537
940_9_gt_tr3	36.79	0.43	21.28	0.00	0.00	13.89	20.55	1.27	5.68	99.882	5.932	0.052	4.044	0.000	0.000	1.873	2.806	0.306	0.981	0.4003	10.2	0.0053	0.03	0.0003	2556.16218	526	531	536	541	546
940_9_gt_tr3	36.13	0.47	20.83	0.00	0.00	13.03	21.70	1.21	5.39	98.751	5.914	0.057	4.018	0.000	0.000	1.784	3.008	0.294	0.945	0.3722	12.24	0.0047	0.023	0.0003	3190.47756	541	546	551	556	561
940_9_gt_tr3	36.68	0.87	20.94	0.00	0.00	12.80	21.58	1.12	5.56	99.552	5.936	0.106	3.994	0.000	0.000	1.733	2.958	0.271	0.964	0.3694	11.22	0.0049	0.023	0.0002	3823.00977	517	522	527	532	537
940_9_gt_tr3	36.71	0.35	21.47	0.00	0.00	12.47	20.40	1.14	7.21	99.732	5.912	0.043	4.075	0.000	0.000	1.679	2.782	0.273	1.244	0.3764	9.69	0.0104	0.02	0.0003	4466.07509	560	565	570	576	581
940_9_gt_tr3	36.59	0.55	21.27	0.00	0.00	12.81	20.05	1.14	7.20	99.606	5.906	0.066	4.045	0.000	0.000	1.729	2.740	0.274	1.245	0.387	9.282	0.0105	0.022	0.0003	5097.61052	548	553	558	563	569
940_9_gt_tr3T	36.58	0.27	21.21	0.00	0.00	13.11	21.78	1.17	5.07	99.18	5.946	0.033	4.063	0.000	0.000	1.782	2.998	0.285	0.884	0.3727	12.24	0.0038	0.026	0.0002						
940_9_gt_tr3B	36.87	0.32	21.26	0.00	0.00	12.97	20.49	1.16	6.44	99.508	5.953	0.038	4.046	0.000	0.000	1.752	2.803	0.279	1.114	0.3846	10.2	0.0076	0.024	0.0003						
9_10_03_1_gt01	36.91	0.15	21.28	0.00	0.00	26.14	8.19	1.29	6.31	100.268	5.939	0.018	4.036	0.000	0.000	3.518	1.116	0.310	1.088	0.7591										
9_10_03_1_gt02	36.86	0.12	21.26	0.00	0.00	23.27	11.28	0.83	6.44	100.066	5.951	0.015	4.046	0.000	0.000	3.142	1.543	0.201	1.114	0.6706										
9_10_03_1_gt_tr1	37.07	0.10	21.40	0.00	0.00	26.00	8.55	1.39	5.87	100.367	5.953	0.011	4.051	0.000	0.000	3.491	1.163	0.332	1.009	0.7502	0.0069	0.0058	0.18	0.0004	0	488	493	498	502	507
9_10_03_1_gt_tr1	36.88	0.15	21.26	0.00	0.00	25.04	9.31	1.07	6.74	100.443	5.932	0.018	4.031	0.000	0.000	3.368	1.269	0.255	1.162	0.7263	0.0089	0.0083	0.15	0.0002	463.479234	451	456	460	465	469
9_10_03_1_gt_tr1	36.81	0.13	21.35	0.00	0.00	23.87	10.43	0.92	6.57	100.075	5.938	0.016	4.059	0.000	0.000	3.221	1.426	0.221	1.135	0.6932	0.013	0.0077	0.14	0.0001	951.47616	416	420	424	429	433
9_10_03_1_gt_tr1	36.68	0.16	21.28	0.00	0.00	23.16	11.14	0.92	6.65	99.997	5.927	0.019	4.053	0.000	0.000	3.130	1.525	0.221	1.151	0.6724	0.016	0.008	0.13	0.0001	1429.3569	423	428	432	436	441
9_10_03_1_gt_tr1	36.93	0.13	21.22	0.00	0.00	23.14	11.31	0.78	6.84	100.359	5.949	0.016	4.028	0.000	0.000	3.117	1.543	0.188	1.181	0.6688	0.016	0.0084	0.13	9E-05	1900.25073	393	387	391	395	399
9_10_03_1_gt_tr1	36.95	0.06	21.36	0.00	0.00	23.60	11.05	0.88	6.42	100.332	5.949	0.008	4.054	0.000	0.000	3.178	1.508	0.212	1.107	0.6783	0.015	0.0071	0.14	0.0001	2344.79319	402	406	410	414	418
9_10_03_1_gt_tr1	36.80	0.26	21.41	0.00	0.00	23.59	10.12	1.09	6.84	100.113	5.924	0.032	4.062	0.000	0.000	3.176	1.380	0.260	1.180	0.6971	0.012	0.0088	0.14	0.0002	2832.27652	464	468	473	477	482
9_10_03_1_gt_tr1	36.77	0.13	21.27	0.00	0.00	25.61	9.17	1.10	6.57	100.607	5.915	0.016	4.032	0.000	0.000	3.445	1.250	0.263	1.133	0.7338	0.0085	0.0077	0.16	0.0002	3325.66582	452	457	461	466	470
9_10_03_1_gt_tr1	36.84	0.05	21.41	0.00	0.00	26.17	8.33	1.27	6.18	100.242	5.931	0.006	4.062	0.000	0.000	3.524	1.135	0.305	1.067	0.7563	0.0064	0.0067	0.18	0.0004	3800.11076	479	484	489	493	498
9_10_03_1_gt_tr1L	36.87	0.27	21.11	0.00	0.00	26.00	7.91	1.26	6.92	100.334	0.000	0.000	0.000	0.000	0.000	0.000	0.000	0.000	0.000	#DIV/0!	0.0054	0.0092	0.17	0.0004						

Table 3: Zircon Data

Analysis_# Data	$^{206}Pb/^{204}Pb$	2%ERR	Raw Ratios: $^{206}Pb/^{238}U$	2%ERR	$^{207}Pb/^{206}Pb$	2%ERR	Age $^{206}Pb/^{238}U$	2SD	Age $^{207}Pb/^{206}Pb$	2SD	U	Th ppm	U/Th	% discordance
AR-4-27-00-9														
NPM-4D-86-1.28	0.00	92.07	0.03512	2.22	0.05108	3.96	273.1	7.2	217	±101	271	96	2.82	-20.4
AR-4-27-00-9-68	0.00	381.66	0.05187	2.09	0.05471	3.06	399.6	9.6	363	±73	287	132	2.17	-9.1
NPM-4D-86-1.54	0.00	141.23	0.05234	2.42	0.05488	2.27	404.3	11.0	371	±59	849	130	6.51	-8.2
NPM-4D-86-1.26	0.00	875.97	0.03787	2.08	0.05235	3.41	293.9	7.1	275	±85	382	420	0.91	-6.6
AR-4-27-00-9-118	0.00	102.60	0.12319	1.80	0.06743	1.48	885.7	18.5	838	±46	868	293	2.97	-5.4
NPM-4D-86-1.31	0.00	2103.15	0.02790	2.24	0.05260	4.80	218.2	5.4	283	±117	181	151	1.20	29.5
NPM-4D-86-1.21	-0.01	134.10	0.03011	1.84	0.05230	3.26	234.5	6.2	275	±78	460	205	2.24	17.3
AR-4-27-00-9-74	0.00	814.72	0.03386	2.04	0.05239	2.71	263.1	6.6	266	±73	473	239	1.98	0.9
NPM-4D-86-1.24	-0.02	918.95	0.03436	1.87	0.05370	2.03	267.0	6.0	334	±56	1464	789	1.86	25.1
AR-4-27-00-9-104	0.00	1341.37	0.03567	1.97	0.05341	3.73	272.1	5.9	323	±91	333	279	1.19	18.7
AR-4-27-00-9-94	0.00	111.60	0.03665	2.21	0.05366	3.49	281.8	7.2	326	±83	180	159	1.13	15.7
AR-4-27-00-9-119	0.00	124.25	0.03941	3.04	0.05348	4.81	296.6	9.6	335	±115	435	173	2.52	13.0
AR-4-27-00-9-87	0.00	115.16	0.04136	2.32	0.05566	4.40	318.3	8.7	406	±100	190	101	1.88	27.6
AR-4-27-00-9-81	0.00	164.13	0.04306	1.83	0.05549	2.73	331.8	7.4	398	±72	363	273	1.33	19.9
NPM-4D-86-1.57	0.00	391.46	0.04390	1.92	0.05653	3.61	340.8	8.0	437	±86	301	326	0.92	28.3
NPM-4D-86-1.41	0.00	308.16	0.04982	1.95	0.05566	2.76	385.2	8.8	406	±71	307	221	1.39	5.4
AR-4-27-00-9-77	0.00	90.72	0.05236	1.71	0.05821	2.00	402.0	9.0	503	±61	921	787	1.17	25.1
AR-4-27-00-9-91	0.00	543.17	0.05280	1.85	0.05560	2.32	402.6	9.6	406	±56	401	304	1.32	0.7
AR-4-27-00-9-71	0.00	182.69	0.05241	1.73	0.05576	1.79	403.1	8.9	407	±59	1269	346	3.66	0.9
AR-4-27-00-9-107	0.00	2672.88	0.05356	2.10	0.05666	2.08	403.4	9.5	457	±60	758	375	2.02	13.3
AR 4-27-00-9.17	4071.78	30.09	0.04189	1.78	0.05793	1.17	403.6	9.3	475	±58	14547	20653	0.70	17.7
AR-4-27-00-9-65	0.00	138.29	0.05291	2.22	0.05694	2.55	407.6	9.4	453	±59	347	129	2.69	11.1
NPM-4D-86-1.25	-0.02	81.32	0.05364	1.70	0.05720	1.77	412.2	8.6	475	±50	1063	130	8.15	15.3
AR-4-27-00-9-86	0.00	111.93	0.05395	1.84	0.05645	2.00	412.2	9.0	437	±47	791	334	2.37	6.1
AR-4-27-00-9-64	0.00	72.91	0.05371	2.12	0.05684	3.35	413.7	9.1	449	±76	161	66	2.46	8.4
AR-4-27-00-9-78	0.00	452.16	0.05440	1.86	0.05608	1.56	417.0	11.0	421	±64	1067	403	2.65	0.8
AR-4-27-00-9-92	0.00	87.70	0.05534	2.06	0.05728	2.07	421.2	10.4	472	±50	736	341	2.16	12.0
NPM-4D-86-1.45	0.00	76.63	0.05473	1.93	0.05916	2.44	422.0	10.0	540	±64	468	245	1.91	28.0
AR-4-27-00-9-108	0.00	204.96	0.05685	1.57	0.05543	1.84	427.1	8.4	409	±48	808	513	1.58	-4.3
AR-4-27-00-9-102	0.00	872.55	0.05687	1.91	0.05858	2.28	428.8	8.5	528	±59	943	1236	0.76	23.1
AR-4-27-00-9-109	0.00	2081.77	0.05722	2.06	0.05583	2.44	429.7	9.4	425	±61	381	221	1.72	-1.1
AR 4-27-00-9.13	7850.19	32.31	0.04517	1.97	0.05809	1.54	433.5	10.4	481	±65	24809	1127	22.02	10.9
NPM-4D-86-1.48	-0.01	80.41	0.05657	1.94	0.05605	1.64	435.8	12.0	420	±52	1243	322	3.86	-3.6
NPM-4D-86-1.19	-0.03	122.52	0.05803	2.02	0.05819	1.77	443.8	13.1	517	±47	1110	146	7.58	16.5
NPM-4D-86-1.5	-0.31	202.13	0.05991	1.81	0.05894	1.36	454.1	10.2	557	±43	5037	4156	1.21	22.7
AR 4-27-00-9.10	10847.37	40.11	0.05257	2.07	0.06119	1.24	501.0	11.6	594	±57	12807	7987	1.60	18.5
NPM-4D-86-1.14	-0.02	176.93	0.06984	3.55	0.06256	3.03	529.2	20.6	678	±76	526	2	301.92	28.0
AR-4-27-00-9-98	0.00	226.62	0.07981	7.38	0.06275	2.06	595.9	42.0	675	±57	770	161	4.78	13.2
NPM-4D-86-1.43	-0.01	2904.13	0.10408	1.98	0.06877	1.62	780.2	17.7	861	±44	632	106	5.95	10.4
AR-4-27-00-9-63	0.00	95.18	0.10557	1.88	0.06780	2.09	789.5	15.4	828	±47	304	244	1.25	4.9
NPM-4D-86-1.39	-0.02	108.42	0.10573	1.86	0.07141	1.68	791.4	17.0	940	±47	1056	189	5.57	18.8
NPM-4D-86-1.50	0.00	93.80	0.10572	2.16	0.06904	2.55	792.1	19.1	868	±60	134	93	1.44	9.6
AR 4-27-00-9.11	21190.24	28.53	0.08735	1.69	0.06682	1.12	813.2	17.3	782	±57	19565	10490	1.87	-3.8
AR-4-27-00-9-61	0.00	181.73	0.11543	1.59	0.06872	1.47	858.7	14.0	856	±42	924	115	8.01	-0.3
AR 4-27-00-9.24	14726.62	52.70	0.09254	2.53	0.06882	1.33	862.3	24.3	845	±57	14966	2398	6.24	-2.0
AR-4-27-00-9-82	0.00	359.21	0.11958	1.79	0.07150	1.71	882.0	16.2	941	±48	418	57	7.33	6.7
AR-4-27-00-9-103	0.00	275.92	0.13195	1.51	0.07206	1.37	954.2	16.0	966	±40	656	213	3.07	1.2
AR 4-27-00-9.5	5290.02	36.44	0.10527	1.49	0.08115	1.07	965.2	17.9	1177	±56	16170	2131	7.59	21.9
AR-4-27-00-9-85	0.00	370.75	0.13549	3.57	0.08010	2.90	990.0	34.7	1170	±59	821	546	1.50	18.2
NPM-4D-86-1.4	-0.15	225.36	0.15061	1.81	0.07829	1.39	1085.1	22.8	1148	±38	857	151	5.67	5.8
NPM-4D-86-1.49	-0.01	141.97	0.16203	2.91	0.08736	2.83	1177.3	36.3	1339	±60	368	195	1.88	13.7
NPM-4D-86-1.55	0.00	1345.05	0.17052	3.44	0.10044	1.98	1233.4	41.5	1602	±44	138	52	2.66	29.9
NPM-4D-86-1.32	0.00	129.26	0.18041	2.06	0.10430	2.02	1295.9	27.7	1678	±50	123	71	1.72	29.5
NPM-4D-86-1.17	-0.02	46.80	0.20129	1.90	0.11287	1.82	1423.3	35.2	1831	±47	172	106	1.63	28.6
AR-4-27-00-9-83	0.00	68.65	0.20511	1.91	0.11480	1.52	1445.9	30.0	1849	±30	460	108	4.25	27.9
AR-4-27-00-9-90	0.00	110.94	0.21014	2.02	0.10964	1.54	1474.3	34.0	1767	±32	446	191	2.33	19.9
NPM-4D-86-1.6	-0.11	384.53	0.21206	1.85	0.10489	1.66	1483.3	27.8	1704	±44	568	317	1.79	14.9
NPM-4D-86-1.20	-0.03	105.96	0.21925	1.66	0.09964	1.34	1537.7	35.3	1600	±31	267	154	1.74	4.1
AR-4-27-00-9-96	0.00	59.86	0.24931	1.74	0.12685	1.27	1705.1	33.3	2033	±30	844	527	1.60	19.2
AR-4-27-00-9-67	0.00	188.08	0.25101	1.64	0.11184	1.65	1738.4	29.9	1800	±35	301	107	2.81	3.5
NPM-4D-86-1.59	-0.02	259.32	0.25404	2.50	0.12009	1.43	1760.8	40.7	1928	±38	1064	201	5.28	9.5
AR-4-27-00-9-105	0.00	1759.65	0.26152	1.86	0.11197	1.71	1769.7	32.5	1813	±40	120	87	1.37	2.5
AR 4-27-00-9.6	12262.37	19.42	0.20702	1.48	0.12054	1.06	1779.5	29.2	1921	±31	21624	6196	3.49	7.9
AR 4-27-00-9.8	-48142.74	78.06	0.21145	2.04	0.12215	1.02	1813.4	37.0	1945	±31	13776	3939	3.50	7.2
AR-4-27-00-9-110	0.00	546.34	0.27484	1.97	0.15573	1.45	1843.0	34.2	2394	±33	767	541	1.42	29.9
NPM-4D-86-1.38	-0.05	58.51	0.27735	2.27	0.12259	1.60	1899.4	39.5	1969	±43	1016	446	2.28	3.7
NPM-4D-86-1.36	-0.01	51.84	0.28197	1.97	0.12507	1.59	1926.4	33.4	2006	±48	213	9	23.41	4.1
NPM-4D-86-1.60	-0.01	145.00	0.28269	3.78	0.16126	1.28	1932.2	63.6	2441	±32	615	627	0.98	26.3
AR-4-27-00-9-62	-0.01	50.59	0.29395	1.72	0.12500	1.34	1995.7	31.2	1999	±34	569	193	2.95	0.2
NPM-4D-86-1.42	-0.01	113.75	0.30299	2.36	0.14524	1.75	2050.8	48.8	2265	±41	153	207	0.74	10.5
AR-4-27-00-9-116	0.00	144.31	0.32569	3.13	0.16570	1.28	2122.0	60.1	2503	±29	417	246	1.70	18.0
AR 4-27-00-9.25	10353.19	33.04	0.26152	2.25	0.17307	1.22	2190.0	51.7	2549	±45	8242	4588	1.80	16.4
NPM-4D-86-1.51	-0.01	61.45	0.33312	2.47	0.14818	1.65	2224.1	53.1	2298	±37	196	81	2.43	3.3
NPM-4D-86-1.53	0.00	99.72	0.33778	1.69	0.17152	1.68	2250.3	41.8	2546	±36	111	59	1.87	13.1
NPM-4D-86-1.37	-0.02	273.19	0.33969	1.76	0.16208	1.29	2258.8	35.2	2454	±42	311	147	2.12	8.6
AR-4-27-00-9-106	0.00	269.59	0.34975	1.78	0.16804	1.35	2269.2	38.8	2522	±33	412	217	1.90	11.1
AR 4-27-00-9.7	-144138.31	79.17	0.31253	2.17	0.17814	1.12	2527.5	51.4	2595	±29	5876	3335	1.76	2.7
AR 4-27-00-9.27	3494.80	18.63	0.31052	1.73	0.16969	0.98	2531.3	53.5	2516	±54	4621	2096	2.21	-0.6
NPM-4D-86-1.10	-0.02	128.28	0.04986	1.82	0.05747	2.40	381.2	8.5	498	±63	565	92	6.12	30.6
AR 4-27-00-9.3	7039.93	41.36	0.04153	1.72	0.05931	1.44	398.0	8.4	525	±66	24606	8957	2.75	32.0
NPM-4D-86-1.3	-0.04	342.04	0.03022	1.78	0.05266	2.51	232.7	5.2	308	±64	1117	372	3.00	32.3
AR-4-27-00-9-117	0.00	671.24	0.05727	1.63	0.05946	2.01	427.1	8.7	569	±54	748	308	2.43	33.3
AR-4-27-00-9-66	0.00	1508.33	0.16440	2.31	0.09989	2.64	1190.1	26.6	1591	±52	94	41	2.29	33.7
AR-4-27-00-9-72	0.00	137.82	0.05660	1.92	0.06055	2.99	434.2	10.4	588	±74	363	70	5.22	35.4
AR-4-27-00-9-114	0.00	874.80	0.03475	1.76	0.05411	2.10	263.2	5.5	358	±54	1134	717	1.58	36.1
NPM-4D-86-1.13	-0.01	829.76	0.03438	2.46	0.05420	4.46	265.9	7.7	363	±106	364	408	0.89	36.7
AR-4-27-00-9-76	0.00	151.09	0.03573	2.32	0.05522	1.74	277.1	7.6	386	±54	1976	1082	1.83	39.2
AR-4-27-00-9-100	0.00	166.39	0.16025	7.32	0.09964	3.14	1144.7	76.6	1596	±65	91	281	0.32	39.4
NPM-4D-86-1.1	-0.02	82.10	0.05151	2.06	0.05868	3.16	391.5	10.7	550	±71	282	194	1.45	40.6
AR-4-27-00-9-93	0.00	482.15	0.24114	3.61	0.15190	1.78	1662.4	56.3	2344	±36	617	179	3.45	41.0
AR 4-27-00-9.30	2923.91	28.27	0.04742	1.69	0.06260	1.86	457.3	11.9	646	±50	10914	4676	2.33	41.2
AR-4-27-00-9-111	0.00	62.88	0.09576	2.28	0.07283	1.95	701.8	16.1	993	±47	335	69	4.88	41.5

Table 3: Zircon Data

Analysis_# Data	$^{206}Pb/^{204}Pb$	2%ERR	Raw Ratios: $^{206}Pb/^{238}U$	2%ERR	$^{207}Pb/^{206}Pb$	2%ERR	Age $^{206}Pb/^{238}U$	2SD	Age $^{207}Pb/^{206}Pb$	2SD	U	Th ppm	U/Th	% discordance
AR-4-27-00-9-70	0.00	70.35	0.04953	1.79	0.05925	1.63	381.9	8.6	540	±55	1110	533	2.08	41.5
NPM-4D-86-1.30	-0.01	103.48	0.05473	3.36	0.06052	3.36	420.9	14.8	596	±80	612	382	1.60	41.6
NPM-4D-86-1.16	-0.01	123.51	0.05042	1.88	0.05921	2.48	386.9	10.3	557	±68	441	61	7.28	43.9
AR-4-27-00-9-69	0.00	228.81	0.05961	2.01	0.06261	2.92	457.1	11.8	660	±70	655	366	1.79	44.4
AR 4-27-00-9.23	4908.38	33.32	0.04353	1.73	0.06150	1.87	419.9	9.7	607	±66	11201	5025	2.23	44.4
AR-4-27-00-9-80	0.00	768.42	0.05249	2.68	0.06076	2.36	402.7	11.7	597	±63	1206	1503	0.80	48.2
AR-4-27-00-9-89	0.00	132.01	0.08385	4.36	0.07118	1.44	629.4	28.6	933	±32	1071	401	2.67	48.2
NPM-4D-86-1.27	0.00	76.37	0.03417	1.99	0.05550	3.31	265.9	6.2	407	±81	333	113	2.94	52.9
NPM-4D-86-1.12	-0.04	49.94	0.05847	1.92	0.06327	2.65	445.7	10.2	703	±65	893	324	2.75	57.7
NPM-4D-86-1.23	0.00	160.50	0.03337	2.64	0.05552	5.46	259.5	7.5	410	±126	125	115	1.09	57.9
NPM-4D-86-1.46	0.00	284.96	0.03424	2.62	0.05635	4.96	267.3	7.9	432	±116	133	107	1.24	61.8
AR 4-27-00-9.28	2553.54	17.10	0.03848	1.63	0.06177	1.07	373.2	9.0	617	±70	28972	12224	2.37	65.2
NPM-4D-86-1.2	-0.01	193.66	0.03217	2.22	0.05516	3.95	247.4	6.7	413	±90	283	83	3.41	67.1
NPM-4D-86-1.8	-0.15	58.18	0.13675	1.71	0.10269	1.38	995.3	17.8	1664	±42	1242	1047	1.19	67.2
AR-4-27-00-9-79	0.00	231.84	0.05447	1.62	0.06384	1.78	417.6	9.4	703	±56	883	1031	0.86	68.4
AR-4-27-00-9-97	0.00	90.91	0.03726	2.41	0.05828	2.77	285.1	6.9	514	±68	443	76	5.83	80.3
AR-4-27-00-9-84	0.00	76.05	0.05591	2.50	0.06592	3.54	427.2	11.6	772	±76	468	248	1.88	80.8
NPM-4D-86-1.18	-0.02	121.43	0.08117	2.47	0.07848	2.11	612.5	20.4	1141	±62	388	133	2.92	86.3
AR-4-27-00-9-101	0.00	234.87	0.04864	1.99	0.06396	4.14	368.7	7.3	717	±94	242	195	1.24	94.6
AR 4-27-00-9.4	1293.37	15.95	0.04288	1.74	0.06754	1.80	410.6	8.7	803	±67	15979	4182	3.82	95.6
NPM-4D-86-1.22	-0.02	83.00	0.03103	1.93	0.05722	1.85	241.5	5.8	477	±52	1988	820	2.43	97.6
AR-4-27-00-9-99	0.00	75.03	0.03747	2.01	0.05978	4.14	286.5	5.8	570	±99	366	178	2.06	99.0
NPM-4D-86-1.58	0.00	53.20	0.03178	2.77	0.05820	2.99	248.4	7.3	502	±74	1132	676	1.67	101.9
NPM-4D-86-1.9	-0.03	95.56	0.04507	1.88	0.06330	2.30	345.4	7.9	707	±59	763	473	1.61	104.8
AR-4-27-00-9-112	0.00	304.01	0.06208	1.69	0.07152	1.71	463.3	9.2	956	±42	1109	1350	0.82	106.3
NPM-4D-86-1.44	0.00	88.88	0.03434	2.12	0.05968	2.88	268.0	6.8	560	±72	916	732	1.25	108.9
NPM-4D-86-1.56	0.00	97.20	0.03017	2.36	0.05837	4.04	236.1	6.4	508	±94	385	340	1.13	115.3
NPM-4D-86-1.29	0.00	145.07	0.03221	2.34	0.05907	5.35	251.0	6.9	544	±123	300	326	0.92	116.6
AR-4-27-00-9-113	0.00	1751.60	0.08037	2.44	0.08443	1.45	593.5	15.3	1287	±37	1121	2303	0.49	116.9
NPM-4D-86-1.47	-0.01	55.26	0.05396	2.26	0.07031	1.60	416.4	11.6	906	±43	1734	615	2.82	117.6
AR-4-27-00-9-120	0.00	60.87	0.16876	5.13	0.17610	2.21	1183.6	57.0	2606	±46	1139	231	4.92	120.2
AR-4-27-00-9-115	0.00	285.79	0.04415	1.63	0.06489	2.41	332.5	6.6	755	±57	546	294	1.86	127.1
AR 4-27-00-9.20	1780.69	16.94	0.02554	1.70	0.06132	1.23	249.2	5.6	600	±57	43837	21700	2.02	140.6
NPM-4D-86-1.52	0.00	286.96	0.02996	6.22	0.05996	11.63	234.5	14.6	568	±255	675	385	1.75	142.0
AR-4-27-00-9-95	0.00	401.81	0.05073	2.76	0.07200	7.16	386.8	11.6	959	±148	47	10	4.76	147.8
AR-4-27-00-9-88	0.00	119.36	0.05172	2.29	0.07361	4.41	395.5	11.7	1001	±90	266	257	1.04	153.2
NPM-4D-86-1.35	-0.03	22.74	0.03350	2.07	0.06387	1.21	261.3	5.4	709	±53	4409	1220	3.61	171.4
AR 4-27-00-9.21	1034.24	36.79	0.02697	2.49	0.06566	2.59	263.3	7.7	746	±75	16194	13756	1.18	183.5
AR-4-27-00-9-75	0.00	44.88	0.02785	2.68	0.06486	2.05	217.1	6.6	736	±56	1955	1427	1.37	239.0
AR-4-27-00-9-73	0.00	68.57	0.03765	3.27	0.07869	4.37	292.0	10.3	1132	±93	477	285	1.67	287.7
NPM-4D-86-1.34	-0.01	92.67	0.02465	2.43	0.06859	3.67	193.2	4.7	859	±89	1588	2171	0.73	344.5
NPM-4D-86-1.15	-0.04	39.89	0.02210	2.43	0.06585	2.54	172.4	5.3	785	±66	3084	1548	1.99	355.6
NPM-4D-86-1.33	0.00	80.81	0.03198	2.30	0.08549	3.76	249.6	5.7	1301	±85	339	385	0.88	421.4
NPM-4D-86-1.7	0.00	170.15	0.03730	3.94	0.09518	9.97	287.0	11.2	1523	±191	144	63	2.30	430.6
AR-6-26-00-7														
AR-6-27-00-7-24	126.10	14.53	0.11526	1.65	0.17052	6.36	924.8	15.4	2544	±107	416	115	3.60	175.1
AR-6-27-00-7-37	511.14	64.62	0.10676	2.26	0.08566	4.91	865.6	18.6	1309	±96	89	206	0.43	51.2
AR-6-27-00-7-41	176.47	10.01	0.11414	2.28	0.15111	3.50	922.9	19.9	2339	±60	1583	184	8.60	153.4
AR-6-27-00-7-62	398.20	48.50	0.12178	2.86	0.10614	6.31	984.9	31.4	1713	±117	96	101	0.95	73.9
AR-6-27-00-7-90	203.13	36.18	0.05014	2.69	0.10041	6.35	424.5	12.0	1609	±119	174	147	1.19	279.1
AR-6-27-00-7-48	1426.93	84.48	0.08271	3.89	0.07891	6.03	682.7	25.7	1147	±120	443	224	1.98	68.0
AR-6-27-00-7-86	-278.32	205.31	0.05835	3.00	0.07581	7.61	491.5	16.7	1066	±154	27	0	8974.54	116.9
AR-6-27-00-7-53	-1066.42	2041.39	0.08578	3.21	0.08212	6.00	707.7	22.6	1226	±118	180	137	1.31	73.2
AR-6-27-00-7-33	396.50	59.02	0.05825	3.18	0.09911	5.30	485.9	15.0	1587	±100	75	0	357.03	226.5
AR-6-27-00-7-105	615.83	72.75	0.07665	2.23	0.06703	3.15	636.9	14.8	813	±69	190	95	1.99	27.7
AR-6-27-00-7-55	-418.46	136.05	0.09798	1.83	0.06596	3.54	802.5	15.9	781	±75	59	39	1.50	-2.7
AR-6-27-00-7-29	1778.01	126.38	0.20244	1.85	0.10330	2.44	1548.2	27.0	1664	±51	65	74	0.88	7.5
AR 6-27-00-7.3	114.61	27.80	0.08346	2.88	0.24914	5.78	653.6	18.2	3163	±92	30	0	335.42	384.0
AR-6-27-00-7-46	5342.97	154.51	0.05379	1.71	0.05892	2.39	452.0	7.9	539	±52	438	355	1.23	19.3
AR-6-27-00-7-94	1333.47	200.59	0.08281	2.66	0.07465	4.15	686.5	20.5	1035	±87	73	494	0.15	50.7
AR 6-27-00-7.7	921.45	60.07	0.04935	2.25	0.06691	3.57	396.3	9.1	816	±77	214	156	1.37	105.8
AR-6-27-00-7-68	615.14	13.17	0.22371	1.35	0.13200	3.07	1708.7	26.0	2104	±56	1208	660	1.83	23.1
AR-6-27-00-7-13	3559.97	167.20	0.11603	1.77	0.07570	2.34	925.8	16.0	1065	±49	251	271	0.93	15.0
AR-6-27-00-7-92	59.46	17.28	0.06359	2.42	0.24930	8.42	533.6	15.2	3161	±135	1242	523	2.38	492.4
AR-6-27-00-7-103	-11316.38	2269.85	0.14974	2.19	0.08471	3.62	1191.0	26.1	1285	±73	451	155	2.92	7.9
AR-6-27-00-7-104	4872.26	68.10	0.09534	1.57	0.06676	2.07	783.2	13.7	805	±49	300	239	1.25	2.8
AR-6-27-00-7-78	3294.22	111.15	0.09296	2.07	0.06854	1.97	766.5	17.2	860	±54	552	443	1.25	12.3
AR-6-27-00-7-73	41.60	11.12	0.07826	1.92	0.37918	3.67	651.1	18.1	3811	±58	1731	837	2.07	485.2
AR 6-27-00-7.1	-2224.53	205.71	0.05898	1.86	0.05947	2.19	467.8	8.9	562	±49	168	109	1.54	20.1
AR-6-27-00-7-34	1500.25	69.50	0.12042	4.15	0.07552	3.66	967.3	37.4	1060	±75	437	232	1.89	9.6
AR-6-27-00-7-118	688.74	30.56	0.07309	2.19	0.08353	2.95	606.7	15.4	1258	±66	640	134	4.76	107.3
AR-6-27-00-7-20	106.43	10.29	0.05115	2.23	0.19037	4.14	425.7	9.7	2727	±69	791	250	3.16	540.6
AR 6-27-00-7.31	4756.98	130.13	0.11300	1.97	0.06811	2.48	886.1	17.0	861	±53	63	34	1.86	-2.8
AR 6-27-00-7.2	1189.75	22.28	0.05398	1.92	0.06736	1.90	429.9	8.3	828	±40	971	362	2.68	92.6
AR-6-27-00-7-82	605.83	78.23	0.06638	1.72	0.06874	2.68	556.5	13.3	866	±59	215	159	1.35	55.7
AR-6-27-00-7-38	-6583.76	480.01	0.10691	1.71	0.07102	1.88	866.9	14.4	935	±40	309	85	3.63	7.9
AR-6-27-00-7-57	428.82	35.77	0.05117	1.89	0.08656	2.51	431.8	9.7	1328	±49	400	139	2.88	207.6
AR-6-27-00-7-15	-5274.55	30917.84	0.05085	2.61	0.06131	2.74	422.4	10.9	626	±61	264	58	4.53	48.3
AR-6-27-00-7-108	320.32	41.45	0.04566	2.31	0.09393	4.09	386.6	8.9	1484	±79	283	677	0.42	283.7
AR-6-27-00-7-52	-3841.90	436.25	0.09667	2.11	0.06733	2.29	792.1	16.7	824	±48	171	230	0.74	4.0
AR-6-27-00-7-85	-14693.07	123.59	0.09518	2.10	0.07465	2.82	783.6	20.8	1035	±61	186	194	0.96	32.1
AR 6-27-00-7.45	2598.63	65.73	0.08385	2.00	0.06425	2.57	670.1	14.4	735	±56	81	46	1.75	9.7
AR-6-27-00-7-70	430.09	14.84	0.11838	1.36	0.11378	2.87	960.3	18.6	1839	±55	483	77	6.24	91.6
AR-6-27-00-7-51	64.09	12.04	0.10839	4.06	0.30869	8.21	881.7	33.8	3497	±127	392	244	1.60	296.6
AR-6-27-00-7-42	2009.91	67.94	0.05303	1.70	0.05744	1.80	445.3	7.8	484	±40	833	4	207.06	8.6
AR-6-27-00-7-40	2650.16	39.00	0.04986	1.92	0.06324	1.93	419.0	8.0	692	±42	1590	572	2.78	65.2
AR-6-27-00-7-115	4182.26	280.23	0.04986	1.98	0.05642	1.90	420.4	9.0	442	±49	676	712	0.95	5.1
AR-6-27-00-7-72	-6583.40	85.96	0.11599	1.65	0.07170	1.68	943.0	20.7	954	±44	415	180	2.31	1.1
AR 6-27-00-7.39	7012.40	274.70	0.05713	2.50	0.06260	2.52	463.4	11.4	682	±55	355	229	1.55	47.2
AR-6-27-00-7-22	-3248.51	105.36	0.07536	2.10	0.06171	1.94	619.1	13.3	640	±43	332	145	2.30	3.4
AR-6-27-00-7-100	10197.80	1428.84	0.20293	1.85	0.09574	1.59	1567.2	29.0	1520	±37	184	132	1.39	-3.0
AR-6-27-00-7-88	13469.50	136.88	0.09747	2.24	0.07173	2.35	801.2	18.9	954	±52	689	36	19.04	19.1
AR-6-27-00-7-30	1051.59	59.27	0.04892	3.43	0.07710	3.47	409.7	13.8	1102	±72	754	231	3.26	168.9

Table 3: Zircon Data

Analysis_# Data	$^{206}Pb/^{204}Pb$	2%ERR	Raw Ratios: $^{206}Pb/^{238}U$	2%ERR	$^{207}Pb/^{206}Pb$	2%ERR	Age $^{206}Pb/^{238}U$	2SD	Age $^{207}Pb/^{206}Pb$	2SD	U	Th ppm	U/Th	% discordance
AR-6-27-00-7-113	2564.86	240.91	0.10176	2.05	0.06665	2.10	830.9	17.7	801	±50	219	117	1.87	-3.6
AR-6-27-00-7-10	-629.41	71.88	0.05459	2.68	0.06497	2.73	451.1	13.5	750	±60	228	73	3.13	66.3
AR-6-27-00-7-67	96.20	10.55	0.06580	2.33	0.22366	4.43	551.2	15.9	2989	±72	288	161	1.79	442.2
AR 6-27-00-7.28	3865.54	293.66	0.11670	2.08	0.06805	2.08	913.3	18.4	860	±46	72	40	1.79	-5.8
AR-6-27-00-7-26	3067.96	939.47	0.05351	3.28	0.06784	3.70	446.3	14.4	841	±79	793	318	2.49	88.3
AR 6-27-00-7.5	-5577.39	698.58	0.09156	2.20	0.06538	2.00	714.6	15.5	766	±43	292	459	0.64	7.2
AR-6-27-00-7-56	68863.93	168.84	0.09664	1.79	0.06576	1.91	792.5	15.5	775	±40	251	191	1.31	-2.3
AR-6-27-00-7-79	7223.95	1672.86	0.05563	2.36	0.06579	2.29	469.5	13.4	775	±54	420	89	4.74	65.1
AR 6-27-00-7.42	918.42	133.82	0.11446	1.96	0.07086	1.98	897.8	18.6	940	±42	107	67	1.59	4.7
AR-6-27-00-7-28	-4564.69	73.17	0.10717	2.20	0.06892	1.63	865.4	18.9	873	±44	594	520	1.14	0.9
AR-6-27-00-7-39	-5833.67	215.47	0.22569	2.89	0.11028	2.60	1710.8	43.9	1783	±48	194	76	2.55	4.2
AR 6-27-00-7.29	593.17	79.06	0.12639	2.06	0.07298	1.91	983.6	20.0	1004	±41	67	245	0.27	2.1
AR-6-27-00-7-50	-2220.92	257.52	0.08797	2.38	0.06143	2.38	724.0	16.8	630	±51	187	60	3.15	-13.0
AR 6-27-00-7.40	8749.37	381.09	0.07787	1.79	0.06217	1.70	623.7	11.1	667	±38	151	111	1.37	7.0
AR-6-27-00-7-111	-1064.87	169.89	0.08519	2.35	0.06123	2.45	702.9	16.5	621	±54	137	84	1.64	-11.7
AR-6-27-00-7-44	4431.22	103.13	0.09785	1.78	0.06684	1.54	799.4	14.1	809	±32	880	564	1.56	1.2
AR-6-27-00-7-96	53.53	12.48	0.07838	3.90	0.30658	7.53	651.4	26.3	3485	±118	1507	273	5.52	435.0
AR-6-27-00-7-114	-24835.66	551.22	0.10306	1.75	0.06780	1.46	840.8	15.8	837	±38	500	304	1.64	-0.5
AR-6-27-00-7-58	58.50	11.71	0.08127	1.90	0.32976	2.21	673.0	16.9	3598	±34	191	130	1.47	434.7
AR-6-27-00-7-3	36067.08	714.11	0.07357	2.23	0.06057	1.90	598.9	15.6	600	±46	1989	1855	1.07	0.3
AR 6-27-00-7.8	6991.74	154.40	0.34531	1.82	0.16339	1.32	2369.0	38.7	2476	±25	90	31	2.89	4.5
AR-6-27-00-7-5	2185.14	75.41	0.08318	1.93	0.06663	1.85	673.7	16.4	803	±44	622	120	5.19	19.3
AR-6-27-00-7-120	-19720.42	340.61	0.39634	1.93	0.19877	1.31	2762.5	55.2	2796	±34	146	96	1.51	1.2
AR-6-27-00-7-107	6351.99	752.17	0.12368	2.37	0.07160	1.84	998.1	22.3	950	±42	303	113	2.67	-4.8
AR-6-27-00-7-71	-9361.93	71.84	0.12693	1.61	0.07205	1.48	1025.2	21.4	963	±37	506	285	1.78	-6.0
AR-6-27-00-7-106	-2731.59	150.66	0.13094	2.21	0.07178	1.89	1052.3	23.5	955	±44	182	81	2.25	-9.3
AR-6-27-00-7-2	-2193.92	2408.28	0.07033	2.41	0.06370	2.24	573.4	15.2	709	±52	494	664	0.74	23.6
AR-6-27-00-7-7	51.39	6.79	0.07619	2.08	0.34824	2.54	620.7	16.0	3683	±44	1539	599	2.57	493.3
AR 6-27-00-7.22	2220.89	60.54	0.06565	1.83	0.06907	3.36	529.8	9.6	892	±71	314	31	10.15	68.3
AR-6-27-00-7-119	-7040.29	83.21	0.24454	2.30	0.11286	1.68	1839.0	44.1	1824	±42	781	173	4.50	-0.8
AR-6-27-00-7-8	2785.30	253.39	0.11567	1.93	0.07741	1.89	920.5	25.1	1110	±43	330	106	3.13	20.6
AR-6-27-00-7-95	143673.33	337.65	0.11135	2.99	0.07195	2.32	907.1	29.1	960	±52	673	240	2.80	5.8
AR-6-27-00-7-18	15099.23	634.87	0.07728	2.01	0.06341	1.78	632.5	12.3	699	±41	876	171	5.13	10.4
AR 6-27-00-7.49	1510.15	128.53	0.10578	1.88	0.06607	1.70	835.5	19.0	793	±38	129	184	0.70	-5.1
AR-6-27-00-7-19	8068.65	110.01	0.11475	1.97	0.07241	1.34	918.5	18.1	975	±32	1001	417	2.40	6.2
AR-6-27-00-7-27	8540.93	64.81	0.07548	1.96	0.06829	1.37	621.2	12.5	854	±35	1547	666	2.32	37.5
AR 6-27-00-7.17	-3767.29	1013.33	0.10671	1.85	0.06537	1.70	836.5	16.6	772	±39	162	191	0.85	-7.8
AR-6-27-00-7-97	3941.57	109.04	0.05111	1.92	0.06278	1.57	432.1	10.5	675	±44	1221	21	57.86	56.2
AR-6-27-00-7-1	-5133.20	1097.45	0.12596	1.69	0.07183	1.56	993.1	20.2	959	±39	312	200	1.56	-3.4
AR 6-27-00-7.14	25675.13	225.66	0.05279	1.67	0.05686	1.20	426.1	8.1	469	±31	938	279	3.36	10.1
AR-6-27-00-7-93	21165.21	445.77	0.11749	1.85	0.07252	1.45	953.7	22.3	976	±37	1142	123	9.26	2.3
AR-6-27-00-7-98	30.30	6.66	0.11563	2.29	0.53452	2.05	939.2	23.7	4322	±39	1752	723	2.42	360.2
AR-6-27-00-7-47	8437.76	575.70	0.10532	1.89	0.06925	1.55	857.3	15.9	883	±32	398	275	1.45	3.0
AR-6-27-00-7-17	59.30	16.57	0.11920	2.51	0.34529	5.58	951.1	22.7	3669	±86	1218	129	9.47	285.8
AR-6-27-00-7-21	-15540.79	128.02	0.35171	1.71	0.16195	1.09	2485.2	38.8	2457	±23	537	327	1.64	-1.1
AR-6-27-00-7-31	7011.75	57.45	0.19109	2.61	0.12714	1.73	1472.8	35.2	2039	±35	875	108	8.09	38.4
AR-6-27-00-7-49	90.90	7.90	0.06264	1.76	0.21556	3.44	523.7	9.5	2929	±56	813	291	2.80	459.4
AR 6-27-00-7.32	4346.23	27.78	0.10645	1.87	0.07295	1.29	838.0	15.5	1002	±29	733	261	2.81	19.6
AR-6-27-00-7-91	13991.90	621.99	0.04779	2.81	0.05631	2.41	405.1	11.9	438	±56	1463	12	119.41	8.1
AR 6-27-00-7.26	2760.92	43.46	0.12989	1.96	0.07121	1.29	1008.9	19.0	954	±30	236	214	1.11	-5.4
AR-6-27-00-7-110	184.74	18.99	0.27526	3.00	0.20480	5.53	2041.5	54.3	2845	±90	2278	750	3.04	39.4
AR-6-27-00-7-64	-3671.08	105.15	0.06306	1.99	0.06748	2.16	528.8	14.0	829	±48	598	51	11.70	56.7
AR-6-27-00-7-80	99.75	10.28	0.06253	1.82	0.21752	2.89	525.5	12.0	2943	±49	356	10	34.11	460.1
AR 6-27-00-7.19	20462.95	59.08	0.09567	1.52	0.06502	1.10	758.8	12.8	766	±26	1158	653	1.77	1.0
AR-6-27-00-7-69	-13148.45	407.28	0.22660	2.42	0.10953	1.69	1728.3	40.3	1770	±35	247	160	1.55	2.4
AR-6-27-00-7-61	-8115.48	161.27	0.12307	2.14	0.07245	1.65	994.5	24.2	975	±35	326	160	2.04	-2.0
AR 6-27-00-7.4	-10073.03	449.42	0.05159	1.81	0.05582	1.25	412.0	7.6	423	±29	964	50	19.11	2.7
AR 6-27-00-7.6	4673.73	37.53	0.41987	1.73	0.18485	1.11	2779.6	42.2	2682	±20	118	67	1.76	-3.5
AR-6-27-00-7-109	-4736.41	221.48	0.05499	1.85	0.05902	1.59	462.8	9.2	541	±37	442	261	1.69	16.9
AR-6-27-00-7-84	7411.31	77.39	0.36336	1.73	0.16954	1.28	2586.1	54.4	2533	±28	266	284	0.94	-2.0
AR-6-27-00-7-35	51.39	15.20	0.07109	3.59	0.30617	7.26	588.5	20.3	3484	±113	1493	413	3.62	492.1
AR-6-27-00-7-74	105.78	15.81	0.20306	3.65	0.26734	5.30	1570.1	59.4	3272	±85	1694	441	3.84	108.4
AR-6-27-00-7-45	4814.43	115.60	0.09866	2.00	0.07424	2.32	805.8	15.8	1025	±47	772	135	5.74	27.2
AR-6-27-00-7-75	4620.77	62.65	0.09511	2.09	0.06738	1.55	783.1	22.4	825	±40	1065	323	3.30	5.4
AR 6-27-00-7.12	2076.45	38.85	0.22880	1.96	0.10850	1.77	1670.8	31.3	1760	±34	269	74	3.62	5.3
AR 6-27-00-7.23	1786.07	46.81	0.08643	2.09	0.06910	1.50	688.8	14.0	893	±33	421	149	2.83	29.6
AR-6-27-00-7-87	-2760.67	321.01	0.05129	1.80	0.05734	1.72	434.0	11.8	478	±41	826	7	126.88	10.2
AR-6-27-00-7-36	95.15	13.76	0.06511	4.22	0.24555	8.24	541.4	22.0	3138	±131	486	18	27.51	479.6
AR 6-27-00-7.44	-2889.33	950.39	0.06044	2.40	0.05771	1.55	489.8	12.4	504	±37	339	193	1.76	2.9
AR-6-27-00-7-11	-210883.50	264.96	0.15622	2.53	0.09132	1.75	1217.0	32.9	1432	±36	919	321	2.87	17.7
AR 6-27-00-7.20	-7102.20	133.11	0.06102	2.54	0.05798	1.57	494.0	12.3	520	±37	490	329	1.49	5.3
AR-6-27-00-7-89	50.25	6.13	0.07489	2.19	0.33755	2.22	624.3	15.3	3633	±36	1558	733	2.13	482.0
AR 6-27-00-7.21	7538.99	77.81	0.05657	2.56	0.05830	1.52	459.1	11.6	532	±36	1211	493	2.46	15.8
AR-6-27-00-7-16	-30074.20	246.34	0.35198	2.38	0.17406	1.40	2480.6	50.3	2579	±26	935	77	12.08	3.9
AR 6-27-00-7.13	-10180.46	372.97	0.05331	2.01	0.05725	1.24	430.0	9.3	484	±30	456	4	104.42	12.5
AR 6-27-00-7.25	-9519.02	184.79	0.10710	2.29	0.06578	1.32	843.0	18.6	790	±31	280	165	1.70	-6.3
AR 6-27-00-7.50	4454.54	106.02	0.05552	2.30	0.05720	1.52	452.0	12.1	482	±37	868	766	1.13	6.7
AR-6-27-00-7-117	18421.37	554.93	0.27759	2.77	0.12955	1.53	2052.4	53.0	2070	±35	315	110	2.87	0.9
AR 6-27-00-7.41	6348.13	109.49	0.10787	2.20	0.06749	1.29	849.2	18.0	840	±29	334	196	1.71	-1.1
AR-6-27-00-7-63	6065.49	291.17	0.11790	1.89	0.07077	1.45	955.8	23.8	927	±33	417	61	6.87	-3.0
AR 6-27-00-7.9	-24172.72	227.46	0.09286	2.51	0.06320	1.47	727.7	18.0	696	±35	328	305	1.07	-4.3
AR-6-27-00-7-43	-24646.02	227.03	0.07764	2.17	0.06007	1.33	642.1	13.7	581	±29	772	122	6.35	-9.5
AR 6-27-00-7.18	7188.20	36.94	0.32417	1.91	0.14118	1.05	2275.3	41.4	2235	±22	535	165	3.25	-1.8
AR-6-27-00-7-77	-14344.30	101.50	0.31903	2.51	0.14186	1.33	2320.9	63.5	2230	±34	489	470	1.04	-3.9
AR 6-27-00-7.47	161178.10	2487.45	0.12402	2.44	0.07320	1.41	968.7	24.7	1005	±32	868	420	2.07	3.7
AR-6-27-00-7-4	100318.45	5415.29	0.27144	2.91	0.15508	1.67	1979.2	56.4	2384	±33	1614	218	7.40	20.5
AR 6-27-00-7.30	4855.99	106.41	0.13505	2.51	0.07247	1.46	1045.7	25.4	989	±32	239	106	2.26	-5.4
AR-6-27-00-7-6	158.85	9.59	0.06129	2.64	0.16105	5.97	503.7	14.5	2448	±103	1061	81	13.09	386.0
AR-6-27-00-7-14	-12722.65	68.03	0.23930	3.32	0.11378	1.83	1783.0	52.4	1841	±35	1230	1221	1.01	3.2
AR 6-27-00-7.35	-11071.49	424.23	0.14503	2.27	0.07576	1.29	1116.7	24.2	1078	±29	284	161	1.76	-3.5
AR 6-27-00-7.24	-5432.82	1093.21	0.08467	2.18	0.06165	1.23	675.4	14.4	653	±30	421	280	1.50	-3.4
AR 6-27-00-7.34	8033.56	119.35	0.13027	2.41	0.07303	1.31	1011.5	23.5	1004	±30	410	254	1.61	-0.7
AR-6-27-00-7-101	3103.64	35.85	0.11815	2.11	0.07398	1.46	957.6	20.6	1016	±37	1025	531	1.93	6.2
AR 6-27-00-7.48	16252.69	135.30	0.24519	2.71	0.21224	1.54	1792.9	48.8	2911	±27	442	147	3.01	62.3
AR-6-27-00-7-60	38490.04	528.59	0.12152	1.95	0.07260	1.23	982.3	22.5	979	±27	1117	252	4.42	-0.3
AR-6-27-00-7-54	-64422.13	113.26	0.33991	1.53	0.16040	0.98	2439.2	37.7	2440	±17	1852	581	3.19	0.1

Table 3: Zircon Data

Analysis_# Data	$^{206}Pb/^{204}Pb$	2%ERR	Raw Ratios: $^{206}Pb/^{238}U$	2%ERR	$^{207}Pb/^{206}Pb$	2%ERR	Age $^{206}Pb/^{238}U$	2SD	Age $^{207}Pb/^{206}Pb$	2SD	U	Th ppm	U/Th	% discordance
AR-6-27-00-7-25	8142.14	895.91	0.11036	5.69	0.07526	3.04	888.3	47.5	1053	±63	286	105	2.72	18.6
AR-6-27-00-7-9	9383.04	67.41	0.10231	2.21	0.06954	1.25	820.9	21.8	892	±31	2242	1515	1.48	8.7
AR-6-27-00-7-59	3395.24	36.48	0.10410	1.71	0.07521	1.37	850.3	20.7	1051	±28	1200	934	1.28	23.6
AR 6-27-00-7.36	40819.44	1217.45	0.30453	2.23	0.13538	1.11	2156.1	42.8	2159	±23	649	269	2.42	0.1
AR 6-27-00-7.46	-10653.38	84.70	0.41510	2.10	0.18666	1.08	2794.5	53.1	2701	±21	197	108	1.82	-3.3
AR-6-27-00-7-76	74.65	32.33	0.20255	8.04	0.36022	5.69	1566.8	115.9	3733	±88	52	92	0.57	138.3
AR-6-27-00-7-66	1043.94	40.82	0.08098	2.41	0.08909	2.08	671.8	19.6	1384	±42	471	38	12.36	106.0
AR 6-27-00-7.27	24889.87	51.80	0.29126	2.15	0.13054	0.99	2075.7	39.9	2097	±22	594	556	1.07	1.0
AR-6-27-00-7-65	-28110.69	473.51	0.25295	1.49	0.12283	0.99	1901.1	39.8	1977	±22	1256	88	14.23	4.0
AR-6-27-00-7-32	126.04	16.73	0.12846	2.30	0.16975	7.25	1026.4	21.9	2536	±122	1046	380	2.75	147.1
AR 6-27-00-7.43	36717.74	145.46	0.17102	2.62	0.08153	1.19	1299.3	33.2	1221	±26	468	237	1.98	-6.0
AR 6-27-00-7.11	38036.57	419.05	0.27600	1.96	0.15375	0.80	1966.5	36.0	2374	±17	647	672	0.96	20.7
AR-6-27-00-7-112	45.69	3.98	0.12495	2.77	0.39333	3.14	1006.3	27.5	3865	±48	1024	193	5.29	284.1
AR-6-27-00-7-116	5683.35	121.12	0.25725	4.97	0.15464	1.53	1922.5	84.1	2377	±32	298	80	3.71	23.6
AR-6-27-00-7-23	58.14	19.07	0.07589	5.24	0.27671	10.24	623.4	31.3	3327	±161	343	137	2.50	433.7
AR 6-27-00-7.37	-165131.62	1017.05	0.12799	3.60	0.08819	1.25	995.3	33.8	1376	±27	377	85	4.42	38.2
AR-6-27-00-7-83	50.67	19.79	0.11196	10.67	0.42532	5.86	912.6	92.1	3983	±89	586	20	29.77	336.5
AR-6-27-00-7-12	62.74	10.23	0.07514	6.05	0.33067	8.38	614.2	36.2	3603	±129	393	142	2.76	486.6
AR-6-27-00-7-99	83.85	17.86	0.22426	12.25	0.30708	11.67	1712.0	184.9	3488	±182	1413	259	5.46	103.7
AR-6-27-00-7-81	80.07	18.76	0.06460	5.30	0.22665	10.17	542.2	28.7	3009	±164	1412	429	3.29	455.0
AR-4-28-00-11a														
AR-4-28-00-11a-9	-3188.8159	91.942941	0.0284901	2.0384333	0.0480951	2.7781461	211.4648	4.635352	135.4537	94.68534	393.583	104.925	3.75107	-35.945044
AR-4-28-00-11a-73	6408.3606	181.70529	0.0271636	1.917989	0.0489449	2.2864182	199.4247	3.839201	165.364	72.39144	754.454	441.543	1.70868	-17.079473
AR-4-28-00-11a-57	-798.58775	128.37275	0.0293959	2.7496439	0.0495339	2.9839042	216.1845	6.952881	196.1199	74.06108	367.723	191.192	1.92332	-9.2812591
AR-4-28-00-11a-67	-1942.0901	142.43069	0.0309611	2.760169	0.0498649	2.3791087	227.0778	7.88913	209.3859	56.84284	535.079	313.16	1.70864	-7.7911192
AR-4-28-00-11a-91	-8022.8604	342.68395	0.0281785	2.1072752	0.0494639	1.8136649	206.1029	4.746216	190.6282	50.31679	1091.7	991.971	1.10053	-7.5082313
AR-4-28-00-11a-78	-6909.27	2658.7276	0.0286504	2.1565339	0.0496106	2.391882	210.0116	4.589441	196.6885	85.31925	583.13	188.982	3.08564	-6.3440102
AR-4-28-00-11a-33	-444.27707	131.37523	0.0312175	2.3600688	0.0498344	2.5167535	230.269	6.878866	217.6161	60.8047	388.968	48.3892	8.03833	-5.4948022
AR-4-28-00-11a-26	-1105.609746	332.5139815	0.02819397	1.892390465	0.04958319	3.170806477	208.635324	6.33718204	208.12994	74.863496	360.53413	149.04999	2.4188806	-0.2422329
AR-4-28-00-11a-24	-2087.713425	138.4246891	0.02759801	1.743888418	0.04948855	1.61233356	204.375505	6.03131008	204.074732	39.9846789	1016.6231	827.57295	1.2284393	-0.147167058
AR-4-28-00-11a-55	23226.85691	110.3856916	0.027011	1.889856725	0.04960508	2.277405862	199.006875	4.75815818	200.204115	56.6493944	607.39749	103.4123	5.8735515	0.601607325
AR-4-28-00-11a-66	12288.89589	350.462063	0.0283119	1.827949731	0.04986061	1.927864501	207.977139	5.86921267	209.266873	46.7620355	761.28452	543.89536	1.3996893	0.620132348
AR-4-28-00-11a-90	-2557.404535	316.3930324	0.02869484	1.96959523	0.04996336	1.809010243	209.922266	4.5783126	213.649836	50.0153349	757.73507	389.16366	1.9470859	1.775690806
AR-4-28-00-11a-25	5643.318067	701.0087626	0.0289346	1.879615063	0.0497973	2.331405518	214.089243	6.4836496	218.403004	55.7632444	661.23709	383.85012	1.7226439	2.014935975
AR-4-28-00-11a-19	-2395.919304	269.7250448	0.02776296	1.673584157	0.04968942	1.851994449	205.797002	3.88427377	213.823602	52.5156511	875.56869	757.59968	1.1557142	3.900251317
AR-4-28-00-11a-71	4006.615142	772.0000239	0.03019991	2.809095458	0.05042479	1.887537658	221.380211	6.32170531	234.613218	65.3508962	883.24974	341.79196	2.5841735	5.977501895
AR-4-28-00-11a-99	-3818.947852	3611.094434	0.02903207	2.113824815	0.05018728	2.420740873	212.209338	5.36791611	225.025742	61.3031998	614.45741	133.17723	4.6138323	6.039509849
AR-4-28-00-11a-43	-4324.432417	16336.15869	0.02776521	1.514422905	0.04990547	1.872242862	204.866568	4.06311591	217.749035	47.1885573	763.63181	500.42755	1.5259588	6.288223033
AR-4-28-00-11a-77	8265.80252	512.6803484	0.02800768	2.158657554	0.05010918	1.888002757	205.398617	4.49439788	219.885799	77.8681618	848.97951	526.46596	1.6126009	7.053203132
AR-4-28-00-11a-113	-2992.334102	211.5212888	0.02920142	2.155886255	0.05023634	2.341131938	212.810997	4.70987616	228.847705	55.7469014	486.01414	246.92915	1.9682331	7.535657572
AR-4-28-00-11a-59	-6933.80369	843.2975719	0.02728163	1.905831873	0.04996823	2.710334146	200.839078	5.14399929	216.097526	65.1389407	590.25477	366.74275	1.6094518	7.597350015
AR-4-28-00-11a-13	-16164.22583	97.50527356	0.02746739	1.929782189	0.04984924	2.945735983	203.797805	4.41130966	220.75602	75.9010885	641.83533	268.54349	2.390061	8.321097669
AR-4-28-00-11a-115	-1885.511802	342.793641	0.02890376	2.000583661	0.05023388	2.545708195	210.634514	4.35560888	228.730846	60.3438148	496.40061	213.84778	2.3212802	8.591342223
AR-4-28-00-11a-88	2452.546982	448.5044814	0.02880764	2.436779271	0.05031603	2.295187041	210.781549	5.78611504	229.801186	63.5075869	446.85535	199.66555	2.2380193	9.023388073
AR-4-28-00-11a-96	3428.396973	103.7994069	0.02794419	1.986833041	0.05014685	1.701122005	204.447156	4.2546066	222.923914	51.0889349	1184.3429	1299.8049	0.9111698	9.037424739
AR-4-28-00-11a-72	-7371.743537	277.8037193	0.02810456	2.013427714	0.05021789	1.94435728	206.242877	4.15858774	225.075743	65.984671	829.5213	894.84323	0.9270018	9.131401542
AR-4-28-00-11a-79	5603.041058	350.349299	0.02900258	2.423834362	0.05037696	2.449860015	212.530948	5.26667249	232.188848	72.9629677	716.82004	476.49792	1.5043508	9.249429446
AR-4-28-00-11a-37	5313.201023	228.1110473	0.02881103	1.806288772	0.05019384	1.804991011	212.681652	6.16507362	233.134584	46.1179582	733.11729	554.00898	1.323295	9.616688863
AR-4-28-00-11a-51	3618.472696	378.816816	0.02739119	2.297271495	0.05007339	2.645456998	201.843145	4.72495661	222.646888	63.2650196	768.30634	684.08761	1.123111	10.30688627
AR-4-28-00-11a-23	-1355.731841	103.3711094	0.02692799	1.879079723	0.04986963	1.831119862	199.51058	6.04829498	221.925901	44.6257868	780.57282	744.69647	1.0481758	11.23515383
AR-4-28-00-11a-61	19015.15247	351.5863223	0.02776333	1.856247071	0.05023352	2.209508711	204.175981	5.15555654	227.348045	53.9456899	731.99765	381.90802	1.9166857	11.34906434
AR-4-28-00-11a-102	-6242.272862	771.8449952	0.02842174	2.35090181	0.05032705	2.035068616	207.60979	5.40191431	232.197753	51.0900646	865.87439	557.41134	1.553385	11.8433543
AR-4-28-00-11a-18	2020.630241	238.1741623	0.02817605	1.744624956	0.05011848	2.203342959	208.831876	4.48276895	233.677599	66.3858676	793.67417	610.64428	1.2997324	11.89747621
AR-4-28-00-11a-31	-1220.027283	438.8895592	0.03053553	2.762248436	0.05060665	2.528663723	225.366036	7.66299923	253.415272	58.9925453	616.36264	53.022472	11.624555	12.4460798
AR-4-28-00-11a-65	8769.419627	983.9305204	0.02911768	2.020999956	0.05053326	2.27477309	213.865233	6.29925848	240.531994	54.1913884	541.76842	245.42067	2.2075093	12.46895567
AR-4-28-00-11a-95	-10835.68507	572.7025723	0.02910776	1.84298517	0.05058794	2.01645491	212.887048	4.14604464	242.91538	56.6886975	799.41161	758.5551	1.053861	14.10528806
AR-4-28-00-11a-110	-2056.351115	124.7814719	0.02825684	2.11385845	0.0503846	1.830908452	206.178631	4.83798019	235.501543	45.8306665	840.90766	560.43189	1.5004636	14.22209095
AR-4-28-00-11a-20	48962.93281	164.4992814	0.02687535	1.764639716	0.04999114	1.989359915	199.299887	3.74542944	227.841498	51.8887186	875.6555	647.05372	1.3532964	14.32093699
AR-4-28-00-11a-94	-4639.309775	181.48581	0.03033028	2.38486951	0.05083197	2.508745972	221.699378	5.4295128	253.920057	66.1733001	481.31153	124.94718	3.8521199	14.53349983
AR-4-28-00-11a-54	-2534.5757	94.28571016	0.02643235	1.906452888	0.05014529	1.920449957	194.82512	4.68451061	225.450931	48.7763324	1172.2142	1178.4706	0.9946911	15.71964155
AR-4-28-00-11a-69	756.7555919	221.8921407	0.02891408	2.213974645	0.05072041	3.06008173	212.248433	4.87687574	248.464553	71.6792252	322.99865	118.18252	2.7330492	17.06307987
AR-4-28-00-11a-80	-8861.834817	247.2160589	0.02699586	2.467045688	0.05039844	2.533489132	198.030646	5.21277673	233.171611	70.4981803	899.07112	631.70149	1.4232531	17.7452156
AR-4-28-00-11a-14	24630.54361	160.107232	0.0275446	2.145945485	0.05028153	2.414658027	204.343458	4.8090212	240.791761	64.8583494	680.23431	304.57482	2.2333898	17.83678488
AR-4-28-00-11a-6	-4203.252273	334.7629662	0.02722575	2.347724489	0.05040151	2.283024854	202.290537	4.80996368	243.506905	89.003207	807.21014	258.4419	3.1233718	20.37483749
AR-4-28-00-11a-97	14308.43543	810.5894715	0.02830544	2.109201623	0.0507377	2.045808147	207.023969	4.69899707	250.032544	52.2759543	788.15962	443.95928	1.7752971	20.77468412
AR-4-28-00-11a-30	-1122.079149	207.4912438	0.03162193	2.465811543	0.05122208	3.019959361	233.412054	7.40048422	282.297208	69.792577	470.39159	194.49189	2.4185666	20.94371461
AR-4-28-00-11a-120	-311.0286629	1223.593937	0.03101823	2.598715336	0.05123767	3.889704586	225.622298	6.17839211	274.037546	89.4184738	207.92254	86.736036	2.3971875	21.45853859
AR-4-28-00-11a-10	-653.2456414	115.6462159	0.02707746	1.915113161	0.05042824	2.676466599	201.119532	4.15093215	245.923181	77.9460304	333.1671	32.490537	10.254281	22.27712489
AR-4-28-00-11a-89	-1576.882408	439.6739762	0.02920364	2.180999355	0.05103847	3.386704186	213.607055	5.27533162	262.688369	82.7795796	267.29571	22.253941	12.011163	22.97738442
AR-4-28-00-11a-1	-1143.702846	2644.228573	0.03104941	2.289910501	0.05135876	3.763731835	230.385717	5.26119951	283.48676	103.572507	193.5528	64.28475	3.0108665	23.0487565
AR-4-28-00-11a-27	1554.553205	78.50739574	0.02871976	1.628464165	0.05076099	2.895897026	212.427762	6.70499642	262.113642	67.4900756	256.01441	62.837714	4.0742159	23.389542
AR-4-28-00-11a-63	1692.829408	409.8444986	0.02606263	2.036919528	0.05045201	2.221025485	191.809536	5.67959228	237.109218	53.0263018	831.24918	578.33005	1.4373266	23.61701277
AR-4-28-00-11a-81	1384.931429	129.8502335	0.02708967	1.626356467	0.05068979	1.911357494	198.592886	3.62755138	246.524148	57.072026	913.47776	586.12387	1.5585063	24.13543739
AR-4-28-00-11a-28	-1141.018454	188.4625076	0.02778291	1.76699309	0.05064233	2.677884292	205.577097	6.63884262	256.555371	62.6264192	437.17797	282.89708	1.5453605	24.79764251
AR-4-28-00-11a-53	-6570.093725	673.9429786	0.02660535	1.653771516	0.05057592	1.80519346	196.102357	4.34428379	245.36487	46.1976869	799.22138	670.37264	1.1922046	25.12081683
AR-4-28-00-11a-68	-1283.674606	71.7268548	0.02817973	1.856260511	0.05096448	1.991534104	206.982522	4.46570601	259.644539	46.8118266	842.87104	541.48552	1.5565902	25.44273644
AR-4-28-00-11a-5	-1252.109862	151.1208782	0.02750785	1.901867285	0.05074619	2.433394507	204.41258	3.94122021	258.197058	78.862498	520.22049	226.30147	2.2987941	26.31172595
AR-4-28-00-11a-82	954.2224637	92.68974633	0.02938174	2.556308442	0.0513583	2.635953682	215.098879	5.74016338	276.632747	67.5822128	678.52735	566.98264	1.1967339	28.60724731
AR-4-28-00-11a-47	48101.55705	2748.052674	0.02889162	2.255072232	0.05119521	1.80676493	212.902126	5.41259584	275.225703	45.1244484	2073.2264	319.98479	6.4791404	29.27334669
AR-4-28-00-11a-29	1742.094682	86.55538981	0.02749157	1.536832927	0.05078917	2.24134594	203.421483	5.82831056	262.990234	52.6713171	535.59836	272.79212	1.9633938	29.28341172
AR-4-28-00-11a-114	-2740.268782	415.6051828	0.02941543	2.122545548	0.05132026	2.44704528	214.322451	4.67558647	277.943094	57.6101821	639.81035	527.91249	1.2119629	29.68454426
AR-4-28-00-11a-7	967.70702	154.10937	0.0265441	2.1781177	0.0506871	2.3823132	197.2819	4.502641	256.826	78.60009	863.588	578.505	1.49279	30.1822427
AR-4-28-00-11a-49	-4815.2452	213.74277	0.0264597	1.9072057	0.0507388	2.0776218	195.1932	3.931751	254.1266	52.00652	912.668	636.547	1.43378	30.1922871
AR-4-28-00-11a-105	48652.933	103.34845	0.0268738	2.5377953	0.0508454	1.5104743	196.3872	5.393505	256.0897	39.99895	2957.02	431.305	6.85599	30.4004293
AR-4-28-00-11a-32	-4643.789	88.087219	0.0274047	1.7149369	0.0508625	2.6026616	202.6001	5.283138	264.8448	60.63445	519.513	526.004	0.98766	30.7229128
AR-4-28-00-11a-11	-24689.144	111.3913	0.0257143	1.8166848	0.0505502	1.5356716	191.0161	3.776987	252.7366	59.31655	1693.72	1592.81	1.06335	32.3116976
AR-4-28-00-11a-60	-16976.756	2125.6421	0.0264541	1.9014266	0.050897	1.9829762	194.8136	4.985801	258.3947	48.74595	754.123	485.619	1.55291	32.636902
AR-4-28-00-11a-83	-1099.8304	89.009622	0.0293717	1.9988145	0.0516223	2.9008405	215.0072	4.777308	288.3851	72.03123	578.917	323.06	1.79198	34.1280819
AR-4-28-00-11a-44	36191.22	384.99261	0.0275906	2.151707	0.0511448	1.689279	203.5755	4.9995	274.0179	42.6786	959.753	852.663	1.12559	34.602588
AR-4-28-00-11a-74	2300.1842	1268.4163	0.0305756	2.1390714	0.0519217	2.1129539	224.0194	4.782969	301.6029	67.75721	780.736	505.857	1.54339	34.6324984
AR-4-28-00-11a-3	2073.7501	217.34666	0.0272437	1.653335	0.0510887	2.4627784	202.5185	3.400608	272.8917	73.95017	483.587	212.172	2.27922	34.7490116
AR-4-28-00-11a-93	-324775.78	330.0591	0.0255136	2.2112594	0.0507993	2.4317816	186.856	4.258738	252.3745	62.63452	1720.49	563.174	3.05499	35.063611

Table 3: Zircon Data

Analysis_# Data	$^{206}Pb/^{204}Pb$	2%ERR	Raw Ratios: $^{206}Pb/^{238}U$	2%ERR	$^{207}Pb/^{206}Pb$	2%ERR	Age $^{206}Pb/^{238}U$	2SD	Age $^{207}Pb/^{206}Pb$	2SD	U	Th ppm	U/Th	% discordance
AR-4-28-00-11a-22	4218.0401	322.74686	0.0283263	1.839926	0.0512272	1.8520285	209.7412	4.223132	283.813	45.40941	755.399	484.653	1.55864	35.315795
AR-4-28-00-11a-75	13195.723	410.35598	0.0277893	1.988181	0.0513769	2.1642764	203.9019	4.062341	277.4712	68.89164	727.804	536.529	1.3565	36.0807148
AR-4-28-00-11a-92	-596.39781	69.019971	0.0288021	2.170907	0.0516295	3.2628885	210.5713	4.966497	289.4744	79.27033	289.476	104.297	2.77549	37.4709832
AR-4-28-00-11a-70	32423.396	236.02847	0.0289457	1.9396048	0.0517141	1.92118	212.4564	4.338565	292.883	65.18242	536.81	260.749	2.05873	37.8555575
AR-4-28-00-11a-116	-1015.7892	109.15773	0.0274349	2.0263325	0.0513661	2.0648022	200.0336	4.188001	279.9305	49.12284	1098.85	854.416	1.28608	39.9417045
AR-4-28-00-11a-21	938.50545	71.279056	0.0268135	1.7515963	0.0511127	1.960517	198.7288	3.711273	278.7428	50.82963	785.972	378.618	2.0759	40.2628884
AR-4-28-00-11a-117	-1949.5018	232.02201	0.0296198	2.0520948	0.0519092	2.6052574	215.6812	4.625631	303.922	59.59509	333.062	141.77	2.34931	40.9126169
AR-4-28-00-11a-52	3012.137	316.46473	0.0270249	2.0081184	0.051429	2.0540987	199.1666	4.173224	283.9178	48.62823	753.766	445.547	1.69178	42.552884
AR-4-28-00-11a-84	830.69064	66.063611	0.0276449	1.9789466	0.0516352	2.3404888	202.5368	4.469544	288.996	60.44591	714.92	461.363	1.54958	42.688191
AR-4-28-00-11a-109	-2709.2202	130.49965	0.0281704	2.3318886	0.0518069	2.8955454	205.5806	5.52932	299.3181	69.40135	492.071	276.291	1.78099	45.5965001
AR-4-28-00-11a-17	-30246.845	265.13332	0.0270849	2.14824	0.0515548	2.1344453	200.8879	4.733032	298.4786	58.79389	824.844	589.532	1.39915	48.5796599
AR-4-28-00-11a-16	-3744.9627	149.78381	0.0258099	1.7547625	0.0513076	2.2257963	191.5886	3.864248	287.4578	60.65073	878.962	427.936	2.05396	50.0391064
AR-4-28-00-11a-62	-1643.8709	151.4801	0.0280574	1.9418044	0.0523595	2.9357488	206.279	5.366268	322.1694	68.19017	361.23	86.9979	4.15217	56.1813904
AR-4-28-00-11a-8	-2274.4258	194.06276	0.0272156	2.2265526	0.0521241	3.278761	202.1715	5.187889	321.0464	121.0685	551.22	184.063	2.99474	58.7990436
AR-4-28-00-11a-42	1111.2901	173.28081	0.0278843	1.8446052	0.0525582	2.5505659	205.7523	4.620399	336.5461	60.34695	388.714	120.75	3.21916	63.5685292
AR-4-28-00-11a-38	-846.73076	420.54918	0.0287967	1.8339015	0.0532099	3.0246137	212.5561	5.142683	366.0356	71.11879	327.159	88.8964	3.68023	72.206588
AR-4-28-00-11a-103	-1185.1058	116.52787	0.0252978	2.1439935	0.052539	1.769935	185.0782	4.44459	330.7533	44.67147	1251.66	1117.73	1.11982	78.7100472
AR-4-28-00-11a-106	3027.0171	63.392039	0.0289777	1.841311	0.0536404	2.4636156	211.4456	4.52421	377.9427	58.72216	758.682	389.136	1.94966	78.7423303
AR-4-28-00-11a-64	2149.322	729.32859	0.0285128	2.0376935	0.053673	2.2254105	209.5165	6.196517	377.8866	51.8044	987.018	918.696	1.07437	80.3612789
AR-4-28-00-11a-58	-1520.8477	568.9873	0.0290334	2.0897996	0.0543935	2.6343705	213.5432	6.850576	409.317	63.57212	621.52	456.523	1.36142	91.6787361
AR-4-28-00-11a-76	676.22905	136.45085	0.0287604	2.1886724	0.0543639	5.4810281	210.8492	4.6077	405.3424	131.3089	434.887	178.365	2.43819	92.2428132
AR-4-28-00-11a-118	781.70669	57.785666	0.0296779	2.2338841	0.0546639	2.0366747	216.0768	5.207172	420.5171	46.01549	825.544	261.394	3.15824	94.6147056
AR-4-28-00-11a-50	-1231.8459	90.351595	0.0264496	1.7218267	0.0538066	2.5711419	195.102	3.512675	387.3457	59.81709	648.627	457.234	1.41859	98.5349155
AR-4-28-00-11a-36	1956.8761	122.91623	0.0281332	2.1513573	0.0546664	1.9529323	207.7765	5.892682	426.9361	46.6714	1173.61	990.834	1.18447	105.478553
AR-4-28-00-11a-108	-14339.093	51.965848	0.0289589	1.366077	0.0554238	2.4047796	211.2661	4.105723	451.138	57.29645	607.672	411.004	1.4785	113.540116
AR-4-28-00-11a-56	7703.9497	332.48633	0.026247	2.1017515	0.0547284	2.5128512	193.3991	4.946808	423.3869	59.3714	825.254	521.975	1.58102	118.918801
AR-4-28-00-11a-39	4076.4052	106.98284	0.028194	2.1023742	0.0555643	2.3379269	208.1568	5.460297	462.6055	55.5092	725.042	245.9	2.94852	122.238914
AR-4-28-00-11a-112	-1950.6111	22016.324	0.0287332	1.7168711	0.0561388	3.1416642	209.4738	3.702989	479.7598	70.29789	391.994	184.099	2.12926	129.030976
AR-4-28-00-11a-85	1547.2788	94.765553	0.0293468	2.5915302	0.05796	3.8026402	214.7765	5.908893	547.1193	87.32214	760.316	481.886	1.57779	154.738923
AR-4-28-00-11a-45	-1947.889	937.40531	0.0277277	2.180881	0.0579944	3.8832335	204.5529	5.073873	554.7574	86.43105	341.587	325.166	1.0505	171.204808
AR-4-28-00-11a-107	1169.0594	49.161891	0.0279794	1.7805488	0.0586031	2.5591078	204.257	4.270064	573.6535	58.73814	716.393	344.98	2.07662	180.84891
AR-4-28-00-11a-111	955.15549	41.460544	0.0294862	1.619838	0.0599574	2.4177828	214.8928	3.935095	623.397	53.8779	1073.27	1002.53	1.07056	190.096726
AR-4-28-00-11a-87	2992.2337	236.90802	0.0292729	2.2147235	0.0600619	6.5409325	214.1509	5.165308	624.5963	143.5174	675.051	421.275	1.6024	191.661799
AR-4-28-00-11a-101	1435.2517	128.15175	0.0282414	1.6092756	0.0606352	3.2206134	206.3373	4.006829	646.7747	71.49666	341.189	320.494	1.06457	213.455009
AR-4-28-00-11a-104	363.59072	29.840182	0.0304358	1.8660211	0.1044604	2.4336658	221.9973	4.79178	1722.559	47.43725	339.403	104.671	3.24259	675.936821
AR-4-27-00-9														
AR-4-27-00-9-70	62.856786	89.171182	0.0395283	1.8251684	0.0522542	1.8575604	300.28	5.747814	279.8503	43.4771	524.588	281.519	1.86342	-6.803549
AR-4-27-00-9-86	45.78791498	362.1908814	0.02808281	2.031039629	0.05159207	2.63611055	210.880325	4.73173696	249.617655	62.6566805	508.75051	226.67614	2.2443937	18.36934288
NPM-4D-86-1.18	58.26597768	190.5135821	0.02717197	1.906124216	0.051598	2.004730804	212.763478	6.55982923	258.494897	52.4345446	675.61575	173.03777	3.904441	21.49401753
AR-4-27-00-9-73	101.1709779	66.40295036	0.02809023	2.344702411	0.05179205	2.218077871	213.948194	5.15781964	258.755627	52.1770385	1101.4089	552.10386	1.9949306	20.94312326
AR-4-27-00-9-104	66.59234443	1075.127879	0.03300401	1.563740285	0.05176862	1.956468996	241.517792	4.23970375	263.511474	47.4116907	626.84678	485.56503	1.2909636	9.106443562
NPM-4D-86-1.30	92.30367627	307.3039465	0.03227299	2.072805464	0.05295357	2.197825378	251.759241	5.64131009	319.260558	54.5809554	911.45281	416.30659	2.1893788	26.8118527
NPM-4D-86-1.16	70.15767579	348.2572941	0.03379737	1.832760656	0.05340783	2.154098004	263.580833	6.67007603	336.822306	55.1464527	677.19885	271.29379	2.4961826	27.78710143
AR-4-27-00-9-82	103.7155052	350.6569989	0.03781592	1.739509974	0.05309225	1.696281472	283.614083	6.02823327	314.915168	42.2238181	864.23716	376.99076	2.2924624	11.03650576
NPM-4D-86-1.2	24.9978623	118.8136658	0.03785867	1.933725353	0.05291449	3.073846124	293.584481	5.85356508	305.803176	71.2762598	210.00187	163.08234	1.2877045	4.161900906
NPM-4D-86-1.52	103.1142225	324.6729906	0.03878721	1.740766093	0.05362577	1.628021565	298.55374	5.59068915	343.207425	39.1312469	838.9459	350.21755	2.3954993	14.95666579
NPM-4D-86-1.23	62.6723156	3615.622777	0.04074439	1.780576663	0.05493358	1.797140656	316.44988	7.83515608	401.715142	45.3231697	503.78337	328.79326	1.5322193	26.94431815
NPM-4D-86-1.38	85.73844898	121.2331486	0.04202089	1.533969176	0.0551504	1.907001581	324.999275	5.35658707	409.772522	43.1837846	675.64418	277.67399	2.4332282	26.08413434
NPM-4D-86-1.20	47.89126047	107.1822997	0.04243042	1.855283309	0.0545161	2.418516732	329.242466	8.03086622	383.781594	57.7557722	344.65094	145.73655	2.3648903	16.56503457
NPM-4D-86-1.22	270.9320347	1983.749578	0.04392362	2.316983436	0.05592163	1.331421849	340.510236	9.7213112	441.432089	36.2084759	1987.1908	1392.3647	1.4272057	29.63841972
AR-4-27-00-9-102	41.79723412	130.9952335	0.05216124	2.301611311	0.05484474	2.427000292	378.282152	9.35941118	393.827416	56.3974637	243.64416	183.66741	1.3265509	4.109436229
NPM-4D-86-1.8	198.9942975	163.7968705	0.05179857	2.008485949	0.05689823	1.457734977	399.249793	9.46194081	474.661768	44.9311648	1278.7278	536.15279	2.3850064	18.88841931
AR-4-27-00-9-76	199.0161149	395.987972	0.05420081	2.053105848	0.05642878	1.336017543	405.331298	8.53947707	452.031718	31.5747514	1153.6714	595.69763	1.9366727	11.52154306
NPM-4D-86-1.41	38.03311061	227.1428642	0.05304106	1.579444679	0.05699542	2.61884376	406.945439	6.56038601	482.065924	58.909206	223.01981	136.36087	1.6355118	18.45959637
NPM-4D-86-1.37	290.9088372	120.5152458	0.05305495	1.573193265	0.05650019	1.305647468	407.766278	6.68600815	463.701435	29.4024452	1802.0846	978.41766	1.8418358	13.71745532
NPM-4D-86-1.15	45.84505391	73.46919652	0.05293805	1.812457013	0.05507125	2.358597272	408.151558	10.15753	405.203583	58.5758797	293.75695	145.73628	2.0156749	-0.72227479
NPM-4D-86-1.43	167.7687696	181.2226202	0.05375992	1.641509697	0.0566544	1.427927398	412.093517	6.96145067	468.540004	34.5533418	980.88473	605.09617	1.6210394	13.69749461
NPM-4D-86-1.39	74.97621518	152.2885878	0.05408433	1.797697965	0.05554572	2.000065892	415.270145	7.66075505	425.621667	46.1783821	448.81908	182.68958	2.4567306	2.492720038
NPM-4D-86-1.10	39.69971455	99.14213661	0.05406125	1.580913871	0.05754021	2.262266683	416.224707	8.2755319	500.035353	56.1061683	231.34093	199.0903	1.16199	20.13591345
NPM-4D-86-1.59	136.6055173	107.6795672	0.05493667	1.717958515	0.05679846	1.436402501	417.501492	8.64843825	470.382872	32.9998583	814.51446	555.86167	1.4653186	12.66615358
NPM-4D-86-1.11	171.922298	265.0134047	0.05516598	2.044176502	0.05817048	1.380633957	424.6745	9.97834837	525.60553	39.706924	1002.2278	480.04979	2.0877579	23.76668017
NPM-4D-86-1.58	97.85019747	85.54031219	0.05591997	1.904949162	0.05782218	1.81972212	424.902131	9.12481311	509.945847	40.4032241	538.03481	253.47359	2.1226464	20.01489505
NPM-4D-86-1.54	163.1105157	554.1236644	0.05579691	1.77431994	0.0564248	1.422783599	424.956463	7.9961028	456.892703	34.085541	909.51075	674.82527	1.3477722	7.515179247
AR-4-27-00-9-114	72.01088707	114.3897305	0.05996133	1.668121771	0.05686272	1.88163352	425.508893	7.94580155	482.73105	44.6830837	392.12226	199.52685	1.9652606	13.44793455
AR-4-27-00-9-72	101.9595827	108.2155185	0.05694483	1.921041822	0.05731237	1.558497232	426.795885	8.38841859	486.851776	35.315123	572.87645	463.39735	1.2362532	14.07133804
NPM-4D-86-1.56	81.61183416	935.9271275	0.05652608	1.995608045	0.05557008	1.484607184	429.68352	8.92945811	422.265583	35.572805	460.2246	320.90655	1.434139	-1.726372056
NPM-4D-86-1.55	108.3853759	209.8805889	0.05705922	1.661661866	0.05742019	1.406021645	434.109467	7.73341283	495.409888	33.5182319	620.63509	461.06463	1.3460913	14.12095935
NPM-4D-86-1.14	28.48741107	260.4302887	0.05648898	1.982393734	0.05665836	2.654587955	434.603394	11.3092509	468.246146	63.90787	159.20596	90.037947	1.7682095	7.741023628
AR-4-27-00-9-99	68.26010414	1523.360057	0.06023836	1.54563006	0.0554936	1.909775181	437.696424	8.1928279	417.937084	45.5773693	352.42775	536.14623	0.6573351	-4.514393922
NPM-4D-86-1.36	167.7322976	532.5214869	0.05731095	1.905934206	0.056318	1.490091623	439.463654	9.142506	456.632196	34.1445273	918.42505	535.82669	1.7140338	3.906703667
AR-4-27-00-9-90	121.4876343	91.56927049	0.05996629	2.090369439	0.05871053	2.399201642	440.875003	9.24940257	539.864916	54.8494564	596.22646	689.62877	0.8645615	22.45305629
NPM-4D-86-1.28	91.54278503	90.87321683	0.05768707	2.162276573	0.05870526	1.605850651	443.399788	11.0769485	548.919833	47.2267342	526.64726	256.51832	2.0530591	23.79794656
NPM-4D-86-1.12	110.1817627	285.9085384	0.05797212	1.777488903	0.0574307	1.415785634	445.575834	10.8759482	497.707748	40.0370114	610.56345	341.47626	1.7880114	11.69989719
AR-4-27-00-9-77	129.485197	349.0223902	0.06015094	1.698199563	0.05578544	1.764066394	448.024607	8.24897238	426.467489	41.5283788	656.1257	199.91396	3.2820404	-4.811592343
AR-4-27-00-9-100	100.5582267	419.9748654	0.06176759	1.633809899	0.05701919	1.496450581	448.083032	8.20909873	478.435255	35.5342621	508.34917	553.54087	0.9183589	6.773794457
AR-4-27-00-9-98	31.36035875	749.1782899	0.06186011	2.032728361	0.05673124	2.919104183	449.432724	10.0617569	466.758191	66.090999	160.32312	115.5135	1.3879167	3.854963193
AR-4-27-00-9-120	66.91221349	212.7786341	0.06527174	2.201700154	0.05938803	2.054179942	457.902243	10.2720024	583.20148	50.8404529	316.15082	292.32573	1.0815019	27.36375271
AR-4-27-00-9-120	66.91221349	212.7786341	0.06527174	2.201700154	0.05938803	2.054179942	457.902243	10.2720024	583.20148	50.8404529	316.15082	292.32573	1.0815019	27.36375271
AR-4-27-00-9-69	77.9678652	61.56634716	0.06128227	1.780249002	0.0565828	1.538627463	459.988069	8.69472619	459.236881	34.8967592	428.54379	202.30981	2.1182551	-0.163305967
AR-4-27-00-9-92	87.53545732	338.1745352	0.06310542	2.147308425	0.05805637	1.894040223	461.037131	9.94551204	516.106641	44.9769987	453.41573	271.69562	1.6688371	11.94470155
AR-4-27-00-9-119	177.9294958	110.1447317	0.0669828	1.716718322	0.05769367	1.370797698	469.995627	8.48004485	519.299841	38.9078567	862.778	851.29192	1.0134925	10.49035585
AR-4-27-00-9-119	177.9294958	110.1447317	0.0669828	1.716718322	0.05769367	1.370797698	469.995627	8.48004485	519.299841	38.9078567	862.778	851.29192	1.0134925	10.49035585
AR-4-27-00-9-118	54.43528237	91.49866136	0.09022989	1.746785904	0.06214832	1.776192824	626.027898	11.3261765	679.720069	44.9103298	194.94083	58.370854	3.3396947	8.576641825
AR-4-27-00-9-118	54.43528237	91.49866136	0.09022989	1.746785904	0.06214832	1.776192824	626.027898	11.3261765	679.720069	44.9103298	194.94083	58.370854	3.3396947	8.576641825
NPM-4D-86-1.31	153.2413013	32463.57003	0.08557079	2.953802343	0.06711289	1.664301746	646.378153	19.1043121	834.034826	40.1211995	578.32596	313.85682	1.8426426	29.03202589
AR-4-27-00-9-112	155.6217191	103.2950511	0.09734184	2.730802089	0.06381379	1.425999772	678.682889	19.0727083	730.940159	34.5938811	504.73199	108.80572	4.6388368	7.699806564
NPM-4D-86-1.35	200.2306847	41.80017401	0.09380064	2.682529671	0.06812185	2.526487463	704.845772	19.1135125	864.79705	52.9998466	790.36526	350.31949	2.256127	22.69308881
AR-4-27-00-9-115	25.09545749	165.2733609	0.1047505	2.141777844	0.06526426	2.577720179	725.102318	16.1248777	780.235526	56.3893588	72.848694	85.700032	0.8500428	7.603507324
NPM-4D-86-1.49	102.5405193	56.54717582	0.1003214	1.64338516	0.06559632	1.851463619	747.220513	12.6691832	783.304888	41.4274589	305.82673	219.33014	1.3943671	4.82914672
AR-4-27-00-9-74	42.04478538	453.8128954	0.1024843	2.297012323	0.06548189	3.157427191	748.052759	16.9891021	773.767727	67.2222621	132.64532	71.739277	1.8489915	3.437587485
AR-4-27-00-9-93	59.23226527	491.386628	0.105027	1.901489141	0.06468145	1.992724344	749.503218	14.5623648	748.955241	43.0651281	174.27936	139.26511	1.2514215	-0.073112049
NPM-4D-86-1.60	67.54702127	178.5752603	0.1053288	2.256071464	0.06779736	1.527631754	777.759275	18.318011	849.695885	32.6102841	199.02615	91.137687	2.1837964	9.249212797

Table 3: Zircon Data

Analysis_# Data	$^{206}Pb/^{204}Pb$	2%ERR	Raw Ratios: $^{206}Pb/^{238}U$	2%ERR	$^{207}Pb/^{206}Pb$	2%ERR	Age $^{206}Pb/^{238}U$	2SD	Age $^{207}Pb/^{206}Pb$	2SD	U	Th ppm	U/Th	% discordance
AR-4-27-00-9-84	299.2444777	145.8690254	0.1150081	1.645787558	0.0710108	1.347575862	825.312461	15.0714022	941.715044	30.9346092	811.19776	783.65708	1.0351438	14.10406212
AR-4-27-00-9-108	24.60818866	332.8047652	0.1230063	2.282597721	0.06786447	3.681827914	852.610439	18.7517414	856.295639	77.50943	62.812538	40.141725	1.5647693	0.432225517
NPM-4D-86-1.50	201.6448986	641.7765827	0.122509	2.216074737	0.07126817	1.438071161	901.139279	19.3259697	955.029203	31.837752	525.11138	175.14377	2.9981733	5.980199233
AR-4-27-00-9-81	98.59902084	246.2575592	0.1299499	2.709449565	0.07450317	1.642012011	927.106325	25.3455199	1039.28662	35.3514052	228.07356	168.27718	1.3553445	12.10004616
AR-4-27-00-9-80	165.0207692	526.3230724	0.1296734	1.828815316	0.06902064	1.405229363	928.225647	18.5782714	883.159922	31.6655823	400.276	250.38797	1.5986231	-4.855039877
AR-4-27-00-9-66	70.48425166	147.8609209	0.1304259	1.689077093	0.07093686	1.59403024	943.683503	15.6275084	941.0481	33.1915699	173.10168	111.02091	1.5591808	-0.279267602
AR-4-27-00-9-113	127.743683	90.92659719	0.1399488	1.8955861	0.07023904	1.614557944	953.561081	18.8745898	931.585342	36.4778558	304.46039	89.760382	3.391924	-2.304596925
AR-4-27-00-9-106	483.628826	434.8213906	0.1420905	2.194141762	0.07217258	0.969810141	977.090015	21.3934609	982.052427	23.9068995	1067.0475	1603.6269	0.6653963	0.507876596
AR-4-27-00-9-75	490.226167	46.45799657	0.1497392	2.157398998	0.07774295	1.288716212	1065.13924	22.3112109	1125.00278	27.4588405	1124.8955	413.9846	2.7172399	5.620254902
NPM-4D-86-1.27	558.5289621	195.1607504	0.154878	2.688621366	0.08492958	1.664755672	1127.76414	30.1119135	1307.46028	39.0923267	1192.8559	289.5132	4.1202123	15.93384135
AR-4-27-00-9-65	386.560721	112.1596495	0.1602758	1.863078518	0.08593799	1.58868156	1144.58347	20.4088063	1323.7224	31.269061	793.31416	253.83417	3.1253245	15.65101484
AR-4-27-00-9-71	78.76814051	79.67225769	0.1681279	1.568822307	0.0813017	1.571781402	1187.12055	18.6788398	1213.90641	31.8936331	160.61999	168.49418	0.9532673	2.256372314
NPM-4D-86-1.7	47.69478402	328.5599877	0.1724884	2.396242878	0.08411446	2.274956054	1243.3571	31.1346955	1283.5045	51.1302516	89.024069	86.998676	1.0232807	3.228951471
NPM-4D-86-1.5	300.3811245	118.5416749	0.1999442	2.091467519	0.1037598	1.251263013	1418.9492	29.2055288	1677.93837	28.8916295	502.66573	224.04336	2.2436092	18.25218062
NPM-4D-86-1.44	202.3211841	143.6740171	0.2152363	1.506440131	0.09828479	1.249605356	1511.45	21.7912939	1583.64494	26.1661736	287.89859	227.7755	1.2639577	4.77653489
AR-4-27-00-9-105	255.7127714	189.7686325	0.2361858	2.105579167	0.09917806	1.107125911	1555.60914	31.4786143	1599.54788	24.0668391	347.43968	146.80588	2.3666605	2.82453588
NPM-4D-86-1.34	164.3947624	1106.070459	0.234643	1.932307804	0.1010173	1.156907777	1636.89784	31.4491179	1636.26411	22.6439103	225.60622	54.433161	4.1446466	-0.038714957
NPM-4D-86-1.1	1091.944089	219.929003	0.2466857	2.094373123	0.135044	1.224283937	1708.91435	32.9677245	2149.36083	24.2668887	1444.4381	110.94508	13.019397	25.77346744
NPM-4D-86-1.6	253.5004058	95.69321099	0.2466041	1.681689396	0.1181827	1.216917535	1711.62182	30.3058652	1917.87931	29.4927907	343.43565	176.57452	1.9449899	12.05041251
AR-4-27-00-9-111	367.1413323	702.4030465	0.2760582	1.544535174	0.106559	0.989503468	1766.06837	27.4482109	1737.02269	22.9555971	416.31198	266.5051	1.5621164	-1.644652293
NPM-4D-86-1.13	243.1683735	1833.56355	0.2681207	2.006032731	0.1257118	1.20885072	1843.26341	43.4199168	2030.66244	29.3289292	290.82925	198.14141	1.4677863	10.16669847
AR-4-27-00-9-107	89.10400594	333.2488488	0.292446	1.995667918	0.1202023	1.44668696	1869.86598	33.1784297	1951.88935	27.357809	94.002617	115.05506	0.8170229	4.38659116
NPM-4D-86-1.46	98.65141536	70.94733509	0.3065814	2.143329961	0.1395787	1.529390229	2057.07003	39.1455186	2213.8839	28.683492	106.21621	117.7105	0.9023512	7.623166081
NPM-4D-86-1.32	390.7721003	130.6145594	0.3342158	1.996963938	0.1640146	1.323240126	2223.47528	41.6944358	2491.56894	26.9331616	384.42111	245.98537	1.5627804	12.0574158
NPM-4D-86-1.40	890.9766146	515.362602	0.3472109	2.083729226	0.196547	0.970776964	2292.5522	41.4432246	2791.31998	17.9085359	801.26105	412.9491	1.9403386	21.7560056
AR-4-27-00-9-94	205.7246854	501.4876215	0.3779908	1.514592154	0.1524709	1.16520923	2365.84927	33.8045611	2361.7931	21.2007861	172.96789	71.198037	2.4293913	-0.17144654
AR-4-27-00-9-91	566.711053	122.1638239	0.4214243	1.592707397	0.1810748	1.150308602	2594.33965	36.2352545	2650.69489	22.5985353	437.11067	217.41019	2.0105344	2.172238502
NPM-4D-86-1.19	61.149667	51.628094	0.03358	1.8479176	0.0534855	2.3079821	261.9374	6.861613	340.591	55.93502	562.712	554.693	1.01446	30.0276617
AR-4-27-00-9-116	50.716052	1572.0615	0.0579039	1.7476472	0.0581311	2.5884445	409.5654	7.93183	533.8515	58.9615	274.425	239.034	1.14806	30.345865
AR-4-27-00-9-67	54.817184	109.94104	0.0857015	1.6295183	0.0675407	2.4907245	635.1099	10.66206	839.6055	52.35439	207.803	86.8275	2.39328	32.1984548
AR-4-27-00-9-89	702.09219	66.504574	0.1559645	2.0276268	0.0923365	1.0096666	1090.204	20.91069	1459.858	25.63497	1471.77	733.627	2.00615	33.9068052
AR-4-27-00-9-87	21.746401	3317.2096	0.0583065	2.2516335	0.0597742	2.9035442	430.0401	9.978258	578.7253	65.63551	116.354	119.856	0.97078	34.5747378
NPM-4D-86-1.57	183.49867	115.78229	0.0528634	3.4602776	0.0586737	2.70861	402.5289	13.93422	542.1402	61.10746	1166.03	898.185	1.29821	34.6835353
NPM-4D-86-1.25	70.877561	161.92955	0.1830185	2.7136137	0.108671	1.6283029	1313.424	38.74363	1771.01	34.23576	128.841	282.529	0.45603	34.8391336
NPM-4D-86-1.29	66.646561	142.14262	0.0340928	1.9927554	0.0540136	1.8636077	265.6904	5.921984	364.1291	49.24173	637.928	359.554	1.77422	37.0501522
NPM-4D-86-1.21	164.09204	116.36153	0.0909627	1.8417201	0.0711594	1.6067997	686.2836	16.22316	954.7234	37.36958	592.812	409.107	1.44904	39.1149905
AR-4-27-00-9-117	187.12776	79.058222	0.0590799	2.000542	0.0595277	1.635558	417.2039	9.116889	586.2161	40.21019	1030.2	711.48	1.44797	40.510708
NPM-4D-86-1.24	234.89354	652.47013	0.1536611	2.0730966	0.0980767	1.3162475	1119.994	28.27714	1581.415	30.1428	485.075	504.927	0.96068	41.1985231
NPM-4D-86-1.33	16.66475	141.85346	0.0526778	2.071596	0.0596164	3.4416632	405.4053	9.037551	582.0066	75.2064	103.549	57.0868	1.81389	43.5616705
NPM-4D-86-1.17	26.688479	144.29348	0.040246	1.7807638	0.05616	2.8367056	312.68	8.511858	449.7074	69.13703	205.215	140.012	1.4657	43.8235423
NPM-4D-86-1.9	242.39562	61.182253	0.0650593	2.3776535	0.0637053	1.242658	497.6574	13.52053	719.7518	40.01665	1280.67	384.833	3.32786	44.627964
AR-4-27-00-9-79	21.898809	302.17032	0.0434501	1.9664388	0.0571371	3.0828655	326.3465	7.274382	479.5488	69.25262	159.069	89.2317	1.78265	46.9446632
AR-4-27-00-9-83	27.615883	1292.9537	0.0390781	1.6586928	0.0561831	2.9308582	292.6225	5.597055	442.209	66.92162	223.698	85.928	2.60332	51.1192648
NPM-4D-86-1.4	965.18909	33.229348	0.1553322	1.7933391	0.1058183	1.1008398	1128.135	20.39651	1713.761	25.51805	2237.06	170.912	13.089	51.9109577
AR-4-27-00-9-88	23.217287	282.36423	0.0409818	2.3481667	0.0568277	2.9878447	305.0232	7.216119	467.9283	69.77002	177.005	104.779	1.68932	53.4074414
AR-4-27-00-9-97	31.770051	123.58567	0.046273	1.4512059	0.0586323	3.1796234	339.3676	5.649437	539.085	70.37737	222.518	121.346	1.83374	58.8499007
AR-4-27-00-9-64	26.900369	474.01243	0.0355705	1.9038626	0.055893	2.629369	272.2654	5.292272	433.2397	58.92066	237.143	244.099	0.9715	59.1240525
NPM-4D-86-1.48	150.6952	56.297901	0.0369384	3.9625544	0.0563815	1.5693936	285.3795	11.30357	456.7782	39.61758	1401.21	454.491	3.08303	60.0599056
NPM-4D-86-1.45	529.42035	54.711874	0.2119901	4.2355185	0.1644077	1.0368584	1490.763	56.91563	2494.026	20.4327	882.174	333.362	2.64629	67.298608
NPM-4D-86-1.3	323.84209	65.81818	0.0430112	2.3108443	0.0594119	1.3524955	332.5872	7.945366	564.2196	34.73433	2560.29	307.911	8.31502	69.6456038
NPM-4D-86-1.26	79.161608	56.055933	0.0551033	1.9742621	0.0651402	2.2186794	424.2377	10.99002	771.8319	50.63331	488.75	223.074	2.19097	81.9338217
NPM-4D-86-1.53	64.296168	93.325799	0.0376051	2.3138887	0.0586571	3.2398306	289.5604	6.927884	542.4978	71.95447	558.606	219.478	2.54515	87.3522335
AR-4-27-00-9-96	76.65199	158.65596	0.0346969	2.0683807	0.0572554	2.3749301	256.3205	5.561547	486.665	53.26906	718.268	751.62	0.95563	89.8658331
AR-4-27-00-9-103	7.3631079	336.39064	0.0555654	3.0324652	0.0650289	5.4299422	401.8874	12.28956	764.2274	115.2751	41.8091	6.16754	6.7789	90.1595641
AR-4-27-00-9-95	61.822379	137.95607	0.0474191	1.749577	0.0633938	2.7122439	348.6932	6.512298	706.6598	58.41344	419.467	310.055	1.35288	102.659483
NPM-4D-86-1.51	62.777908	80.983566	0.0517155	2.4858374	0.0662139	2.584435	395.2003	9.809956	802.0362	55.55779	401.189	170.667	2.35071	102.944225
AR-4-27-00-9-109	16.534447	153.58555	0.0293286	2.4884229	0.0592366	3.8482201	213.5775	5.665138	567.6872	85.48123	183.895	278.891	0.65938	165.799196
AR-4-27-00-9-101	29.390095	62.520315	0.0616364	2.2175165	0.0857577	4.1110429	445.048	10.39631	1322.02	80.4551	158.536	108.435	1.46204	197.051154
AR-4-27-00-9-78	38.963918	31.592239	0.0607363	1.9704901	0.0885025	4.8373577	451.9763	9.36418	1378.405	93.98181	230.59	99.119	2.32639	204.972761
AR-4-27-00-9-85	262.17095	46.185629	0.0308806	2.158931	0.0646966	1.6603683	232.0221	5.4588	748.0147	37.91456	2964.51	999.491	2.96602	222.389421
AR-4-27-00-9-110	237.31013	26.141675	0.0300099	1.5570514	0.0654164	1.1606369	218.2571	3.836433	780.3344	29.24101	2777.26	1166.81	2.38021	257.529881
AR-4-27-00-9-68	96.519654	23.902004	0.0243489	6.1318477	0.0710207	2.1290176	186.8058	11.38486	943.2603	44.46058	1485.75	905.81	1.64025	404.941709
NPM-4D-86-1.42	259.04459	10.842307	0.0440387	3.3216656	0.113311	1.1198498	339.5831	11.08467	1845.47	22.65352	2607.06	664.33	3.92435	443.451617
NPM-4D-86-1.47	68.160207	11.764974	0.005801	2.0444015	0.1557736	1.5330987	45.67501	0.985818	2402.242	29.15023	5167.28	1839.25	2.80945	5159.4234
AR-9-10-03-7														
AR 9-10-03-7.1	4411.07	145.34	0.02287	2.75	0.05171	1.72	194.2	6.0	11	±231	2782	736	3.78	-94.1
AR 9-10-03-7.6	7326.75	276.03	0.02214	2.79	0.05250	3.17	188.7	6.6	99	±197	2223	532	4.18	-47.4
AR 9-10-03-7.10	6746.34	288.08	0.02599	1.89	0.05241	1.52	221.4	6.3	125	±117	1619	627	2.58	-43.8
AR 9-10-03-7.11	4082.26	66.21	0.02395	2.14	0.05163	1.50	204.8	6.1	132	±116	1936	190	10.20	-35.4
AR 9-10-03-7.8	3533.62	75.71	0.02329	1.65	0.05319	1.97	198.5	5.9	143	±100	2766	739	3.74	-27.8
AR 9-10-03-7.18	9420.97	59.59	0.02518	1.80	0.05063	1.19	216.2	4.6	158	±165	5527	2069	2.67	-26.8
AR 9-10-03-7.3	2371.62	104.59	0.02190	2.82	0.05428	3.67	186.2	6.6	144	±200	2911	316	9.22	-22.6
AR 9-10-03-7.20	-6809.53	931.49	0.02501	2.27	0.05059	1.35	215.0	5.4	170	±166	2379	331	7.19	-20.7
AR 9-10-03-7.19	183538.47	158.27	0.02507	1.94	0.05093	1.31	215.5	4.8	178	±165	3243	958	3.38	-17.2
AR 9-10-03-7.15	4076.90	56.12	0.02394	1.83	0.05198	1.63	205.2	5.8	180	±117	2178	475	4.59	-12.4
AR 9-10-03-7.16	10276.64	62.08	0.02430	2.05	0.05166	1.35	208.5	6.2	188	±115	5736	947	6.06	-9.8
ar-9-10-03-7-22	-11402.45	281.53	0.02731	2.72	0.04984	1.35	205.2	6.1	185	±43	15834	4901	3.23	-9.6
AR 9-10-03-7.13	2625.71	52.08	0.02509	1.79	0.05281	1.57	214.6	5.5	201	±101	1896	716	2.65	-6.3
AR 9-10-03-7.14	3631.37	54.12	0.02411	1.82	0.05249	1.61	206.5	5.8	196	±117	2001	301	6.66	-5.3
ar-9-10-03-7-15	-8325.07	4471.13	0.02473	1.98	0.05092	1.36	188.4	4.3	232	±40	22472	8964	2.51	22.9
ar-9-10-03-7-29	-4408.77	1836.17	0.02583	3.33	0.05066	3.47	192.7	6.8	226	±81	18655	6265	2.98	17.3
ar-9-10-03-7-12	21191.83	958.44	0.02524	1.86	0.05038	1.46	192.8	4.2	206	±40	31713	5436	5.83	7.0
ar-9-10-03-7-28	-24210.98	247.41	0.02615	1.70	0.05044	1.12	195.2	4.2	215	±28	22657	12854	1.76	10.3
ar-9-10-03-7-20	###########	347.14	0.02611	1.91	0.05095	1.41	197.5	4.2	235	±41	13481	2666	5.06	19.0
ar-9-10-03-7-24	-8734.72	1149.73	0.02632	2.33	0.05060	1.58	197.6	5.2	221	±48	8008	8159	0.98	12.0
ar-9-10-03-7-27	-13591.84	220.39	0.02660	1.95	0.04999	1.70	198.7	4.7	194	±58	12498	2704	4.62	-2.3
ar-9-10-03-7-25	6523.68	119.05	0.02656	2.47	0.05025	1.53	199.2	5.5	205	±47	14234	3039	4.68	3.1
AR 9-10-03-7.17	6995.59	68.65	0.02337	2.70	0.05298	2.27	200.8	7.6	256	±140	2567	869	2.95	27.4
ar-9-10-03-7-4	-3912.94	702.71	0.02703	2.15	0.05185	1.84	208.9	7.7	268	±47	6653	3561	1.87	28.4
ar-9-10-03-7-9	-3989.76	483.69	0.02763	2.74	0.05061	1.73	212.1	6.2	215	±41	11938	5246	2.28	1.3
ar-9-10-03-7-26	17431.10	319.02	0.02864	2.17	0.05141	3.01	213.9	5.3	259	±76	2432	589	4.13	21.0
ar-9-10-03-7-19	-5748.37	560.32	0.02881	2.53	0.05098	1.74	217.8	6.0	236	±47	7978	3347	2.38	8.4
ar-9-10-03-7-2	-22172.54	764.29	0.02848	1.91	0.05178	2.39	220.3	7.6	265	±58	3976	613	6.49	20.2

Table 3: Zircon Data

Analysis_#			Raw Ratios:				Age	2SD	Age	2SD	U	Th	U/Th	% discordance
Data	$^{206}Pb/^{204}Pb$	2%ERR	$^{206}Pb/^{238}U$	2%ERR	$^{207}Pb/^{206}Pb$	2%ERR	$^{206}Pb/^{238}U$		$^{207}Pb/^{206}Pb$			ppm		
ar-9-10-03-7-30	-39735.44	580.36	0.02555	1.94	0.05122	1.46	190.4	4.4	252	±35	16343	9373	1.74	32.1
ar-9-10-03-7-17	6867.84	98.19	0.02505	1.79	0.05143	1.58	190.1	4.0	256	±44	16257	3578	4.54	34.6
ar-9-10-03-7-10	-75593.86	382.57	0.02354	2.15	0.05125	1.34	181.0	4.2	244	±37	26744	26402	1.01	34.7
ar-9-10-03-7-14	5863.61	284.38	0.02475	2.42	0.05151	2.05	188.7	5.0	258	±53	14006	1941	7.22	36.5
ar-9-10-03-7-7	2664.16	70.43	0.02697	2.26	0.05220	1.91	207.4	9.2	285	±53	7467	2075	3.60	37.6
ar-9-10-03-7-1	-3374.81	166.37	0.02359	2.49	0.05161	2.10	183.2	6.9	257	±52	18088	10888	1.66	40.3
ar-9-10-03-7-16	20289.41	103.68	0.02578	2.09	0.05189	2.05	195.7	4.6	276	±53	12037	1626	7.40	40.9
ar-9-10-03-7-3	-2568.23	690.81	0.02768	2.44	0.05286	1.95	214.0	8.0	312	±48	7175	1474	4.87	45.9
ar-9-10-03-7-13	10261.78	74.69	0.02586	1.93	0.05223	1.54	197.2	4.4	289	±43	12359	3424	3.61	46.7
AR 9-10-03-7.12	2180.91	43.09	0.02271	2.49	0.05509	2.28	194.5	6.0	292	±108	2896	549	5.27	50.1
ar-9-10-03-7-21	-109675.28	111.21	0.02465	2.38	0.05213	1.14	185.7	4.7	289	±36	30619	21036	1.46	55.6
ar-9-10-03-7-18	-4447.26	510.54	0.02879	1.81	0.05369	2.23	217.8	4.7	354	±56	4360	2262	1.93	62.5
ar-9-10-03-7-6	2930.03	62.71	0.02639	2.16	0.05338	1.91	203.2	8.9	336	±50	8095	1726	4.69	65.3
ar-9-10-03-7-5	2709.47	78.23	0.02899	2.02	0.05484	2.98	223.6	8.0	396	±70	3123	1480	2.11	77.0
ar-9-10-03-7-8	-984.63	156.05	0.02430	3.53	0.05465	3.07	187.1	7.2	389	±70	7134	2330	3.06	108.1
ar-9-10-03-7-23	1606.68	70.60	0.03235	3.39	0.05749	1.84	242.2	8.6	509	±50	6939	2606	2.66	110.0
AR 9-10-03-7.7	73.25	14.51	0.02545	3.02	0.21642	2.95	216.5	8.5	2814	±73	200	3	70.23	1199.9
AR-9-10-03-4														
AR-9-10-03-4-9	17798.05383	143.7475061	0.07129283	1.87511423	0.05629488	1.139358499	500.907025	10.5118973	473.204995	31.5909437	3357.4374	1011.8473	3.3181264	-5.530373731
AR-9-10-03-4-14	9752.2734	148.16712	0.0605863	2.1518737	0.058203	1.408563	429.6949	9.922084	543.1308	42.31388	3080.77	2251.88	1.36808	26.3991619
AR-9-10-03-4-5	28747.609	336.32807	0.0646271	1.5875417	0.0571155	1.0220739	454.5278	7.772286	507.4655	25.77936	5514.5	2151.55	2.56303	11.6467361
AR-9-10-03-4-21	10487.321	149.95114	0.0642137	1.8831555	0.0579559	1.4416325	457.0841	9.910054	528.666	48.28139	1726.08	666.125	2.59122	15.6605484
AR-9-10-03-4-19	21550.994	194.98774	0.0653981	2.3817749	0.0573129	1.4660991	463.9522	11.71512	506.6987	57.76179	2488.34	1345.78	1.849	9.21356178
AR-9-10-03-4-23	-23550.561	103.18133	0.0654045	1.7138657	0.0567808	1.405101	465.616	10.07495	482.8932	37.93887	2778.51	1860.14	1.49371	3.71060274
AR-9-10-03-4-25	6021.3844	119.85732	0.0654222	2.2175882	0.059618	1.6032364	466.2234	11.90608	588.6432	40.85309	1851.05	628.452	2.94541	26.2577561
AR-9-10-03-4-7	5939.7708	517.63915	0.0672388	2.3145279	0.0593438	3.2792491	473.0431	11.26414	589.5051	73.07715	821.323	445.529	1.84348	24.6197452
AR-9-10-03-4-12	-278794.9	1126.4771	0.0669953	2.7829165	0.0558763	2.0478632	473.1788	14.06838	453.9386	58.29699	4338.05	4077.2	1.06398	-4.0661537
AR-9-10-03-4-22	-5616.4058	72.897222	0.0669696	2.9658837	0.0580705	2.1786264	476.1728	14.70933	532.6438	55.51109	2606.77	808.578	3.22389	11.8593675
AR-9-10-03-4-8	-46855.029	244.36805	0.0678307	2.0003211	0.0571673	1.2974244	477.2381	10.53179	507.5528	34.2429	2283.18	719.13	3.17492	6.35209873
AR-9-10-03-4-6	-5058.7325	143.89159	0.0680497	1.6899352	0.0583199	1.6270273	478.3396	8.728459	552.0183	38.42432	833.393	545.381	1.52809	15.4030046
AR-9-10-03-4-3	-61346.502	1762.2912	0.0682258	1.8242301	0.0571297	1.194285	478.55	9.193721	508.7211	30.2014	2625.12	1305.44	2.01092	6.304689
AR-9-10-03-4-11	-70531.219	210.68718	0.0678512	1.5146	0.0578672	1.3870611	478.7606	8.214045	531.6023	40.41078	2682.75	902.847	2.97144	11.0371974
AR-9-10-03-4-15	7560.7284	91.382922	0.0678138	2.2717718	0.0582147	1.3017557	479.2803	11.52607	543.2165	40.64591	2342.71	1767.72	1.32528	13.340035
AR-9-10-03-4-30	19474.366	192.61356	0.0673755	1.9648727	0.057175	1.0134596	481.0488	13.57875	494.4215	27.39534	3826.36	1391.97	2.74888	2.77990741
AR-9-10-03-4-13	-24647.223	76.217979	0.0691265	1.7227352	0.056997	1.2913733	487.8359	9.440478	497.5433	40.80418	2864.48	915.309	3.12952	1.98988279
AR-9-10-03-4-29	19322.535	146.34277	0.0684095	1.9796841	0.0577863	1.1764488	487.9749	13.81367	518.1707	30.27274	2579.43	906.1	2.84673	6.18799826
AR-9-10-03-4-28	-20987.233	67.742086	0.0692039	1.8924549	0.058199	1.1507442	493.2462	13.68216	534.123	29.7119	4033.74	1233.95	3.26898	8.28730694
AR-9-10-03-4-2	-8497.1047	97.28873	0.0707234	2.3582923	0.0573919	1.3779056	495.2248	11.82627	519.1302	32.1396	1624.5	783.809	2.07257	4.82718169
AR-9-10-03-4-17	7135.1446	107.38964	0.071779	2.2948864	0.0569543	1.4522427	507.1098	12.88063	493.5626	47.906	3091.46	1312.52	2.35536	-2.6714482
AR-9-10-03-4-20	-7342.2455	48.413705	0.0718501	1.8188833	0.0582537	1.3573069	508.1624	10.71296	542.0482	46.98597	1669.51	783.621	2.1305	6.66830205
AR-9-10-03-4-18	-32675.342	66.100566	0.0721432	1.8035444	0.0578855	1.2353092	509.7655	10.31925	528.8749	54.88068	1983.69	803.15	2.46988	3.74866949
AR-9-10-03-4-1	-53273.017	349.41002	0.0736185	2.8685862	0.0570531	1.3483291	514.5141	14.68482	506.4679	31.5978	1304.21	583.84	2.23386	-1.5638411
AR-9-10-03-4-26	27701.499	297.50108	0.0825242	2.1166569	0.059042	1.3094065	583.5522	14.30164	566.2481	35.71921	1230.53	461.54	2.66613	-2.9653039
AR-9-10-03-4-4	7214.974565	38.1316214	0.05466972	3.020679455	0.05803562	1.439803004	386.398345	11.6225661	542.863972	34.0158084	8506.8181	3469.509	2.4518795	40.49334824
AR-9-10-03-4-24	8178.09446	184.7063816	0.06526472	4.154313387	0.06519512	3.329154084	464.965259	19.7218084	779.915647	72.9982349	2858.4616	1295.0467	2.2072267	67.73632691
AR-9-10-03-4-16	1086.47612	58.60669351	0.0736878	4.366530145	0.06998781	3.426140924	519.877514	22.3981865	931.846298	75.4072944	802.01951	487.10056	1.6465173	79.24343175
AR-9-10-03-4-10	1411.435502	65.43970974	0.05528437	3.859258955	0.06741998	4.572729034	391.920281	15.2564708	859.05918	97.1167634	2067.6921	693.85775	2.9799942	119.1923261
AR-9-10-03-4-7	350.9812672	44.86322059	0.06582126	3.962282095	0.09105316	3.708150272	463.434017	18.3944046	1456.25812	72.3988658	606.61761	242.04932	2.5061735	214.2320289
AR-9-10-03-4-27	98.19763929	34.3336326	0.08569133	5.333792812	0.1359077	15.32388525	605.16114	32.0874958	2173.4866	267.356585	2049.2365	563.99534	3.6334281	259.158322

Table 4: Mapping Data

Latitude	Longitude	Z (m)	Station Number	Lithology / Structure	Bedding Strike	Bedding Dip Azimuth	Bedding Dip	Bedding Dip Direction	Foliation	Foliation Strike	Foliation Dip Azimuth	Foliation Dip	Dip Direction	Fracture Strike	Fracture Dip	Fracture Dip Direction	Fault Strike	Fault Dip	Dip Direction	Lineation T	&P	Rake Angle	Rake Direction
			7-15-10-1	Quartzite					S1	145	55	31	NE										
			7-15-10-2	Quartzite					S1	143	53	26	NE										
			7-15-10-3	Quartzite					S1	40	130	14	SE										
			7-15-10-4	Quartzite					S1	100	10	42	NE										
			7-15-10-4	Marble					S1	88	358	44	NE										
			7-15-10-4	FS													125	68	NE				
			7-15-10-4	FS													122	72	NE				
			7-15-10-4	FS													74	49	NW	326	48	78	S
			7-15-10-4	Striation																327	48	79	S
			7-15-10-4	Striation																327	48	79	S
			7-15-10-5	Marble					S1	128	38	54	NE										
			7-15-10-5	Fold Axis					Axis	114	24	38	NE										
			7-15-10-5	Fold Hinge																14	67		
			7-15-10-6	Qtz Bio Schist					S1	292	202	27	SW										
			7-15-10-6	Fold Axis																			
			7-15-10-6	Fold Hinge																			
			7-15-10-7	Bio Schist					S1	110	20	21	NE										
			7-15-10-7	Crenulation Cleavage					S2	102	12	84	NE										
			7-15-10-8	Shear Zone					S1	127	37	34	NW										
			7-15-10-8	Rake																105	14	26	S
			7-15-10-8	Rake																103	15	28	S
			7-15-10-8	Rake																102	16	29	S
			7-15-10-8	Rake																106	14	25	S
			7-15-10-9	Shear Zone					S1	19	109	30	SE										
			7-15-10-10	Amphibolite					S1	80	350	53	NW										
			7-15-10-10	Mica Qzt																			
			7-15-10-11	Thrust													123	52	NE				
37.57187	75.4315	3622	7-16-10-1	Mylonitic Gr					S1	102	12	70	NE										
37.57187	75.43149	3626	7-16-10-2	Shear Zone					S1	123	33	58	NE										
37.57368	75.43851	3690	7-16-10-2	Rake						118		72	NE									32	E
37.57368	75.43851	3690	7-16-10-2	Rake						118		72	NE									32	E
37.57367	75.43851	3690	7-16-10-2	Rake						118		72	NE									33	E
37.57367	75.43851	3690	7-16-10-2	Rake						118		72	NE									37	E
37.57575	75.44391	3749	7-16-10-3	Mylonitic granite					S1	124	34	70	NE										
37.57575	75.44391	3749	7-16-10-3	Shear zone						50		57	NW										
37.57575	75.44391	3749	7-16-10-3	Rake																105	34	36	E
37.57575	75.44391	3749	7-16-10-3	Rake																106	33	35	E
37.57575	75.44391	3749	7-16-10-3	Rake																105	34	36	E
37.57575	75.44391	3749	7-16-10-3	Rake																105	34	36	E
37.57855	75.45063	3829	7-16-10-4	Qz Bio Schist					S1	125	35	26	NE										
37.57855	75.45063	3829	7-16-10-4	Lineation																98	11		
37.57855	75.45063	3829	7-16-10-4	Lineation																100	10		
37.57855	75.45063	3829	7-16-10-4	Lineation																98	22		
37.57855	75.45063	3829	7-16-10-4	Lineation																100	17		
37.5803	75.45655	3885	7-16-10-5	Qz Bio Schist					S1	130	40	59	NE										
37.58223	75.4619	3942	7-16-10-6	Qz Bio Schist					S1	120	30	35	NE										
37.58346	75.47291	4088	7-16-10-7	Augen Gneiss					S1	118	28	74	SW										
37.58346	75.47291	4088	7-16-10-7	Rake						122		85	SW							301	8	8	N
37.58346	75.47291	4088	7-16-10-7	Rake						122		85	SW							301	8	8	N
37.58346	75.47291	4088	7-16-10-7	Rake						122		85	SW							301	9	9	N
37.48007	75.3083	3769	7-17-10-1	Bio Gneiss					S1	55	145	52	SE										
37.47998	75.3082	3784	7-17-10-1	Fault													15	10	SE				
37.47998	75.3082	3784	7-17-10-1	Fault													5	55	SE				
37.47854	75.29639	3939	7-17-10-2	Micaceous Qzt					S1	144	54	28	NE										
37.47507	75.29504	3905	7-17-10-3	Bio Granit																			
37.47507	75.29504	3905	7-17-10-3	FS													171	51	NE				
37.47507	75.29504	3905	7-17-10-3	Rake																10	22	29	W
37.47507	75.29504	3905	7-17-10-3	Rake																10	22	29	W
37.47507	75.29504	3905	7-17-10-3	Rake																10	22	29	W
37.47507	75.29504	3905	7-17-10-3	Rake																11	23	30	W
37.47507	75.29504	3905	7-17-10-3	Rake																12	24	31	W
37.47507	75.29504	3905	7-17-10-3	FS													178	34	NE				
37.47507	75.29504	3905	7-17-10-3	FS													163	63	NE				
37.47336	75.2876	3996	7-17-10-4	Hbl Bio Granite																			
37.47336	75.2876	3996	7-17-10-4	FS													107	87	NE				
37.47336	75.2876	3996	7-17-10-4	Rake																294	67	67	W
37.47336	75.2876	3996	7-17-10-4	Rake																294	66	66	W
37.47336	75.2876	3996	7-17-10-4	Rake																294	67	67	W
37.47336	75.2876	3996	7-17-10-4	Rake																299	76	76	W
37.47336	75.2876	3996	7-17-10-4	Rake																298	75	75	W
37.4712	75.26301	4243	7-17-10-5	Bio Granite																			
37.4712	75.26301	4243	7-17-10-5	FS													160	74	NW				
37.4712	75.26301	4243	7-17-10-5	Rake																91	73	84	E
37.4712	75.26301	4243	7-17-10-5	Rake																91	73	84	E
37.4712	75.26301	4243	7-17-10-5	Rake																94	73	83	E
37.4712	75.26301	4243	7-17-10-5	Rake																91	73	84	E
37.4712	75.26301	4243	7-17-10-5	FS													170	48	SW				
37.4712	75.26301	4243	7-17-10-5	FS													315	30	SW				
37.52218	75.28221	3635	7-18-10-1																				
37.52205	75.28126	3649	7-18-10-2	Bio Hbl Schist					S1	173	83	46	NE										
37.52205	75.28126	3649	7-18-10-2	FS													142	25	NE				
37.52205	75.28126	3649	7-18-10-2	Rake																28	23	68	N
37.52205	75.28126	3649	7-18-10-2	Rake																24	22	64	N
37.52205	75.28126	3649	7-18-10-2	Rake																22	22	62	N
37.52205	75.28126	3649	7-18-10-2	Rake																33	24	73	N
37.52205	75.28126	3649	7-18-10-2	Rake																30	23	70	N
37.52205	75.28126	3649	7-18-10-2	FS													122	23	NE				
37.52205	75.28126	3649	7-18-10-2	Rake																86	14	38	E
37.52205	75.28126	3649	7-18-10-2	Rake																87	14	37	E
37.52205	75.28126	3649	7-18-10-2	Rake																82	15	42	E
37.52205	75.28126	3649	7-18-10-2	Rake																77	17	47	E
37.52153	75.27541	3687	7-18-10-3	Bio Schist???					S1	22	112	73	SE										
37.52153	75.27541	3687	7-18-10-3	Bio Schist???					S1?	174	84	48	NE										
37.51126	75.30381	3708	7-18-10-4	Marble					S1	70	340	53	NW										
37.50386	75.31585	3586	7-18-10-5	Marble					S1	131	41	51	NE										
37.50385	75.31584	3587	7-18-10-6	Marble					S1	174	84	63	NE										
37.50168	75.31626	3603	7-18-10-7	Marble					S1	143	53	45	NE										
37.49424	75.3134	3727	7-18-10-8	Marble					S1	170	80	46	NE										
37.24541	75.4363	3619	7-18-10-9	Marble					S1	17	107	22	SE										
37.28433	75.46999	3695	7-20-10-1	Slate					S1	96	6	45	NE										
37.28433	75.46999	3695	7-20-10-1	Tension Gash										75	47	NW							
37.28433	75.46999	3695	7-20-10-1	Tension Gash										77	49	NW							
37.28433	75.46999	3695	7-20-10-1	Tension Gash										74	36	NW							
37.28433	75.46999	3695	7-20-10-1	Tension Gash										78	45	NW							
37.28433	75.46999	3695	7-20-10-1	Tension Gash										74	36	NW							
37.28537	75.47108	3754	7-20-10-2	Slate					S1	106	16	58	NE										
37.28663	75.47226	3767	7-20-10-3	Marble					S1	71	339	38	NW										
#N/A	#N/A	#N/A		Marble					S1	125	35	46	NE										
#N/A	#N/A	#N/A		Slate					S1	122	32	45	NE										
#N/A	#N/A	#N/A	7-20-10-4																				
#N/A	#N/A	#N/A	7-20-10-4																				
37.28918	75.47776	3819	7-20-10-5	Phyllitic Schist					S1	119	29	48	NE										
37.28918	75.47776	3819	7-20-10-5	Phyllitic Schist					S2	138	48	75	NE										
37.29221	75.4934	3942	7-20-10-6	Slates/Pilites					S1	28	298	31	NW										
37.29221	75.4934	3942	7-20-10-6	Fold limb 1						72	342	44	NW										
37.29221	75.4934	3942	7-20-10-6	Fold limb 2						144	234	44	SW										
37.29222	75.50108	4002	7-20-10-7	Marble/Slate					S1	97	7	18	NE										
37.29222	75.50108	4002	7-20-10-7	Fold limb 2					S1	137	227	21	SW										
37.29222	75.50108	4002	7-20-10-7	Fold 1 Limb 1						60	150	90	SE										
37.29222	75.50108	4002	7-20-10-7	Fold 1 Limb 2						0		0											
37.29222	75.50108	4002	7-20-10-7	Fold 2 Limb 1						55	145	13	SE										
37.29222	75.50108	4002	7-20-10-7	Fold 2 Limb 2						64	334	54	NW										
37.29222	75.50108	4002	7-20-10-7	Fold 3 Limb 1						54	144	29	SE										
37.29222	75.50108	4002	7-20-10-7	Fold 3 Limb 2						108	18	21	NE										
37.29222	75.50108	4002	7-20-10-7	Fold 4 axial plane						10	100	67	SE										
37.29222	75.50108	4002	7-20-10-7	Fold 4 Hinge																32	48		
37.29525	75.50727	4061	7-20-10-8	Marble					S1	162	72	74	NE										
37.29525	75.50727	4061	7-20-10-8	Fold 1 Hinge																72	18		
37.29525	75.50727	4061	7-20-10-8	Fold 1 Axial plane						80	350	83	NW										
37.29525	75.50727	4061	7-20-10-8	Fold 2						?		?	?										
37.30013	75.51777	4191	7-20-10-9	Phyllite/Marble					S1	100	10	19	NE										
37.30478	75.52011	4289	7-20-10-10	Qzt					S1	108	18	28	NE										
37.31218	75.45181	3720	7-20-10-11	Axial Planer cleavage					S1	118	28	40	NE										
37.31218	75.45181	3720	7-20-10-11	Fold Axis																296	21		
37.31139	75.45729	3718	7-20-10-12	cleavage					S1	119	29	47	NE										
37.31328	75.46559	3740	7-20-10-13	Marble					S1	0	90	61	E										
37.31745	75.4755	3781	7-20-10-14	Marble					S1	143	53	22	NE										
37.71641	75.34727	3292	7-21-10-1	Migmatitic Schist					S1	104	14	86	NE										
37.71866	75.38042	3936	7-21-10-2	Migmatitic Schist					S1	116	206	46	SW										
37.71605	75.38703	4027	7-21-10-3	Migmatitic Schist					S1	143	233	51	SW										
37.71755	75.39057	3993	7-21-10-4	Metabasalt? Chert? Qzt?					S1	112	202	55	SW										
37.71755	75.39057	3993	7-21-10-4	Migmatitic Schist					S1	132	222	66	SW										
37.71755	75.39057	3993	7-21-10-4	mineral stretching																300	36		
37.7194	75.37465	3791	7-21-10-5	Migmatitic Schist					S1	115	205	75	SW										
37.7194	75.37465	3791	7-21-10-5	other measurement					S1	121	211	61	SW										
37.72066	75.37087	3694	7-21-10-6	Migmatitic Schist					S1	120	210	84	SW										
37.72173	75.36741	3632	7-21-10-7	Migmatitic Schist					S1	109	199	81	SW										
37.7236	75.36039	3537	7-21-10-8	Migmatitic Schist					S1	101	191	78	SW										
37.72118	75.35616	3465	7-21-10-9	Migmatitic Schist					S1	95	185	68	SW										
37.72118	75.35616	3465	7-21-10-9	plane of lineations						93	183	68	SW										
37.72118	75.35616	3465	7-21-10-9	Mineral stretching																234	57	65	W
37.72118	75.35616	3465	7-21-10-9	Mineral stretching																235	56	64	W
37.72118	75.35616	3465	7-21-10-9	Mineral stretching																234	57	65	W
37.70745	75.33838	3219	7-21-10-10	Migmatitic Schist					S1	135	45	80	NE										
37.30644	75.3972	3179	7-22-10-1	Slate					S1	130	40	46	NE										
37.6225	75.73546	4096	7-25-10-1	L Tectonite					S1	108	198	53	SW										
37.6225	75.73546	4096	7-25-10-1	L Tectonite																257	39		
37.62148	75.73612	4101	7-25-10-2	Conglomerate	143	233	28	SW															
37.6226	75.73809	4144	7-25-10-3	sighted fault, same below													332	69	SW				
37.62228	75.73863	4171	7-25-10-3	Foliation in gouge													125	67	SW				
37.62309	75.73868	4166	7-25-10-4	Chert																			
37.62309	75.73868	4166	7-25-10-4	FS													164	57	SW				
37.62309	75.73868	4166	7-25-10-4	Rake																332	17	21	N
37.62309	75.73868	4166	7-25-10-4	Rake																334	15	18	N
37.62309	75.73868	4166	7-25-10-4	Rake																334	15	18	N
37.62309	75.73868	4166	7-25-10-4	Rake																336	13	15	N
37.62309	75.73868	4166	7-25-10-4	Rake																336	13	15	N
37.6248	75.74165	4277	7-25-10-5	Chert	124	214	62	SW															
37.6248	75.74165	4277	7-25-10-5	FS													11	83	NW				
37.6248	75.74165	4277	7-25-10-5	Rake																8	22	22	N

Table 4: Mapping Data

Latitude	Longitude	Z (m)	Station Number	Lithology / Structure	Bedding Strike	Bedding Dip Azimuth	Bedding Dip	Bedding Dip Direction	Foliation	Foliation Strike	Foliation Dip Azimuth	Foliation Dip	Dip Direction	Fracture Strike	Fracture Dip	Fracture Dip Direction	Fault Strike	Fault Dip	Dip Direction	Lineation T	&P	Rake Angle	Rake Direction
37.6248	75.74165	4277	7-25-10-5	Rake																8	22	22	N
37.6248	75.74165	4277	7-25-10-5	Rake																7	27	27	N
37.6248	75.74165	4277	7-25-10-5	Rake																8	20	20	N
37.6248	75.74165	4277	7-25-10-5	Rake																8	26	26	N
37.62597	75.74379	4369	7-25-10-6	Chert																			
37.62597	75.74379	4369	7-25-10-6	FS													155	81	SW				
			7-25-10-7														166	60	sw				
			7-25-10-7														156	62	sw				
			7-25-10-7														158	72	sw				
			7-25-10-7														176	65	sw				
37.62545	75.74266	4391	7-25-10-8														159	65	ne				
																						83	n
																						82	n
																						85	n
#N/A	#N/A	#N/A	7-25-10-8																			86	n
37.62294	75.73753	4171	7-25-10-9	Conglomerate	150	240	15	SW															
37.61853	75.72182	3875	7-25-10-10	Conglomerate	88	358	14	NW															
37.61853	75.72182	3875	7-25-10-10	FS													6	85	NW				
37.61853	75.72182	3875	7-25-10-10	Rake																3	35	35	N
37.61853	75.72182	3875	7-25-10-10	Rake																3	35	35	N
37.61853	75.72182	3875	7-25-10-10	Rake																4	21	21	N
37.61853	75.72182	3875	7-25-10-10	Rake																4	20	20	N
37.61853	75.72182	3875	7-25-10-10	Rake																4	19	19	N
37.61853	75.72182	3875	7-25-10-10	Rake																4	25	25	N
37.61869	75.71635	3841	7-25-10-11	Conglomerate	115	25	19	NE															
37.61745	75.70789	3817	7-25-10-12	Conglomerate???	5	95	34	SE															
37.61745	75.70789	3817	7-25-10-12	FS													0	57	W				
37.6129	75.70333	3765	7-25-10-13	Shale	29	119	17	SE															
37.61014	75.70006	3739	7-25-10-14	FS													156	61	SW				
37.61014	75.70006	3739	7-25-10-14	Rake																284	55	69	N
37.61014	75.70006	3739	7-25-10-14	Rake																290	52	65	N
37.61014	75.70006	3739	7-25-10-14	Rake																281	56	71	N
37.61014	75.70006	3739	7-25-10-14	Rake																281	56	71	N
37.61014	75.70006	3739	7-25-10-14	Rake																287	54	67	N
37.61014	75.70006	3739	7-25-10-14	FS													86	32	SE				
37.61179	75.6946	3688	7-25-10-15	Diorite or Gabbro																			
37.61179	75.6946	3688	7-25-10-16	metavolcanic																			
37.61179	75.6946	3688	7-25-10-16	FS													54	53	NW				
37.61179	75.6946	3688	7-25-10-16	Rake																9	43	59	E
37.61179	75.6946	3688	7-25-10-16	Rake																358	48	68	E
37.61179	75.6946	3688	7-25-10-16	Rake																357	48	69	E
37.61179	75.6946	3688	7-25-10-16	Rake																357	48	69	E
37.61179	75.6946	3688	7-25-10-16	Rake																357	48	69	E
#N/A	#N/A	#N/A	7-25-10-17	amphibolite																			
#N/A	#N/A	#N/A	7-25-10-18	Shale/Basement	162	252	8	SW															
37.60825	75.67632	3556	7-25-10-19	Conglomerate	20	290	8	NW															
37.60666	75.66919	3504	7-25-10-20	Chert + Basalt on outcrop																			
37.60515	75.66527	3475	7-25-10-20	Shale	121	31	4	NE															
#N/A	#N/A	#N/A	7-25-10-21	Shale	88	358	14	NW															
#N/A	#N/A	#N/A	7-25-10-22	Shale	63	333	32																
#N/A	#N/A	#N/A	7-25-10-23	Shale	11	281	19	NE															
#N/A	#N/A	#N/A	7-25-10-23	FS													13	50	SE				
#N/A	#N/A	#N/A	7-25-10-23	Rake																75	46	71	N
#N/A	#N/A	#N/A	7-25-10-23	Rake																75	46	71	N
#N/A	#N/A	#N/A	7-25-10-23	Rake																73	46	70	N
37.57634	75.67658	3351	7-26-10-1	L-Tectonite					S1	107	197	42	SW										
37.57634	75.67658	3351	7-26-10-1	Mineral streatching																246	26		
37.57194	75.67113	3377	7-26-10-2	Sandstone	102	12	22	NE															
37.57194	75.67113	3377	7-26-10-2	Schist					S1	126	216	51	SW										
37.57194	75.67113	3377	7-26-10-2	Lineation																129	2		
37.57261	75.67114	3379	7-26-10-3	Mylonitic Schist					S1	65	55	39	SE										
37.5613	75.66609	3493	7-26-10-3	lineation																135	32		
37.5613	75.66609	3536	7-26-10-4	Mylonitic Schist					S1	134	224	19	SW										
37.5613	75.66609	3536	7-26-10-4	Lineation																167	9		
37.54312	75.65833	3586	7-26-10-5	Migmatitic Schist					S1	166	256	22	SW										
37.54312	75.65833	3586	7-26-10-5	Lineation																186	12		
37.53638	75.6588	3633	7-26-10-6	Schist					S1	99	189	33	SW										
37.4959	75.60376	4030	7-26-10-7	Gneiss					S1	152	62	53	NE										
37.48883	75.58799	4156	7-26-10-8	Diorite					S1	181	91	67	SE										
37.48132	75.5823	4319	7-26-10-9	Schist					S1	140	50	51	NE										
37.48132	75.5823	4319	7-26-10-9	lineation																139	10		
37.47043	75.57366	4564	7-26-10-10	Amphibolite					S1	80	350	34	NW										
37.47043	75.57366	4564	7-26-10-10	Amphibolite					S2	96	6	48	NE										
37.47043	75.57366	4564	7-26-10-10	Mineral stretching																92	11		
37.46873	75.57035	4509	7-26-10-11	Amphibolite					S1	104	14	48	NE										
37.46873	75.57035	4509	7-26-10-11	Mineral stretching																295	4		
37.65548	75.58548	3229	7-27-10-1	Ss/mstn	90	0	14	N															
37.65548	75.58548	3229		Ss/mdst	358	88	5	E															
#N/A	#N/A	#N/A	7-27-10-2	Ss/mdst	110	20	15	NE															
37.65993	75.55557	3175	7-27-10-3	Schist					S1	139	229	49	SW										
37.65993	75.55557	3175	7-27-10-3	Mineral stretching																148	11		
37.78074	75.49954	3083	7-27-10-4	Mylonitic schist					S1	76	166	30	SE										
37.78883	75.46096	3005	7-27-10-4	Fold hinge						45		23	NW										
37.82509	75.44272	2987	7-27-10-4	Fold axis																250	16		
37.79245	75.47667	3023	7-27-10-4	mineral stretching																166	25		
37.795	75.48778	3105	7-27-10-5	conglomerates/Ss	134	224	55	SW															
37.795	75.48778	3105	7-27-10-5	Conglomerate	143	234	56	SW															
37.66852	75.70435	4269	7-28-10-1	granodiorite					S1	109	199	71	SW										
37.66852	75.70435	4269	7-28-10-1	FS													206	80	NW				
37.66852	75.70435	4269	7-28-10-1	Rake																19	34	35	N
37.66852	75.70435	4269	7-28-10-1	Rake																20	32	33	N
37.66852	75.70435	4269	7-28-10-1	Rake																20	32	33	N
37.66852	75.70435	4269	7-28-10-1	Rake																21	25	25	N
37.66852	75.70435	4269	7-28-10-1	Rake																19	33	34	N
37.66852	75.70435	4269	7-28-10-1	Rake																19	34	35	N
37.66779	75.70361	4311	7-28-10-2	Granite					S1	115	205	53	SW										
37.66589	75.70172	4234	7-28-10-3	Marble					S1	143	53	78	NE										
37.66589	75.70172	4234	7-28-10-3	Fold Axis																327	6		
37.66589	75.70172	4234	7-28-10-3	Fold Plane						126	216	32	SW										
#N/A	#N/A	#N/A	7-28-10-4	Marble	110	20	29	SW															
#N/A	#N/A	#N/A	7-28-10-4	FS													130	46	SW				
#N/A	#N/A	#N/A	7-28-10-5	Schist					S1	135	45	54	NE										
37.66135	75.6916	3985	7-28-10-6	Qzt					S1	132	42	72	NE										
37.66135	75.6916	3985	7-28-10-6	FS													90	45	S				
37.66135	75.6916	3985	7-28-10-6	Rake																107	16	23	E
37.66135	75.6916	3985	7-28-10-6	Rake																105	15	21	E
37.66135	75.6916	3985	7-28-10-6	Rake																102	12	17	E
37.66135	75.6916	3985	7-28-10-6	Rake																102	12	17	E
#N/A	#N/A	#N/A	7-28-10-7	Qzt					S1	106	196	73	SW										
#N/A	#N/A	#N/A	7-28-10-8	Amphibolite					S1	121	31	43	NE										
37.65915	75.68287	3879	7-28-10-9	Amphibolite					S1	99	209	26	SW										
37.65915	75.68287	3879	7-28-10-9	Mineral oriented																179	25		
#N/A	#N/A	#N/A	7-28-10-10	Amphibolite					S1	122	212	60	SW										
#N/A	#N/A	#N/A	7-28-10-10	mineral stretching																155	41		
#N/A	#N/A	#N/A	7-28-10-11	Phyllite					S1	101	191	63	SW										
#N/A	#N/A	#N/A	7-28-10-11	mineral streatching																157	48		
#N/A	#N/A	#N/A	7-28-10-12	Phyllite					S1	140	230	69	SW										
#N/A	#N/A	#N/A	7-28-10-12	Kink axial plane						48	318	44	NW										
37.65229	75.66984	3668	7-28-10-13	Phyllite																			
37.65229	75.66984	3668	7-28-10-13	axial plane of folds						191	101	35	SE										
37.65097	75.66753	3641	7-28-10-14	Phyllite					S1	83	173	43	SE										
37.65097	75.66753	3641	7-28-10-14	Axial plane of folds						147	57	36	NE										
37.64792	75.6613	3603	7-28-10-15	Qzt					S1	120	210	62	SW										
37.78952	75.46406	2984	7-29-10-1	Qzt					S1	65	155	53	SE										
37.78952	75.46406	2984	7-29-10-1	mineral stretching																240	16		
37.7909	75.47244	2994	7-29-10-2	Migmatitic Schist					S1	50	140	43	SE										
37.78666	75.48548	3021	7-29-10-3	Qzt/Migmatitic Schist					S1	73	163	52	SE										
37.76349	75.50543	3033	7-29-10-4	Migmatitic Schist																			
37.74726	75.51974	3065	7-29-10-5	Migmatitic Schist					S1	117	207	64	SW										
37.73231	75.50748	3088	7-29-10-6	Migmatitic Schist					S1	124	214	42	SW										
37.73231	75.50748	3088	7-29-10-6	Fold Axial Plane						116	206	63	SW										
37.73231	75.50748	3088	7-29-10-6	Hinge																179	56		
37.73231	75.50748	3088	7-29-10-6	Isoclinal Fold						126	216	45	SW										
37.73231	75.50748	3088	7-29-10-6	Qz rod elongation																306	4		
37.71837	75.50867	3092	7-29-10-7	Migmatitic Schist					S1	88	178	55	SE										
37.71837	75.50867	3092	7-29-10-7	Migmatitic Schist					S1	66	156	31	SE										
37.71447	75.5153	3100	7-29-10-8	Schist					S1	107	197	55	SW										
37.67826	75.5349	3156	7-29-10-9	Schist					S1	85	175	31	SE										
37.67826	75.5349	3156	7-29-10-9	Mineral stretching																260	12		
37.67826	75.5349	3156	7-29-10-9	Schist						100	190	35	SW										
37.67826	75.5349	3156	7-29-10-9	mineral stretching																137	24		
37.67134	75.54328	3165	7-29-10-10	Granite (deformed)					S1	96	186	54	SW										
37.67134	75.54328	3165	7-29-10-10	Lineation																158	47		
37.67134	75.54328	3165	7-29-10-10	FS													142	20	SW				
37.67134	75.54328	3165	7-29-10-10	Rake																173	11	33	E
37.67134	75.54328	3165	7-29-10-10	Rake																174	11	34	E
37.67134	75.54328	3165	7-29-10-10	Rake																174	11		
37.58296	75.6762	3423	7-29-10-11	Granite																			
37.57488	75.67439	3438	7-29-10-12	Schist					S1	116	206	29	SW										
37.57488	75.67439	3438	7-29-10-12	Marbles					S1	146	236	22	SW										
37.57488	75.67439	3438	7-29-10-12	Marble					S1	1963	243	34	SW										
37.57488	75.67439	3438	7-29-10-12	Lineation																228	37		
37.56678	75.68664	3447	7-29-10-13	Qzt					S1	14	284	38	NW										
37.56678	75.68664	3447	7-29-10-13	lineation																230	33		
37.55441	75.70205	3488	7-29-10-14	Qzt					S1	90	180	51	S										
37.5503	75.70248	3494	7-29-10-15	Migmatitic Schist					S1	48	138	49	SE										
37.5503	75.70248	3494	7-29-10-15	Lineation																76	38		
37.7859	75.50539	3123	7-30-10-1	Schist					S1	82	172	77	SE										
37.78594	75.50595	3131	7-30-10-1	Phillite					S1	122	202	41	SW										
37.78731	75.50769	3145	7-30-10-2	Qzt					S1	111	201	80	SW										
37.86597	75.31255	3083	7-30-10-3	Schist					S1	83	173	53	SE										
37.86598	75.31249	3087	7-30-10-4	Schist					S1	111	201	72	SW										
37.86598	75.31249	3087	7-30-10-4	mineral stretching																195	46		
37.85081	75.42108	3089	7-30-10-5	granite																			
37.85081	75.42108	3089	7-30-10-5	FS													136	62	SW				
37.85081	75.42108	3089	7-30-10-5	Rake																305	19	22	W
37.85081	75.42108	3089	7-30-10-5	Rake																303	23	26	W
37.85081	75.42108	3089	7-30-10-5	Rake																304	22	25	W

Table 4: Mapping Data

Latitude	Longitude	Z (m)	Station Number	Lithology / Structure	Bedding Strike	Bedding Dip Azimuth	Bedding Dip	Bedding Dip Direction	Foliation	Foliation Strike	Foliation Dip Azimuth	Foliation Dip	Dip Direction	Fracture Strike	Fracture Dip	Fracture Dip Direction	Fault Strike	Fault Dip	Dip Direction	Lineation T	&P Angle	Rake Direction
37.85081	75.42108	3089	7-30-10-5	Rake																304	22	25	W
37.83519	75.41604	3067	7-30-10-7	Migmatitic Schist					S1	75	165	46	SW									
37.83519	75.41604	3067	7-30-10-7	FS													2	65	SE			
37.83519	75.41604	3067	7-30-10-7	Rake																180	12	
37.81753	75.43972	2955	7-30-10-8	Migmatitic Schist					S1	83	173	67	SE									
37.796	75.45153	2956	7-30-10-9	Granite																		
37.796	75.45153	2956	7-30-10-9	Schist					S1	84	174	49	SE									
37.69388	75.64943	4191	8-1-10-1	Marble/qzt					S1	162	252	17	SW									
37.69251	75.64597	4112	8-1-10-2	Schist					S1	150	60	29	NE									
37.69251	75.64597	4112	8-1-10-2	Mineral stretching																62	16	
37.69109	75.64066	4050	8-1-10-3	Schist/Qzt					S1	127	37	67	NE									
37.68932	75.63783	3997	8-1-10-4	Schist					S1	135	45	39	NE									
37.68932	75.63783	3997	8-1-10-4	lineation																146	13	
37.6889	75.63654	3960	8-1-10-5	Schist					S1	136	46	53	NE									
37.68578	75.63181	3873	8-1-10-6	Schist					S1	130	40	67	NE									
37.68578	75.63181	3873	8-1-10-6	lineation																129	4	
37.68496	75.62885	3814	8-1-10-7	Schist					S1	130	220	74	SW									
37.68354	75.62499	3786	8-1-10-8	Marble					S1	127	37	77	NE									
37.68354	75.62499	3786	8-1-10-8	Lineation						136	46	81	NE							130	33	
37.68284	75.62302	3731	8-1-10-9	Qzt					S1	127	37	80	NE									
37.68284	75.62302	3731	8-1-10-9	mineral stretching																125	8	
37.68206	75.62073	3709	8-1-10-10	Qzt					S1	124	34	74	SW									
37.67921	75.61464	3627	8-1-10-11	Conglomerate	138	228	4	SW														
37.67593	75.60893	3566	8-1-10-12	Schist/qzt					S1	150	240	34	SW									
37.76918	75.57678	3906	8-1-10-13	Conglomerate	178	268	6	SW														
37.76918	75.57678	3906	8-2-10-1	Schist					S1	126	216	47	SW									
37.76678	75.56993	3699	8-2-10-2	Marble					S1	52	142	33	SE									
37.76559	75.56674	3622	8-2-10-3	Schist					S1	147	57	34	NE									
37.76559	75.56674	3622	8-2-10-3	Lineation																142	14	
37.76333	75.55814	3463	8-2-10-4	Schist					S1	140	50	26	NE									
37.76333	75.55814	3463	8-2-10-4	lineation																132	1	
37.76145	75.55629	3410	8-2-10-5	Schist					S1	110	20	76	NE									
37.75657	75.55306	3263	8-2-10-6	Granite					S1	115	205	48	SW									
37.75657	75.55306	3263	8-2-10-6	mineral stretching																305	51	
#N/A	#N/A	#N/A																				
#N/A	#N/A	#N/A																				
37.29149	75.41744	3615	6-12-2011-1	Granite																		
37.29064	75.41234	3626	6-12-2011-2	Schist					S1	137	47	51	NE									
37.29022	75.40859	3636	6-12-2011-3	Schist - grnt bearing					S1	109	19	70	NE									
37.28836	75.40222	3646	6-12-2011-4	Schist - Bio, Grnt					S1	99	9	67	NE									
37.33001	75.39484	3434	6-12-2011-5	Schist - Bio					S1	107	17	68	NE									
37.32853	75.39007	3443	6-12-2011-6	Schist - Bio, grnt bearing					S1	113	203	74	SW									
37.32029	75.34339	3662	6-12-2011-7	Schist - grnt bio					S1	113	203	70	SW									
37.32074	75.3428	3639	6-12-2011-8	sheared granite					S1	114	24	85	NE									
37.32216	75.33721	3601	6-12-2011-9	sheared granite					S1	120	30	79	NE									
37.32812	75.3894	3532	6-12-2011-10	Schist - Bio					S1	121	31	72	NE									
37.27587	75.38057	3603	6-12-2011-11	Granite																		
37.27591	75.37984	3629	6-12-2011-12	sheared granite					S1	122	32	58	NE									
37.27386	75.37935	3618	6-12-2011-13	Schist - bio					S1	93	3	57	NE									
37.25682	75.36792	3656	6-12-2011-14	Schist - bio					S1	123	33	48	NE									
#N/A	#N/A	#N/A	6-13-2011-1	Schist					S1	141	41	30	NE									
#N/A	#N/A	#N/A	6-13-2011-1	mineral stretching																33	29	74	N
#N/A	#N/A	#N/A	6-13-2011-1	mineral stretching																33	29	74	N
#N/A	#N/A	#N/A	6-13-2011-1	mineral stretching																33	29	74	N
#N/A	#N/A	#N/A	6-13-2011-1	mineral stretching																33	29	74	N
#N/A	#N/A	#N/A	6-13-2011-1	mineral stretching																32	29	73	N
#N/A	#N/A	#N/A	6-13-2011-1	mineral stretching																32	29	73	N
#N/A	#N/A	#N/A	6-13-2011-1	Schist					S1	150	60	35	NE									
#N/A	#N/A	#N/A	6-13-2011-1	mineral stretching																15	26	51	N
#N/A	#N/A	#N/A	6-13-2011-1	mineral stretching																16	27	52	N
#N/A	#N/A	#N/A	6-13-2011-1	mineral stretching																14	26	50	N
#N/A	#N/A	#N/A	6-13-2011-1	mineral stretching																12	25	48	N
37.7883	75.2701	3084	6-14-2011-1	migmatitic schist					S1	88	358	33	NW									
37.7883	75.2701	3087	6-14-2011-2	migmatitic schist					S1	103	13	39	NW									
37.7883	75.2701	3087	6-14-2011-2	migmatitic schist					S1	113	23	34	NE									
37.7883	75.2701	3087	6-14-2011-2	mineral stretching																100	9	16	S
37.7883	75.2701	3087	6-14-2011-2	mineral stretching																101	8	14	S
37.7883	75.2701	3087	6-14-2011-2	mineral stretching																99	9	17	S
37.7906	75.2662	3083	6-14-2011-3	granite					S1	123	33	66	NE									
37.7864	75.2759	3105	6-14-2011-4	migmatitic schist					S1	113	23	71	NE									
37.7803	75.2848	3113	6-14-2011-5b	migmatitic schist					S1	116	26	65	NE									
37.7791	75.2932	3141	6-14-2011-6	schist- bio					S1	111	21	82	NE									
37.7731	75.2969	3141	6-14-2011-7	migmatitic schist					S1	99	9	71	W									
37.768	75.2928	3122	6-14-2011-8	migmatitic schist					S1	108	18	76	NE									
37.767	75.2917	3125	6-14-2011-9a	Schist - Bio					S1	106	16	78	NE									
37.767	75.2917	3125	6-14-2011-9a	mineral stretching																97	35	36	E
37.767	75.2917	3125	6-14-2011-9a	mineral stretching																98	33	34	E
37.767	75.2917	3125	6-14-2011-9a	mineral stretching																97	35	36	E
37.767	75.2917	3125	6-14-2011-9a	mineral stretching																99	29	30	E
37.7626	75.2994	3123	6-14-2011-9b	migmatitic schist					S1	119	29	45	NE									
37.7602	75.3066	3131	6-14-2011-10	migmatitic schist					S1	97	7	73	NE									
37.7472	75.3035	3149	6-14-2011-11	Schist- Bio					S1	94	4	74	NE									
37.7472	75.3035	3149	6-14-2011-11	mineral stretching																303	60	64	W
37.7472	75.3035	3149	6-14-2011-11	mineral stretching																303	60	64	W
37.7472	75.3035	3149	6-14-2011-11	mineral stretching																305	61	65	W
37.7472	75.3035	3149	6-14-2011-11	mineral stretching																303	60	64	W
37.7472	75.3035	3149	6-14-2011-11	mineral stretching																303	60	64	W
37.7472	75.3035	3149	6-14-2011-11	Schist- Bio					S1	94	4	74	N									
37.7472	75.3035	3149	6-14-2011-11	mineral stretching																306	61	66	W
37.7472	75.3035	3149	6-14-2011-11	mineral stretching																300	56	60	W
37.7472	75.3035	3149	6-14-2011-11	mineral stretching																307	62	67	W
37.7472	75.3035	3149	6-14-2011-11	mineral stretching																306	61	66	W
37.7472	75.3035	3149	6-14-2011-11	mineral stretching																307	62	67	W
37.7458	75.3076	3147	6-14-2011-12	migmatitic schist					S1	101	11	72	NE									
37.7429	75.312	3152	6-14-2011-13	migmatitic schist					S1	122	32	48	NE									
37.7293	75.3177	3165	6-14-2011-14	Schist					S1	113	23	72	NE									
#N/A	#N/A	#N/A	6-15-2011-1	Conglomerate																		
37.6447	75.722	4099	6-15-2011-2	Chert	300	210	23	SE														
37.6459	75.7206	4114	6-15-2011-2	FS													143	56	SE			
37.6459	75.7206	4114	6-15-2011-2	slickenline																284	43	55	NW
37.6459	75.7206	4114	6-15-2011-2	slickenline																280	45	59	NW
37.6459	75.7206	4114	6-15-2011-2	slickenline																280	45	59	NW
37.6459	75.7206	4114	6-15-2011-2	slickenline																288	40	51	NW
37.6459	75.7206	4114	6-15-2011-2	FS													112	84	NE			
37.6459	75.7206	4114	6-15-2011-2	slickenline																111	10	10	E
37.6459	75.7206	4114	6-15-2011-2	slickenline																111	9	9	E
37.6459	75.7206	4114	6-15-2011-2	slickenline																111	10	10	E
#N/A	#N/A	#N/A	6-16-2011-0	granite																		
#N/A	#N/A	#N/A	6-17-2011-1		68	338	22	NW														
#N/A	#N/A	#N/A	6-17-2011-2	ss & sltstn	59	329	25	NW														
#N/A	#N/A	#N/A	6-17-2011-3																			
#N/A	#N/A	#N/A	6-17-2011-4	Conglomerate	32	122	27	SE														
#N/A	#N/A	#N/A	6-17-2011-4	FS													7	86	W			
#N/A	#N/A	#N/A	6-17-2011-5	ss & sltstn	173	83	6	E														
#N/A	#N/A	#N/A	6-17-2011-5	FS													17	50	E			
37.4731	75.6572	3802	6-18-2011-1	Schist - Amphibole					S1	83	173	51	NW									
37.4741	75.6559	3792	6-18-2011-2	Schist - Amphibole					S1	113	23	34	NE									
37.4773	75.6539	3777	6-18-2011-3	same as previous					S1	99	9	50	NE									
37.4862	75.6585	3728	6-18-2011-4	same as previous					S1	110	20	41	NE									
37.4862	75.6585	3728	6-18-2011-4	same as previous					S2	123	33	72	NE									
37.4886	75.6585	3718	6-18-2011-5	marble					S1	63	153	21	NW									
37.4948	75.6606	3718	6-18-2011-6	schist - brnt, musc, bio					S1	150	60	43	NE									
37.4986	75.6628	3716	6-18-2011-7	schist - grnt, musc, bio					S1	8	98	66	SE									
37.5009	75.6643	3709	6-18-2011-8	same as previous					S1	178	268	50	SW									
37.5009	75.6643	3709	6-18-2011-8	same as previous					S1	165	255	22	SW									
37.5021	75.6651	3736	6-18-2011-8	same as previous					S1	158	248	81	SW									
37.506	75.6674	3721	6-18-2011-9	migmatitic _					S1	348	258	70	SW									
37.51	75.6728	3696	6-18-2011-10	migmatitic					S1	131	221	65	SW									
37.5169	75.6774	3663	6-18-2011-11	same as previous					S1	110	200	85	SW									
37.5201	75.679	3655	6-18-2011-12	schist- bio, migmatitic					S1	103	13	80	NE									
37.5227	75.6791	3646	6-18-2011-13	migmatitic					S1	105	195	60	SW									
37.5244	75.6792	3641	6-18-2011-13	migmatitic					S1	183	273	19	W									
37.5285	75.681	3626	6-18-2011-14a	same as previous					S1	161	251	31	SW									
37.5309	75.6814	3617	6-18-2011-14b	same as previous					S1	122	212	30	SW									
37.5359	75.6834	3603	6-18-2011-15	schist - musc, bio					S1	125	215	33	SW									
37.5359	75.6835	3584	6-18-2011-16	same as previous					S1	103	193	64	SW									
37.5421	75.6846	3577	6-18-2011-17	same as previous					S1	168	258	55	SW									
37.5463	75.6861	3561	6-18-2011-18	same as previous					S1	133	223	60	SW									
37.5463	75.6858	3537	6-18-2011-19	same as previous					S1	83	353	25	W									
37.5532	75.7007	2972	6-19-2011-1	schist - bio					S1	128	218	75	SW									
37.8306	75.5123	2989	6-19-2011-2	bio					S1	97	187	78	SW									
37.8306	75.5123	2989	6-19-2011-2	mineral stretching																2	78	89	W
37.8306	75.5123	2989	6-19-2011-2	mineral stretching																2	78	89	W
37.8306	75.5123	2989	6-19-2011-2	mineral stretching																2	78	89	W
37.8306	75.5123	2989	6-19-2011-2	mineral stretching																2	78	89	W
37.8308	75.5105	3007	6-19-2011-3	greenschist					S1	131	221	38	SW									
37.8275	75.5093	3017	6-19-2011-4	FS													138	69	SW			
37.8272	75.5089	3045	6-19-2011-5	greenschist					S1	145	235	58	SW									
37.8272	75.5089	3045	6-19-2011-5	FS													149	45	NE			
37.8272	75.5089	3045	6-19-2011-5	slickenline																350	20	29	W
37.8272	75.5089	3045	6-19-2011-5	slickenline																350	19	28	W
37.8272	75.5089	3045	6-19-2011-5	slickenline																350	20	29	W
37.8272	75.5089	3045	6-19-2011-5	slickenline																350	20	29	W
37.8272	75.5089	3045	6-19-2011-5	FS													157	85	SW			
37.7582	75.5288	3073	6-20-2011-1	Conglomerate	48	138	1	SE														
37.7547	75.5322	3165	6-20-2011-2	Conglomerate	133	43	5	NE														
37.7523	75.5303	3178	6-20-2011-3	same as previous	119	209	5	SW														
37.7575	75.5263	3122	6-20-2011-4	Conglomerate	118	28	1	NE														
37.7571	75.525	3112	6-20-2011-5	same as previous	34	304	0	nw														
37.7565	75.5232	3102	6-20-2011-6	same as previous	34	304	0	NW														
37.7559	75.5208	3085	6-20-2011-7	same as previous	34	304	0	nw														
37.755	75.5176	3068	6-20-2011-8	same as previous	34	304	1	NW														
37.7835	75.5017	3090	6-20-2011-9	same as previous	28	304	3	NW														
37.7898	75.4981	3188	6-20-2011-10	same as previous	130	220	15	SW														
37.7899	75.4978	3182	6-20-2011-11	same as previous	120	210	18	SW														
37.7893	75.4955	3135	6-20-2011-12	same as previous	123	213	33	SW														
37.7893	75.4955	3134	6-20-2011-13	same as previous	23	293	18	NW														
37.7894	75.4953	3127	6-20-2011-14	Conglomerate	113	203	18	SW														
37.7893	75.4937	3111	6-20-2011-15	same as previous	123	213	31	SW														
37.7904	75.4933	3121	6-20-2011-16	same as previous	110	200	33	SW														

Table 4: Mapping Data

Latitude	Longitude	Z (m)	Station Number	Lithology / Structure	Bedding Strike	Bedding Dip Azimuth	Bedding Dip	Bedding Dip Direction	Foliation	Foliation Strike	Foliation Dip Azimuth	Foliation Dip	Dip Direction	Fracture Strike	Fracture Dip	Fracture Dip Direction	Fault Strike	Fault Dip	Dip Direction	Lineation T	&P	Rake Angle	Rake Direction
37.7906	75.4936	3136	6-20-2011-17	Conglomerate	133	223	29	sw															
#N/A	#N/A	#N/A	6-22-2011-1	schist - bio chlorite musc					S1	177	86	49	E										
#N/A	#N/A	#N/A	6-22-2011-1	main fault													115	60	SW				
37.744	75.6219	4399	6-22-2011-1	FS																			
37.7437	75.6213	4366	6-22-2011-1	FS													123	45	NE				
37.7433	75.6212	4347	6-22-2011-1	FS													253	77	SW				
37.7421	75.6198	4273	6-22-2011-1	Schist					S1	163	73	48	NE				163	48	NE				
37.7421	75.6198	4272	6-22-2011-1	Schist					S1	147	57	50	NE				147	50	NE				
37.7401	75.6182	4194	6-22-2011-1	Schist					S1	181	91	44	NE				178	44	NE				
37.7387	75.6146	4103	6-22-2011-2	schist-bio musc					S1	128	38	81	NE										
37.738	75.6142	4071	6-22-2011-3	same as previous					S1	120	30	68	NE										
37.738	75.6142	4071	6-22-2011-3	mineral lineation																312	28	30	NW
37.738	75.6142	4071	6-22-2011-3	mineral lineation																313	29	31	NW
37.738	75.6142	4071	6-22-2011-3	mineral lineation																314	30	33	NW
37.738	75.6142	4071	6-22-2011-3	mineral lineation																314	31	34	NW
37.738	75.6142	4071	6-22-2011-3	Axial Plane Fold 1						148	58	49	NE										
37.738	75.6142	4071	6-22-2011-3	Hinge Fold 1																150	4		
37.738	75.6142	4071	6-22-2011-3	Axial Plane Fold 2						138	48	29	NE										
37.738	75.6142	4071	6-22-2011-3	Hinge Fold 2																129	6		
37.7373	75.6137	4061	6-22-2011-4	schist - musc bio					S1	95	5	13	NE										
37.7373	75.6137	4061	6-22-2011-4	mineral stretching																107	4		
37.7373	75.6137	4061	6-22-2011-5	same as previous					S1	157	67	36	NE										
37.7368	75.6135	4042	6-22-2011-6	chlorite rich quartzite					S1	82	352	64	NW										
37.7355	75.6128	4029	6-22-2011-7	schist (almost a phyllite)					S1	122	32	31	NE										
37.7342	75.6121	4001	6-22-2011-8	Marble	76	166	31	SE															
37.7326	75.6106	3938	6-22-2011-9	marble/gypsum																			
37.7283	75.6048	3856	6-22-2011-10	back in marble																			
37.727	75.6022	3833	6-22-2011-11	phyllite					S1	156	66	78	NE										
37.7263	75.6011	3811	6-22-2011-12	phyllite/marble																			
37.7263	75.6011	3811	6-22-2011-12	Axial Plane Fold 1						141	51	31	NE										
37.7263	75.6011	3811	6-22-2011-12	Hinge Fold 1																151	2		
37.7263	75.5999	3798	6-22-2011-13	quartzite - micaceous					S1	124	34	64	NE										
37.7261	75.5964	3749	6-22-2011-14	Phyllite (qtz rich)					S1	105	15	49	NE										
37.7261	75.5964	3749	6-22-2011-14	mineral lineation																336	43		
37.7235	75.596	3726	6-22-2011-15	Phyllite (qtz rich)					S1	129	39	65	NE										
37.723	75.5947	3698	6-22-2011-16	same as previous					S1	113	23	60	NE										
37.723	75.5947	3698	6-22-2011-16	Kink Fold Limb 1						123	33	64	NE										
37.723	75.5947	3698	6-22-2011-16	Kink Fold Limb 2						140	230	75	SW										
37.722	75.5922	3670	6-22-2011-17	granite																			
#N/A	#N/A	#N/A	6-22-2011-18	granite					S1	88	178	74	SE										
37.7059	75.5462	3275	6-23-2011-1	schist - musc, bio					S1	128	218	77	SW										
37.7603	75.5891	3937	6-23-2011-2	marble																			
37.76	75.5896	3933	6-23-2011-3	marble/phyllite																			
37.7593	75.5852	3853	6-23-2011-4	qtzite - bio rich					S1	94	4	35	N										
37.7593	75.5852	3853	6-23-2011-4	qtzite - bio rich					S1	128	38	35	NE										
37.7589	75.5834	3810	6-23-2011-5	same as previous					S1	138	228	32	SW										
37.7564	75.5808	3718	6-23-2011-6	schist - bio					S1	133	223	62	SW										
37.7564	75.5808	3718	6-23-2011-6	schist - bio					S1	150	60	38	NE										
37.7558	75.5792	3661	6-23-2011-7	schist - chlorite, bio					S1	148	58	47	NE										
37.7558	75.5792	3661	6-23-2011-7	mineral stretching																138	10	14	SE
37.7558	75.5792	3661	6-23-2011-7	mineral stretching																136	12	17	SE
37.7558	75.5792	3661	6-23-2011-7	mineral stretching																138	11	15	SE
37.7553	75.577	3610	6-23-2011-8	same as previous					S1	151	61	45	NE										
37.755	75.5748	3580	6-23-2011-9	schist - bio , qtz rich					S1	154	64	32	NE										
37.756	75.5721	3530	6-23-2011-10	same as previous					S1	152	62	41	NE										
37.7565	75.5703	3499	6-23-2011-11	same as previous					S1	163	73	52	NE										
37.7562	75.5657	3438	6-23-2011-12	qtzite - bio musc rich					S1	163	73	65	SW										
37.7566	75.562	3401	6-23-2011-13	Schist - Must, bio					S1	73	163	19	SE										
37.7578	75.5549	3334	6-23-2011-14	phyllite - green					S1	135	225	50	SW										
37.7944	75.551	3700	6-24-2011-1	schist - bio plag					S1	134	224	65	SW										
37.7941	75.5503	3714	6-24-2011-2	schist - mustc bio					S1	139	229	51	SW										
37.7926	75.5485	3654	6-24-2011-3	same as previous					S1	134	224	90	W										
37.792	75.5475	3627	6-24-2011-4	schist - bio					S1	126	36	82	NE										
37.7915	75.5459	3608	6-24-2011-5	cobble conglomerate	12	282	9	W															
37.7917	75.5464	3602	6-24-2011-6	qtzite- bio rich					S1	123	213	80	SW										
37.7912	75.546	3582	6-24-2011-7						S1	107	197	53	SW										
37.7905	75.5454	3563	6-24-2011-8	qtzite - bio rich					S1	148	238	70	SW										
37.7905	75.5454	3563	6-24-2011-8	FS													104	72	NE				
37.7905	75.5454	3563	6-24-2011-8	FS													96	68	N				
37.79	75.5449	3548	6-24-2011-9	Schist - Bio					S1	147	237	49	SW										
37.7894	75.544	3528	6-24-2011-10	schist , bio epidote					S1	133	223	81	SW										
37.7885	75.5422	3500	6-24-2011-11	conglomerate	27	117	5	SE															
37.7862	75.5385	3429	6-24-2011-12	qtzite - bio and musc					S1	125	35	38	NE										
37.7847	75.5359	3389	6-24-2011-13	phyllite/schist - bio					S1	125	35	52	NE										
37.7847	75.5359	3389	6-24-2011-13	mineral stretching																314	12	15	N
37.7847	75.5359	3389	6-24-2011-13	mineral stretching																314	12	15	N
37.7847	75.5359	3389	6-24-2011-13	mineral stretching																315	13	16	N
37.7847	75.5359	3389	6-24-2011-13	mineral stretching																316	14	18	N
37.7844	75.535	3366	6-24-2011-14	Axial Plane Fold 1						110	20	26	NE										
37.7844	75.535	3366	6-24-2011-14	Hinge Fold 1																307	23		
37.784	75.5344	3368	6-24-2011-15	phyllite					S1	119	29	53	NE										
37.7825	75.5313	3326	6-24-2011-16	marble																			
37.7821	75.5302	3313	6-24-2011-17	phyllite- bio rich					S1	138	228	71	SW										
37.7805	75.5248	3250	6-24-2011-18	granite																			
37.7462	75.6024	3811	6-25-2011-1	qtzite/schist bio rich					S1	170	80	9	NE										
37.7462	75.6024	3811	6-25-2011-1	mineral lineation																147	5		
37.7446	75.599	3813	6-25-2011-2	qtzite/schist bio rich					S1	146	56	37	NE										
37.7446	75.599	3813	6-25-2011-2	mineral stretching																103	21		
37.7443	75.5978	3791	6-25-2011-3	schist - qtz rich bio					S1	147	57	30	NE										
37.7445	75.5957	3756	6-25-2011-4	qtite - bio rich					S1	159	69	24	NE										
37.7435	75.5932	3719	6-25-2011-5	qtzite - bio rich					S1	159	69	40	NE										
37.743	75.5894	3721	6-25-2011-6	boulder conglomerate																			
37.7436	75.5852	3619	6-25-2011-7	schist - bio					S1	143	233	37	SW										
37.7436	75.5852	3619	6-25-2011-7	schist - bio					S1	100	190	47	SW										
37.7427	75.5777	3542	6-25-2011-8	qtzite - micaceous					S1	150	240	57	SW										
37.7427	75.5777	3542	6-25-2011-8	Fold Limb 1						176	266	28	SW										
37.7427	75.5777	3542	6-25-2011-8	Fold Limb 2						47	137	17	SE										
37.7427	75.5777	3542	6-25-2011-8	Fold Limb 3						127	217	30	SW										
37.7427	75.5777	3542	6-25-2011-8	Fold Limb 4						141	51	39	NE										
37.7464	75.5702	3453	6-25-2011-9	phyllite					S1	123	213	59	SW										
37.7456	75.5637	3383	6-25-2011-10	granite																336	24		
37.7451	75.557	3336	6-25-2011-11	marble																			
37.6121	75.5432	3577	6-26-2011-1	schist - bio					S1	153	243	53	SW										
37.614	75.5435	3575	6-26-2011-2	schist - bio					S1	153	243	90	W										
37.6336	75.5611	3331	6-26-2011-3	schist - bio migmatitic					S1	150	240	53	SW										
37.6418	75.5581	3327	6-26-2011-4	same as previous					S1	156	246	86	NE										
37.6491	75.5593	3260	6-26-2011-5	same as previous					S1	147	237	90	W										
#N/A	#N/A	#N/A	6-27-2011-1	conglomerate	23	293	9	NW															